

**DEVELOPMENT OF ADVANCED TECHNOLOGY FOR PHOTOCATALYTIC
DEGRADATION OF ORGANIC POLLUTANTS IN AQUEOUS SOLUTION
WITH MODIFIED g-C₃N₄ COMPOSITES**

**A Dissertation Submitted to the Graduate School of Engineering, Mie University
in Partial Fulfillment of the Requirement for the Degree of Doctor of Philosophy**

By

Mahmudul Hassan Suhag



**Analytical & Environmental Chemistry Laboratory
Department of Applied Chemistry
Graduate School of Engineering
Mie University
Mie, Japan
September, 2024**

Table of Contents

Table of Contents	II
List of Figures	IX
List of Tables	XVII

Chapter One: General Introduction

1.1 Introduction	2
1.2 Endocrine Disrupting Chemicals	2
1.2.1 Bisphenols	2
1.2.2 Sources of Bisphenols	5
1.2.3 Impacts of Bisphenols	6
1.2.4 Bisphenol E, Uses, Sources and Toxicity	7
1.3 Pharmaceuticals Waste	7
1.3.1 Diclofenac	8
1.3.2 Sources of Diclofenac	9
1.3.3 Impacts of Diclofenac	9
1.4 Synthetic Dyes	10
1.4.1 Sources of Dyes	11
1.4.2 Impacts of Dyes	12
1.5 Pollutants Removal Techniques	13
1.5.1 Physical Approaches	14

1.5.1.1 Adsorption	14
1.5.1.2 Ion Exchange	15
1.5.1.3 Membrane Filtration	16
1.5.2 Chemical Methods	17
1.5.2.1 Coagulation-Flocculation	17
1.5.2.2 Electrochemical Treatments	18
1.5.3 Biological Methods	19
1.5.4 Advanced Oxidation Process (AOPs)	20
1.5.4.1 Photolysis	20
1.5.4.2 Ozonation	21
1.5.4.3 Fenton and Photo-Fenton	21
1.5.4.4 Sonochemical Oxidation	22
1.5.4.5 Heterogeneous Photocatalysis	22
1.5.5 Hybrid Treatments	25
1.6 Graphitic Carbon Nitride	25
1.6.1 g-C ₃ N ₄ as Adsorbent	26
1.6.2 g-C ₃ N ₄ as Photocatalyst	27
1.7 Objectives of the Research	33
□ General Objectives	33
□ Specific Objectives	33

1.8 References	34
----------------	----

Chapter Two: One-Step Fabrication of the ZnO/g-C₃N₄ Composite for Visible Light -Responsive Photocatalytic Degradation of Bisphenol E in Aqueous Solution

2.1 Introduction	67
2.2 Materials and Methods	70
2.2.1 Materials	70
2.2.2 Synthesis of the ZnO/g-C ₃ N ₄ Composite	71
2.2.3 Characterization	72
2.2.4 Photocatalytic Degradation	73
2.3 Results and Discussion	75
2.3.1 TG Analysis	75
2.3.2 FTIR Analysis	76
2.3.3 XRD Analysis	78
2.3.4 XPS Analysis	79
2.3.5 Morphological Study	81
2.3.6 BET and BJH Analysis	84
2.3.7 DRS Analysis	86
2.3.8 PL Analysis	87
2.3.9 EIS Analysis	88
2.3.10 Photocatalytic Activity	89

2.3.11 Effect of ZnO Amount	90
2.3.12 Effect of Calcination Process	92
2.3.13 Effect of Catalyst Dosage	94
2.3.14 Effect of Initial BPE Concentration	95
2.3.15 Effect of pH	97
2.3.16 Scavenger Role	98
2.3.17 Stability Test	100
2.3.18 Mechanism	100
2.4 Conclusions	103
2.5 References	104

Chapter Three: Visible Light Induced Photocatalytic Degradation of Diclofenac in Aqueous Solution Using Fabricated ZnO/g-C₃N₄ by Facile Calcination Technique

3.1 Introduction	115
3.2 Materials AND Methods	116
3.2.1 Materials	118
3.2.2 Synthesis of g-C ₃ N ₄	118
3.2.3 Preparation of ZnO/g-C ₃ N ₄ Composite	118
3.2.4 Characterization	119
3.2.5 Photocatalytic Degradation Experiment	120
3.3 Results and Discussion	122

3.3.1 FTIR Analysis	122
3.3.2 XRD Analysis	122
3.3.3 XPS Analysis	123
3.3.4 DRS Analysis	126
3.3.5 PL Analysis	126
3.3.6 EIS Analysis	126
3.3.7 Morphological Study	128
3.3.8 BET Surface Area and Pore Size Distribution Analysis	130
3.3.9 Mott–Schottky Plot and Valence Band (VB)-XPS Analysis	132
3.3.10 Photocatalytic Degradation of DCF	133
3.3.11 Effect of ZnO Content	134
3.3.12 Effect of Calcination Temperature	136
3.3.13 Effect of Types of ZnO and g-C ₃ N ₄	137
3.3.14 Effect of Catalyst Dosage	139
3.3.15 Effect of Initial Concentration of DCF	141
3.3.16 Scavenger Role	142
3.3.17 Stability	144
3.3.18 Mechanism	145
3.4 Conclusions	148
3.5 References	149

Chapter Four: Purification of aqueous orange II solution through adsorption and visible-light-induced photodegradation using ZnO-modified g-C₃N₄ composites

4.1 Introduction	162
4.2 Materials and Methods	165
4.2.1 Fabrication of the ZCN Composites	165
4.2.2 Characterization	166
4.2.3 Adsorption Study	167
4.2.4 Photocatalytic Degradation Study	167
4.3 Results and Discussion	168
4.3.1 XRD Analysis	168
4.3.2 FTIR Analysis	169
4.3.3 XPS Analysis	170
4.3.4 Morphological Analysis	173
4.3.5 Textural Characterization	175
4.3.6 UV-Vis DRS Analysis	177
4.3.7 PL Analysis	179
4.3.8 EIS Analysis	179
4.3.9 Adsorption of Orange II Solution	180
4.3.10 Photocatalytic Degradation of Orange II Solution	187
4.3.11 Mechanism	190

4.4 Conclusions	192
4.5 References	193
Chapter Five: Summary and Thesis Conclusions	
5.1 Summary and Thesis Conclusions	206
List of Published Articles	209
List of Attending Conference	210

List of Figures

Figure name	Page No.
1.1 Structure of diclofenac sodium.	8
1.2 Structure of a synthetic dye, orange II.	11
1.3 Commonly applied wastewater treatment methods.	13
1.4 General mechanism of photocatalytic degradation of organic pollutants.	24
1.5 Type II heterojunction in g-C ₃ N ₄ -metal oxide photocatalysts.	31
1.6 Z-scheme heterojunction in g-C ₃ N ₄ -metal oxide photocatalysts	32
2.1 Schematic diagram for (a) the synthesis of the ZnO/g-C ₃ N ₄ Composite, stepwise decomposition of (b) urea and (c) zinc acetate.	71-72
2.2 TG analysis curve of ZnO/g-C ₃ N ₄ composite.	76
2.3 FTIR spectra of ZnO, g-C ₃ N ₄ , ZnO/g-C ₃ N ₄ composite and ZnO/g-C ₃ N ₄ composite after degradation reaction.	77
2.4 XRD patterns of (a) g-C ₃ N ₄ , (b) ZnO, (c) ZnO/g-C ₃ N ₄ composite, and (d) ZnO/g-C ₃ N ₄ composite after degradation reaction.	79
2.5 (a) Survey XPS spectra of g-C ₃ N ₄ and ZnO/g-C ₃ N ₄ composite; overlap high resolution XPS (b) C 1s, (c) N 1s and (d) O1s spectra of g-C ₃ N ₄ and	81

ZnO/g-C ₃ N ₄ composite and (e) High resolution XPS Zn 2p spectra of ZnO/g-C ₃ N ₄ composite.	
2.6 SEM images of (a) ZnO and (b) g-C ₃ N ₄ , (c) ZnO/g-C ₃ N ₄ composite and (d) ZnO/g-C ₃ N ₄ composite after degradation reaction; and TEM images of (e) ZnO, (f) g-C ₃ N ₄ , (g) ZnO/g-C ₃ N ₄ composite and (h) ZnO/g-C ₃ N ₄ composite after degradation reaction.	82-83
2.7 Elemental mapping of (a) N, (b) O, (c) Zn and (d) C of ZnO/g-C ₃ N ₄ composite by FE-EPMA. In the case of C, the concentration of the surrounding of the composite was very high because of carbon tap for the analysis.	84
2.8 (a) Nitrogen adsorption desorption isotherm and (b) pore size distribution curve of g-C ₃ N ₄ and ZnO/g-C ₃ N ₄ composite.	85
2.9 (a) Kubelka-Munk function of UV-Vis DRS of prepared ZnO, g-C ₃ N ₄ , ZnO/g-C ₃ N ₄ composite and ZnO/g-C ₃ N ₄ composite after degradation reaction, Tauc plots. (b) $(\alpha h\nu)^{1/2}$ vs $h\nu$ for g-C ₃ N ₄ , ZnO g-C ₃ N ₄ composite and ZnO/g-C ₃ N ₄ composite after degradation reaction; and (c) $(\alpha h\nu)^2$ vs $h\nu$ for ZnO.	87
2.10 (a) PL spectra (upon the excitation at 360 nm wavelength) of prepared ZnO, g-C ₃ N ₄ , ZnO/g-C ₃ N ₄ composite and ZnO/g-C ₃ N ₄ composite after degradation reaction; and (b) EIS Nyquist plots of g-C ₃ N ₄ and ZnO/ g-C ₃ N ₄ .	89

2.11	(a) Photocatalytic degradation of BPE with different catalyst under visible light irradiation and (b) the plot of $-\ln(C/C_0)$ versus irradiation time; BPE: 3 ppm (30 mL), photocatalyst: 30 mg.	90
2.12	(a) Effect of ZnO amount on the composite (varying the amount of zinc acetate in composite preparation) on photocatalytic degradation of BPE with ZnO/g-C ₃ N ₄ composite and (b) the plot of $-\ln(C/C_0)$ versus irradiation time; BPE: 3 ppm (30 mL), ZnO/g-C ₃ N ₄ composite: 30 mg.	91
2.13	(a) Effect of calcination process of composite preparation on photocatalytic degradation of BPE with ZnO/g-C ₃ N ₄ composite and (b) the plot of $-\ln(C/C_0)$ versus irradiation time; BPE: 3 ppm (30 mL), ZnO/g-C ₃ N ₄ composite: 30 mg.	93
2.14	(a) Effect of catalyst dosage on photocatalytic degradation of BPE with ZnO/g-C ₃ N ₄ composite and (b) the plot of $-\ln(C/C_0)$ versus irradiation time; BPE: 3 ppm (30 mL).	94
2.15	(a) Effect of initial BPE concentration on photocatalytic degradation of BPE with ZnO/g-C ₃ N ₄ composite and (b) the plot of $-\ln(C/C_0)$ versus irradiation time; BPE: 30 mL, ZnO/g-C ₃ N ₄ composite: 30 mg.	96
2.16	(a) Effect of solution pH on photocatalytic degradation of BPE with ZnO/g-C ₃ N ₄ composite and (b) the plot of $-\ln(C/C_0)$ versus irradiation time; BPE: 3 ppm (30 mL), ZnO/g-C ₃ N ₄ composite: 30 mg.	97

2.17	(a) Effect of scavenger role on photocatalytic degradation of BPE with ZnO/g-C ₃ N ₄ composite and (b) the plot of $-\ln(C/C_0)$ versus irradiation time; BPE: 3 ppm (30 mL), photocatalyst: 30 mg.	99
2.18	Reusability of ZnO/g-C ₃ N ₄ composite on photocatalytic degradation of BPE.	100
2.19	VB XPS of ZnO/g-C ₃ N ₄ composite.	101
2.20	(a) Conventional charge transfer mechanism and (b) IFCT mechanism for photocatalytic degradation of BPE with ZnO/g-C ₃ N ₄ composite.	103
3.1	Schematic diagram for the synthesis of ZnO/g-C ₃ N ₄ composite.	119
3.2	(a) FTIR spectra of g-C ₃ N ₄ and ZnO/g-C ₃ N ₄ , and (b) XRD patterns of ZnO, g-C ₃ N ₄ and ZnO/g-C ₃ N ₄ .	123
3.3	(a) Survey XPS spectra of g-C ₃ N ₄ and ZnO/g-C ₃ N ₄ ; overlap high resolution XPS (b) C 1s, (c) N 1s and (d) O1s spectra of g-C ₃ N ₄ and ZnO/g-C ₃ N ₄ and (e) High resolution XPS Zn 2p spectra of ZnO/g-C ₃ N ₄ .	125
3.4	(a) Kubelka-Munk function of UV-Vis DRS, (b) Tauc plot, and (c) PL spectra (upon the excitation at 340 nm wavelength) of ZnO, g-C ₃ N ₄ , ZnO/g-C ₃ N ₄ , and (d) EIS resultant Nyquist plot of g-C ₃ N ₄ and ZnO/g-C ₃ N ₄ .	127-128

3.5 SEM images of (a) g-C ₃ N ₄ and (b) ZnO/g-C ₃ N ₄ , and TEM images of (c) g-C ₃ N ₄ and (d) ZnO/g-C ₃ N ₄ .	129
3.6 (a) SEM and EDS elemental mapping of (b) C, (c) N, (d) O and (e) Zn of ZnO/g-C ₃ N ₄ .	130
3.7 (a) N ₂ adsorption-desorption isotherms, (b) pore size distribution curves of g-C ₃ N ₄ and ZnO/g-C ₃ N ₄ .	131
3.8 (a) Mott-Schottky and (b) VB-XPS plot of ZnO/g-C ₃ N ₄ composite.	133
3.9 (a) Photocatalytic degradation of DCF using different catalyst with the irradiation of visible light and (b) the plot of -ln(C/C ₀) versus irradiation time; DCF: 10 mg L ⁻¹ (30 mL), photocatalyst: 30 mg.	134
3.10 (a) Effect of ZnO content on the composite on the photocatalytic degradation of DCF using ZnO/g-C ₃ N ₄ , and (b) the plot of -ln(C/C ₀) versus irradiation time; DCF: 10 mg L ⁻¹ (30 mL), photocatalyst: 30 mg.	135
3.11 (a) Effect of calcination temperature of the composite fabrication on the photocatalytic degradation of DCF using ZnO/g-C ₃ N ₄ , and (b) the plot of -ln(C/C ₀) versus irradiation time; DCF: 10 mg L ⁻¹ (30 mL), photocatalyst: 30 mg.	137
3.12 (a) Effect of types of ZnO and g-C ₃ N ₄ on the photocatalytic degradation of DCF using ZnO/g-C ₃ N ₄ , and (b) the plot of -ln(C/C ₀) versus irradiation time; DCF: 10 mg L ⁻¹ (30 mL), photocatalyst: 30 mg.	138

3.13	(a) Effect of catalyst dosage on the photocatalytic degradation of DCF using ZnO/g-C ₃ N ₄ , and (b) the plot of $-\ln(C/C_0)$ versus irradiation time; DCF: 10 mg L ⁻¹ (30 mL).	140
3.14	(a) Effect of initial concentration of DCF on the photocatalytic degradation of DCF using ZnO/g-C ₃ N ₄ , (b) the corresponding plot of $-\ln(C/C_0)$ versus irradiation time, and (c) effect of initial concentration of DCF on degraded amount of DCF using ZnO/g-C ₃ N ₄ composite; DCF: 30 mL, ZnO/g-C ₃ N ₄ : 30 mg.	141-142
3.15	(a) Effect of scavenger on the photocatalytic degradation of DCF using ZnO/g-C ₃ N ₄ , and (b) the plot of $-\ln(C/C_0)$ versus irradiation time; DCF: 10 mg L ⁻¹ (30 mL), ZnO/g-C ₃ N ₄ : 30 mg.	143
3.16	Photocatalytic stability test of ZnO/g-C ₃ N ₄ on photocatalytic degradation of DCF.	145
3.17	Formation of internal electric field in the ZnO/g-C ₃ N ₄ composite.	146
3.18	Mechanism of the photocatalytic degradation of DCF using ZnO/g-C ₃ N ₄ composite.	148
4.1	XRD patterns of ZnO, g-CN and different ZCN composites and (b) Enlarged (2θ range 10-50°) XRD patterns of ZCN-2.5, 5, 10 and 15 composites.	169
4.2	FTIR spectra of g-CN and all fabricated ZCN Composites.	170

4.3 (a) Survey XPS spectra of g-CN and ZCN-2.5; overlap high resolution XPS (b) C 1s, (c) N 1s and (d) O1s spectra of g-CN and ZCN-2.5 and (e) High resolution XPS Zn 2p spectra of ZCN-2.5.	172-173
4.4 SEM images of ZCN composites, ZnO, and g-CN.	174
4.5 (a) TEM image and (b-f) EDS elemental mapping with corresponding SEM image of ZCN-2.5.	175
4.6 N ₂ adsorption-desorption isotherms (inset: pore size distribution curves) of (a) g-CN, (b) ZCN-1, (c) ZCN-2.5, (d) ZCN-5, (e) ZCN-10, and (f) ZCN-15.	176-177
4.7 (a) Kubelka-Munk function of UV-Vis DRS, (b) Tauc plot of g-CN and different ZCN composites. (c) Tauc plot of ZnO, and (d) Photographs for appearance of all ZCN composites and bare g-CN.	178-179
4.8 (a) PL spectra (upon the excitation at 340 nm wavelength) of ZnO, g-CN, and all fabricated ZCN composites and (b) EIS resultant Nyquist plot of g-CN and different ZCN composites.	180
4.9 (a) Effect of contact time on the adsorption of orange II by prepared pure g-CN and different ZCN composites; Orange II solution, 10 mg L ⁻¹ (30 mL); adsorbents, 30 mg. (b) Effect of equilibrium concentration on the adsorption of orange II prepared pure g-CN and different ZCN composites; Orange II solution, 30 mL (3~100 mg L ⁻¹); adsorbents, 30 mg.	181

4.10	(a) Langmuir isotherm and (b) Freundlich isotherm for adsorption of Orange II dye by pure g-CN and different ZCN composites.	183
4.11	(a) The relationship between temperature and amount of orange II dye (10 ppm) adsorbed q_e on ZCN-2.5 composite as well as corresponding Gibbs free energy change (ΔG^0); (b) the plot of $\ln K_d$ versus $1/T$.	186
4.12	The effect of pH for adsorption of orange II dye (10 ppm) on ZCN-2.5 composite.	187
4.13	(a) Photocatalytic degradation of orange II dye solution using different catalyst with the irradiation of visible light and (b) the plot of $-\ln(C/C_0)$ versus irradiation time; orange II: 10 mg L^{-1} (30 mL), photocatalyst: 30 mg.	189
4.14	Photocatalytic reusability of ZCN-2.5 composite on photocatalytic degradation of orange II solution.	190
4.15	Proposed mechanism of (a) adsorption and (b) photocatalytic degradation of orange II dye solution using ZCN composites.	192

List of Tables

Table names	Page No.
1.1 Chemical name, molecular formula and chemical structure of bisphenols	3-4
2.1 Surface area, pore size and pore volume of the g-C ₃ N ₄ and ZnO/g-C ₃ N ₄ composite	85
2.2 Kinetic parameters for photocatalytic degradation of BPE	90
2.3 Effect of ZnO amount in composite (varying the amount of zinc acetate in composite preparation) on kinetic parameters for photocatalytic degradation of BPE with ZnO/g-C ₃ N ₄ composite	92
2.4 Effect of calcination process of composite preparation on kinetic parameters for photocatalytic degradation of BPE with ZnO/g-C ₃ N ₄ composite	93
2.5 Effect of catalyst dosages on kinetic parameters for photocatalytic degradation of BPE with ZnO/g-C ₃ N ₄ composite	95
2.6 Effect of initial BPE concentration on kinetic parameters for photocatalytic degradation of BPE with ZnO/g-C ₃ N ₄ composite	96
2.7 Effect of solution pH on kinetic parameters for photocatalytic degradation of BPE with ZnO/g-C ₃ N ₄ composite	98

2.8 Effect of scavenger role on kinetic parameters for photocatalytic degradation of BPE with ZnO/g-C ₃ N ₄ composite	99
3.1 Surface area, pore volume, and pore diameter of the g-C ₃ N ₄ and ZnO/g-C ₃ N ₄	131
3.2 Kinetic parameters for photocatalytic degradation of DCF	134
3.3 Effect of ZnO content in the ZnO/g-C ₃ N ₄ composite on kinetic parameters for photocatalytic degradation of DCF using ZnO/g-C ₃ N ₄	136
3.4 Effect of calcination temperature in the preparation of ZnO/g-C ₃ N ₄ composite on kinetic parameters for photocatalytic degradation of DCF using ZnO/g-C ₃ N ₄	137
3.5 Effect of types of ZnO and g-C ₃ N ₄ in the ZnO/g-C ₃ N ₄ composite on kinetic parameters for photocatalytic degradation of DCF using ZnO/g-C ₃ N ₄	139
3.6 Effect of catalyst dosage on kinetic parameters for photocatalytic degradation of DCF using ZnO/g-C ₃ N ₄	140
3.7 Effect of initial concentration of DCF on kinetic parameters for photocatalytic degradation of DCF using ZnO/g-C ₃ N ₄	142
3.8 Impact of scavenger on kinetic parameters for photocatalytic degradation of DCF using ZnO/g-C ₃ N ₄	144

4.1 Surface atomic ratios of g-CN and ZCN-2.5 composite	173
4.2 Surface area, pore volume, and pore diameter of the pure g-CN and all fabricated ZCN composites	177
4.3 Langmuir isotherm model fitting results	184
4.4 Freundlich isotherm model fitting results	184
4.5 Thermodynamics parameters for adsorption of orange II dye on ZCN- 2.5 composite	186
4.6 Kinetic parameters on photocatalytic degradation of Orange (II) solution (10 mg L ⁻¹) using pure g-CN and different ZCN composites	189

CHAPTER ONE

General Introduction

1.1 Introduction

Water is a fundamental necessity for every living organism in order to survive. Human well-being is directly correlated with the quality of the water, which makes it a critical concern for mankind [1–3]. Because of rapid industrialization, civilization, and other environmental and global changes, the pollution of the aquatic environment is becoming a more serious issue [3–6]. Due to the rapid development of the chemical, pharmaceutical, and agricultural industries, various chemical compounds, including pesticides, steroid hormones, pharmaceutical waste, synthetic dyes, and heavy metals, reach the aquatic environment [7]. Since most organic pollutants are found in aquatic environments at low concentrations (ng/L to $\mu\text{g/L}$), they are classified as micro pollutants [8,9]. The main source of contaminated water is thought to be organic contaminants, which are very harmful to aquatic life and human health [3,10]. Thus, it is crucial to remove organic contaminants from waste water in order to maintain aquatic life and enhance water quality. Several studies have been reported over the years to remediate discharged effluents using physical, chemical, and biological, approaches [3].

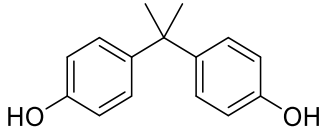
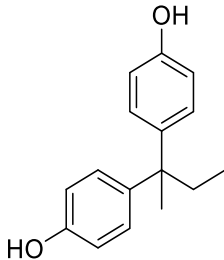
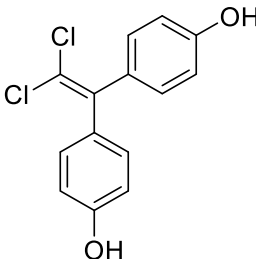
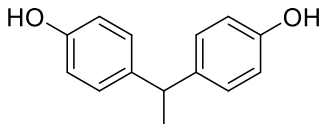
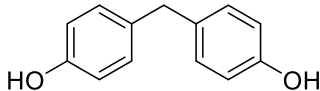
1.2 Endocrine Disrupting Chemicals

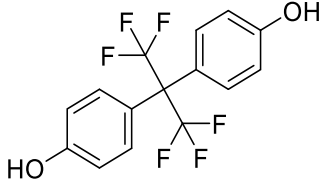
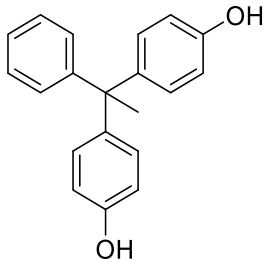
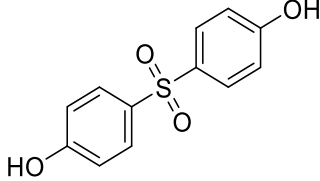
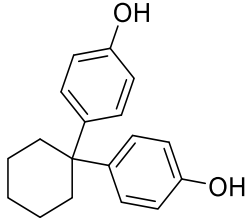
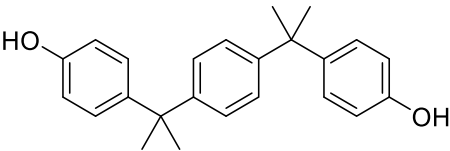
1.2.1 Bisphenols

(BPs) are phenolic compounds in which two phenols are connected through a bridging carbon [11]. They are distinguished into different analogues by the insertion of distinct functional groups at the phenolic ring and bridging carbon (Table 1.1) [12]. BPs are one of the most widely used monomers for the synthesis of polycarbonates, which are utilized in consumer products and food and drink storage containers [13,14]. In addition, these are also applied in the manufacture of epoxy resin linings for metal-based beverages

and food cans, along with other consumer goods such as medical equipment, thermal paper, toys, electronics, rubber, aerospace, and water pipes [15,16].

Table 1.1 Chemical name, molecular formula and chemical structure of bisphenols

Compound name	Chemical name	Molecular formula	Structure
BPA	2,2-bis (4 hydroxyphenyl) propane	$C_{15}H_{16}O_2$	
BPB	2,2-bis (4-hydroxyphenyl) butane	$C_{16}H_{18}O$	
BPC	4,4'-(2,2-dichloroethene-1,1-diyl) diphenol	$C_{14}H_{10}Cl_2O_2$	
BPE	4,4'-ethylidenebisphenol	$C_{14}H_{14}O_2$	
BPF	4,4'-dihydroxydiphenyl methane	$C_{13}H_{12}O_2$	

BPAF	4,4'-(hexafluoroisopropylidene)diphenol	$C_{15}H_{10}F_6O$	
BPAP	4,4'-(1-phenylethylidene)bisphenol	$C_{20}H_{18}O$	
BPS	4,4'-sulfonyldiphenol	$C_{12}H_{10}O_4S$	
BPZ	4,4'-cyclohexylidenebisphenol	$C_{18}H_{20}O_2$	
BPP	4,4'-(1,4-phenylenediisopropylidene)bisphenol	$C_{24}H_{26}O_2$	

Among all BPs, bisphenol A (BPA) was first synthesized in 1981, and it is a chemical with one of the largest manufacturing quantities in the world [17,18]. BPA has been used in the production of plastics as building blocks chemical. Nevertheless, it could contaminate the surroundings, and it has been classified as an environmental pollutant,

with evidence of its presence in air, water, soil, sediment, indoor dust, and human tissues [11,19]. There have also been reports of the ubiquitous presence of BPA in human serum, urine, placental tissue, umbilical cord blood, and breast milk, indicating a worldwide exposure [18,20,21]. Furthermore, BPA was identified as an endocrine disruptor chemical, which has some vital adverse effects on reproduction, including breast cancer, miscarriage, early delivery, male genital abnormalities, sperm quality, sex hormone concentration, and fertility; development effects include male genital abnormalities, birth weight, neurodevelopment, and childhood asthma; metabolic diseases include type 2 diabetes, cardiovascular diseases, and hypertension; and other effects include oxidative stress, inflammation, immune function, epigenetics, and gene expression [22]. In consequence of these issues, the use of BPA in a variety of consumer items has been restricted in several countries. Consequently, the scientific community has been focusing more and more attention on the hunt for safe substitutes [12,23]. Currently, sixteen BPs whose physicochemical characteristics are comparable to those of BPA have been employed as alternative substances for BPA in a variety of applications [16,24]. Although it was previously believed that alternative BPs were less harmful than BPA, recent study have revealed that BPs have just as many negative consequences, preferably more [24–26]. Hence, all bisphenols have been detected to differing extents, have adverse effects on human health, and are connected to conditions including cancer, obesity, cardiovascular disease, allergic illnesses, and neurodegenerative illnesses like Alzheimer's and Parkinson's disease [12].

1.2.2 Sources of Bisphenols

1. Since most people spend their time inside, indoor dust is one of the possible causes of human exposure to bisphenols (BPs). Dust exposure through the skin and

inhalation are two ways that BPs can enter the human body. BPA contamination was measured in a variety of microenvironments, including workplaces, homes, clothing stores, museums, public libraries, and high schools. The majority of the contamination was found to be caused by floor made from epoxy resins [27,28].

2. Wastewater treatment plants (WWTPs) receive wastewaters containing BPs discharged from residences, commercial buildings, and many industries for purification. It has been claimed that before being discharged into the environment, BPs are not entirely removed from wastewater. As a result, WWTPs are regarded as one of the main environmental sources of BPs [29,30]. Furthermore, during the conventional removal procedures in the WWTPs, BPs are adsorbed onto the solid particles or sludge. As a result, sewage sludge is also thought to be a possible environmental source of BPs [31].

3. BPs were found in a variety of consumer goods, including toys, paper products, jewelry, and baby bottles [23]. Additionally, BPs were detected in drinks in baby bottles, canned foods, canned feed, and canned beverages [32].

1.2.3 Impacts of Bisphenols

1. Available research have reported on the estrogenic and anti-androgenic properties of BPs [16]. BPs belong to potential aspects influencing the health of human reproduction. BPs have adverse effects on fertilization success, ovarian response, embryo quality, and implantation success [33]. BPs also damage the sperm DNA. BPs are also inducing the miscarriage and early delivery [22].

2. It has been reported that BPA and other BPs have cytotoxic and genotoxic effects [34,35].

3. BPs causes the different types of cancer. Exposure to BPs stimulates the ovarian cancer cells' migration and invasiveness and promotes the cancer cells to propagate. The role of BPs in migrating breast cancer cells has also been reported [36,37].

4. BPs are linked to the cardiovascular disease and hypertension [38].

5. Additionally, BPs have been correlated with diabetes. Several studies indicate that BPs affect glucose metabolism by means of a variety of pathways [39].

6. BPs were correlated with childhood asthma and obesity. It has been proposed that BPs impair immune system function, which promotes the growth of allergy-related syndromes like asthma [40].

7. BPA is strongly correlated with the advancement of neurodegenerative illnesses, such as Parkinson's and Alzheimer's diseases [41].

1.2.4 Bisphenol E, Uses, Sources and Toxicity

BPs analogous, bisphenol E (4,4'-ethylidenebisphenol, BPE) is an important industrial compound and is now utilized as an alternative to BPA as a raw material in the manufacture of epoxy resins and polycarbonate polymers. Though at a lesser extent than BPA, BPE has been found in drinking water, bottled water, and source waters [42]. Similar to BPA, BPE was shown to be harmful and to have notable estrogenic activity at the concentration range of $10^{-6} - 10^{-4}$ M [43].

1.3 Pharmaceuticals Waste

Numerous pharmaceuticals have been detected in a variety of aquatic environments (surface waters, groundwater, and tap water) across various countries. Wastewater treatment plants (WWTPs) are not able to eliminate these drugs properly. Considering the fact that WWTPs are usually constructed to handle organic waste in the

mg L⁻¹ range, remediation efficiency in the case of pharmaceuticals may be less than 10% [44,45].

1.3.1 Diclofenac

Diclofenac (2-[2-(2,6-dichloroanilino)phenyl]acetic acid, DCF) as its sodium salt, a synthetic non-steroidal anti-inflammatory medicine, is most commonly used in the treatment of inflammatory diseases, animal and human dysmenorrhea, and personal care products [46–48].

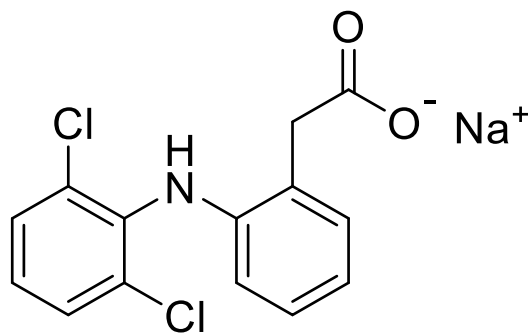


Figure 1.1 Structure of diclofenac sodium.

Being a chlorinated micropollutant, it has high toxicity, limited biodegradability, a persistent nature in the environment over time, and a large bio accumulative potential, making it very hazardous [49]. The commonly used DCF is frequently discharged into the aquatic environment through a number of procedures, including the metabolism of excrement and urine from people and animals following medical treatment, disposal of waste from homes, and domestic waste disposal [50,51]. Due to long environmental persistence and limited biodegradability of DCF, it is commonly found in groundwater, surface water, drinking water, ocean, sediments, suspended soil, landfills, and sludge as well as WWTPs [52,53]. They might possess adverse effects on human health or ecosystems even at very lower concentration [54,55].

1.3.2 Sources of Diclofenac

1. Wastewater discharge and solid waste are the main paths that DCF contaminates the environment. The most hazardous method of DCF contamination in soil, groundwater, and surface waters may be drugs waste disposal. A substantial threat is posed by landfill percolation into surface and groundwater [55,56].

2. Another method by which DCF might enter surface water is through the pharmaceutical sector or hospital effluents [45].

3. The DCF treated human and animal sources may pose an imminent danger of contaminating water and land. The treated DCF releases continuously into the aquatic environment through the metabolism of human and animal urine and feces [51].

4. Another factor of DCF pollution in the aquatic environment is the dermal treatment that uses it. The skin absorbs only about 6% of the administered DCF; the remaining 94% is flushed into the sewage system [57].

1.3.3 Impacts of Diclofenac

1. DCF has adverse effects on human health. Renal difficulties may occur from DCF in older people and children [58].

2. It may cause severe gill cell, kidney, and liver mutations in aquatic species, such as brown and rainbow trout [48].

3. The negative impacts of DCF on a few animals are more concerning due to its endocrine-disrupting abilities, which may cause a population shift from male to female [57].

4. Due to the detrimental impacts of DCF on the food chain, there may be further hazards to endangered species. For instance, the dead bodies of animals and birds administered DFC are deadly to vultures [54,59].

1.4 Synthetic Dyes

Synthetic organic dyes are the aromatic water soluble dispersible organic coloring substances. It has been estimated that over 100,000 synthetic organic dyes are commercially available around the world [60,61]. Dyes are extensively utilized in the textile, printing, paper, food processing, tannery, and pharmaceuticals industries [10,62,63]. Around the world, about 70 million tons of synthetic dyes are produced annually, and the textile industry uses over 10,000 tons of these dyes [64].

Dyes are organic substances with two components, such as auxochromes and chromophores, in their chemical structure. Chromophores are composed of atoms and electrons forming part of dye that causes it to be colored and contain a variety of functional groups, such as -C=C- (ethenyl), -C=O (carbonyl), -C=N- (imino), -C=S (thiocarbonyl), -N=N (azo), -N-O (nitroso), and NO_2 (nitro). An additional component of dyes that helps increase the affinity of chromophores for the materials is called auxochromes. Usual auxochromes are -NH_2 (amino), -COOH (carboxylic), $\text{-SO}_3\text{H}$ (sulphonic), and -OH (hydroxyl) [10].

Depending on their source, composition, and use, dyes are frequently classified into several categories. The textile industries utilize a variety of synthetic dyes, including azo, direct, reactive, mordant, acid, basic, dispersion, and sulfide dyes [64,65]. Every day, millions of liters of wastewater from textile mills are dumped into public drains and WWTPs, where it eventually ends up in rivers. Furthermore, certain synthetic organic dyes are slow- or nonbiodegradable, which makes it more challenging for WWTPs to clean up wastewater using conventional treatment methods [66,67]. Available literature data supports the toxic properties of some of them, including carcinogenic, allergic, and dermatic effects on humans [66,68]. Moreover, they pose a serious threat to aquatic plants

and animals [69]. Therefore, it might not be safe to produce and utilize these dye compounds.

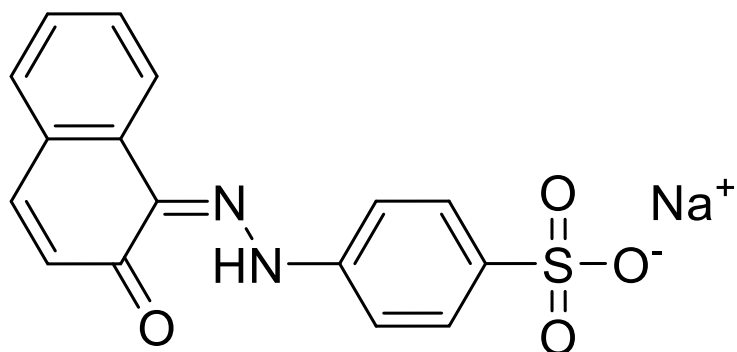


Figure 1.2 Structure of a synthetic dye, orange II.

1.4.1 Sources of Dyes

1. The textile, tannery, and paper industries are the main primary sources of water pollution since they use an extensive amount of water and release large amounts of effluent into aquatic environments. Wastewater containing dye is produced throughout various dyeing processes, and the amount of dye lost greatly varies depending on the kind of cloth and synthetic organic dye class [8,66].

2. A further source of synthetic organic dyes in aquatic environments is household wastewater, which is released into sewers and eventually ends up at WWTPs or is released directly into the environment. This includes hair coloring, cosmetics containing dye, and expired or unused medication derived from dyes [9,70,71].

3. Sewage sludge, which is primarily deposited in landfills, and effluents, which are released directly into the aquatic environment, are the two primary byproducts of wastewater treatment. These byproducts frequently include a variety of contaminants, including dyes, heavy metals, and antibiotics [72,73].

4. Hospitals and the pharmaceutical industry release an immense amount of hazardous wastewater that contains colors, pigments, disinfectants, and pharmaceuticals [74,75].

5. Aquaculture is another direct potential source of dyes in aquatic environments. The illicit use of some synthetic organic colors, such as crystal violet, methylene blue, and malachite green, to cure and prevent bacterial, fungal, and parasitic illnesses in fish because of their great efficacy, affordability, and simplicity of acquisition [61].

1.4.2 Impacts of Dyes

1. The discharge of wastewater from textile industries into the environment results in aesthetic issues, such as the darkening of water bodies like rivers and lakes [10].

2. Sunlight penetration in the water body is reduced by several dyes and their degraded derivatives, which reduce photosynthetic activity, dissolved oxygen content, and water quality and have acute toxic impacts on aquatic life (aquatic plants, microorganisms, fish, and mammals) [76–78].

3. The many chemical components of organic textile dyes may be extremely harmful to people. While textile dyes leak into bodies of water, fish and other aquatic organisms absorb the environmental contaminants, and throughout the food chain, they are able to access human organs. Hence, dyes have the potential to be harmful to human health, ranging from dermatitis to the central nervous system, which includes the liver, kidney, enzymatic system, reproductive system, human chromosomes, neurological system, and skin. Furthermore, direct inhalation and ingestion of wastewater containing dyes can cause a number of health problems in humans, including respiratory issues, asthma, burns, allergies, immune system suppression, coughing, heart disease, skin irritation, and itching [10,79].

1.5 Pollutants Removal Techniques

Pure water supplies are vital for agriculture, industry, energy generation, domestic consumption, and so on. The removal of pollutants from effluent containing textile pollutants, pharmaceutical pollutants, and other organic pollutants has become a serious concern around the world. Hence, it is very necessary to choose a suitable treatment technique for the purification of the wastewater. There are numerous treatment approaches that can be used for the treatment of wastewater. For instance, physical, chemical, biological, advanced, and hybrid processes are shown in Figure 1.3, and some of the common methods in each approach are explained below [65].

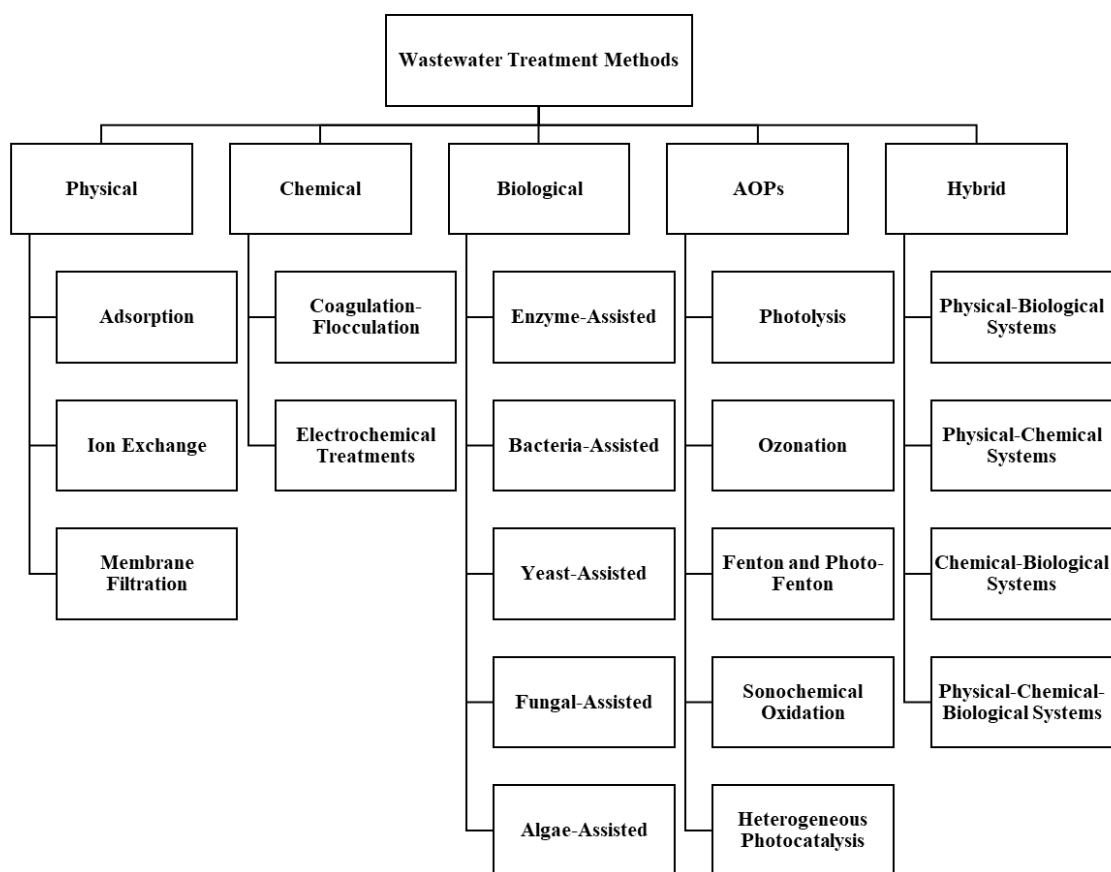


Figure 1.3 Commonly applied wastewater treatment methods.

1.5.1 Physical Approaches

Several physical techniques, including adsorption, ion exchange, and membrane filtration, are widely used to treat the wastewater. Physical techniques have a number of benefits, such as a simple strategy, simplicity in use, cost-effectiveness, lower chemical necessities, and the existence of hazardous substances having no detrimental impacts [80,81]. However, due to a variety of disadvantages, such as the creation of sludge and hazardous byproducts, and their limited implementation, these methods are usually not preferred [64].

1.5.1.1 Adsorption

The surface-based process of adsorption involves the attraction of adsorbed molecules or ions to a solid adsorbent surface. Adsorption may be classified into two categories, such as chemisorption and physisorption. Based on the way the dye molecule is adsorbed onto the adsorbent surface, the classification is generated [82]. Physisorption is a reversible process in which the identity of the adsorbed molecules is not altered. On the contrary, molecules that have been chemisorbed are bound to the adsorbent by larger electrostatic forces, frequently undergo reactions, are impacted by the procedure irreversibly, and cannot be retrieved by desorption [83,84].

It is believed that the specific surface area of adsorbents, π - π interaction, hydrophobic interaction, and hydrogen bonds are the primary factors influencing the adsorption process of organic compounds [85,86]. The adsorption technique has several benefits, such as high efficiency, rapid reaction times for wastewater color removal, and the ability to recycle adsorbents [87,88]. Moreover, it has been considered that adsorption is the most cost-effective and highly effective treatment technique for removing contaminants from wastewater effluents [89,90]. It has been considered that a large

specific surface area, developed pore structure, strong mechanical strength, and ease of regeneration are essential for an efficient adsorbent. Adsorption performance, availability, and pricing are all considered while choosing the suitable adsorbent [91]. Biomass from industrial and agro-industrial processes, such as leather waste, rice hulls, eggshells, sugar cane bagasse, clays, and grape bagasse, are common sources of adsorbents with low acquisition costs and extensive availability [84]. Furthermore, several adsorbents, such as zeolites, alumina, silica gel, carbon nanotubes, activated carbon, charcoal, activated sludge, and graphite, are widely used for the efficient adsorption of organic pollutants from wastewater [63,64].

1.5.1.2 Ion Exchange

The ion exchange technique has attracted significant interest in the treatment of wastewater and effluents recently considering several advantages, including cost effectiveness, regeneration, simplicity in utilization, flexibility, and high efficiency [64]. Synthetic organic ion exchange resins are the solid matrix particles that are most often utilized. Inorganic zeolites and other natural resins are also used. Nonetheless, because of their ability to be designed for specific requirements, synthetic resins are extensively used. Likewise, ion exchange resins are divided into two categories as cation exchangers which contain positive charged mobile ions available for exchange, and anion exchangers, whose exchangeable ions are negatively charged [92]. Strong bindings are formed between the solutes and the resins in a packed bed reactor to facilitate effective separation in the ion exchange process. Strong interactions between the charges of dye molecules and the functional groups of resins support the ion exchange process used in pollutants removal [93].

1.5.1.3 Membrane Filtration

One of the most advanced physical approaches for treating wastewater containing dyes and pharmaceuticals wastes is membrane filtration [64]. The most common membrane modules are plate, tubular, spiral, and hollow fiber. Membranes are barriers used in the transport of materials under potential gradients (chemical, mechanical, or electrical). They act as a physical barrier that separates the flow of feed into permeate and concentrate. Different materials (polymeric, ceramic, or mixed matrix compounds), forms, and morphologies, as well as charged or neutral, solid or liquid, porous or non-porous, can be used to construct membranes [94]. This method produces a pollutant free solution because the tiny holes in the membranes catch solutes bigger than these pores. Despite the ease of use and efficacy of this approach, the membranes require frequent replacement [95].

Based on the pore size of membrane, the membrane filtration processes are categorized as reverse osmosis (RO), nanofiltration (NF), ultrafiltration (UF), and microfiltration (MF) [94]. RO is a membrane filtering technique that produces high-quality water by treating wastewater containing organic pollutants and it has several industrial applications [96,97]. One of the benefits of RO technology is that it can accomplish separation and concentration without requiring thermal energy or condition change [98].

Recently, wastewater has been treated with NF, a sophisticated membrane technology. NF membranes typically have a diameter of 0.5 to 0.2 nm [80]. UF membranes with membrane widths ranging from 0.1 to 0.001 μm can also be utilized to extract organic contaminants from wastewater. The high membrane pore size of ultrafiltration results in a low separation rate even though it is less costly and needs less pressure than NF [99,100].

MF is a technique that separates suspended particles and dyes from wastewater by using a standard membrane with pore diameters ranging from 0.1 to 10 μm [64]. Removal of pollutants in low concentrations and/or dispersed in colloidal form is one of the primary benefits of membranes. Since NF and RO have narrower pores and can remove more than 90% of pollutants when used separately, they are thought to be more effective techniques to carry out [101–104].

1.5.2 Chemical Methods

The most common chemical methods for treating wastewater containing organic pollutants are coagulation-flocculation, electrochemical, photolysis, and oxidation. These methods are typically more costly than biological and physical methods. The main challenges to wastewater treatment using chemical techniques are high energy, enormous amounts of chemicals, and suitable equipment. A further drawback of using chemical methods is the generation of toxic metabolites and byproducts during the treatment process [64,105,106].

1.5.2.1 Coagulation-Flocculation

The processes of flocculation and coagulation are widely used to purify wastewater that has a high level of pollutants and contaminants. Metal salts and polymers can be employed as coagulants in this treatment method, whereas polymers that promote flocculation improve the aggregation of flocs to facilitate easier separation [107]. A number of chemical coagulants were used in the coagulation-flocculation method. Organic contaminants and their byproducts are purified using iron coagulants, such as ferrous sulfate and ferric chloride, and other chemical coagulants, such as magnesium carbonate and hydrated lime [108,109]. While a coagulant is added to a solution and well agitated, impurities and organic pollutants are trapped as it precipitates. Clean water can

be obtained through physically filtering these precipitated chemicals [110]. This method is crucial for treating wastewater from textiles that include dyes and is also very cost-effective. However, it produces concentrated sludge and is pH dependent, which are drawbacks [95].

1.5.2.2 Electrochemical Treatments

In recent years, three electrochemical techniques such as electrocoagulation, electro-Fenton, and anodic oxidation have been utilized to remove organic pollutants from wastewater. There is no sludge produced by electrochemical treatment systems, and no chemicals required to be introduced. Nevertheless, these methods have drawbacks, such as expensive electricity costs and lower efficacy compared to alternative treatment technologies [111,112]. Two metallic electrodes are used in the electrocoagulation method to provide direct power and to create in-situ coagulant particles and the electrocoagulation mechanism is used to treat wastewater [95]. Another kind of electrochemical method used to extract organic contaminants from wastewater through direct and indirect processes is anodic oxidation. Organic chemicals are adsorbed onto the surface of the anode in the direct oxidation process, where they are subsequently degraded by the anodic electron transfer pathway. In contrast, the indirect oxidation process is an electrochemical method that produces powerful oxidants like O_3 and H_2O_2 . The effective removal of dyes and other organic contaminants distinguishes this approach apart from others. Nevertheless, it has certain disadvantages, such as high operating costs and limited stability [113,114]. The electro-Fenton method, which is regarded as one of the most extensively utilized techniques in practical application, combines two processes of oxidation and coagulation to remove organic contaminants. This approach differs in

that it uses less chemicals, preserves the environment, and produces no hazardous byproducts [115].

1.5.3 Biological Methods

To eliminate contaminants from industrial wastewater, several biological species or techniques are used in biological treatment. The purpose of this strategy is to develop an efficient mechanism to obtain disposal of degraded products. The use of biological methods is advantageous to chemical and physical methods for wastewater purification due to its simplicity of usage, lack of sludge, fewer chemical reagents requirements, energy-saving features, environmental friendliness, and non-toxic byproducts. Because of their wide range of genetics and flexibility, biological techniques are the most effective for degrading down and mineralizing wastewater pollutants. Biological methods of wastewater treatment are both affordable and practical for usage in developing countries. However, the biological technique has several disadvantages, including a lengthy operating duration and ineffectiveness against potentially hazardous chemical substances [65,106,116].

Enzyme-based systems, bacteria, yeast, algae, and fungi are the most promising biological candidates for treating organic effluent. The aforementioned microbes have the ability to improve mineralization, decolorization, and removal performance while also reducing the chemical oxygen demand, biological oxygen demand, total suspended solids, total dissolved solids, and turbidity levels of wastewater containing organic pollutants [65,117]. Out of the microorganisms mentioned, bacteria have the most promise for treating wastewater containing organic substances since they are easy to culture, have a short life cycle, and can grow on a wide range of substrates. It is well known that a wide variety of bacterial species may greatly reduce toxicity while simultaneously eliminating

dyes and other organic pollutants [65,118,119]. In order to significantly wastewater containing organic pollutants, a number of researchers have assembled consortia of bacteria and yeast, bacteria and fungi, yeast and fungus, and bacteria and algae [65,120].

1.5.4 Advanced Oxidation Process (AOPs)

The required degradation of organic compounds in wastewater may not always be accomplished by the traditional and conventional methods. After been evaluated for the first time in the 1980s to treat drinking water, AOPs are now widely employed in the treatment of industrial wastewater. AOPs are innovative, expeditious, eco-friendly, affordable, and highly efficient methods for removing contaminants from wastewater from the paper, textile, and pharmaceutical industries without producing sludge [65,121,122]. The most common AOPs for treating wastewater containing organic pollutants are photolysis, ozonation, photo-fenton, sonochemical oxidation and heterogeneous photocatalysis.

1.5.4.1 Photolysis

In the photolysis reaction, energy is released in the form of photons upon excitation with UV light irradiation, which are subsequently introduced into the molecules in the medium. The particular electron of the molecule attains an excited state, which creates free radicals and initiates a chain reaction that continues until a final product is produced. The homolysis of weak bonds or the transfer of electrons to oxygen molecules produces these radicals. The benefits of the photolysis reaction are minimal maintenance and operating expenses and the absence of chemicals. However, the appearance of organic compounds that might lead to turbidity may limit the efficacy of the photolysis reaction [84,123,124].

1.5.4.2 Ozonation

Organic pollutants are eliminated by ozonation, either directly through a reaction with dissolved O_3 or indirectly through the generation of hydroxyl radicals ($\bullet OH$). Ozone directly interacts with electron-rich functional groups in direct oxidation. Conversely, in indirect oxidation, it decomposes with $\bullet OH$ in a basic medium, where it interacts with most compounds. In combination with other oxidizing agents like O_3/UV , O_3/H_2O_2 , and $O_3/UV/H_2O_2$, ozonation may have a higher ability to produce hydroxyl radicals [84,125,126].

1.5.4.3 Fenton and Photo-Fenton

On the basis of different free radicals, advanced oxidation processes may also be classified into Fenton systems, which are represented by hydrogen peroxide (H_2O_2) ($\bullet OH$), peroxymonosulfate (PMS) ($SO_4^{\bullet -}$), and persulfate (PDS) ($SO_4^{\bullet -}$). Since $SO_4^{\bullet -}$ had a longer half-life (30-40 s) and a greater oxidative power (2.5-3.1 V) than $\bullet OH$ (1.8-2.7 V and 20 ns), it was more effective in degrading aquatic pollutants [127–129].

The photo-fenton process, which employs iron ions as photocatalysts, hydrogen peroxide as an oxidizing agent, and UV light to increase the production of $\bullet OH$ radicals, degrades organic pollutants. This method converts Fe^{3+} by photoreduction into Fe^{2+} , which then combines with H_2O_2 to produce $\bullet OH$ radicals. In addition, Fe^{3+} undergoes a reduction reaction to generate ferric aqua-complexes, which are then further reduced by UV light to produce $\bullet OH$ radicals. Hydrogen peroxide-based methods offer the advantages of being simple to use and effective in degrading pollutants. But they have drawbacks as well. For example, the sludge contains iron, which leads to secondary pollution, and the reaction needs acidic conditions, which increases the expense of pH correction [84,123,126,130].

1.5.4.4 Sonochemical Oxidation

The sonochemical processes use ultrasonic waves with a frequency range of 20 - 500 kHz to sonify the effluent. Ultrasonic cavitation is the process that forms microbubbles. When these bubbles reach a critical resonance size, they collapse, producing massive pressures (>1000 bar) and temperatures (>5000 K) inside the bubble for a short period of time (milliseconds). Therefore, the thermal cleavage of molecules into H and •OH radicals and their oxidation by •OH radicals are the two steps involved in the degradation of pollutants. However, its efficiency is lower than that of other methods. In order to improve efficiency, sonochemical oxidation can be combined with other technologies [84,123,125].

1.5.4.5 Heterogeneous Photocatalysis

The combination of photochemistry and catalysis is referred to as photocatalysis [131]. It suggests that, in order to initiate or accelerate a chemical change, light and catalysts are required. In other words, photocatalysis is the process of accelerating a photoreaction when a catalyst is present [132]. The surface of a heterogeneous photocatalysis system is where photoinduced molecular transformations or reactions take place [133]. A semiconductor is able to act as a photocatalyst in the photodegradation process because of its distinct electronic structure which is defined by an empty conduction band (CB) and a filled valence band (VB). TiO₂ semiconductor was used by Fujishima and Honda to report the photocatalytic activity of the semiconductor for the first time in water splitting [134]. As shown in Figure 1.4, an overview of the semiconducting material-based heterogeneous photocatalytic degradation mechanism is as follows. The reaction is started when a photoelectron is transferred from the filled VB to the empty CB of a semiconductor photocatalyst with the irradiation of light. The energy

of the absorbed photon ($h\nu$) is either higher or equal to the band gap of the semiconductor photocatalyst. There is a hole created in the VB by the excitation process. Thus, as shown in eq. 1.1, electron and hole pair (e^-/h^+) are generated. Afterwards, the photogenerated holes at the VB react with water to produce the $\bullet\text{OH}$ radical (eq. 1.2). The formed $\bullet\text{OH}$ radical on the surface of the irradiated semiconductor is a very potent oxidizing agent. It degrades organic molecules that have been adsorbed or are in close contact with the catalyst surface (eq. 1.3). Electrons in the CB react with adsorbed oxygen and produce superoxide radicals ($\bullet\text{O}_2^-$) (eq. 1.4). Hence, the electron hole pair recombination process has been prevented. Moreover, the formed $\bullet\text{O}_2^-$ radicals react with organic molecules to produce degraded and mineralized products (eq. 1.5). The generated $\bullet\text{O}_2^-$ radicals are protonated, resulting in the formation of hydroperoxyl radicals ($\text{HO}_2\bullet$) and subsequently H_2O_2 , which further dissociates into very reactive $\bullet\text{OH}$ radicals (eq. 1.6). The organic pollutants may degrade or mineralize by directly accepting electrons on the CB and holes on the VB through reduction and oxidation reactions, respectively (eqs. 1.7-1.8) [135].

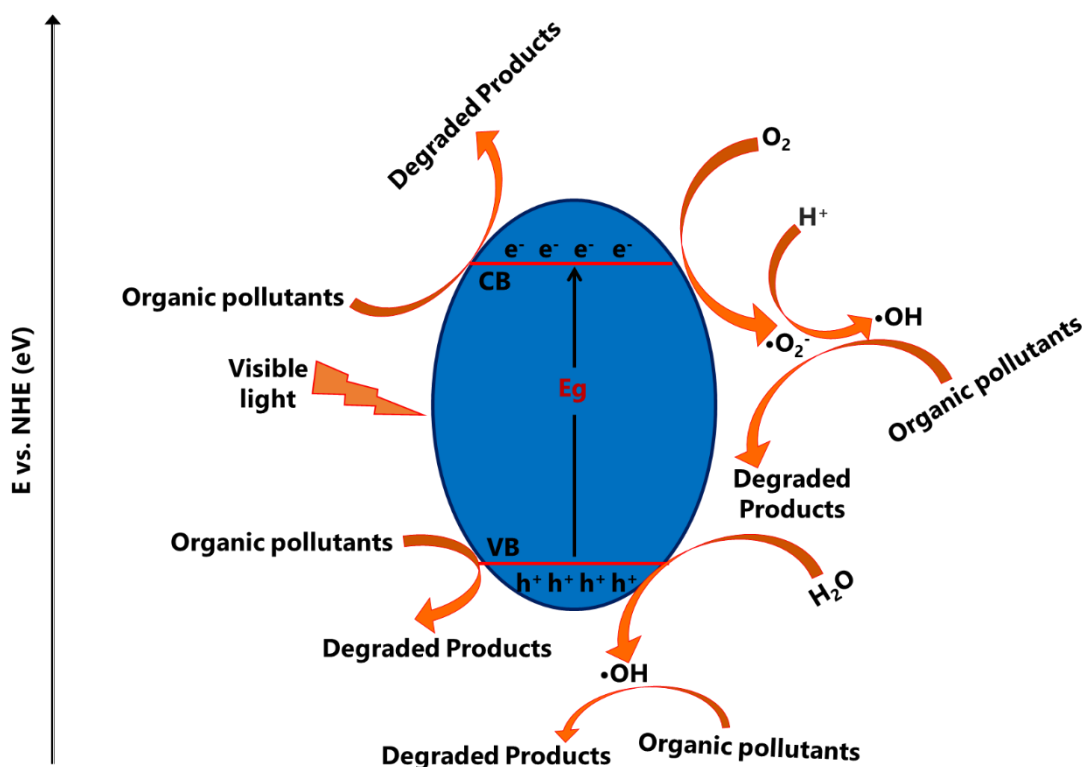
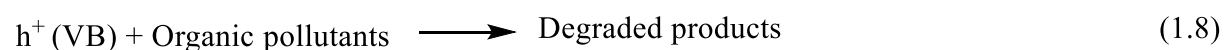
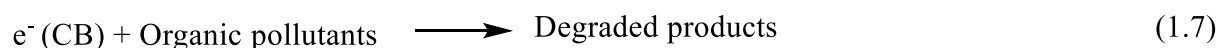
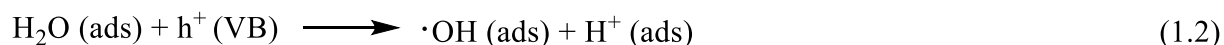
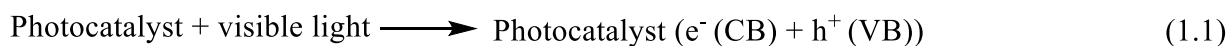


Figure 1.4 General mechanism of photocatalytic degradation of organic pollutants.



1.5.5 Hybrid treatments

Hybrid wastewater treatment is a process of combining two or more organic pollutants removal techniques. The primary benefits of hybrid treatment are its stability, effectiveness, sustainability, and energy efficiency; nevertheless, its drawbacks include high maintenance, operating protocol, and costs [65,136]. Several studies have demonstrated that utilizing hybrid strategies can increase the efficiency of purifying wastewater while also saving electricity [137]. There are four primary categories of hybrid systems, such as physical-biological systems, physical-chemical systems, chemical-biological systems, and physical-chemical-biological systems. A hybrid technique is more suited, quicker, more successful, and more efficient for the simultaneous removal of organic pollutants and energy generation than a single strategy, such as chemical or physical, which may be fairly challenging [136].

1.6 Graphitic Carbon Nitride

Carbon-based material graphitic carbon nitride, also known as g-C₃N₄, has received notable focus and attention and is employed in several fields such as photocatalysis, electrogenerated chemiluminescence, lithium-ion batteries, hydrogen storage, fluorescence sensors, and adsorption [138–145]. Because of its easy synthesis, attractive electrical band structure, great physicochemical stability, and "earth-abundant" nature, it has generated interest in the scientific community as the next generation photocatalyst [146,147]. Not at all new, carbon nitride (C₃N₄) is regarded as one of the

first artificial polymers that have been reported in scientific literature. A linear polymer of linked tri-s-triazine through secondary nitrogen, the embryonic form of melon was first produced by Berzelius and termed by Liebig in 1834. This is the point where the history of C_3N_4 polymers and their precursors starts [148,149]. About eighteen years ago, in 2006, g- C_3N_4 was first used in the field of heterogeneous catalysis [150]. Wang et al. first published the finding of g- C_3N_4 as a metal-free conjugated semiconductor photocatalyst for H_2 evolution in 2009 [151]. This may have caused the focus of research to shift from inorganic to polymeric conjugated semiconductor photocatalysts [152]. Generally, C_3N_4 has seven phases, such as α - C_3N_4 , β - C_3N_4 , cubic C_3N_4 , pseudocubic C_3N_4 , g-h-triazine, g-o-triazine, and g-h-heptazine [153]. In terms of energy preference, the most stable phase of C_3N_4 under ambient conditions was tri-s-triazine-based g- C_3N_4 [154]. The majority of studies suggested that melamine, cyanamide, dicyandiamide, or urea polycondensation produced a melon polymer from the melem units. Consequently, it is well acknowledged that tri-s-triazine can act as the building blocks for the standard synthesis of g- C_3N_4 . It is readily generated through the thermal polymerization of several nitrogen-rich precursors, including ammonium thiocyanate, urea, dicyandiamide, melamine, and cyanamide [146].

1.6.1 g- C_3N_4 as Adsorbent

The use of g- C_3N_4 , a two-dimensional metal-free semiconductor, as an adsorbent to remove pollutants from the environment is growing in acceptance [145]. Numerous interactions with organic pollutants, such as π - π interaction, hydrophobic effect, hydrogen bond, acid-base interaction, and electrostatic interaction, make g- C_3N_4 an efficient adsorbent candidate for wastewater purification [63,145,155–157]. Tri-s-triazine units constitute the hexagonal ring-based C-N network of g- C_3N_4 . The π - π interaction and hydrophobic effect attract aromatic organic molecules to g- C_3N_4 because of the

delocalized π -electrons in tri-s-triazine units [145,157]. The electrostatic attraction between the g-C₃N₄ framework and organic pollutant molecules may enhance adsorption [155,158]. The heterocyclic N-atoms may interact with the organic molecule through hydrogen bonding during adsorption [155]. The g-C₃N₄ network may have slightly basic properties due to the presence of N atoms [159]. Hence, acid-base interaction may involve g-C₃N₄ and the acidic character of organic pollutants during adsorption [155]. Although pure g-C₃N₄ has several potential interactions for adsorption, its adsorption capacity is not sufficient. It is therefore preferable to continue improving the adsorption ability of the g-C₃N₄ material [158]. Several strategies have been implemented to modify the π stacking of the s-triazine units for enhancement of π - π interaction, increase in the amount and variety of functional groups on the surface of g-C₃N₄ for enhancement of hydrogen bonding interaction, change the charge density to increase the electrostatic interactions, and modify the basic character for increment of acid-base interaction [145,155,158,160].

1.6.2 g-C₃N₄ as Photocatalyst

g-C₃N₄ is considered as new generation of photocatalyst and has been extensively applied in the field of environmental photocatalysis [161]. Having a moderate band gap of ~2.7 eV, pure g-C₃N₄ can be stimulated by visible light up to 460 nm in wavelength [162]. Additionally, metal-free g-C₃N₄ possesses a number of characteristics that are important for photocatalysis reactions, including a layered crystal structure, π conjugated electronic structure, low cost, non-toxic nature, high chemical and thermal stability, high electron conductivity, and relatively simple production [163–165]. Meanwhile, because of the low specific surface area, insufficient absorption of visible light, quick photoinduced electron-hole pair recombination, poor photoinduced charge separation, and insufficient number of active sites of g-C₃N₄, its visible-light-responsive

photocatalytic efficiency is relatively low [166–168]. To enhance the photocatalytic performance of g-C₃N₄, a number of approaches have been used, including surface sensitization, nanostructure design, elemental doping, heterojunction construction with other semiconductors, and molecular doping [169–174].

g-C₃N₄ morphology engineering is an important field of current study. It has been possible to successfully synthesize g-C₃N₄ in a variety of fascinating morphologies, such as nanosphere, nanosheet, nanotube, and nanoflower [161]. Element doping can modify the VB and CB of g-C₃N₄ to change its energy band structure, but it can also change the surface characteristics of the photocatalyst to enhance its photocatalytic activity [175]. The charge redistribution of g-C₃N₄ will alter upon the introduction of non-metallic elements with distinct electronegativity and atomic radii from C and N elements, which could result in a modification of the photocatalytic behavior. Furthermore, adding nonmetallic elements can enhance the π -conjugated electrons' delocalization, which lowers the band gap and enhances the absorption of visible light [176]. The incorporation of metal doping increases the charge transfer ability, reduces the band gap of the photocatalyst, and enhances its adsorption capacity, thereby improving the photocatalytic activity [161,175].

The incorporation of additional organic monomers into g-C₃N₄ through molecular doping is an exclusive and efficient way to change the molecular and electrical structures of the compound. It is relatively simple to introduce organic monomers into g-C₃N₄ by copolymerization with the g-C₃N₄ precursor, including heterocycles, benzene and its derivatives, and other small compounds [177–179]. The addition of benzene rings to the g-C₃N₄ framework resulted in a large number of CH defects, which enhanced the

photoexcited charge separation of g-C₃N₄ and extended the delocalized π -conjugated system [178].

During the generation of an appropriate band structure, heterojunctions, such as isotype heterojunction and g-C₃N₄-metal oxide heterojunction, have shown effectiveness in enhancing charge separation, decreasing the band gap, and producing a more negative conduction band. As a result, heterojunction composites may effectively increase the photocatalytic efficiency of g-C₃N₄ while minimizing the rate of electron hole pair recombination and maximizing the use of visible light. It has been observed that the generation of isotype heterojunctions of g-C₃N₄ with different band structures in its two different crystal phases works efficiently for separating photogenerated electrons and holes [180–182].

The formation of heterostructures with different types of metal oxides, such as TiO₂, ZnO, WO₃, iron oxide, tin oxide, etc., enhanced the photocatalytic efficiency of the g-C₃N₄ by reducing electron-hole recombination and promoting the charge carriers' separation. Because of their improved electric, magnetic, and photocatalytic characteristics, metal oxide-based g-C₃N₄ nanocomposites can be applied to a variety of techniques, including the production of H₂, the reduction of CO₂ and NO, the oxidation of NO, the degradation of organic and inorganic dyes and other organic materials, the removal of toxic metal species, particularly Cr (VI) from water, antibody decontamination, solar cells, and sensing [182,183].

For g-C₃N₄-metal oxide heterostructure photocatalysts, there are five different forms of charge carrier separation, such as type I, type II, Z-scheme, p-n, and Schottky junctions. Most g-C₃N₄-metal oxide photocatalysts show type II and Z-scheme mechanisms for charge carrier separation [182].

In type II heterojunctions, it is inevitable for two semiconductors to form a stable heterojunction, and the position of the VB of semiconductor A is higher than that of semiconductor B (Figure 1.5). In this instance, the photogenerated hole migrates from the VB of semiconductor B to that of semiconductor A, and the photogenerated electrons are transferred from the CB of semiconductor A to that of semiconductor B. The improved electron and hole separation will decrease the electron-hole pair recombination rate and increase the lifetime of photoinduced electrons. The construction of type II systems is very important for photocatalytic reactions in numerous fields [182,184].

The direct Z-scheme photocatalytic system, first proposed by Bard et al. in 1995, is the other type of heterojunction. In this type of heterojunction, the photogenerated electrons on the CB of semiconductor B shift to the VB of semiconductor A and combine with the photogenerated holes (Figure 1.6). By increasing the electron hole pair separation, this type of heterojunction photocatalyst can be effective for reducing the recombination electron hole pair and improving the redox ability [182,184,185].

For decreasing the electron-hole pair recombination, suitable matching of band position is required during the preparation of a heterojunction composite of g-C₃N₄ with metal oxide. Because of the proper band alignment, a composite (ZnO/g-C₃N₄) with a medium band gap in g-C₃N₄ and a broader band gap in ZnO may provide an excellent heterostructure for accelerating charge separation [186,187]. Numerous studies on the production of ZnO/g-C₃N₄ composites and their use in the degradation of organic pollutants in waste water have been reported [183].

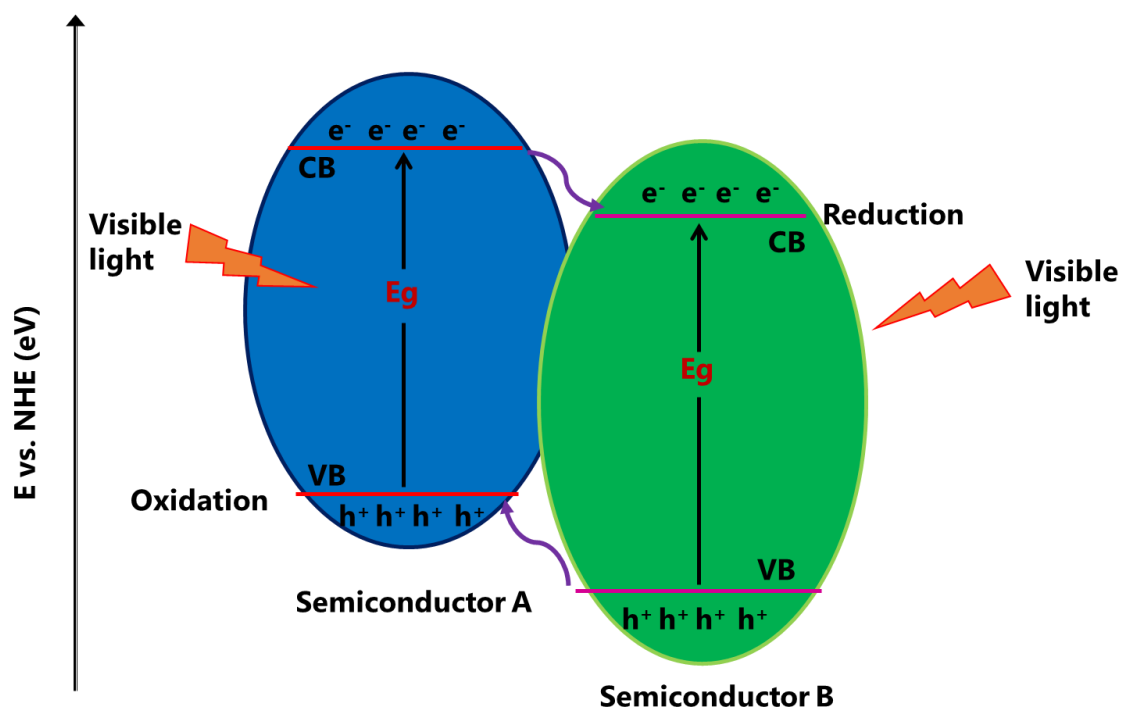


Figure 1.5 Type II heterojunction in g-C₃N₄-metal oxide photocatalysts.

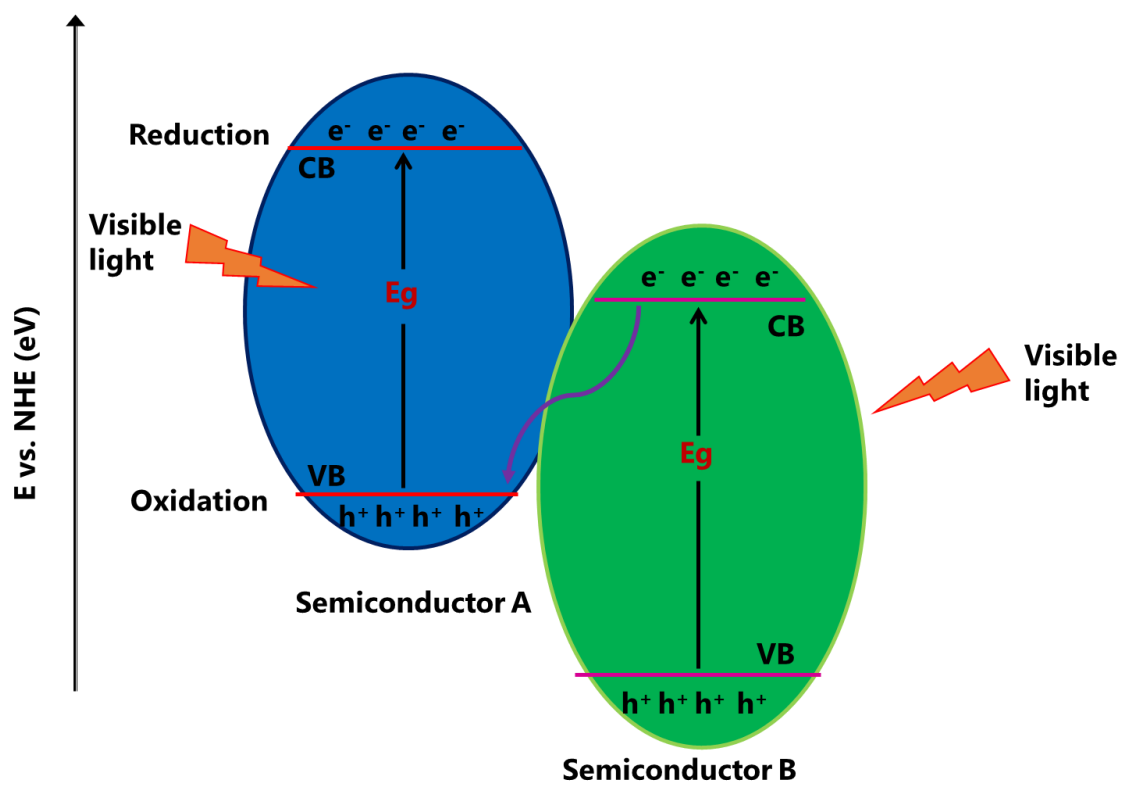


Figure 1.6 Z-scheme heterojunction in g-C₃N₄-metal oxide photocatalysts.

1.7 Objectives of the Research

● General Objectives

To fabricate and characterize the different types of ZnO/g-C₃N₄ composites and evaluate the application of ZnO/g-C₃N₄ composites for the removal of endocrine disrupting chemical BPE, pharmaceuticals waste DCF, and organic dye.

● Specific Objectives

- To fabricate the different types of ZnO/g-C₃N₄ composites by simple calcination technique and characterize using various analytical technique such as TGA, FTIR, XRD, XPS, SEM, TEM, FE-EPMA, UV-Vis DRS, PL, EIS and nitrogen adsorption and desorption isotherm.
- To investigate the photocatalytic degradation of endocrine disrupting chemical, BPE under visible light radiation using prepared ZnO/g-C₃N₄ composites.
- To evaluate the photocatalytic degradation efficiency of prepared ZnO/g-C₃N₄ composites on the degradation of pharmaceuticals waste, diclofenac in aqueous solution under visible light radiation.
- To investigate the purification of aqueous orange II solution through adsorption and visible-light-induced photodegradation using prepared ZnO/g-C₃N₄ composites.
- To study the kinetic parameters of all photocatalytic degradation reactions.
- To study the thermodynamic parameters and isotherm of orange II adsorption.
- To propose the respective photocatalytic degradation and adsorption mechanisms.

1.8 References

1. Haouti, R. El; Anfar, Z.; Et-Taleb, S.; Benafqir, M.; Lhanafi, S.; Alem, N. El Removal of Heavy Metals and Organic Pollutants by a Sand Rich in Iron Oxide. *Euro-Mediterranean J. Environ. Integr.* **2018**, 3, 17, doi:10.1007/s41207-018-0058-9.
2. Akter, N.; Hossain, M.A.; Hassan, M.J.; Amin, M.K.; Elias, M.; Rahman, M.M.; Asiri, A.M.; Siddiquey, I.A.; Hasnat, M.A. Amine Modified Tannin Gel for Adsorptive Removal of Brilliant Green Dye. *J. Environ. Chem. Eng.* **2016**, 4, 1231–1241, doi:10.1016/j.jece.2016.01.013.
3. Elias, M.; Akter, S.; Hossain, M.A.; Suhag, M.H. Fabrication of $\text{Zn}_3(\text{PO}_4)_2$ /carbon Nanotubes Nanocomposite Thin Film via Sol-Gel Drop Coating Method with Enhanced Photocatalytic Activity. *Thin Solid Films* **2021**, 717, 138472, doi:10.1016/j.tsf.2020.138472.
4. Li, H.; Yuan, Z.; Bittencourt, C.; Li, X.; Li, W.; Chen, M.; Li, W.; Snyders, R. Anion Exchange Synthesis of Hollow $\beta\text{-In}_2\text{S}_3$ Nanoparticles: Adsorption and Visible Light Photocatalytic Performances. *J. Environ. Chem. Eng.* **2019**, 7, 102910, doi:10.1016/j.jece.2019.102910.
5. Laysandra, L.; Sari, M.W.M.K.; Soetaredjo, F.E.; Foe, K.; Putro, J.N.; Kurniawan, A.; Ju, Y.-H.; Ismadji, S. Adsorption and Photocatalytic Performance of Bentonite-Titanium Dioxide Composites for Methylene Blue and Rhodamine B Decoloration. *Heliyon* **2017**, 3, e00488, doi:10.1016/j.heliyon.2017.e00488.
6. Wang, H.-J.; Cao, Y.; Wu, L.-L.; Wu, S.-S.; Raza, A.; Liu, N.; Wang, J.-Y.;

- Miyazawa, T. ZnS-Based Dual Nano-Semiconductors (ZnS/PbS, ZnS/CdS or ZnS/Ag₂S,): A Green Synthesis Route and Photocatalytic Comparison for Removing Organic Dyes. *J. Environ. Chem. Eng.* **2018**, 6, 6771–6779, doi:10.1016/j.jece.2018.10.034.
7. Zuccato, E.; Castiglioni, S.; Fanelli, R. Identification of the Pharmaceuticals for Human Use Contaminating the Italian Aquatic Environment. *J. Hazard. Mater.* **2005**, 122, 205–209, doi:10.1016/j.jhazmat.2005.03.001.
 8. Pereira, L.; Alves, M. Dyes—Environmental Impact and Remediation. In *Environmental Protection Strategies for Sustainable Development*; Springer Netherlands: Dordrecht, 2012; pp. 111–162.
 9. Kümmerer, K. Pharmaceuticals in the Environment. *Annu. Rev. Environ. Resour.* **2010**, 35, 57–75, doi:10.1146/annurev-environ-052809-161223.
 10. Verma, A.K.; Dash, R.R.; Bhunia, P. A Review on Chemical Coagulation/flocculation Technologies for Removal of Colour from Textile Wastewaters. *J. Environ. Manage.* **2012**, 93, 154–168, doi:10.1016/j.jenvman.2011.09.012.
 11. Roark, A.M. Endocrine Disruptors and Marine Systems. In *Encyclopedia of the World's Biomes*; Elsevier, 2020; pp. 188–194.
 12. Catenza, C.J.; Farooq, A.; Shubear, N.S.; Donkor, K.K. A Targeted Review on Fate, Occurrence, Risk and Health Implications of Bisphenol Analogues. *Chemosphere* **2021**, 268, 129273, doi:10.1016/j.chemosphere.2020.129273.
 13. Rochester, J.R.; Bolden, A.L. Bisphenol S and F: A Systematic Review and

- Comparison of the Hormonal Activity of Bisphenol A Substitutes. *Environ. Health Perspect.* **2015**, *123*, 643–650, doi:10.1289/ehp.1408989.
14. Barboza, L.G.A.; Cunha, S.C.; Monteiro, C.; Fernandes, J.O.; Guilhermino, L. Bisphenol A and Its Analogs in Muscle and Liver of Fish from the North East Atlantic Ocean in Relation to Microplastic Contamination. Exposure and Risk to Human Consumers. *J. Hazard. Mater.* **2020**, *393*, 122419, doi:10.1016/j.jhazmat.2020.122419.
 15. Lehmler, H.-J.; Liu, B.; Gadogbe, M.; Bao, W. Exposure to Bisphenol A, Bisphenol F, and Bisphenol S in U.S. Adults and Children: The National Health and Nutrition Examination Survey 2013–2014. *ACS Omega* **2018**, *3*, 6523–6532, doi:10.1021/acsomega.8b00824.
 16. Chen, D.; Kannan, K.; Tan, H.; Zheng, Z.; Feng, Y.-L.; Wu, Y.; Widelka, M. Bisphenol Analogues Other Than BPA: Environmental Occurrence, Human Exposure, and Toxicity—A Review. *Environ. Sci. Technol.* **2016**, *50*, 5438–5453, doi:10.1021/acs.est.5b05387.
 17. Rubin, B.S. Bisphenol A: An Endocrine Disruptor with Widespread Exposure and Multiple Effects. *J. Steroid Biochem. Mol. Biol.* **2011**, *127*, 27–34, doi:10.1016/j.jsbmb.2011.05.002.
 18. Vandenberg, L.N.; Hauser, R.; Marcus, M.; Olea, N.; Welshons, W. V. Human Exposure to Bisphenol A (BPA). *Reprod. Toxicol.* **2007**, *24*, 139–177, doi:10.1016/j.reprotox.2007.07.010.
 19. Kang, J.-H.; Kondo, F.; Katayama, Y. Human Exposure to Bisphenol A.

- Toxicology* **2006**, 226, 79–89, doi:10.1016/j.tox.2006.06.009.
20. Geens, T.; Aerts, D.; Berthot, C.; Bourguignon, J.-P.; Goeyens, L.; Lecomte, P.; Maghuin-Rogister, G.; Pironnet, A.-M.; Pussemier, L.; Scippo, M.-L.; et al. A Review of Dietary and Non-Dietary Exposure to Bisphenol-A. *Food Chem. Toxicol.* **2012**, 50, 3725–3740, doi:10.1016/j.fct.2012.07.059.
 21. Rochester, J.R. Bisphenol A and Human Health: A Review of the Literature. *Reprod. Toxicol.* **2013**, 42, 132–155, doi:10.1016/j.reprotox.2013.08.008.
 22. Uzzaman, M.; Hasan, M.K.; Mahmud, S.; Yousuf, A.; Islam, S.; Uddin, M.N.; Barua, A. Physicochemical, Spectral, Molecular Docking and ADMET Studies of Bisphenol Analogues; A Computational Approach. *Informatics Med. Unlocked* **2021**, 25, 100706, doi:10.1016/j.imu.2021.100706.
 23. Adeyemi, J.A.; Gallimberti, M.; Olise, C.C.; Rocha, B.A.; Adedire, C.O.; Barbosa Jr, F. Evaluation of Bisphenol A Levels in Nigerian Thermal Receipts and Estimation of Daily Dermal Exposure. *Environ. Sci. Pollut. Res.* **2020**, 27, 37645–37649, doi:10.1007/s11356-020-09898-4.
 24. Zhang, H.; Zhang, Y.; Li, J.; Yang, M. Occurrence and Exposure Assessment of Bisphenol Analogues in Source Water and Drinking Water in China. *Sci. Total Environ.* **2019**, 655, 607–613, doi:10.1016/j.scitotenv.2018.11.053.
 25. Eladak, S.; Grisin, T.; Moison, D.; Guerquin, M.-J.; N'Tumba-Byn, T.; Pozzi-Gaudin, S.; Benachi, A.; Livera, G.; Rouiller-Fabre, V.; Habert, R. A New Chapter in the Bisphenol A Story: Bisphenol S and Bisphenol F Are Not Safe Alternatives to This Compound. *Fertil. Steril.* **2015**, 103, 11–21,

- doi:10.1016/j.fertnstert.2014.11.005.
26. Shi, J.; Jiao, Z.; Zheng, S.; Li, M.; Zhang, J.; Feng, Y.; Yin, J.; Shao, B. Long-Term Effects of Bisphenol AF (BPAF) on Hormonal Balance and Genes of Hypothalamus-Pituitary-Gonad Axis and Liver of Zebrafish (*Danio Rerio*), and the Impact on Offspring. *Chemosphere* **2015**, *128*, 252–257, doi:10.1016/j.chemosphere.2015.01.060.
 27. Caban, M.; Stepnowski, P. Determination of Bisphenol A in Size Fractions of Indoor Dust from Several Microenvironments. *Microchem. J.* **2020**, *153*, 104392, doi:10.1016/j.microc.2019.104392.
 28. Zhang, H.; Quan, Q.; Zhang, M.; Zhang, N.; Zhang, W.; Zhan, M.; Xu, W.; Lu, L.; Fan, J.; Wang, Q. Occurrence of Bisphenol A and Its Alternatives in Paired Urine and Indoor Dust from Chinese University Students: Implications for Human Exposure. *Chemosphere* **2020**, *247*, 125987, doi:10.1016/j.chemosphere.2020.125987.
 29. Česen, M.; Lenarčič, K.; Mislej, V.; Levstek, M.; Kovačič, A.; Cimrmančič, B.; Uranjek, N.; Kosjek, T.; Heath, D.; Dolenc, M.S.; et al. The Occurrence and Source Identification of Bisphenol Compounds in Wastewaters. *Sci. Total Environ.* **2018**, *616-617*, 744–752, doi:10.1016/j.scitotenv.2017.10.252.
 30. Luo, Y.; Guo, W.; Ngo, H.H.; Nghiem, L.D.; Hai, F.I.; Zhang, J.; Liang, S.; Wang, X.C. A Review on the Occurrence of Micropollutants in the Aquatic Environment and Their Fate and Removal during Wastewater Treatment. *Sci. Total Environ.* **2014**, *473-474*, 619–641, doi:10.1016/j.scitotenv.2013.12.065.

31. Sun, Q.; Wang, Y.; Li, Y.; Ashfaq, M.; Dai, L.; Xie, X.; Yu, C.-P. Fate and Mass Balance of Bisphenol Analogues in Wastewater Treatment Plants in Xiamen City, China. *Environ. Pollut.* **2017**, *225*, 542–549, doi:10.1016/j.envpol.2017.03.018.
32. González, N.; Cunha, S.C.; Ferreira, R.; Fernandes, J.O.; Marquès, M.; Nadal, M.; Domingo, J.L. Concentrations of Nine Bisphenol Analogues in Food Purchased from Catalonia (Spain): Comparison of Canned and Non-Canned Foodstuffs. *Food Chem. Toxicol.* **2020**, *136*, 110992, doi:10.1016/j.fct.2019.110992.
33. Shen, J.; Kang, Q.; Mao, Y.; Yuan, M.; Le, F.; Yang, X.; Xu, X.; Jin, F. Urinary Bisphenol A Concentration Is Correlated with Poorer Oocyte Retrieval and Embryo Implantation Outcomes in Patients with Tubal Factor Infertility Undergoing in Vitro Fertilisation. *Ecotoxicol. Environ. Saf.* **2020**, *187*, 109816, doi:10.1016/j.ecoenv.2019.109816.
34. Audebert, M.; Riu, A.; Jacques, C.; Hillenweck, A.; Jamin, E.L.; Zalko, D.; Cravedi, J.-P. Use of the γ H₂AX Assay for Assessing the Genotoxicity of Polycyclic Aromatic Hydrocarbons in Human Cell Lines. *Toxicol. Lett.* **2010**, *199*, 182–192, doi:10.1016/j.toxlet.2010.08.022.
35. Fic, A.; Žegura, B.; Sollner Dolenc, M.; Filipič, M.; Peterlin Mašič, L. Mutagenicity and DNA Damage of Bisphenol a and Its Structural Analogues in Hepg2 Cells. *Arch. Ind. Hyg. Toxicol.* **2013**, *64*, 189–200, doi:10.2478/10004-1254-64-2013-2319.
36. Guo, Y.; Li, B.; Yan, X.; Shen, X.; Ma, J.; Liu, S.; Zhang, D. Bisphenol A and Polychlorinated Biphenyls Enhance the Cancer Stem Cell Properties of Human

- Ovarian Cancer Cells by Activating the WNT Signaling Pathway. *Chemosphere* **2020**, *246*, 125775, doi:10.1016/j.chemosphere.2019.125775.
37. Huang, Z.; Zhao, J.-L.; Yang, Y.-Y.; Jia, Y.-W.; Zhang, Q.-Q.; Chen, C.-E.; Liu, Y.-S.; Yang, B.; Xie, L.; Ying, G.-G. Occurrence, Mass Loads and Risks of Bisphenol Analogues in the Pearl River Delta Region, South China: Urban Rainfall Runoff as a Potential Source for Receiving Rivers. *Environ. Pollut.* **2020**, *263*, 114361, doi:10.1016/j.envpol.2020.114361.
 38. Cai, S.; Rao, X.; Ye, J.; Ling, Y.; Mi, S.; Chen, H.; Fan, C.; Li, Y. Relationship between Urinary Bisphenol a Levels and Cardiovascular Diseases in the U.S. Adult Population, 2003–2014. *Ecotoxicol. Environ. Saf.* **2020**, *192*, 110300, doi:10.1016/j.ecoenv.2020.110300.
 39. Rezg, R.; El-Fazaa, S.; Gharbi, N.; Mornagui, B. Bisphenol A and Human Chronic Diseases: Current Evidences, Possible Mechanisms, and Future Perspectives. *Environ. Int.* **2014**, *64*, 83–90, doi:10.1016/j.envint.2013.12.007.
 40. Liu, B.; Lehmler, H.-J.; Sun, Y.; Xu, G.; Sun, Q.; Snetselaar, L.G.; Wallace, R.B.; Bao, W. Association of Bisphenol A and Its Substitutes, Bisphenol F and Bisphenol S, with Obesity in United States Children and Adolescents. *Diabetes Metab. J.* **2019**, *43*, 59, doi:10.4093/dmj.2018.0045.
 41. Musachio, E.A.S.; Araujo, S.M.; Bortolotto, V.C.; de Freitas Couto, S.; Dahleh, M.M.M.; Poetini, M.R.; Jardim, E.F.; Meichtry, L.B.; Ramborger, B.P.; Roehrs, R.; et al. Bisphenol A Exposure Is Involved in the Development of Parkinson like Disease in Drosophila Melanogaster. *Food Chem. Toxicol.* **2020**, *137*, 111128,

- doi:10.1016/j.fct.2020.111128.
42. Tian, B.; Wu, N.; Pan, X.; Wang, Z.; Yan, C.; Sharma, V.K.; Qu, R. Ferrate(VI) Oxidation of Bisphenol E–Kinetics, Removal Performance, and Dihydroxylation Mechanism. *Water Res.* **2022**, *210*, 118025, doi:10.1016/j.watres.2021.118025.
43. Pozdnyakov, I.P.; Guo, L.; Glebov, E.M.; Wu, F.; Plyusnin, V.F.; Grivin, V.P.; Deng, N. Aqueous Photochemistry of Bisphenol E in the Presence of β -Cyclodextrin. *High Energy Chem.* **2011**, *45*, 214–221, doi:10.1134/S001814391103012X.
44. Jiménez-Salcedo, M.; Monge, M.; Tena, M.T. The Photocatalytic Degradation of Sodium Diclofenac in Different Water Matrices Using g-C₃N₄ Nanosheets: A Study of the Intermediate by-Products and Mechanism. *J. Environ. Chem. Eng.* **2021**, *9*, 105827, doi:10.1016/j.jece.2021.105827.
45. Patel, M.; Kumar, R.; Kishor, K.; Mlsna, T.; Pittman, C.U.; Mohan, D. Pharmaceuticals of Emerging Concern in Aquatic Systems: Chemistry, Occurrence, Effects, and Removal Methods. *Chem. Rev.* **2019**, *119*, 3510–3673, doi:10.1021/acs.chemrev.8b00299.
46. He, J.; Yang, J.; Jiang, F.; Liu, P.; Zhu, M. Photo-Assisted Peroxymonosulfate Activation via 2D/2D Heterostructure of Ti₃C₂/g-C₃N₄ for Degradation of Diclofenac. *Chemosphere* **2020**, *258*, 127339, doi:10.1016/j.chemosphere.2020.127339.
47. Zhang, W.; Zhou, L.; Deng, H. Ag Modified g-C₃N₄ Composites with Enhanced Visible-Light Photocatalytic Activity for Diclofenac Degradation. *J. Mol. Catal. A*

- Chem.* **2016**, 423, 270–276, doi:10.1016/j.molcata.2016.07.021.
48. Lara-Pérez, C.; Leyva, E.; Zermelo, B.; Osorio, I.; Montalvo, C.; Moctezuma, E. Photocatalytic Degradation of Diclofenac Sodium Salt: Adsorption and Reaction Kinetic Studies. *Environ. Earth Sci.* **2020**, 79, 277, doi:10.1007/s12665-020-09017-z.
49. Nieto-Sandoval, J.; Munoz, M.; de Pedro, Z.M.; Casas, J.A. Catalytic Hydrodechlorination as Polishing Step in Drinking Water Treatment for the Removal of Chlorinated Micropollutants. *Sep. Purif. Technol.* **2019**, 227, 115717, doi:10.1016/j.seppur.2019.115717.
50. Tanveer, M.; Tezcanli, G.; Sadiq, M.T.; Kazmi, S.M.; Noshad, N.; Abbas, G.; Ali, A. Degradation of Diclofenac under Irradiation of UV Lamp and Solar Light Using ZnO Photo Catalyst. *Eng. Proc.* **2022**, 12, 1–13, doi:10.3390/engproc2021012076.
51. Zhang, W.; Zhou, L.; Shi, J.; Deng, H. Fabrication of Novel Visible-Light-Driven AgI/g-C₃N₄ Composites with Enhanced Visible-Light Photocatalytic Activity for Diclofenac Degradation. *J. Colloid Interface Sci.* **2017**, 496, 167–176, doi:10.1016/j.jcis.2017.02.022.
52. Liu, W.; Li, Y.; Liu, F.; Jiang, W.; Zhang, D.; Liang, J. Visible-Light-Driven Photocatalytic Degradation of Diclofenac by Carbon Quantum Dots Modified Porous g-C₃N₄: Mechanisms, Degradation Pathway and DFT Calculation. *Water Res.* **2019**, 151, 8–19, doi:10.1016/j.watres.2018.11.084.
53. Gerbaldo, M.V.; Marchetti, S.G.; Mendoza, S.M.; Elias, V.R.; Mendieta, S.N.; Crivello, M.E. Photocatalytic Degradation of Sodium Diclofenac Using Spinel

- Ferrites: Kinetic Aspects. *Top. Catal.* **2022**, 65, 1419–1426, doi:10.1007/s11244-022-01627-0.
54. Oaks, J.L.; Gilbert, M.; Virani, M.Z.; Watson, R.T.; Meteyer, C.U.; Rideout, B.A.; Shivaprasad, H.L.; Ahmed, S.; Chaudhry, M.J.I.; Arshad, M.; et al. Diclofenac Residues as the Cause of Vulture Population Decline in Pakistan. *Nature* **2004**, 427, 630–633, doi:10.1038/nature02317.
 55. Lonappan, L.; Brar, S.K.; Das, R.K.; Verma, M.; Surampalli, R.Y. Diclofenac and Its Transformation Products: Environmental Occurrence and Toxicity - A Review. *Environ. Int.* **2016**, 96, 127–138, doi:10.1016/j.envint.2016.09.014.
 56. Bound, J.P.; Voulvoulis, N. Household Disposal of Pharmaceuticals as a Pathway for Aquatic Contamination in the United Kingdom. *Environ. Health Perspect.* **2005**, 113, 1705–1711, doi:10.1289/ehp.8315.
 57. Tüzün, S.C.; Karapınar, I. A Review on Diclofenac Degradation, Transformation Products and Their Fate in the Environment. *Pamukkale Univ. J. Eng. Sci.* **2022**, 28, 937–952, doi:10.5505/pajes.2022.71363.
 58. Borghi, S.M.; Fattori, V.; Ruiz-Miyazawa, K.W.; Bertozzi, M.M.; Lourenco-Gonzalez, Y.; Tatakihara, R.I.; Bussmann, A.J.C.; Mazzuco, T.L.; Casagrande, R.; Verri, W.A. Pyrrolidine Dithiocarbamate Inhibits Mouse Acute Kidney Injury Induced by Diclofenac by Targeting Oxidative Damage, Cytokines and NF-κB Activity. *Life Sci.* **2018**, 208, 221–231, doi:10.1016/j.lfs.2018.07.038.
 59. Green, R.E.; Newton, I.; Shultz, S.; Cunningham, A.A.; Gilbert, M.; Pain, D.J.; Prakash, V. Diclofenac Poisoning as a Cause of Vulture Population Declines

- across the Indian Subcontinent. *J. Appl. Ecol.* **2004**, *41*, 793–800, doi:10.1111/j.0021-8901.2004.00954.x.
60. Arora, S. Textile Dyes: It's Impact on Environment and Its Treatment. *J. Bioremediation Biodegrad.* **2014**, *05*, doi:10.4172/2155-6199.1000e146.
 61. Tkaczyk, A.; Mitrowska, K.; Posyniak, A. Synthetic Organic Dyes as Contaminants of the Aquatic Environment and Their Implications for Ecosystems: A Review. *Sci. Total Environ.* **2020**, *717*, 137222, doi:10.1016/j.scitotenv.2020.137222.
 62. Dawood, S.; Sen, T.K.; Phan, C. Synthesis and Characterisation of Novel-Activated Carbon from Waste Biomass Pine Cone and Its Application in the Removal of Congo Red Dye from Aqueous Solution by Adsorption. *Water, Air, Soil Pollut.* **2014**, *225*, 1818, doi:10.1007/s11270-013-1818-4.
 63. Yagub, M.T.; Sen, T.K.; Afroze, S.; Ang, H.M. Dye and Its Removal from Aqueous Solution by Adsorption: A Review. *Adv. Colloid Interface Sci.* **2014**, *209*, 172–184, doi:10.1016/j.cis.2014.04.002.
 64. Al-Tohamy, R.; Ali, S.S.; Li, F.; Okasha, K.M.; Mahmoud, Y.A.-G.; Elsamahy, T.; Jiao, H.; Fu, Y.; Sun, J. A Critical Review on the Treatment of Dye-Containing Wastewater: Ecotoxicological and Health Concerns of Textile Dyes and Possible Remediation Approaches for Environmental Safety. *Ecotoxicol. Environ. Saf.* **2022**, *231*, 113160, doi:10.1016/j.ecoenv.2021.113160.
 65. Solayman, H.M.; Hossen, M.A.; Abd Aziz, A.; Yahya, N.Y.; Leong, K.H.; Sim, L.C.; Monir, M.U.; Zoh, K.-D. Performance Evaluation of Dye Wastewater

- Treatment Technologies: A Review. *J. Environ. Chem. Eng.* **2023**, *11*, 109610, doi:10.1016/j.jece.2023.109610.
66. Carmen, Z.; Daniel, S. Textile Organic Dyes – Characteristics, Polluting Effects and Separation/Elimination Procedures from Industrial Effluents – A Critical Overview. In *Organic Pollutants Ten Years After the Stockholm Convention - Environmental and Analytical Update*; InTech, 2012; pp. 55–86.
 67. Ali, H. Biodegradation of Synthetic Dyes—A Review. *Water, Air, Soil Pollut.* **2010**, *213*, 251–273, doi:10.1007/s11270-010-0382-4.
 68. Drumond Chequer, F.M.; de Oliveira, G.A.R.; Anastacio Ferraz, E.R.; Carvalho, J.; Boldrin Zanoni, M.V.; de Oliveir, D.P. Textile Dyes: Dyeing Process and Environmental Impact. In *Eco-Friendly Textile Dyeing and Finishing*; InTech, 2013.
 69. Parmar, S.; Daki, S.; Bhattacharya, S.; Shrivastav, A. Microorganism. In *Development in Wastewater Treatment Research and Processes*; Elsevier, 2022; pp. 175–193.
 70. Zhou, Q. Chemical Pollution and Transport of Organic Dyes in Water–Soil–Crop Systems of the Chinese Coast. *Bull. Environ. Contam. Toxicol.* **2001**, *66*, 0784–0793, doi:10.1007/s00128-001-0077-z.
 71. Eriksson, E.; Auffarth, K.; Eilersen, A.-M.; Henze, M.; Ledin, A. Household Chemicals and Personal Care Products as Sources for Xenobiotic Organic Compounds in Grey Wastewater. *Water SA* **2003**, *29*, 135–146, doi:10.4314/wsa.v29i2.4848.

72. Yang, G.; Zhang, G.; Wang, H. Current State of Sludge Production, Management, Treatment and Disposal in China. *Water Res.* **2015**, *78*, 60–73, doi:10.1016/j.watres.2015.04.002.
73. Carneiro, P.A.; Umbuzeiro, G.A.; Oliveira, D.P.; Zanoni, M.V.B. Assessment of Water Contamination Caused by a Mutagenic Textile Effluent/dyehouse Effluent Bearing Disperse Dyes. *J. Hazard. Mater.* **2010**, *174*, 694–699, doi:10.1016/j.jhazmat.2009.09.106.
74. Rezaee, A.; Ansari, M.; Khavanin, A.; Sabzali, A.; Aryan, M.M. Hospital Wastewater Treatment Using an Integrated Anaerobic Aerobic Fixed Film Bioreactor. *Am. J. Environ. Sci.* **2005**, *1*, 259–263, doi:10.3844/ajessp.2005.259.263.
75. Gupta, P.; Mathur, N.; Bhatnagar, P.; Nagar, P.; Srivastava, S. Genotoxicity Evaluation of Hospital Wastewaters. *Ecotoxicol. Environ. Saf.* **2009**, *72*, 1925–1932, doi:10.1016/j.ecoenv.2009.05.012.
76. Merzouk, B.; Madani, K.; Sekki, A. Using Electrocoagulation–electroflotation Technology to Treat Synthetic Solution and Textile Wastewater, Two Case Studies. *Desalination* **2010**, *250*, 573–577, doi:10.1016/j.desal.2009.09.026.
77. Kim, T.-H.; Park, C.; Yang, J.; Kim, S. Comparison of Disperse and Reactive Dye Removals by Chemical Coagulation and Fenton Oxidation. *J. Hazard. Mater.* **2004**, *112*, 95–103, doi:10.1016/j.jhazmat.2004.04.008.
78. Üstün, G.E.; Solmaz, S.K.A.; Birgül, A. Regeneration of Industrial District Wastewater Using a Combination of Fenton Process and Ion exchange—A Case

- Study. *Resour. Conserv. Recycl.* **2007**, 52, 425–440, doi:10.1016/j.resconrec.2007.05.006.
79. Tounsadi, H.; Metarfi, Y.; Taleb, M.; El Rhazi, K.; Rais, Z. Impact of Chemical Substances Used in Textile Industry on the Employee's Health: Epidemiological Study. *Ecotoxicol. Environ. Saf.* **2020**, 197, 110594, doi:10.1016/j.ecoenv.2020.110594.
80. Behera, M.; Nayak, J.; Banerjee, S.; Chakraborty, S.; Tripathy, S.K. A Review on the Treatment of Textile Industry Waste Effluents towards the Development of Efficient Mitigation Strategy: An Integrated System Design Approach. *J. Environ. Chem. Eng.* **2021**, 9, 105277, doi:10.1016/j.jece.2021.105277.
81. Cao, G.; Wang, R.; Ju, Y.; Jing, B.; Duan, X.; Ao, Z.; Jiang, J.; Li, F.; Ho, S.-H. Synchronous Removal of Emulsions and Soluble Organic Contaminants via a Microalgae-Based Membrane System: Performance and Mechanisms. *Water Res.* **2021**, 206, 117741, doi:10.1016/j.watres.2021.117741.
82. Burakov, A.E.; Galunin, E. V.; Burakova, I. V.; Kucheroval, A.E.; Agarwal, S.; Tkachev, A.G.; Gupta, V.K. Adsorption of Heavy Metals on Conventional and Nanostructured Materials for Wastewater Treatment Purposes: A Review. *Ecotoxicol. Environ. Saf.* **2018**, 148, 702–712, doi:10.1016/j.ecoenv.2017.11.034.
83. Gruchlik, Y.; Linge, K.; Joll, C. Removal of Organic Micropollutants in Waste Stabilisation Ponds: A Review. *J. Environ. Manage.* **2018**, 206, 202–214, doi:10.1016/j.jenvman.2017.10.020.
84. Alessandretti, I.; Rigueto, C.V.T.; Nazari, M.T.; Rosseto, M.; Dettmer, A.

- Removal of Diclofenac from Wastewater: A Comprehensive Review of Detection, Characteristics and Tertiary Treatment Techniques. *J. Environ. Chem. Eng.* **2021**, 9, 106743, doi:10.1016/j.jece.2021.106743.
85. Xing, J.; Zhang, S.; Zhang, M.; Hou, J. A Critical Review of Presence, Removal and Potential Impacts of Endocrine Disruptors Bisphenol A. *Comp. Biochem. Physiol. Part C Toxicol. Pharmacol.* **2022**, 254, 109275, doi:10.1016/j.cbpc.2022.109275.
 86. Bhatnagar, A.; Anastopoulos, I. Adsorptive Removal of Bisphenol A (BPA) from Aqueous Solution: A Review. *Chemosphere* **2017**, 168, 885–902, doi:10.1016/j.chemosphere.2016.10.121.
 87. Li, F.; Katz, L.; Hu, Z. Adsorption of Major Nitrogen-Containing Components in Microalgal Bio-Oil by Activated Carbon: Equilibrium, Kinetics, and Ideal Adsorbed Solution Theory (IAST) Model. *ACS Sustain. Chem. Eng.* **2019**, 7, 16529–16538, doi:10.1021/acssuschemeng.9b03804.
 88. Akpomie, K.G.; Conradie, J. Advances in Application of Cotton-Based Adsorbents for Heavy Metals Trapping, Surface Modifications and Future Perspectives. *Ecotoxicol. Environ. Saf.* **2020**, 201, 110825, doi:10.1016/j.ecoenv.2020.110825.
 89. Shakib, F.; Dadvand Koohi, A.; Kamran Pirzaman, A. Adsorption of Methylene Blue by Using Novel Chitosan-G-Itaconic Acid/bentonite Nanocomposite – Equilibrium and Kinetic Study. *Water Sci. Technol.* **2017**, 75, 1932–1943, doi:10.2166/wst.2017.077.
 90. Ahmadifar, Z.; Dadvand Koohi, A. Characterization, Preparation, and Uses of

- Nanomagnetic Fe₃O₄ Impregnated onto Fish Scale as More Efficient Adsorbent for Cu²⁺ Ion Adsorption. *Environ. Sci. Pollut. Res.* **2018**, 25, 19687–19700, doi:10.1007/s11356-018-2058-3.
91. Hu, X.; Cheng, Z. Removal of Diclofenac from Aqueous Solution with Multi-Walled Carbon Nanotubes Modified by Nitric Acid. *Chinese J. Chem. Eng.* **2015**, 23, 1551–1556, doi:10.1016/j.cjche.2015.06.010.
92. Al-Asheh, S.; Aidan, A. A Comprehensive Method of Ion Exchange Resins Regeneration and Its Optimization for Water Treatment. In *Promising Techniques for Wastewater Treatment and Water Quality Assessment*; IntechOpen, 2021.
93. Ahmad, A.; Mohd-Setapar, S.H.; Chuong, C.S.; Khatoon, A.; Wani, W.A.; Kumar, R.; Rafatullah, M. Recent Advances in New Generation Dye Removal Technologies: Novel Search for Approaches to Reprocess Wastewater. *RSC Adv.* **2015**, 5, 30801–30818, doi:10.1039/C4RA16959J.
94. Kapoor, A.; Balasubramanian, S.; Kavitha, E.; Poonguzhali, E.; Prabhakar, S. Role of Membranes in Wastewater Treatment. In *Water Pollution and Remediation: Photocatalysis*; 2021; pp. 247–281.
95. Samsami, S.; Mohamadizani, M.; Sarrafzadeh, M.-H.; Rene, E.R.; Firoozbahr, M. Recent Advances in the Treatment of Dye-Containing Wastewater from Textile Industries: Overview and Perspectives. *Process Saf. Environ. Prot.* **2020**, 143, 138–163, doi:10.1016/j.psep.2020.05.034.
96. Wang, X.; Xia, J.; Ding, S.; Zhang, S.; Li, M.; Shang, Z.; Lu, J.; Ding, J. Removing Organic Matters from Reverse Osmosis Concentrate Using Advanced Oxidation-

- Biological Activated Carbon Process Combined with Fe^{3+} /humus-Reducing Bacteria. *Ecotoxicol. Environ. Saf.* **2020**, 203, 110945, doi:10.1016/j.ecoenv.2020.110945.
97. Wang, A.-J.; Wang, H.-C.; Cheng, H.-Y.; Liang, B.; Liu, W.-Z.; Han, J.-L.; Zhang, B.; Wang, S.-S. Electrochemistry-Stimulated Environmental Bioremediation: Development of Applicable Modular Electrode and System Scale-Up. *Environ. Sci. Ecotechnology* **2020**, 3, 100050, doi:10.1016/j.es.2020.100050.
 98. Liang, C.; Wei, D.; Zhang, S.; Ren, Q.; Shi, J.; Liu, L. Removal of Antibiotic Resistance Genes from Swine Wastewater by Membrane Filtration Treatment. *Ecotoxicol. Environ. Saf.* **2021**, 210, 111885, doi:10.1016/j.ecoenv.2020.111885.
 99. Dasgupta, J.; Singh, M.; Sikder, J.; Padarthy, V.; Chakraborty, S.; Curcio, S. Response Surface-Optimized Removal of Reactive Red 120 Dye from Its Aqueous Solutions Using Polyethyleneimine Enhanced Ultrafiltration. *Ecotoxicol. Environ. Saf.* **2015**, 121, 271–278, doi:10.1016/j.ecoenv.2014.12.041.
 100. Dasgupta, J.; Mondal, D.; Chakraborty, S.; Sikder, J.; Curcio, S.; Arafat, H.A. Nanofiltration Based Water Reclamation from Tannery Effluent Following Coagulation Pretreatment. *Ecotoxicol. Environ. Saf.* **2015**, 121, 22–30, doi:10.1016/j.ecoenv.2015.07.006.
 101. Cartagena, P.; El Kaddouri, M.; Cases, V.; Trapote, A.; Prats, D. Reduction of Emerging Micropollutants, Organic Matter, Nutrients and Salinity from Real Wastewater by Combined MBR–NF/RO Treatment. *Sep. Purif. Technol.* **2013**, 110, 132–143, doi:10.1016/j.seppur.2013.03.024.

102. Vona, A.; di Martino, F.; Garcia-Ivars, J.; Picó, Y.; Mendoza-Roca, J.-A.; Iborra-Clar, M.-I. Comparison of Different Removal Techniques for Selected Pharmaceuticals. *J. Water Process Eng.* **2015**, *5*, 48–57, doi:10.1016/j.jwpe.2014.12.011.
103. Licona, K.P.M.; Geaquinto, L.R. de O.; Nicolini, J.V.; Figueiredo, N.G.; Chiapetta, S.C.; Habert, A.C.; Yokoyama, L. Assessing Potential of Nanofiltration and Reverse Osmosis for Removal of Toxic Pharmaceuticals from Water. *J. Water Process Eng.* **2018**, *25*, 195–204, doi:10.1016/j.jwpe.2018.08.002.
104. Cuhorka, J.; Wallace, E.; Mikulášek, P. Removal of Micropollutants from Water by Commercially Available Nanofiltration Membranes. *Sci. Total Environ.* **2020**, *720*, 137474, doi:10.1016/j.scitotenv.2020.137474.
105. Katheresan, V.; Kansedo, J.; Lau, S.Y. Efficiency of Various Recent Wastewater Dye Removal Methods: A Review. *J. Environ. Chem. Eng.* **2018**, *6*, 4676–4697, doi:10.1016/j.jece.2018.06.060.
106. Kishor, R.; Purchase, D.; Saratale, G.D.; Saratale, R.G.; Ferreira, L.F.R.; Bilal, M.; Chandra, R.; Bharagava, R.N. Ecotoxicological and Health Concerns of Persistent Coloring Pollutants of Textile Industry Wastewater and Treatment Approaches for Environmental Safety. *J. Environ. Chem. Eng.* **2021**, *9*, 105012, doi:10.1016/j.jece.2020.105012.
107. Al-Mutairi, N.Z. Coagulant Toxicity and Effectiveness in a Slaughterhouse Wastewater Treatment Plant. *Ecotoxicol. Environ. Saf.* **2006**, *65*, 74–83, doi:10.1016/j.ecoenv.2005.05.013.

108. Dotto, J.; Fagundes-Klen, M.R.; Veit, M.T.; Palácio, S.M.; Bergamasco, R. Performance of Different Coagulants in the Coagulation/flocculation Process of Textile Wastewater. *J. Clean. Prod.* **2019**, *208*, 656–665, doi:10.1016/j.jclepro.2018.10.112.
109. Badawi, A.K.; Zaher, K. Hybrid Treatment System for Real Textile Wastewater Remediation Based on Coagulation/flocculation, Adsorption and Filtration Processes: Performance and Economic Evaluation. *J. Water Process Eng.* **2021**, *40*, 101963, doi:10.1016/j.jwpe.2021.101963.
110. Lau, Y.-Y.; Wong, Y.-S.; Teng, T.-T.; Morad, N.; Rafatullah, M.; Ong, S.-A. Coagulation-Flocculation of Azo Dye Acid Orange 7 with Green Refined Laterite Soil. *Chem. Eng. J.* **2014**, *246*, 383–390, doi:10.1016/j.cej.2014.02.100.
111. Zhang, X.; Li, F.; Wang, J.; Zhao, H.; Yu, X.-F. Strategy for Improving the Activity and Selectivity of CO₂ Electroreduction on Flexible Carbon Materials for Carbon Neutral. *Appl. Energy* **2021**, *298*, 117196, doi:10.1016/j.apenergy.2021.117196.
112. Yadav, K.K.; Kumar, S.; Pham, Q.B.; Gupta, N.; Rezaia, S.; Kamyab, H.; Yadav, S.; Vymazal, J.; Kumar, V.; Tri, D.Q.; et al. Fluoride Contamination, Health Problems and Remediation Methods in Asian Groundwater: A Comprehensive Review. *Ecotoxicol. Environ. Saf.* **2019**, *182*, 109362, doi:10.1016/j.ecoenv.2019.06.045.
113. Hamad, H.; Bassyouni, D.; El-Ashtoukhy, E.-S.; Amin, N.; Abd El-Latif, M. Electrocatalytic Degradation and Minimization of Specific Energy Consumption

- of Synthetic Azo Dye from Wastewater by Anodic Oxidation Process with an Emphasis on Enhancing Economic Efficiency and Reaction Mechanism. *Ecotoxicol. Environ. Saf.* **2018**, *148*, 501–512, doi:10.1016/j.ecoenv.2017.10.061.
114. Montañés, M.T.; García-Gabaldón, M.; Roca-Pérez, L.; Giner-Sanz, J.J.; Mora-Gómez, J.; Pérez-Herranz, V. Analysis of Norfloxacin Ecotoxicity and the Relation with Its Degradation by Means of Electrochemical Oxidation Using Different Anodes. *Ecotoxicol. Environ. Saf.* **2020**, *188*, 109923, doi:10.1016/j.ecoenv.2019.109923.
 115. Khataee, A.R.; Vatanpour, V.; Amani Ghadim, A.R. Decolorization of C.I. Acid Blue 9 Solution by UV/Nano-TiO₂, Fenton, Fenton-Like, Electro-Fenton and Electrocoagulation Processes: A Comparative Study. *J. Hazard. Mater.* **2009**, *161*, 1225–1233, doi:10.1016/j.jhazmat.2008.04.075.
 116. Coria-Oriundo, L.L.; Battaglini, F.; Wirth, S.A. Efficient Decolorization of Recalcitrant Dyes at Neutral/alkaline pH by a New Bacterial Laccase-Mediator System. *Ecotoxicol. Environ. Saf.* **2021**, *217*, 112237, doi:10.1016/j.ecoenv.2021.112237.
 117. Kumar, A.; Sharma, G.; Naushad, M.; Al-Muhtaseb, A.H.; García-Peñas, A.; Mola, G.T.; Si, C.; Stadler, F.J. Bio-Inspired and Biomaterials-Based Hybrid Photocatalysts for Environmental Detoxification: A Review. *Chem. Eng. J.* **2020**, *382*, 122937, doi:10.1016/j.cej.2019.122937.
 118. Louati, I.; Elloumi-Mseddi, J.; Cheikhrouhou, W.; Hadrich, B.; Nasri, M.; Aifa, S.; Woodward, S.; Mechichi, T. Simultaneous Cleanup of Reactive Black 5 and

- Cadmium by a Desert Soil Bacterium. *Ecotoxicol. Environ. Saf.* **2020**, *190*, 110103, doi:10.1016/j.ecoenv.2019.110103.
119. Suhag, M.H.; Haque, K.A.U.; Hossen, M.Z.; Azad, A.K.; Younus, M. Biodegradation of Azo Dyes and Dyes Present in Textile Wastewaters Using Bacillus Sp. az28, Obtained from Industrial Effluents. *J. Bangladesh Acad. Sci.* **2021**, *45*, 117–122, doi:10.3329/jbas.v45i1.54263.
 120. Sepehri, A.; Sarrafzadeh, M.-H.; Avateffazeli, M. Interaction between Chlorella Vulgaris and Nitrifying-Enriched Activated Sludge in the Treatment of Wastewater with Low C/N Ratio. *J. Clean. Prod.* **2020**, *247*, 119164, doi:10.1016/j.jclepro.2019.119164.
 121. Kurian, M. Advanced Oxidation Processes and Nanomaterials -a Review. *Clean. Eng. Technol.* **2021**, *2*, 100090, doi:10.1016/j.clet.2021.100090.
 122. Titchou, F.E.; Zazou, H.; Afanga, H.; El Gaayda, J.; Ait Akbour, R.; Nidheesh, P.V.; Hamdani, M. Removal of Organic Pollutants from Wastewater by Advanced Oxidation Processes and Its Combination with Membrane Processes. *Chem. Eng. Process. - Process Intensif.* **2021**, *169*, 108631, doi:10.1016/j.cep.2021.108631.
 123. Cuerda-Correa, E.M.; Alexandre-Franco, M.F.; Fernández-González, C. Advanced Oxidation Processes for the Removal of Antibiotics from Water. An Overview. *Water* **2019**, *12*, 102, doi:10.3390/w12010102.
 124. Rosman, N.; Salleh, W.N.W.; Mohamed, M.A.; Jaafar, J.; Ismail, A.F.; Harun, Z. Hybrid Membrane Filtration-Advanced Oxidation Processes for Removal of Pharmaceutical Residue. *J. Colloid Interface Sci.* **2018**, *532*, 236–260,

- doi:10.1016/j.jcis.2018.07.118.
125. Miklos, D.B.; Remy, C.; Jekel, M.; Linden, K.G.; Drewes, J.E.; Hübner, U. Evaluation of Advanced Oxidation Processes for Water and Wastewater Treatment – A Critical Review. *Water Res.* **2018**, *139*, 118–131, doi:10.1016/j.watres.2018.03.042.
126. Prada-Vásquez, M.A.; Estrada-Flórez, S.E.; Serna-Galvis, E.A.; Torres-Palma, R.A. Developments in the Intensification of Photo-Fenton and Ozonation-Based Processes for the Removal of Contaminants of Emerging Concern in Ibero-American Countries. *Sci. Total Environ.* **2021**, *765*, 142699, doi:10.1016/j.scitotenv.2020.142699.
127. Kumari, H.; Sonia; Suman; Ranga, R.; Chahal, S.; Devi, S.; Sharma, S.; Kumar, S.; Kumar, P.; Kumar, S.; et al. A Review on Photocatalysis Used For Wastewater Treatment: Dye Degradation. *Water, Air, Soil Pollut.* **2023**, *234*, 349, doi:10.1007/s11270-023-06359-9.
128. Huo, X.; Zhou, P.; Liu, Y.; Cheng, F.; Liu, Y.; Cheng, X.; Zhang, Y.; Wang, Q. Removal of Contaminants by Activating Peroxymonosulfate (PMS) Using Zero Valent Iron (ZVI)-Based Bimetallic Particles (ZVI/Cu, ZVI/Co, ZVI/Ni, and ZVI/Ag). *RSC Adv.* **2020**, *10*, 28232–28242, doi:10.1039/D0RA03924A.
129. Huang, Y.; Li, J.; Du, P.; Lu, X. Rational Design of Copper Encapsulated within Nitrogen-Doped Carbon Core-Shell Nanosphere for Efficiently Photocatalytic Peroxymonosulfate Activation. *J. Colloid Interface Sci.* **2021**, *597*, 206–214, doi:10.1016/j.jcis.2021.04.016.

-
130. Wang, J.; Zhuan, R. Degradation of Antibiotics by Advanced Oxidation Processes: An Overview. *Sci. Total Environ.* **2020**, *701*, 135023, doi:10.1016/j.scitotenv.2019.135023.
131. Herrmann, J. Photocatalysis. In *Kirk-Othmer Encyclopedia of Chemical Technology*; Wiley, 2017; pp. 1–44.
132. Fujishima, A.; Zhang, X.; Tryk, D. TiO₂ Photocatalysis and Related Surface Phenomena. *Surf. Sci. Rep.* **2008**, *63*, 515–582, doi:10.1016/j.surfrep.2008.10.001.
133. Ni, M.; Leung, M.K.H.; Leung, D.Y.C.; Sumathy, K. A Review and Recent Developments in Photocatalytic Water-Splitting Using TiO₂ for Hydrogen Production. *Renew. Sustain. Energy Rev.* **2007**, *11*, 401–425, doi:10.1016/j.rser.2005.01.009.
134. Fujishima, A.; Honda, K. Electrochemical Photolysis of Water at a Semiconductor Electrode. *Nature* **1972**, *238*, 37–38, doi:10.1038/238037a0.
135. Ajmal, A.; Majeed, I.; Malik, R.N.; Idriss, H.; Nadeem, M.A. Principles and Mechanisms of Photocatalytic Dye Degradation on TiO₂ Based Photocatalysts: A Comparative Overview. *RSC Adv.* **2014**, *4*, 37003–37026, doi:10.1039/C4RA06658H.
136. Tee, P.F.; Abdullah, M.O.; Tan, I.A.W.; Rashid, N.K.A.; Amin, M.A.M.; Nolasco-Hipolito, C.; Bujang, K. Review on Hybrid Energy Systems for Wastewater Treatment and Bio-Energy Production. *Renew. Sustain. Energy Rev.* **2016**, *54*, 235–246, doi:10.1016/j.rser.2015.10.011.
137. Patel, S.; Mondal, S.; Majumder, S.K.; Das, P.; Ghosh, P. Treatment of a

- Pharmaceutical Industrial Effluent by a Hybrid Process of Advanced Oxidation and Adsorption. *ACS Omega* **2020**, *5*, 32305–32317, doi:10.1021/acsomega.0c04139.
138. Zhang, H.; Huang, Q.; Huang, Y.; Li, F.; Zhang, W.; Wei, C.; Chen, J.; Dai, P.; Huang, L.; Huang, Z.; et al. Graphitic Carbon Nitride Nanosheets Doped Graphene Oxide for Electrochemical Simultaneous Determination of Ascorbic Acid, Dopamine and Uric Acid. *Electrochim. Acta* **2014**, *142*, 125–131, doi:10.1016/j.electacta.2014.07.094.
 139. Khatun, A.; Suhag, M.H.; Tateishi, I.; Furukawa, M.; Katsumata, H.; Kaneco, S. Facile Synthesis of ZnO/g-C₃N₄ with Enhanced Photocatalytic Performance for the Reduction of Cr(VI) in Presence of EDTA Under Visible Light Irradiation. *Int. J. Environ. Res.* **2023**, *17*, 1–17, doi:10.1007/s41742-023-00522-0.
 140. Cheng, C.; Huang, Y.; Wang, J.; Zheng, B.; Yuan, H.; Xiao, D. Anodic Electrogenated Chemiluminescence Behavior of Graphite-Like Carbon Nitride and Its Sensing for Rutin. *Anal. Chem.* **2013**, *85*, 2601–2605, doi:10.1021/ac303263n.
 141. Wu, M.; Wang, Q.; Sun, Q.; Jena, P. Functionalized Graphitic Carbon Nitride for Efficient Energy Storage. *J. Phys. Chem. C* **2013**, *117*, 6055–6059, doi:10.1021/jp311972f.
 142. Uzzaman, M.; Suhag, M.H.; Katsumata, H.; Tateishi, I.; Furukawa, M.; Kaneco, S. A Graphitic Carbon Nitride Photocatalyst with a Benzene-Ring-Modified Isotype Heterojunction for Visible-Light-Driven Hydrogen Production. *Catal. Sci.*

- Technol.* **2024**, *14*, 267–278, doi:10.1039/D3CY01461D.
143. Tian, J.; Liu, Q.; Asiri, A.M.; Al-Youbi, A.O.; Sun, X. Ultrathin Graphitic Carbon Nitride Nanosheet: A Highly Efficient Fluorosensor for Rapid, Ultrasensitive Detection of Cu²⁺. *Anal. Chem.* **2013**, *85*, 5595–5599, doi:10.1021/ac400924j.
144. Shalom, M.; Inal, S.; Fettkenhauer, C.; Neher, D.; Antonietti, M. Improving Carbon Nitride Photocatalysis by Supramolecular Preorganization of Monomers. *J. Am. Chem. Soc.* **2013**, *135*, 7118–7121, doi:10.1021/ja402521s.
145. Yan, L.; Gao, H.; Chen, Y. Na-Doped Graphitic Carbon Nitride for Removal of Aqueous Contaminants via Adsorption and Photodegradation. *ACS Appl. Nano Mater.* **2021**, *4*, 7746–7757, doi:10.1021/acsanm.1c01035.
146. Ong, W.-J.; Tan, L.-L.; Ng, Y.H.; Yong, S.-T.; Chai, S.-P. Graphitic Carbon Nitride (g-C₃N₄)-Based Photocatalysts for Artificial Photosynthesis and Environmental Remediation: Are We a Step Closer To Achieving Sustainability? *Chem. Rev.* **2016**, *116*, 7159–7329, doi:10.1021/acs.chemrev.6b00075.
147. Wang, X.; Blechert, S.; Antonietti, M. Polymeric Graphitic Carbon Nitride for Heterogeneous Photocatalysis. *ACS Catal.* **2012**, *2*, 1596–1606, doi:10.1021/cs300240x.
148. Liebig, J. V. Über Einige Stickstoff - Verbindungen. *Ann. Pharm.* **1834**, *10*, 1–47, doi:10.1002/jlac.18340100102.
149. Huang, H.; Yang, S.; Vajtai, R.; Wang, X.; Ajayan, P.M. Pt-Decorated 3D Architectures Built from Graphene and Graphitic Carbon Nitride Nanosheets as Efficient Methanol Oxidation Catalysts. *Adv. Mater.* **2014**, *26*, 5160–5165,

doi:10.1002/adma.201401877.

150. Goettmann, F.; Fischer, A.; Antonietti, M.; Thomas, A. Metal-Free Catalysis of Sustainable Friedel–Crafts Reactions: Direct Activation of Benzene by Carbon Nitrides to Avoid the Use of Metal Chlorides and Halogenated Compounds. *Chem. Commun.* **2006**, 4530–4532, doi:10.1039/B608532F.
151. Wang, X.; Maeda, K.; Thomas, A.; Takanabe, K.; Xin, G.; Carlsson, J.M.; Domen, K.; Antonietti, M. A Metal-Free Polymeric Photocatalyst for Hydrogen Production from Water under Visible Light. *Nat. Mater.* **2009**, 8, 76–80, doi:10.1038/nmat2317.
152. Wang, X.; Chen, X.; Thomas, A.; Fu, X.; Antonietti, M. Metal-Containing Carbon Nitride Compounds: A New Functional Organic–Metal Hybrid Material. *Adv. Mater.* **2009**, 21, 1609–1612, doi:10.1002/adma.200802627.
153. Teter, D.M.; Hemley, R.J. Low-Compressibility Carbon Nitrides. *Science* (80-.). **1996**, 271, 53–55, doi:10.1126/science.271.5245.53.
154. Zheng, Y.; Lin, L.; Wang, B.; Wang, X. Graphitic Carbon Nitride Polymers toward Sustainable Photoredox Catalysis. *Angew. Chemie Int. Ed.* **2015**, 54, 12868–12884, doi:10.1002/anie.201501788.
155. Yousefi, M.; Villar-Rodil, S.; Paredes, J.I.; Moshfegh, A.Z. Oxidized Graphitic Carbon Nitride Nanosheets as an Effective Adsorbent for Organic Dyes and Tetracycline for Water Remediation. *J. Alloys Compd.* **2019**, 809, 151783, doi:10.1016/j.jallcom.2019.151783.
156. Andrade, J.R. de; Oliveira, M.F.; Silva, M.G.C. da; Vieira, M.G.A. Adsorption of

- Pharmaceuticals from Water and Wastewater Using Nonconventional Low-Cost Materials: A Review. *Ind. Eng. Chem. Res.* **2018**, 57, 3103–3127, doi:10.1021/acs.iecr.7b05137.
157. Hu, R.; Wang, X.; Dai, S.; Shao, D.; Hayat, T.; Alsaedi, A. Application of Graphitic Carbon Nitride for the Removal of Pb(II) and Aniline from Aqueous Solutions. *Chem. Eng. J.* **2015**, 260, 469–477, doi:10.1016/j.cej.2014.09.013.
158. Ren, B.; Xu, Y.; Zhang, L.; Liu, Z. Carbon-Doped Graphitic Carbon Nitride as Environment-Benign Adsorbent for Methylene Blue Adsorption: Kinetics, Isotherm and Thermodynamics Study. *J. Taiwan Inst. Chem. Eng.* **2018**, 88, 114–120, doi:10.1016/j.jtice.2018.03.041.
159. Yao, Y.; Xu, F.; Chen, M.; Xu, Z.; Zhu, Z. Adsorption Behavior of Methylene Blue on Carbon Nanotubes. *Bioresour. Technol.* **2010**, 101, 3040–3046, doi:10.1016/j.biortech.2009.12.042.
160. Panneri, S.; Ganguly, P.; Mohan, M.; Nair, B.N.; Mohamed, A.A.P.; Warriar, K.G.; Hareesh, U.S. Photoregenerable, Bifunctional Granules of Carbon-Doped g-C₃N₄ as Adsorptive Photocatalyst for the Efficient Removal of Tetracycline Antibiotic. *ACS Sustain. Chem. Eng.* **2017**, 5, 1610–1618, doi:10.1021/acssuschemeng.6b02383.
161. Luo, Y.; Zhu, Y.; Han, Y.; Ye, H.; Liu, R.; Lan, Y.; Xue, M.; Xie, X.; Yu, S.; Zhang, L.; et al. g-C₃N₄-Based Photocatalysts for Organic Pollutant Removal: A Critical Review. *Carbon Res.* **2023**, 2, 14, doi:10.1007/s44246-023-00045-5.
162. Ismael, M. The Photocatalytic Performance of the ZnO/g-C₃N₄ Composite

- Photocatalyst toward Degradation of Organic Pollutants and Its Inactivity toward Hydrogen Evolution: The Influence of Light Irradiation and Charge Transfer. *Chem. Phys. Lett.* **2020**, 739, 136992, doi:10.1016/j.cplett.2019.136992.
163. Sun, Q.; Sun, Y.; Zhou, M.; Cheng, H.; Chen, H.; Dorus, B.; Lu, M.; Le, T. A 2D/3D g-C₃N₄/ZnO Heterojunction Enhanced Visible-Light Driven Photocatalytic Activity for Sulfonamides Degradation. *Ceram. Int.* **2022**, 48, 7283–7290, doi:10.1016/j.ceramint.2021.11.289.
 164. Zhang, Z.; Sun, Y.; Wang, Y.; Yang, Y.; Wang, P.; Shi, L.; Feng, L.; Fang, S.; Liu, Q.; Ma, L.; et al. Synthesis and Photocatalytic Activity of g-C₃N₄/ZnO Composite Microspheres under Visible Light Exposure. *Ceram. Int.* **2022**, 48, 3293–3302, doi:10.1016/j.ceramint.2021.10.104.
 165. Ravichandran, K.; Kalpana, K.; Ibrahim, M.M.; Seelan, K.S. Effect of Source Material of g-C₃N₄ on the Photocatalytic Activity of ZnO/g-C₃N₄ thin Film Coated on Stainless Steel Mesh Substrate. In *Proceedings of the Materials Today: Proceedings*; Elsevier Ltd, 2019; Vol. 48, pp. 207–215.
 166. Yu, Y.; Yan, W.; Gao, W.; Li, P.; Wang, X.; Wu, S.; Song, W.; Ding, K. Aromatic Ring Substituted g-C₃N₄ for Enhanced Photocatalytic Hydrogen Evolution. *J. Mater. Chem. A* **2017**, 5, 17199–17203, doi:10.1039/c7ta05744j.
 167. Yang, Y.; Zhang, C.; Huang, D.; Zeng, G.; Huang, J.; Lai, C.; Zhou, C.; Wang, W.; Guo, H.; Xue, W.; et al. Boron Nitride Quantum Dots Decorated Ultrathin Porous g-C₃N₄: Intensified Exciton Dissociation and Charge Transfer for Promoting Visible-Light-Driven Molecular Oxygen Activation. *Appl. Catal. B*

- Environ.* **2019**, *245*, 87–99, doi:10.1016/j.apcatb.2018.12.049.
168. Yılmaz, S.; Acar, E.G.; Yanalak, G.; Aslan, E.; Kılıç, M.; Hatay Patır, İ.; Metin, Ö. Enhanced Hydrogen Evolution by Using Ternary Nanocomposites of Mesoporous Carbon Nitride/black Phosphorous/transition Metal Nanoparticles (M-gCN/BP-M; M = Co, Ni, and Cu) as Photocatalysts under Visible Light: A Comparative Experimental and Theoretical St. *Appl. Surf. Sci.* **2022**, *593*, 153398, doi:10.1016/j.apsusc.2022.153398.
 169. Liu, Q.; Chen, T.; Guo, Y.; Zhang, Z.; Fang, X. Grafting Fe(III) Species on Carbon nanodots/Fe-Doped g-C₃N₄ via Interfacial Charge Transfer Effect for Highly Improved Photocatalytic Performance. *Appl. Catal. B Environ.* **2017**, *205*, 173–181, doi:10.1016/j.apcatb.2016.12.028.
 170. Ding, W.; Liu, S.; He, Z. One-Step Synthesis of Graphitic Carbon Nitride Nanosheets for Efficient Catalysis of Phenol Removal under Visible Light. *Cuihua Xuebao/Chinese J. Catal.* **2017**, *38*, 1711–1718, doi:10.1016/S1872-2067(17)62907-3.
 171. He, Q.; Zhou, F.; Zhan, S.; Yang, Y.; Liu, Y.; Tian, Y.; Huang, N. Enhancement of Photocatalytic and Photoelectrocatalytic Activity of Ag Modified Mp g-C₃N₄ Composites. *Appl. Surf. Sci.* **2017**, *391*, 423–431, doi:10.1016/j.apsusc.2016.07.005.
 172. Kim, J.S.; Oh, J.W.; Woo, S.I. Investigation for the Effects of Ball Milling Process on the Physical Characteristics, the Behaviors of Carriers and the Photocatalytic Activity of Sulfur Doped g-C₃N₄. *Int. J. Hydrogen Energy* **2017**, *42*, 5485–5495,

- doi:10.1016/j.ijhydene.2016.08.077.
173. Wang, Y.; Jiang, W.; Luo, W.; Chen, X.; Zhu, Y. Ultrathin Nanosheets g-C₃N₄@Bi₂WO₆ Core-Shell Structure via Low Temperature Reassembled Strategy to Promote Photocatalytic Activity. *Appl. Catal. B Environ.* **2018**, *237*, 633–640, doi:10.1016/j.apcatb.2018.06.013.
174. Katsumata, H.; Tateishi, I.; Furukawa, M.; Kaneco, S. Highly Photocatalytic Hydrogen Generation over P-Doped g-C₃N₄ with Aromatic Ring Structure. *Mater. Lett.* **2021**, *299*, 130068, doi:10.1016/j.matlet.2021.130068.
175. Xing, J.; Wang, N.; Li, X.; Wang, J.; Taiwaikuli, M.; Huang, X.; Wang, T.; Zhou, L.; Hao, H. Synthesis and Modifications of g-C₃N₄-Based Materials and Their Applications in Wastewater Pollutants Removal. *J. Environ. Chem. Eng.* **2022**, *10*, 108782, doi:10.1016/j.jece.2022.108782.
176. Tang, C.; Cheng, M.; Lai, C.; Li, L.; Yang, X.; Du, L.; Zhang, G.; Wang, G.; Yang, L. Recent Progress in the Applications of Non-Metal Modified Graphitic Carbon Nitride in Photocatalysis. *Coord. Chem. Rev.* **2023**, *474*, 214846, doi:10.1016/j.ccr.2022.214846.
177. Li, C.; Wu, H.; Zhu, D.; Zhou, T.; Yan, M.; Chen, G.; Sun, J.; Dai, G.; Ge, F.; Dong, H. High-Efficient Charge Separation Driven Directionally by Pyridine Rings Grafted on Carbon Nitride Edge for Boosting Photocatalytic Hydrogen Evolution. *Appl. Catal. B Environ.* **2021**, *297*, 120433, doi:10.1016/j.apcatb.2021.120433.
178. Bellamkonda, S.; Shanmugam, R.; Gangavarapu, R.R. Extending the π -Electron

- Conjugation in 2D Planar Graphitic Carbon Nitride: Efficient Charge Separation for Overall Water Splitting. *J. Mater. Chem. A* **2019**, *7*, 3757–3771, doi:10.1039/C8TA10580D.
179. Zhang, J.; Chen, X.; Takanabe, K.; Maeda, K.; Domen, K.; Epping, J.D.; Fu, X.; Antonietti, M.; Wang, X. Synthesis of a Carbon Nitride Structure for Visible-Light Catalysis by Copolymerization. *Angew. Chemie* **2010**, *49*, 441–444, doi:10.1002/anie.200903886.
180. Gogoi, D.; Shah, A.K.; Qureshi, M.; Golder, A.K.; Peela, N.R. Silver Grafted Graphitic-Carbon Nitride Ternary Hetero-Junction Ag/ g-C₃N₄ (Urea)- g-C₃N₄ (Thiourea) with Efficient Charge Transfer for Enhanced Visible-Light Photocatalytic Green H₂ Production. *Appl. Surf. Sci.* **2021**, *558*, 149900, doi:10.1016/j.apsusc.2021.149900.
181. Mohammadi, R.; Alamgholiloo, H.; Gholipour, B.; Rostamnia, S.; Khaksar, S.; Farajzadeh, M.; Shokouhimehr, M. Visible-Light-Driven Photocatalytic Activity of ZnO/g-C₃N₄ Heterojunction for the Green Synthesis of Biologically Interest Small Molecules of Thiazolidinones. *J. Photochem. Photobiol. A Chem.* **2020**, *402*, 112786, doi:10.1016/j.jphotochem.2020.112786.
182. Alaghmandfard, A.; Ghandi, K. A Comprehensive Review of Graphitic Carbon Nitride (g-C₃N₄)–Metal Oxide-Based Nanocomposites: Potential for Photocatalysis and Sensing. *Nanomaterials* **2022**, *12*, 294, doi:10.3390/nano12020294.
183. Kumar, S.G.; Kavitha, R.; Manjunatha, C. Review and Perspective on Rational

- Design and Interface Engineering of g-C₃N₄/ZnO: From Type-II to Step-Scheme Heterojunctions for Photocatalytic Applications. *Energy & Fuels* **2023**, *37*, 14421–14472, doi:10.1021/acs.energyfuels.3c01032.
184. Ren, Y.; Zeng, D.; Ong, W.-J. Interfacial Engineering of Graphitic Carbon Nitride (g-C₃N₄)-Based Metal Sulfide Heterojunction Photocatalysts for Energy Conversion: A Review. *Chinese J. Catal.* **2019**, *40*, 289–319, doi:10.1016/S1872-2067(19)63293-6.
185. Bard, A.J.; Fox, M.A. Artificial Photosynthesis: Solar Splitting of Water to Hydrogen and Oxygen. *Acc. Chem. Res.* **1995**, *28*, 141–145, doi:10.1021/ar00051a007.
186. Kumar, K.V.A.; Vinodkumar, T.; Selvaraj, M.; Suryakala, D.; Subrahmanyam, C. Visible Light-Induced Catalytic Abatement of 4-Nitrophenol and Rhodamine B Using ZnO/g-C₃N₄ Catalyst. *J. Chem. Sci.* **2021**, *133*, 41, doi:10.1007/s12039-021-01903-8.
187. Adhikari, S.P.; Pant, H.R.; Kim, H.J.; Park, C.H.; Kim, C.S. Deposition of ZnO Flowers on the Surface of g-C₃N₄ Sheets via Hydrothermal Process. *Ceram. Int.* **2015**, *41*, 12923–12929, doi:10.1016/j.ceramint.2015.06.134.

CHAPTER TWO

One-Step Fabrication of the ZnO/g-C₃N₄ Composite for Visible Light-Responsive Photocatalytic Degradation of Bisphenol E in Aqueous Solution

2.1 Introduction

Bisphenols are endocrine disrupting chemicals which are widely used in the production of high temperature composite materials in various polycarbonate plastics, rubber, epoxy resins, aerospace and electronics industries [1,2]. Solutions of bisphenol compounds even at small concentrations cause hormonal anomalies, and disrupt the reproductive growth activities and cancer [3,4]. The most widely used bisphenol compound, Bisphenol A (BPA), is considered a threat to human and animals due to its toxicity [5]. Therefore, BPA has been banned in several countries since few years [1]. Another bisphenol compound, BPE, become alternative for BPA due to its similar properties and it is extensively used industrially [1]. However, BPE is also reported as toxic compound and have significant estrogenic activity [6]. Thus, it is a matter of public health issue which needs an urgent response. It is necessary to develop treatment technique of unused or remaining BPE during production process before the discharge into natural environment, especially surface water. Several types of methods such as chemical, biological, electrochemical and photochemical methods are applied into the treatment of wastewater containing solution of bisphenol compounds [7–10].

Photocatalysis has been considered to be one of the effective methods for degradation of bisphenols [11]. Because photocatalytic method with irradiation of visible light to degrade water pollutants is cost effective, clean and sustainable compared to other waste water treatment technique [12]. A semiconductor material can produce electron-hole pairs by absorbing photon of energy from sunlight. The generated electron-hole pairs can react with target pollutant by redox reactions and degrade it. The energy of absorbed photon depends on the band gap of semiconductor [12]. Generally, photocatalytic reactions can

depend on surface area, pore size, electron-hole pair recombination, band gap position and morphology of the photocatalysts [13].

Recently, g-C₃N₄ has received great attention as interesting photocatalyst for wastewater detoxification, hydrogen production and photoreduction of CO₂ under visible light irradiation. Pure g-C₃N₄ possess a moderate band gap of ~2.7 eV, which enables it to be excited by visible light up to 460 nm [14–16]. Furthermore, metal free g-C₃N₄ has several features required for photocatalysis reactions such as π conjugated electronic structure, layered crystal structure, low cost, non-toxic nature, high chemical and thermal stability, high electron conductivity and facile fabrication [15,17–22]. However, photocatalytic efficiency of g-C₃N₄ is greatly reduced by low quantum efficiency and fast recombination rate of photogenerated electron hole pairs [14,23]. Hence, to reduce the drawback of g-C₃N₄ several methods such as coupling with metal organic frameworks, covalent organic frameworks and other semiconductors (metal oxides and metal sulfides), doping with elements and monitoring its structure and morphology have been proposed [19,24–27]. For instance, Kuila et al. reported the synthesis of cerium ion-adsorbed g-C₃N₄ for enhancing photocatalytic degradation of methylene blue dye under sunlight irradiation [28]. Sousa et al. prepared a ternary photocatalyst of ZnO/g-C₃N₄/carbon xerogel, which was used in efficient photocatalytic degradation of 4-chlorophenol under visible light irradiation[29]. Zhang et al. prepared a novel porous g-C₃N₄([Mo₇O₂₄]⁶⁻·pCN) catalyst for improving photocatalytic degradation of BPA and 4-chlorophenol [30].

On the other hand, ZnO is a promising photocatalyst for degradation of organic and inorganic pollutants in waste water due to its low price, non-toxicity, chemical stability and high photocatalytic activity [16,21,31]. However, ZnO possess a higher band gap of

~3.2 eV and it is active only in the ultraviolet region. ZnO has almost no activity in the visible region [31,32].

It is a good strategy to prepare composite with two photocatalyst by suitable matching of band level positions for decreasing the electron-hole pairs recombination. For example, Kumbhakar et al. reported the synthesis of ZnO anchored reduced graphene oxide nanocomposite via a simple hydrothermal treatment for superior photocatalytic degradation of dyes and tea stain on cotton fabrics [33]. Due to appropriate band alignment, composite of ZnO containing wider band gap with g-C₃N₄ containing medium band gap (ZnO/g-C₃N₄) might generate an admirable heterostructure to progress charge separation [34,35].

Many research works have been reported on the synthesis of ZnO/g-C₃N₄ composite by several methods such as chemisorption method, ball milling method, calcination method, reflux method, electrospinning method, reflux and vapor condensation method, deposition-precipitation method, monolayer dispersion method and ultrasonic dispersion method. Excellent photocatalytic activity of the synthesized composites on the degradation of organic pollutants in waste water are also reported [31,36–43]. For instance, Gayathri et al. prepared g-C₃N₄ based ZnO nanocomposite via precipitation-assisted thermal condensation method, which was used in enhanced photocatalytic degradation of methylene blue and acid blue 113 dyes under sunlight irradiation [44]. Zhang et al reported the synthesis of ZnO/g-C₃N₄ composite microsphere via a self-assembly method followed by calcination in the air for effective photocatalytic degradation of methyl orange and tetracycline under visible light irradiation [22]. However, there are little works have been reported on the fabrication of ZnO/g-C₃N₄ composite by simple and convenient methods. Furthermore, the degradation of endocrine

disrupting material BPE with ZnO/g-C₃N₄ composite under visible light irradiation has been not reported yet.

In the present work, ZnO/g-C₃N₄ composite has been synthesized by very facile calcination technique using zinc acetate and urea as precursors of ZnO and g-C₃N₄, respectively. The photocatalytic degradation of BPE with the simply synthesized ZnO/g-C₃N₄ composite under visible light radiation has been investigated. The different parameters such as ZnO amount in the composite, synthesize calcination condition, amount of ZnO/g-C₃N₄ composite, initial concentration of BPE and solution pH have been optimized for the photocatalytic degradation. Furthermore, The ZnO/g-C₃N₄ composite was characterized by using several techniques. In addition, photocatalytic experiment using different radical scavenger was investigated to assess the probable reaction pathway.

2.2 Materials and Methods

2.2.1 Materials

BPE (1,1-Bis(4-hydroxyphenyl)ethane, 98.0%), urea (99.0%) and zinc acetate dihydrate (99.0%), isopropyl alcohol (IPA, 99.7%), ethylenediaminetetraacetic acid (EDTA, 98.0%) benzoquinone (BQ, 98.0%), sodium hydroxide (97.0%) and nitric acid (61%) were purchased from FUZIFILM wako pure chemical corporation, Japan. Acetonitrile (99.5%) was obtained from Kanto chemical co., Inc., Japan. All the chemicals were used without further purification. Pure water was obtained from an ultrapure water system (Advantec MFS Inc., Tokyo, Japan).

2.2.2 Synthesis of the ZnO/g-C₃N₄ Composite

Composite of ZnO/g-C₃N₄ was synthesized by facile one step calcination of the mixture of urea and zinc acetate dihydrate (Figure 2.1). Typically, 20 g of urea and 2 g of zinc acetate were mixed and dispersed with 5 mL of water in a 30 mL of crucible with a lid. Then, the crucible was covered by aluminum foil and placed in a muffle furnace, and heated to 550 °C at a heating increment rate 2 °C/min and held at 550 °C temperature for 2 h as calcined temperature. Finally, the sample was manually ground in an agate mortar into a light-yellow powder. Pure ZnO and g-C₃N₄ were synthesized from zinc acetate and urea by the same method, respectively. Stepwise urea and zinc acetate decomposition during the formation of g-C₃N₄ and ZnO, respectively are illustrated in Figure 2.1 [45–47].

(a)

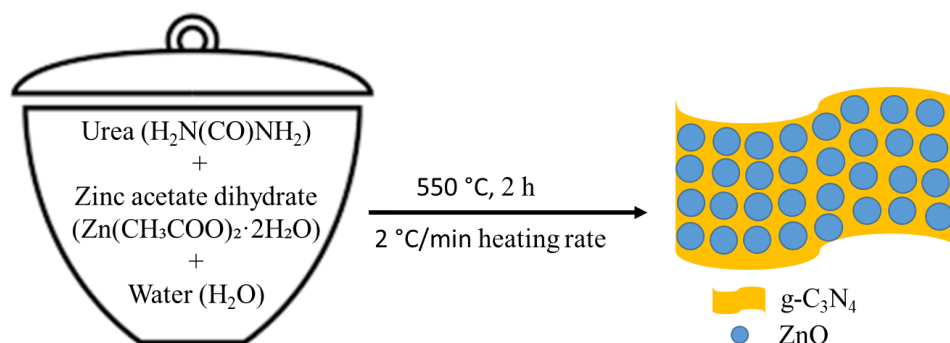
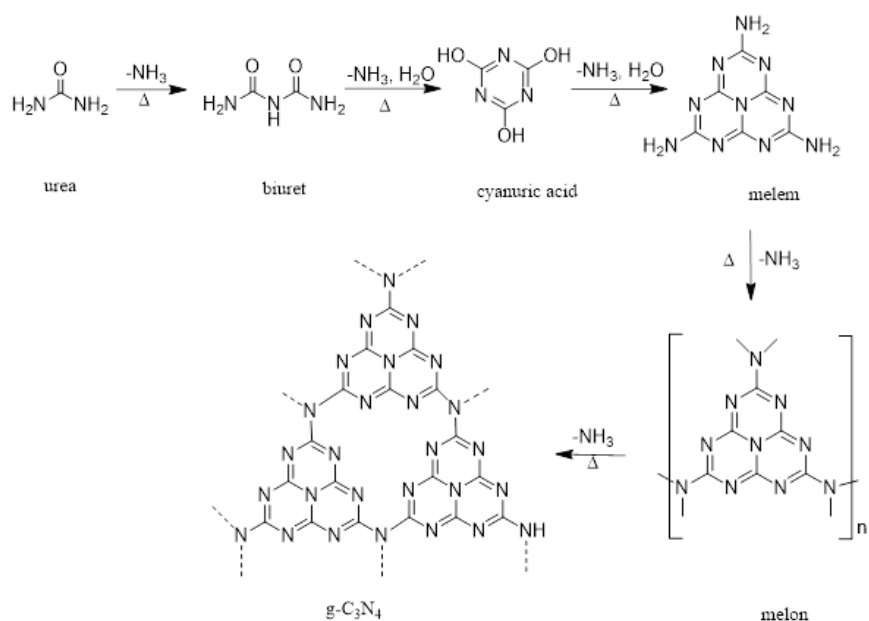


Figure 2.1 (a) Schematic diagram for the synthesis of the ZnO/g-C₃N₄ Composite

(b)



(c)

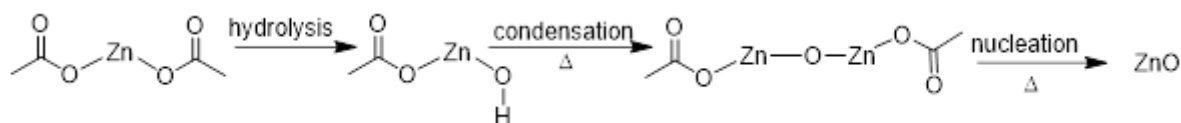


Figure 2.1 Schematic diagram for stepwise decomposition of (b) urea and (c) zinc acetate.

2.2.3 Characterization

ZnO/g-C₃N₄ composite, g-C₃N₄ and ZnO were characterized by TGA, FTIR, XRD, XPS, SEM, TEM, FE-EPMA, UV-Vis DRS, PL, EIS and nitrogen adsorption and desorption isotherm analysis. TGA of the prepared composite was performed in air at a heating rate of 10 °C/min on the SII (EXSTAR 6000, TG/DTA 6200) thermal analysis system and the temperature was ranged from 25 to 950 °C. The FTIR spectra of the photocatalysts were recorded on a SPECTRUM 100 FTIR spectrometer (Perkin Elmer) with an attenuated total reflection (ATR) assembly. XRD measurements were performed by using a Rigaku RINT Ultima-IV diffractometer by Cu K α radiation at a scan rate of 0.04 °/s in a scan range of 10–80°. XPS characterization of the photocatalysts was

performed by using a PHI Quantera SXM photoelectron spectrometer with Al K α radiation. SEM and TEM images of photocatalysts were used to analyze the surface morphology by using a Hitachi S-4000 SEM and a JEOL JEM-1011 TEM, respectively. FE-EPMA images of the composite were used to analyze the elemental mapping by using a JEOL JX-A-8530F FE-EPMA.

The specific surface area, average pore size and total pore volume of photocatalysts were estimated from the N₂ adsorption-desorption isotherm on the BELSORP-miniII (MicrotracBEL) apparatus using the Brunauer-Emmett-Teller (BET) equilibrium equation and Barrett-Joyner-Halenda (BJH) analysis. The UV-vis DRS of photocatalysts were examined by a JASCO V-750 UV-vis instrument equipped with an integrating sphere attachment. Photoluminescence (PL) spectra of the photocatalysts were attained with a Shimadzu RF-5300PC system with an excitation wavelength of 360 nm. The EIS measurement of photocatalysts was performed on an electrochemical Versa STAT 3 workstation (Princeton Applied Research) equipped with a conventional three-electrode system. A uniform photocatalyst slurry with nafion solution was coated on an FTO glass plate to prepare the working electrode, and a 0.5 mol L⁻¹ Na₂SO₄ aqueous solution was used as the electrolyte.

2.2.4 Photocatalytic Degradation

The photocatalytic degradation of BPE by synthesized ZnO/g-C₃N₄ composite was carried out up to 3 h with visible light irradiation at ambient temperature. A pyrex glass cell (inner volume, 50 mL) was used for photocatalytic degradation. Typically, 30 mL of 3 ppm BPE solution and 30 mg of ZnO/g-C₃N₄ composite were added to the glass cell and magnetically stirred before and during irradiation. Before irradiation, the photocatalyst suspension containing BPE was allowed to reach adsorption-desorption

equilibrium for 30 minutes in the dark. Then, the BPE solution was irradiated with a LED lamp (TOSHIBA LDA14L-G/100W) with a UV (400 nm) cut off filter (Y-44, HOYA), which was placed on the one side of the reaction cell. During the degradation, 1.5 mL of suspensions were taken out at 30 minutes regular intervals and centrifuged at 10000 rpm for 5 minutes to separate the photocatalyst. Then, the supernatant was analyzed for BPE concentration determination. The amount of BPE in the solution was measured using a high-performance liquid chromatograph equipped with a SHIMADZU UV/Vis detector (UV 7750) and a separation column ODS-2 (GL Science Inc.). The chromatogram was monitored at wavelength of 274 nm. The mobile phase consisted of solvent mixture of acetonitrile and water (60:40, v/v) at isocratic mode. The flow rate of the mobile phase was 1.0 mL/min. The photocatalytic degradation of BPE by synthesized bare g-C₃N₄ and bare ZnO was also carried out at similar degradation conditions. Moreover, the degradation in the absence of photocatalysts (photolysis) was also carried out under similar degradation conditions. To determine optimum condition of degradation of BPE by synthesized ZnO/g-C₃N₄ composite, effect of operating conditions such as ZnO amount in the composite, calcination condition of the composite synthesis, photocatalyst amount, initial BPE concentration and initial pH of the solution were also investigated. To inspect the role of reactive species for photocatalytic degradation of BPE with ZnO/g-C₃N₄ composite, three scavenger tests were carried out in the same optimal condition. In the scavenger tests, solutions of IPA, EDTA and BQ were used as $\cdot\text{OH}$, h^+ and $\cdot\text{O}_2^-$ radicals scavenger, respectively. The reusability of the ZnO/g-C₃N₄ composite for photodegradation of BPE was studied.

In addition, the kinetics and reaction rate of the photocatalytic degradation process has been studied according to the Langmuir–Hinshelwood (L–H) model, which was developed by Turchi and Ollis [48]. The model was expressed as eq. 2.1,

$$r_0 = -\frac{dC}{dt} = \frac{kKC}{1 + KC} \quad (2.1)$$

where, r_0 is the degradation rate on the reaction, k is the rate constant, and K and C are the adsorption equilibrium constant and reactant concentration, respectively. If the initial concentration C_0 is very small, it can be simplified to eq. 2.2.

$$-\ln\left(\frac{C}{C_0}\right) = kKt = k_{obs}t \quad (2.2)$$

The equation becomes a linear expression on time t with respect to $-\ln(C/C_0)$, where k_{obs} is reaction rate constant. The values of k_{obs} were calculated by plotting $-\ln(C/C_0)$ versus t .

2.3 Results and Discussion

2.3.1 TG Analysis

In order to understand the thermal stability and amount of ZnO content in the prepared ZnO/g-C₃N₄ composite, TG analysis was carried out from 25 °C to 950 °C at a heating increment rate 10 °C/min. It was reported that ZnO is very stable till more than 900 °C temperature [19]. There are two steps of weight loss in TGA curve, as shown in Figure 2.2. The major weight loss was observed from 400 °C to 640 °C, which could be assigned to the combustion of g-C₃N₄ composite [19]. The weight percentage of ZnO in the prepared composite was 38.9% observed in the case of 2 g for (CH₃COO)₂Zn.

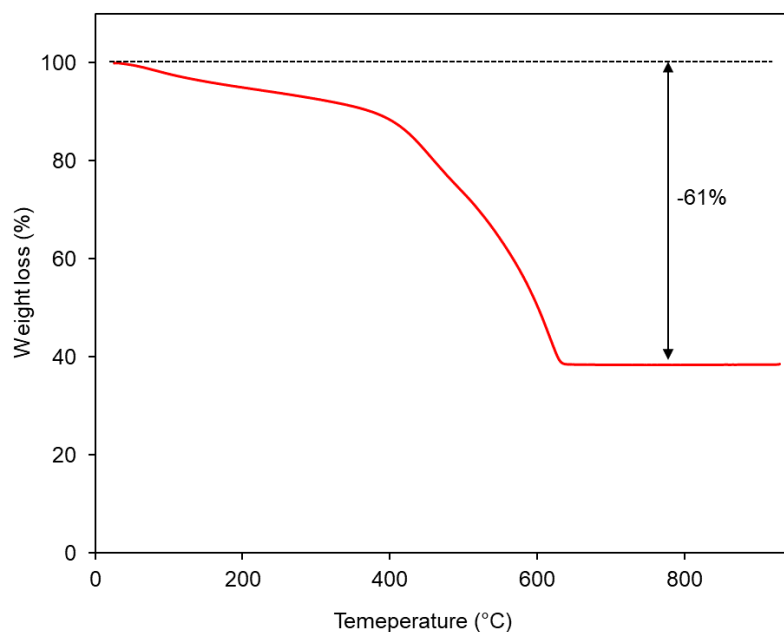


Figure 2.2 TG analysis curve of ZnO/g-C₃N₄ composite.

2.3.2 FTIR Analysis

The formation of ZnO/g-C₃N₄ composite was studied by FTIR spectroscopy. Figure 2.3 shows the corresponding FTIR spectra of prepared ZnO, g-C₃N₄, ZnO/g-C₃N₄ composite and ZnO/g-C₃N₄ composite after degradation of BPE. Pure C₃N₄ showed several peaks between 1200-1650 cm⁻¹ associated with different C-N stretching mode for the presence of extended C₃N₄ arrangement [15,49]. The intense peak at 810 cm⁻¹ was assigned to the out of plane vibration of heterocyclic C-N bending mode of triazine ring [12].

The broad band between 3000 cm⁻¹ to 3300 cm⁻¹ appeared due to stretching modes of deformed N-H bond and -OH groups of absorbed water molecules [50]. The FTIR spectra of prepared ZnO was not observed clearly, as shown in figure. In the FTIR spectra of ZnO/g-C₃N₄ composite, all characteristics peaks of g-C₃N₄ were observed. The intensities of the peaks observed at 1200-1650 cm⁻¹ for different aromatic C-N stretching decreased and merged to a broad peak, compared to the g-C₃N₄ [12]. The results could occur due to

the existence of ZnO in the composite. Also, the peak for the out of plane vibration of heterocyclic C-N bending mode of triazine ring was red shifted to lower wavenumber at 794 cm^{-1} with smaller intensity, compared to the peak of g- C_3N_4 . The result indicated the weakening of the bond strength of C=N and C-N due to lower conjugation of pure g- C_3N_4 and ZnO in the composite [12]. A weak peak was formed at 2204 cm^{-1} for the formation of new C-N bond. ZnO may cleavage the triazine units and gave new C-N bonds from sp^2 C-N bonds of triazine units [12]. However, there was few peaks observed at $3000\text{--}3300\text{ cm}^{-1}$, compared to spectra of pure g- C_3N_4 . Despite the absence of Zn-O stretching peak in the FTIR spectra, above results supported the formation of hybrid structure rather than physical mixture of ZnO and g- C_3N_4 . The peaks in the FTIR spectra of ZnO/g- C_3N_4 composite could not change after the photocatalytic degradation of BPE, which indicated the chemical stability of the composite.

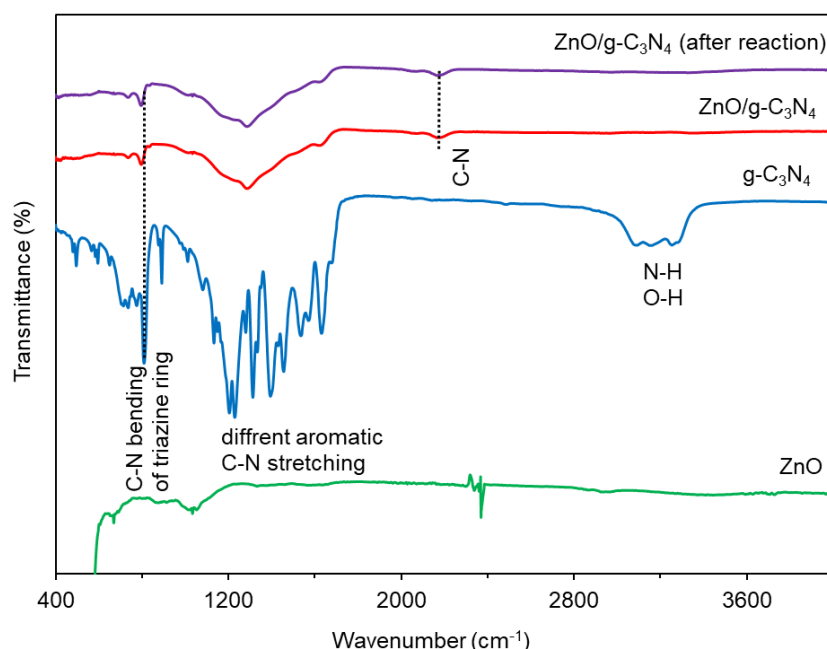


Figure 2.3 FTIR spectra of ZnO, g- C_3N_4 , ZnO/g- C_3N_4 composite and ZnO/g- C_3N_4 composite after degradation reaction.

2.3.3 XRD Analysis

XRD patterns of prepared ZnO, g-C₃N₄, ZnO/g-C₃N₄ composite and ZnO/g-C₃N₄ composite after degradation reaction of BPE are shown in Figure 2.4. The 2θ values for the diffraction peak of prepared ZnO sample were 31.76°, 34.38°, 36.22°, 47.54°, 56.60°, 62.86°, 66.52°, 67.94° and 69.10° corresponding to (100), (002), (101), (102), (110), (103), (200), (112) and (201) crystals planes are ascribed to the hexagonal wurtzite structure of ZnO, respectively [24]. Furthermore, the 2θ values for the diffraction peak of prepared g-C₃N₄ sample were 13.01° and 27.8° corresponding to (100) and (002) planes, respectively. Intense peak of 27.8° is related to interlayer C-N stacking of conjugated aromatic system and weak peak of 13.01° corresponds to the periodic arrangement of the s-triazine units. The observed results are consistent with the reported literature [20,51].

A broad peak with low intensity at 2θ value around 27° was observed for XRD pattern of ZnO/g-C₃N₄ composite, which indicate that the ZnO could restrict the g-C₃N₄ crystal growth and innate structure of the pure g-C₃N₄ could not be retained well [12]. However, any peak for ZnO were not present in the pattern. The result showed the lower crystallization of the composite. It can be suggested that the ZnO and g-C₃N₄ lost their crystallinity upon the composite formation and the ZnO/g-C₃N₄ composite existed as amorphous state. Same XRD pattern was also observed for ZnO/g-C₃N₄ composite after degradation reaction. The crystalline size of the photocatalysts from the diffraction peaks of the full width at half maximum (FWHM) was determined by using Scherrer's equation. It was speculated that the crystalline sizes of ZnO and g-C₃N₄ are 42 nm and 8.7 nm, respectively.

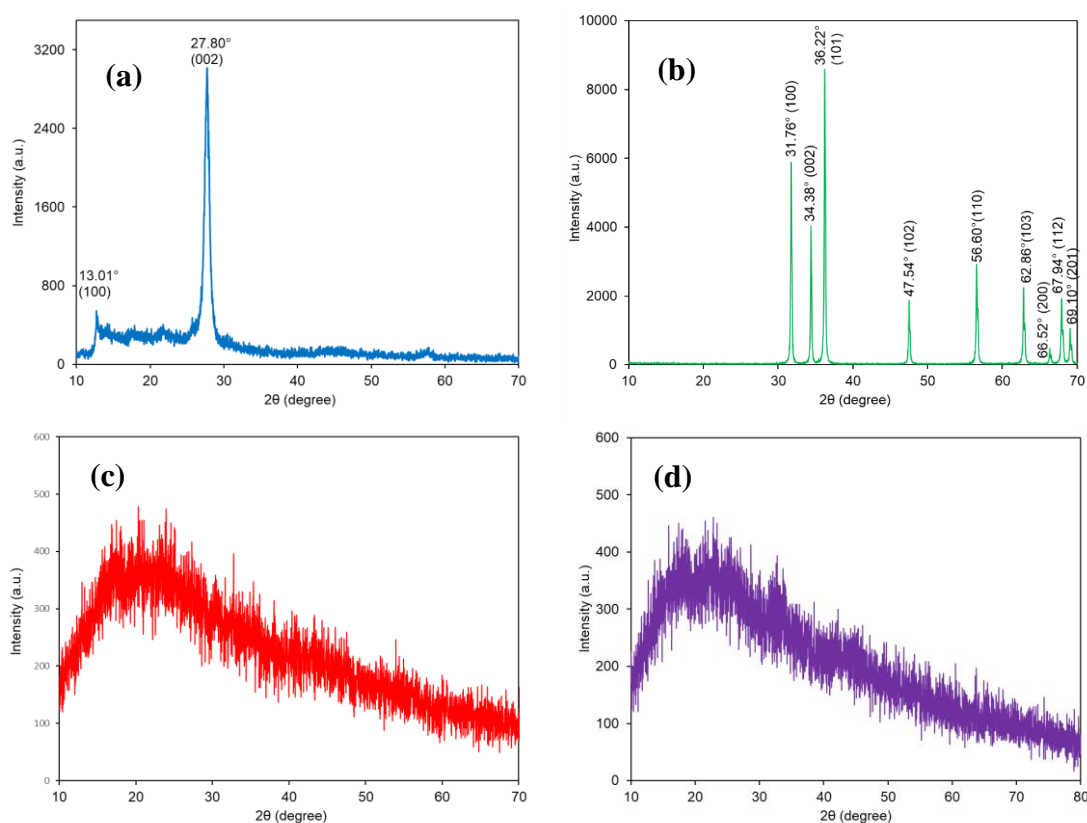


Figure 2.4. XRD patterns of (a) g-C₃N₄, (b) ZnO, (c) ZnO/g-C₃N₄ composite, and (d) ZnO/g-C₃N₄ composite after degradation reaction.

2.3.4 XPS Analysis

XPS measurement was taken to investigate the surface chemical composition and interaction between the ZnO and g-C₃N₄ in the prepared composite. Survey XPS spectra of prepared g-C₃N₄ and ZnO/g-C₃N₄ composite are shown in Figure 2.5a. C and N elements were detected in the both survey spectra. In addition, Zn and O were detected in the spectra of ZnO/g-C₃N₄ composite [44,52]. The results confirmed the association of ZnO with g-C₃N₄ and purity of the composite.

Overlap high resolution C1s, N1s and O1s XPS spectra of g-C₃N₄ and ZnO/g-C₃N₄ composite are shown in Figure 2.5b-d and high resolution Zn 2p XPS spectra of ZnO/g-C₃N₄ composite are shown in Figure 2.5e.

High resolution C1s XPS spectrum of g-C₃N₄ can be deconvoluted into four components located at 287.6 eV, 285.1 eV, 284 eV and 288.4 eV, which are related to the N=C-N groups of s-triazine ring, sp³ C-N bond, sp² C=C bond and C-O groups induced by unavoidable oxidation of sample, respectively (Figure 2.5b) [53].

As shown in Figure 2.5c, the high resolution XPS N1s spectrum of g-C₃N₄ was fitted by three peaks of 398.1 eV, 399.7 eV and, 403.9 eV which can be ascribed to sp²N (C=N-C) involved in triazine ring, tertiary nitrogen atom (NC₃) or secondary nitrogen atoms (HNC₂) and charging effects or positive charge localized in heterocycles, respectively [54]. Moreover, the position and relative intensity of the peaks in high resolution C 1s and N 1s XPS spectra of ZnO/g-C₃N₄ composite were changed as shown in Figure 2.5b-c [51,53].

Furthermore, the high resolution O 1s XPS spectra of g-C₃N₄ showed one peak at 532.2 eV, which is assigned to the surface -OH groups on the g-C₃N₄ or in adsorbed H₂O [54]. In contrast, the high resolution O 1s XPS spectra of ZnO/g-C₃N₄ illustrated two peaks at 530.9 eV and 531.9 eV for O₂²⁻ in the ZnO wurtzite structure and surface -OH groups adsorbed on the composite, respectively (Figure 2.5d) [50].

In the case of high resolution Zn 2p XPS spectrum of ZnO/g-C₃N₄ composite as shown in Figure 2.5e, the binding energy value of Zn 2p_{3/2} and Zn 2p_{1/2} were located at 1021.8 eV and 1044.9 eV representing Zn²⁺ oxidation state of ZnO material, respectively. Furthermore, the difference between the two binding energy peaks was about 23.1 eV. The results proved good match with the reported ZnO binding energy values in the ZnO/g-C₃N₄ composite [55]. In addition, the structure of the Zn LMM augur peaks in survey spectrum of ZnO/g-C₃N₄ composite revealed the presence of Zn-N bonds [51]

(Figure 2.5a). Thus, the XPS analysis further confirmed the existence of ZnO in the composite.

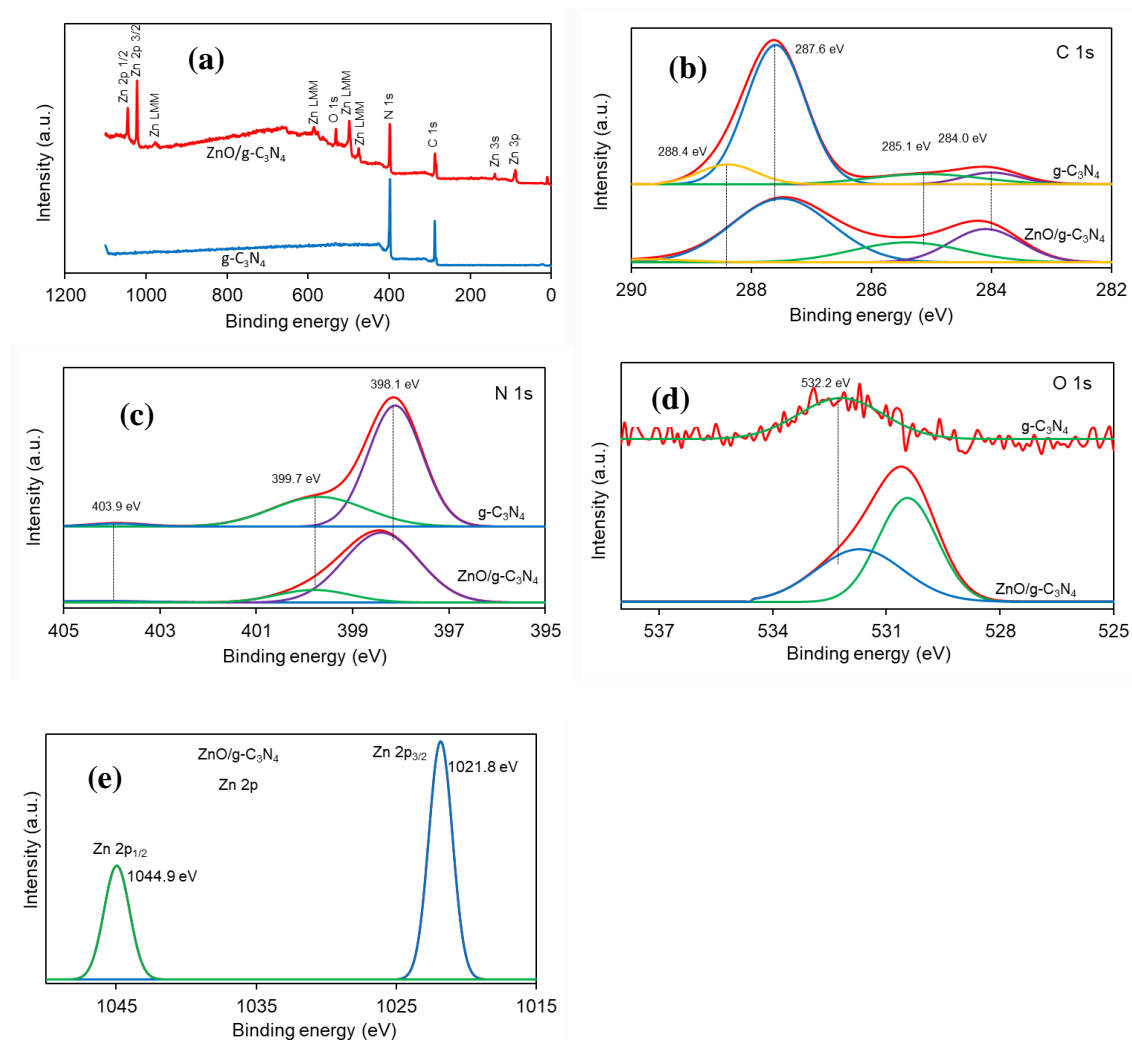


Figure 2.5 (a) Survey XPS spectra of g-C₃N₄ and ZnO/g-C₃N₄ composite; overlap high resolution XPS (b) C 1s, (c) N 1s and (d) O1s spectra of g-C₃N₄ and ZnO/g-C₃N₄ composite and (e) High resolution XPS Zn 2p spectra of ZnO/g-C₃N₄ composite.

2.3.5 Morphological Study

The formation of ZnO/g-C₃N₄ composite was investigated by SEM and TEM analysis of ZnO, g-C₃N₄ and ZnO/g-C₃N₄ composite. Figure 2.6 shows the SEM and TEM images of ZnO, g-C₃N₄ and ZnO/g-C₃N₄ composite and ZnO/g-C₃N₄ composite after degradation of BPE. The SEM image of prepared ZnO (Figure 2.6a) showed the

irregular surface morphology with different size and shape of particles. The ZnO particles had a combination of rod-like, semi spherical and flower-like structure with different sizes. Figure 2.6b illustrated the sheet-like structure of g-C₃N₄. From Figure 2.6c, it was seen that the composite was composed of flower-like ZnO and sheet-like g-C₃N₄.

The TEM image showed the random arrangement of ZnO particles with semispherical or hexagonal shape (Figure 2.6e). The pure g-C₃N₄ had the sheet-like structure in the TEM analysis (Figure 2.6f). For the composite, it was observed that ZnO particles were imbedded in the g-C₃N₄ sheet, as shown in Figure 2.6g. Hence, ZnO could be inserted into the g-C₃N₄ sheet successfully. The composite may be expected to reduce the electron hole pair recombination rate and to increase the photocatalytic degradation efficiency under visible light [24]. Elemental mapping of N, C, Zn, and O of the ZnO/g-C₃N₄ composite was observed by FE-EPMA. Figure 2.7 proved the uniform distribution of all elements through the whole composite. From SEM and TEM images, it was also observed that the surface morphology of the composite could not change significantly after the degradation of BPE (Figure 2.6d and 2.6h). It was indicated the stability and proficiency of the ZnO/g-C₃N₄ composite.

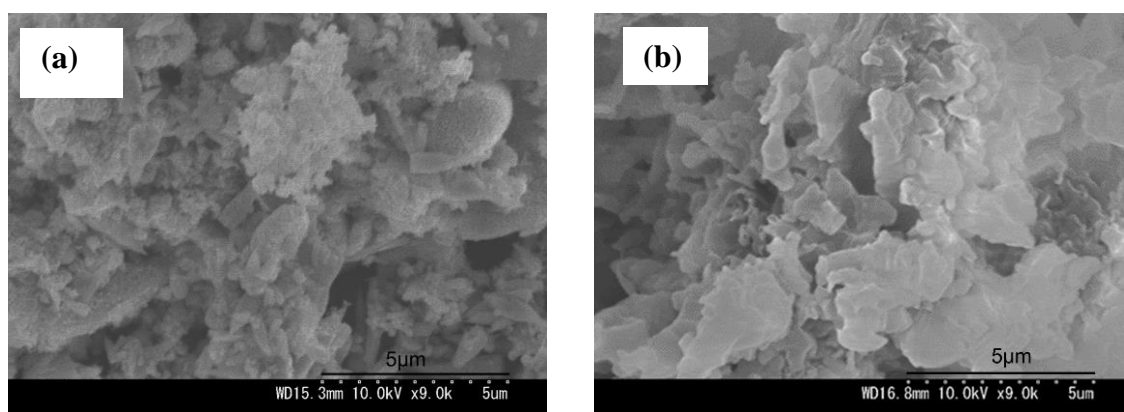


Figure 2.6 SEM images of (a) ZnO and (b) g-C₃N₄.

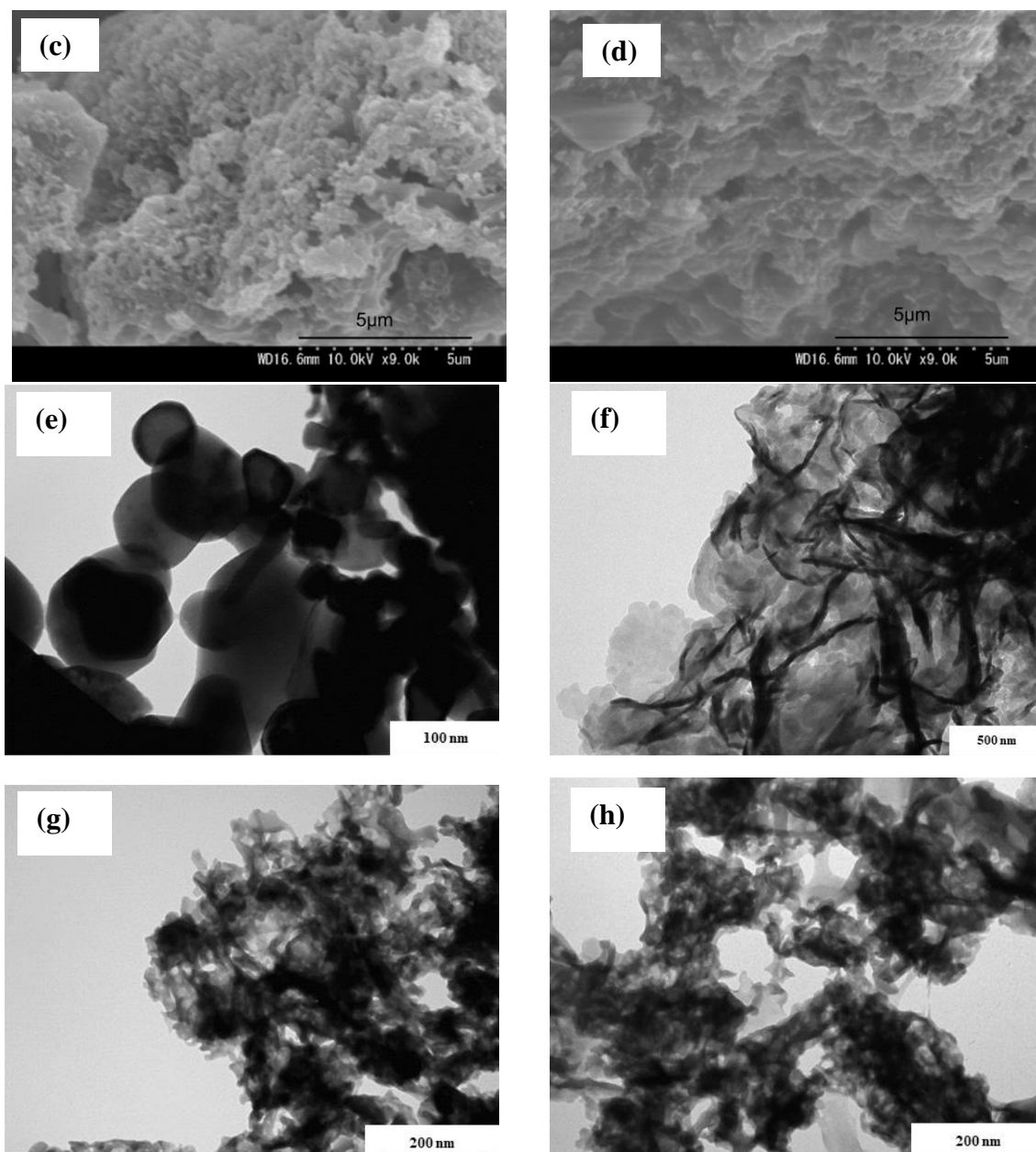


Figure 2.6 SEM images of (c) ZnO/g-C₃N₄ composite and (d) ZnO/g-C₃N₄ composite after degradation reaction; and TEM images of (e) ZnO, (f) g-C₃N₄, (g) ZnO/g-C₃N₄ composite and (h) ZnO/g-C₃N₄ composite after degradation reaction.

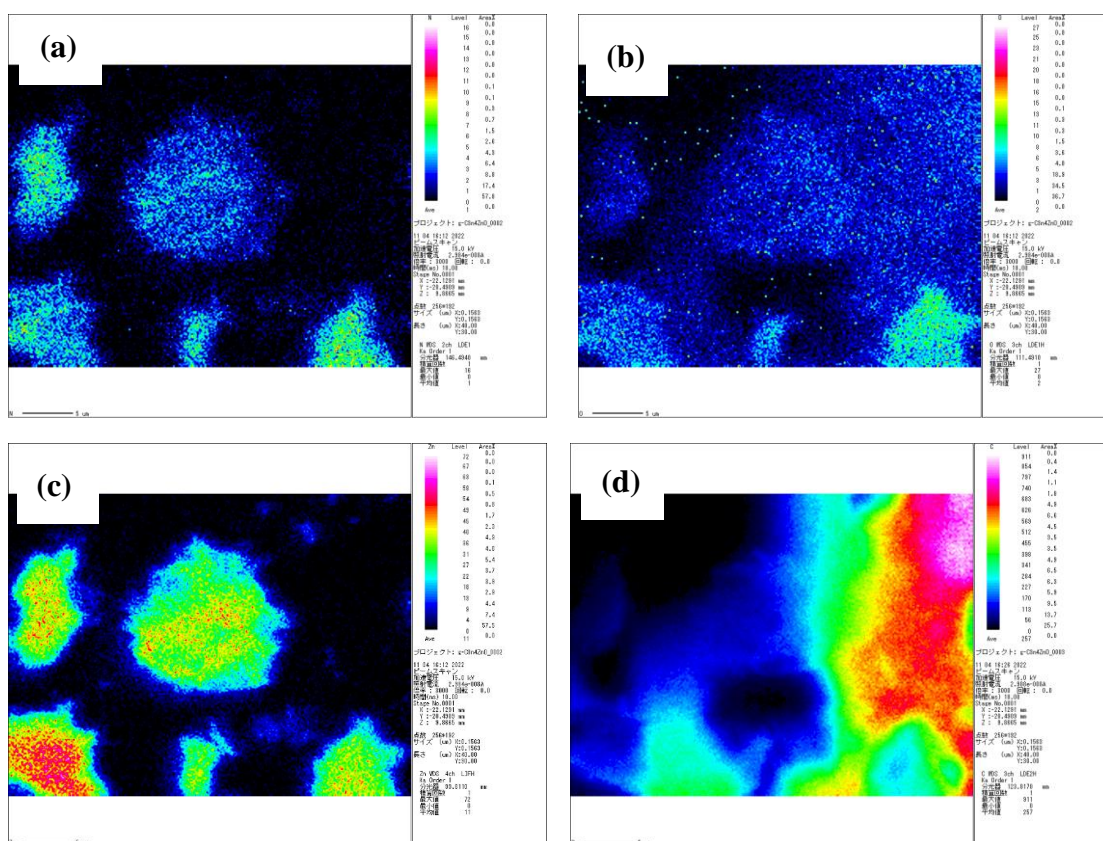


Figure 2.7 Elemental mapping of (a) N, (b) O, (c) Zn and (d) C of ZnO/g-C₃N₄ composite by FE-EPMA. In the case of C, the concentration of the surrounding of the composite was very high because of carbon tap for the analysis.

2.3.6 BET and BJH Analysis

In order to investigate porous structure and surface area of the g-C₃N₄ and ZnO/g-C₃N₄ composite, the nitrogen adsorption desorption isotherm was measured. Figure 2.8a,b shows the nitrogen adsorption desorption isotherm curve and pore size distribution curve of materials, respectively. As shown in Figure 2.8a adsorption isotherm of g-C₃N₄ and ZnO/g-C₃N₄ composite corresponded to the type IV with H3 hysteresis loops. The results indicated the mesoporous structure of g-C₃N₄ and ZnO/g-C₃N₄ composite [56].

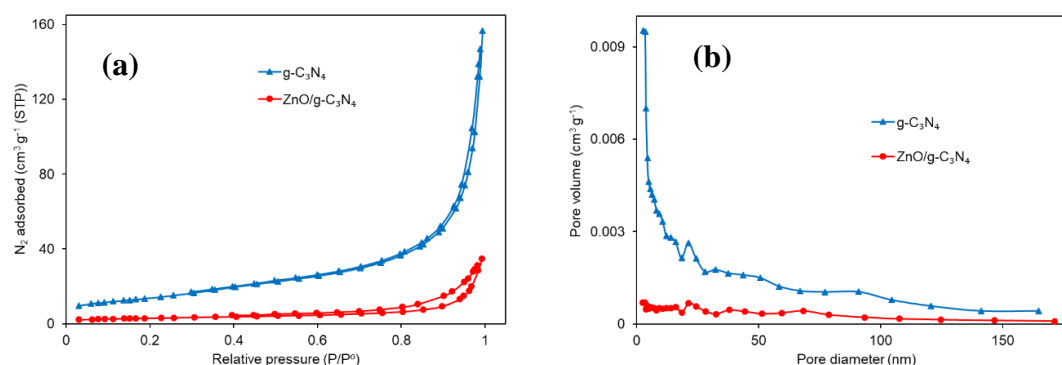


Figure 2.8 (a) Nitrogen adsorption desorption isotherm and (b) pore size distribution curve of $g-C_3N_4$ and $ZnO/g-C_3N_4$ composite.

The surface area, average pore diameter and total pore volume of $g-C_3N_4$ and $ZnO/g-C_3N_4$ composite are presented in Table 2.1 by BET and BJH analysis. It was observed that surface area and pore volume were decreased and pore diameter was increased, owing to the formation of $ZnO/g-C_3N_4$ composite from $g-C_3N_4$. The growth of ZnO might be loaded into the pores of $g-C_3N_4$, which could strengthen the interfacial structure of ZnO and $g-C_3N_4$ [57]. Lower surface area and pore volume and higher pore diameter of $ZnO/g-C_3N_4$ composite are also previously reported, compare to $g-C_3N_4$ [22].

Table 2.1 Surface area, pore size and pore volume of the $g-C_3N_4$ and $ZnO/g-C_3N_4$ composite

Photocatalyst	BET			BJH		
	$S/m^2 g^{-1}$	$V_{pore}/cm^3 g^{-1}$	D_{pore}/nm	$S/m^2 g^{-1}$	$V_{pore}/cm^3 g^{-1}$	D_{pore}/nm
$g-C_3N_4$	52.9	0.270	16.7	60.9	0.225	2.59
$ZnO/g-C_3N_4$	10.4	0.051	19.5	8.26	0.0493	3.32

2.3.7 DRS Analysis

The photo catalytical activity depends on optical properties. Hence, to investigate the light absorption properties of prepared ZnO, g-C₃N₄ and ZnO/g-C₃N₄ composite, the UV-Vis DRS was measured at room temperature. Figure 2.9a shows the Kubelka-Munk function of UV-Vis DRS of prepared ZnO, g-C₃N₄ and ZnO/g-C₃N₄ composite and ZnO/g-C₃N₄ composite after degradation reaction of BPE. It was observed that the prepared ZnO and g-C₃N₄ had the absorption edge at about 390 nm [15] and 430 nm [54], respectively. Moreover, the absorption edge of the prepared ZnO/g-C₃N₄ composite was significantly red shifted to higher wavelength, compared to the both pure ZnO and g-C₃N₄ [20]. The results suggested the higher absorption and utilization of visible light capacity by prepared ZnO/g-C₃N₄ composite. The optical band gap of prepared ZnO, g-C₃N₄ and ZnO/g-C₃N₄ composite was calculated by Tauc equation.

$$\alpha h\nu = A(h\nu - E_g)^n \quad (2.3)$$

where α , h , ν , A , and E_g are absorption coefficient, Planck's constant, light frequency, characteristic constant and band gap energy respectively. The value of n depends on the transition in a semiconductor; $n = 1/2$ for direct transition and $n = 2$ for indirect transition. The indirect band gap of g-C₃N₄ and ZnO/g-C₃N₄ composite was determined by plotting the value of $(\alpha h\nu)^{1/2}$ Vs $h\nu$ (Figure 2.9b). On the other hand, ZnO has direct transition, hence band gap of ZnO was calculated by plotting the value of $(\alpha h\nu)^2$ vs $h\nu$ (Figure 2.9c) [22,24]. The calculated band gap for ZnO, g-C₃N₄ and ZnO/g-C₃N₄ composite are 3.20 eV, 2.89 eV and 2.22 eV, respectively. The lower band gap of the composite compared to the pure ZnO and g-C₃N₄ supported the higher charge separation and better photocatalytic activity of the composite. Furthermore, absorption edge in the Kubelka-Munk function of UV-Vis DRS and band gap of the ZnO/g-C₃N₄ composite could not

change meaningfully after the treatment of BPE, which was indicted the chemical stability of the composite.

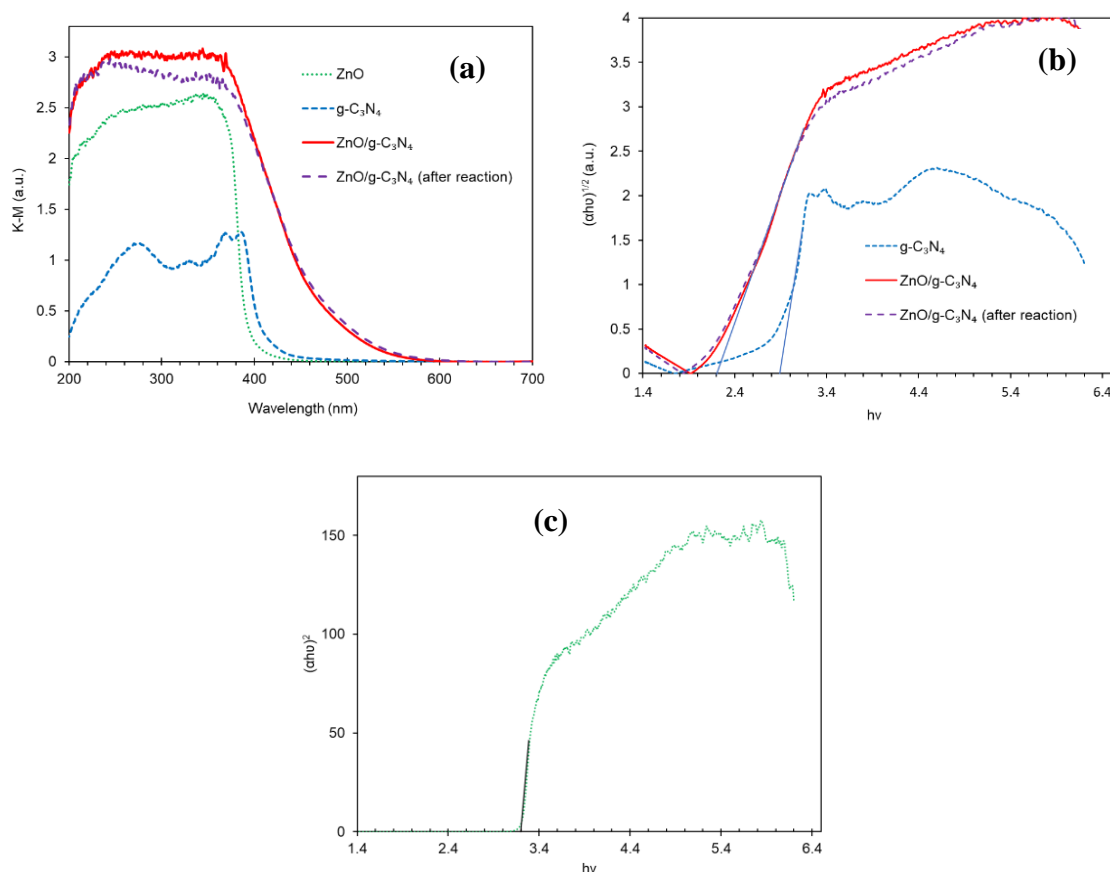


Figure 2.9 (a) Kubelka-Munk function of UV-Vis DRS of prepared ZnO, $g-C_3N_4$, ZnO/ $g-C_3N_4$ composite and ZnO/ $g-C_3N_4$ composite after degradation reaction, Tauc plots. (b) $(\alpha h\nu)^{1/2}$ vs $h\nu$ for $g-C_3N_4$, ZnO/ $g-C_3N_4$ composite and ZnO/ $g-C_3N_4$ composite after degradation reaction; and (c) $(\alpha h\nu)^2$ vs $h\nu$ for ZnO.

2.3.8 PL Analysis

PL intensity is directly proportional to electron hole pair recombination rate. Hence, PL spectra are one of the most effective parameters for the investigation of photogenerated electron hole pairs migration, transfer and recombination of photocatalysts [18,22]. Figure 2.10a shows the PL emission spectra of ZnO, $g-C_3N_4$ and ZnO/ $g-C_3N_4$ composite and ZnO/ $g-C_3N_4$ composite after degradation reaction of BPE in

the range from 410 nm to 750 nm upon excitation at 360 nm. It was seen that PL intensity of ZnO/g-C₃N₄ composite was significantly reduced relative to both of ZnO and g-C₃N₄. The results indicated that higher efficient electron transfer from valence band to conduction band as well as lower electron hole pair recombination. The recombination rate of electron hole pairs could be reduced by synergic effect between the ZnO and g-C₃N₄ components [34]. In addition, PL intensity of the ZnO/g-C₃N₄ composite remained almost same after the degradation of BPE. The observation implicated the stability of the composite.

2.3.9 EIS Analysis

To know the photogenerated charge transfer and migration efficiency of the photocatalysts, the EIS were conducted. Usually, the smaller semicircle radius in EIS Nyquist plot suggest the lower charge transfer resistance across the photoelectrode surface [22]. Figure 2.10b shows the EIS Nyquist plots for g-C₃N₄ and ZnO/g-C₃N₄ composite. It was observed that ZnO/g-C₃N₄ composite exhibited the smaller semicircle radius than g-C₃N₄ electrode. The result indicated the higher photoinduced electron hole transfer and migration, which support the better photocatalytic activity of ZnO/g-C₃N₄ composite.

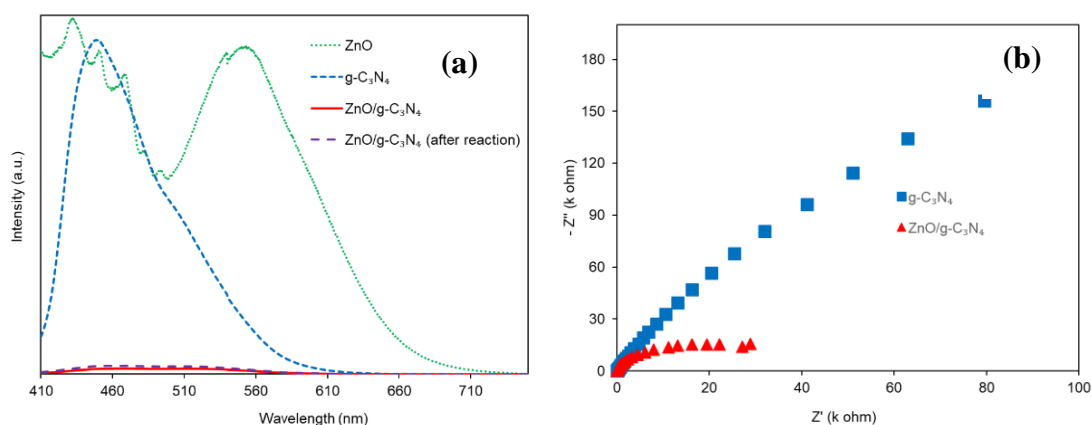


Figure 2.10 (a) PL spectra (upon the excitation at 360 nm wavelength) of prepared ZnO, g-C₃N₄, ZnO/g-C₃N₄ composite and ZnO/g-C₃N₄ composite after degradation reaction; and (b) EIS Nyquist plots of g-C₃N₄ and ZnO/g-C₃N₄.

2.3.10 Photocatalytic Activity

Photocatalytic activity of ZnO/g-C₃N₄ composite on degradation of BPE with visible light irradiation is shown in Figure 2.11. For comparison photocatalytic activity of pure ZnO and g-C₃N₄ is also illustrated. Furthermore, photolysis properties of BPE have been studied. The results indicated that the BPE is very stable under visible light irradiation without any photocatalyst. The ZnO exhibited almost no degradation of BPE due to its limited visible light absorption. Furthermore, ZnO/g-C₃N₄ composite showed superior photocatalytic activity than g-C₃N₄. The rate constant was calculated according to pseudo first order kinetics, as shown in Figure 2.11b. From Table 2.2, it was observed that degradation rate of BPE with ZnO/g-C₃N₄ composite was 8 times better than those obtained with pure g-C₃N₄.

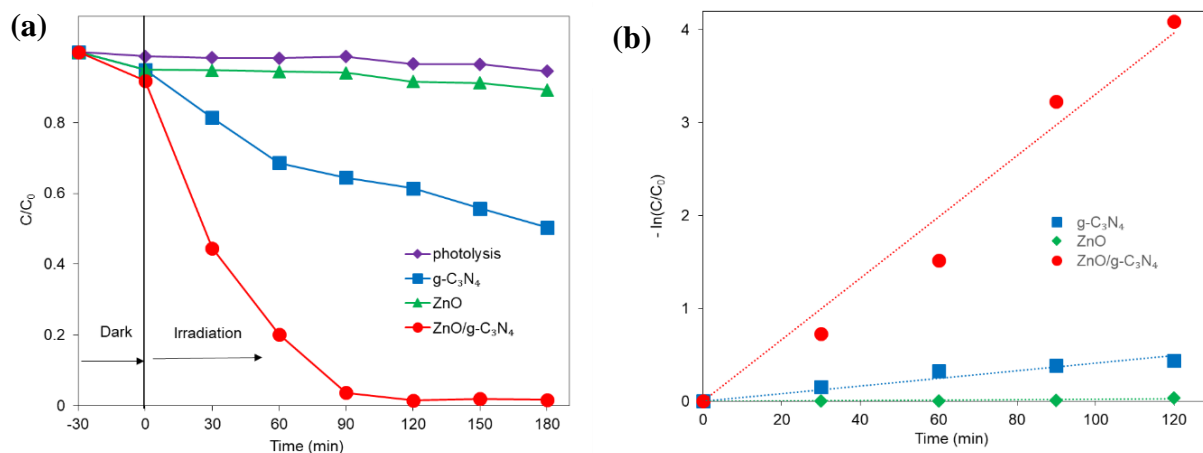


Figure 2.11 (a) Photocatalytic degradation of BPE with different catalyst under visible light irradiation and (b) the plot of $-\ln(C/C_0)$ versus irradiation time; BPE: 3 ppm (30 mL), photocatalyst: 30 mg.

Table 2.2 Kinetic parameters for photocatalytic degradation of BPE

Photocatalyst	Rate constant (min^{-1})	$t_{1/2}$ (min)	R^2
ZnO	0.2×10^{-3}	3465	0.67
$g-C_3N_4$	4.1×10^{-3}	169	0.92
ZnO/ $g-C_3N_4$	3.3×10^{-2}	21	0.97

2.3.11 Effect of ZnO Amount

To study the effect of ZnO amount in the ZnO/ $g-C_3N_4$ composite on photocatalytic degradation of BPE, different composite of ZnO/ $g-C_3N_4$ has been prepared by varying zinc acetate amount (0.1, 0.2, 0.5, 1.0, 2 and 2.5 g) with 20 g of urea. Figure 2.12 shows the photocatalytic degradation of BPE with ZnO/ $g-C_3N_4$ composites by varying amount

of ZnO (different amount of zinc acetate in preparation of composite). It can be found that the composite prepared from 20 g of urea and 2 g of zinc acetate showed maximum photocatalytic activity. The photocatalytic degradation was enhanced with increasing amount of zinc acetate from 0.1 g to 2.0 g as precursor of ZnO in composite and decreased with further increasing zinc acetate (Figure 2.12 and Table 2.3). It means that optimal amount of zinc acetate was 2 g with 20 g of urea to prepare ZnO/g-C₃N₄ composite for photocatalytic degradation of BPE, respectively. Photogenerated electrons-holes separation enhancing by the synergistic effect between ZnO and g-C₃N₄ could be responsible for better photocatalytic degradation of BPE [55]. However, excess ZnO may produce electron hole pairs recombination site and reduce the photoinduced charge separation [50].

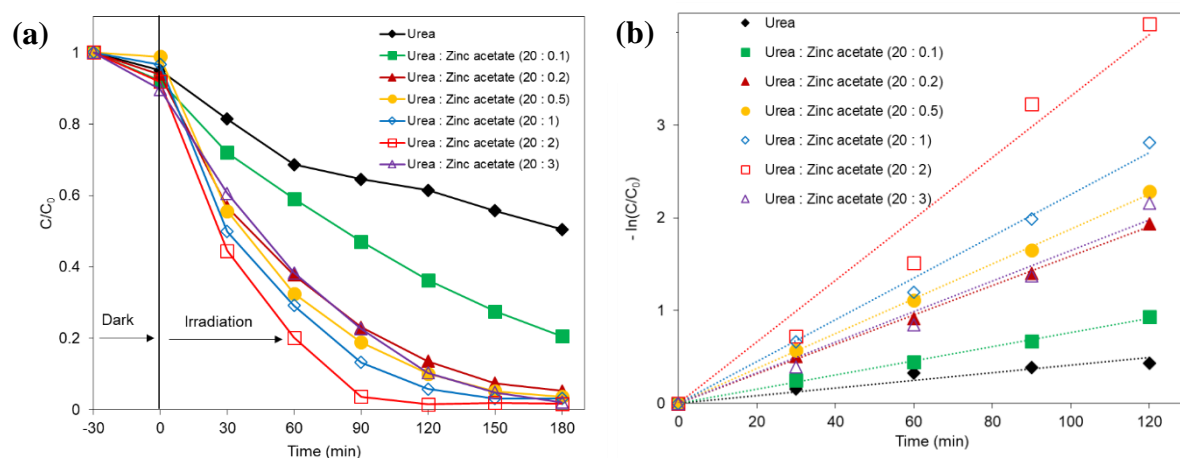


Figure 2.12 (a) Effect of ZnO amount on the composite (varying the amount of zinc acetate in composite preparation) on photocatalytic degradation of BPE with ZnO/g-C₃N₄ composite and (b) the plot of $-\ln(C/C_0)$ versus irradiation time; BPE: 3 ppm (30 mL), ZnO/g-C₃N₄ composite: 30 mg.

Table 2.3 Effect of ZnO amount in composite (varying the amount of zinc acetate in composite preparation) on kinetic parameters for photocatalytic degradation of BPE with ZnO/g-C₃N₄ composite

Precursor ratio		Rate constant (min ⁻¹)	t _{1/2} (min)	R ²
NH ₂ (CO)NH ₂	(CH ₃ COO) ₂ Zn			
20	0	4.1×10 ⁻³	169	0.92
20	0.1	7.6×10 ⁻³	91	1
20	0.2	1.6×10 ⁻²	44	1
20	0.5	1.8×10 ⁻²	37	1
20	1	2.3×10 ⁻²	31	0.99
20	2	3.3×10 ⁻²	21	0.97
20	3	1.7×10 ⁻²	42	0.97

2.3.12 Effect of Calcination Process

In order to understand the effect of calcination process to prepare ZnO/g-C₃N₄ composite on photocatalytic degradation of BPE, composite has been prepared by two step calcination process with different intermediate calcination temperature. Before the calcination of mixture of zinc acetate and urea at 550 °C temperature for 2 h, it was additionally calcined at 100 °C, 200 °C and 300 °C temperature for 2 h as intermediate calcination step to prepare different composites. Figure 2.13 shows the photocatalytic degradation of BPE with ZnO/g-C₃N₄ composites prepared at one step and different two

step calcination processes. It can be seen that the composite prepared at direct one step calcination of 550 °C temperature showed maximum photocatalytic activity (Figure 2.13 and Table 2.4). It means that optimal conditions of composite preparation were direct one step calcination at 550 °C temperature for 2 h.

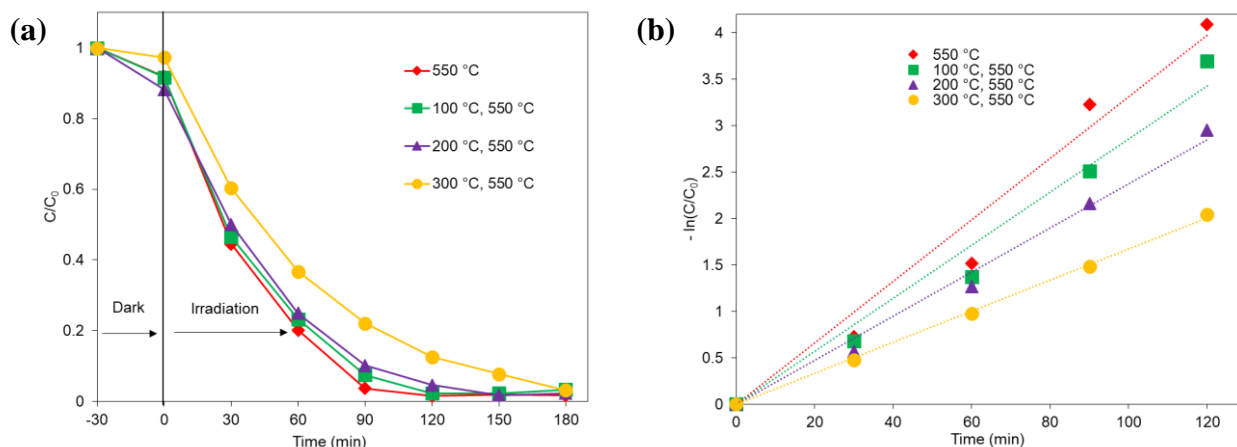


Figure 2.13 (a) Effect of calcination process of composite preparation on photocatalytic degradation of BPE with ZnO/g-C₃N₄ composite and (b) the plot of $-\ln(C/C_0)$ versus irradiation time; BPE: 3 ppm (30 mL), ZnO/g-C₃N₄ composite: 30 mg.

Table 2.4 Effect of calcination process of composite preparation on kinetic parameters for photocatalytic degradation of BPE with ZnO/g-C₃N₄ composite

Calcination process		Rate constant (min ⁻¹)	$t_{1/2}$ (min)	R^2
Pre-calcination temperature (°C)	Calcination temperature (°C)			
-	550	3.3×10^{-2}	21	0.97
100	550	2.9×10^{-2}	24	0.97
200	550	2.4×10^{-2}	29	0.99
300	550	1.7×10^{-2}	41	1

2.3.13 Effect of Catalyst Dosage

It is known that the catalyst dosage shows the impact on the photocatalytic reaction. The effect of ZnO/g-C₃N₄ dosage on the photocatalytic degradation of BPE under visible light irradiation was studied by the variation of 5 mg to 50 mg of ZnO/g-C₃N₄. The results are presented in Figure 2.14. The degradation of BPE was increased with increasing amount of ZnO/g-C₃N₄ up to 30 mg, which could be caused by increasing the number of active sites on catalyst surface [35]. On further increasing the catalyst above 30 mg, the degradation of BPE was not increased significantly, which may be due to the increasing light screening effect by excess amount of catalyst (Figure 2.14 and Table 2.5). For excess overdosage of ZnO/g-C₃N₄, the number of active site of ZnO/g-C₃N₄ may remain almost same.[20] Therefore, 30 mg of ZnO/g-C₃N₄ was selected as the optimal amount of photocatalyst for the present study.

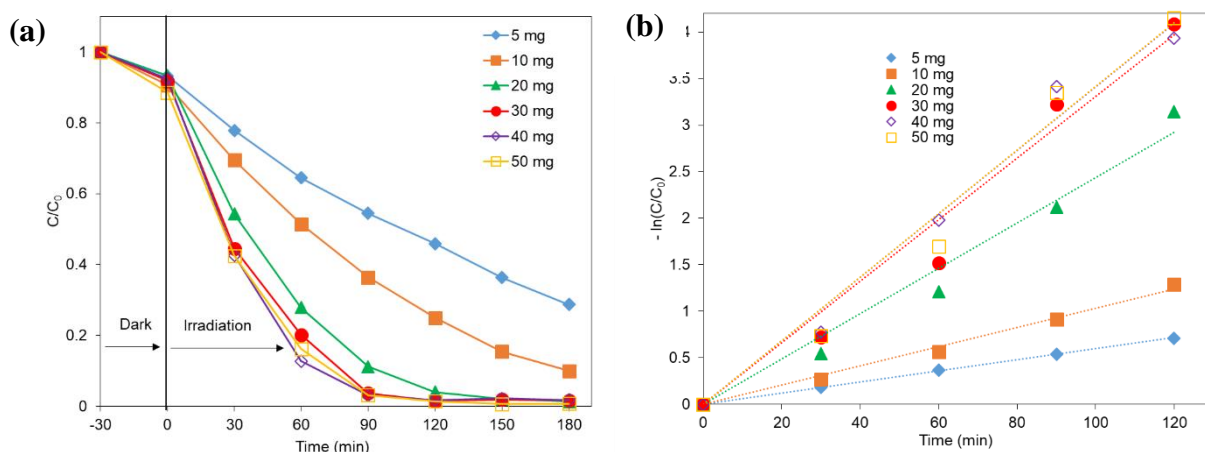


Figure 2.14 (a) Effect of catalyst dosage on photocatalytic degradation of BPE with ZnO/g-C₃N₄ composite and (b) the plot of $-\ln(C/C_0)$ versus irradiation time; BPE: 3 ppm (30 mL).

Table 2.5 Effect of catalyst dosages on kinetic parameters for photocatalytic degradation of BPE with ZnO/g-C₃N₄ composite

Amount of ZnO/g-C ₃ N ₄ (mg)	Rate constant (min ⁻¹)	t _{1/2} (min)	R ²
5	6.0×10 ⁻³	116	1
10	1.0×10 ⁻²	67	0.99
20	2.4×10 ⁻²	29	0.98
30	3.3×10 ⁻²	21	0.97
40	3.4×10 ⁻²	20	0.98
50	3.4×10 ⁻²	20	0.98

2.3.14 Effect of Initial BPE Concentration

It is necessary to study the effect of initial substrate concentration on BPE photocatalytic degradation with ZnO/g-C₃N₄. The effect of initial concentration of BPE was studied by variation from 3 to 10 mg L⁻¹. The results are shown in Figure 2.15. It was investigated that as initial BPE concentration increased from 3 to 10 mg L⁻¹ the degradation efficiency gradually decreased (Figure 2.15 and Table 2.6). Increasing the presence of molecules amount of BPE on the catalyst surface could be responsible for the decrement of photocatalytic degradation efficiency with increasing concentration of BPE. These phenomena may mean that the degradation amount of BPE did not increase even if the substrate concentration increased from 3 to 10 mg L⁻¹. Simultaneously, the probabilities of the reactive species formation on the catalyst surface are also decreased

[24,35]. Hence, 3 mg L^{-1} of BPE was selected to study the photo degradation of BPE with ZnO/g- C_3N_4 composite.

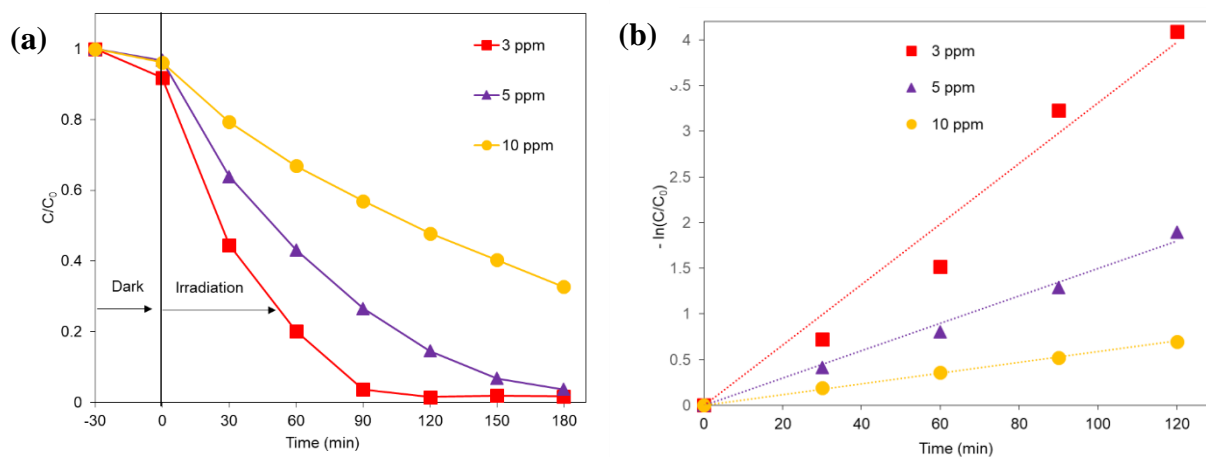


Figure 2.15 (a) Effect of initial BPE concentration on photocatalytic degradation of BPE with ZnO/g- C_3N_4 composite and (b) the plot of $-\ln(C/C_0)$ versus irradiation time; BPE: 30 mL, ZnO/g- C_3N_4 composite: 30 mg.

Table 2.6 Effect of initial BPE concentration on kinetic parameters for photocatalytic degradation of BPE with ZnO/g- C_3N_4 composite

BPE concentration (mgL^{-1})	Rate constant (min^{-1})	$t_{1/2}$ (min)	R^2
3	3.3×10^{-2}	21	0.97
3	1.5×10^{-2}	46	0.99
10	5.9×10^{-3}	117	1

2.3.15 Effect of pH

The effect of pH is considered as an important factor during the photocatalytic degradation procedure. Therefore, the influence of initial pH on the degradation efficiency of BPE with ZnO/g-C₃N₄ was investigated in the pH range 2-10. As seen in Figure 2.16, the degradation efficiency increased with increasing the initial pH of the solution. However, the degradation at pH 8 was slightly worse relative to that at pH 6 (Figure 2.16 and Table 2.7). Dependence of surface charge properties of with ZnO/g-C₃N₄ composite on pH of the solution may affect the degradation of BPE [3]. In addition, at high initial pH, more hydroxide ion (OH⁻) exist in the solution, which induced the generation of hydroxide free radical ([•]OH). The photocatalytical degradation of BPE may be accelerated by generated [•]OH radical [10]. Therefore, pH 6 which is actual initial pH of 3 mg L⁻¹ BPE solution was selected as optimal pH to avoid unwanted chemical treatment for pH adjustment.

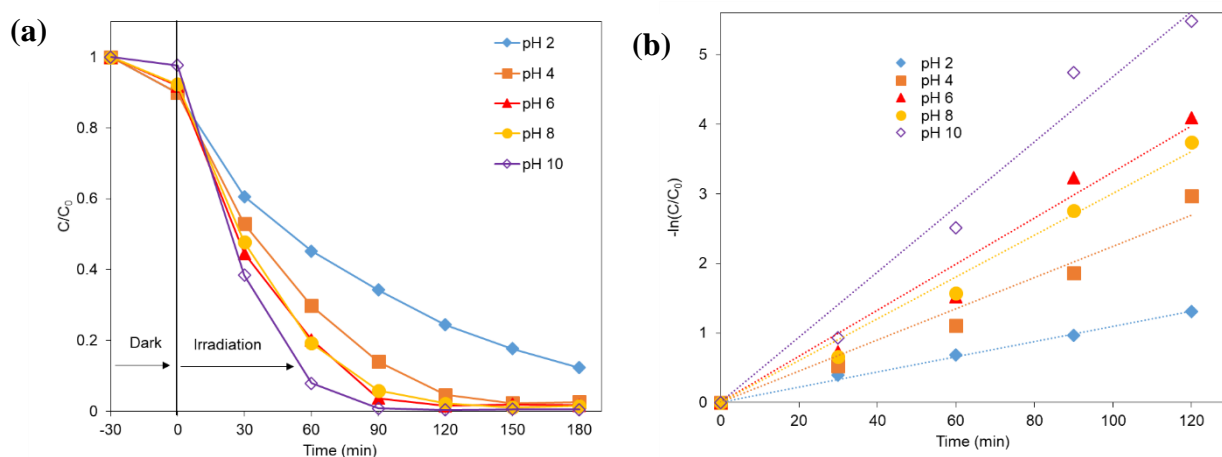


Figure 2.16 (a) Effect of solution pH on photocatalytic degradation of BPE with ZnO/g-C₃N₄ composite and (b) the plot of $-\ln(C/C_0)$ versus irradiation time; BPE: 3 ppm (30 mL), ZnO/g-C₃N₄ composite: 30 mg.

Table 2.7 Effect of solution pH on kinetic parameters for photocatalytic degradation of BPE with ZnO/g-C₃N₄ composite

Solution pH	Rate constant (min ⁻¹)	t _{1/2} (min)	R ²
2	1.1×10 ⁻²	63	0.99
4	2.2×10 ⁻²	31	0.97
6	3.3×10 ⁻²	21	0.97
8	3.0×10 ⁻²	23	0.99
10	4.7×10 ⁻²	15	0.97

2.3.16 Scavenger Role

It is widely known that the holes (h⁺), hydroxyl radical (·OH) and superoxide anion radical anion (·O₂⁻) are reactive species to degrade the pollutants during the photocatalytic degradation reaction. Therefore, in order to understand the photocatalytic degradation mechanism of BPE with ZnO/g-C₃N₄ composite, the scavenging tests were performed by adding EDTA, BQ and IPA corresponding to h⁺, ·O₂⁻ and ·OH radicals, respectively [22]. The results are shown in Figure 2.17 and Table 2.8. It was inspected that the presence of IPA slightly decreased the photocatalytic degradation of BPE compared to the case without scavenger. On the other hand, BQ significantly influenced the photocatalytic degradation. In addition, EDTA impacted on the degradation process moderately. The results suggested that ·O₂⁻ could become the major active species in the photocatalytic reaction and h⁺ seems to play an important role in the photocatalytic activity of ZnO/g-C₃N₄ composite, whereas ·OH radical may play a minor part in the photocatalytic reaction

of BPE. The results showed good agreement with the scavenger role of photocatalytic degradation of methylene blue by composite of ZnO/g-C₃N₄ [16].

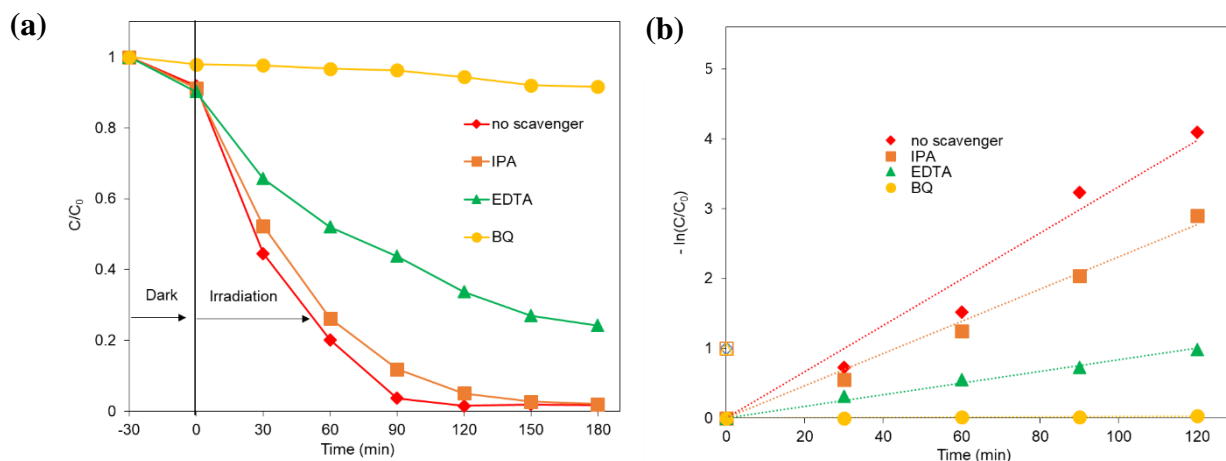


Figure 2.17 (a) Effect of scavenger role on photocatalytic degradation of BPE with ZnO/g-C₃N₄ composite and (b) the plot of $-\ln(C/C_0)$ versus irradiation time; BPE: 3 ppm (30 mL), photocatalyst: 30 mg.

Table 2.8 Effect of scavenger role on kinetic parameters for photocatalytic degradation of BPE with ZnO/g-C₃N₄ composite

Scavenger	Rate constant (min ⁻¹)	T _{1/2} (min)	R ²
without	3.3×10^{-2}	21	0.97
IPA	2.3×10^{-2}	30	0.99
EDTA	8.4×10^{-3}	83	0.99
BQ	3.0×10^{-4}	2310	0.87

2.3.17 Stability Test

Stability of ZnO/g-C₃N₄ composite is important factor for its practical application into the bisphenol degradation. The stability of the system ZnO/g-C₃N₄ composite was investigated through reusability test for 3 cycles towards degradation of BPE. It is clearly investigated that after three cycles of reusability the degradation ability of composite slightly decreased (Figure 2.18). The results were attributed to the chemical and photo stability of the composite [44]. From SEM, TEM, PL, DRS, XRD and FTIR analysis it was also inspected that the properties of composite could not change after the photocatalytic reaction. The results confirmed the chemical stability of the composite.

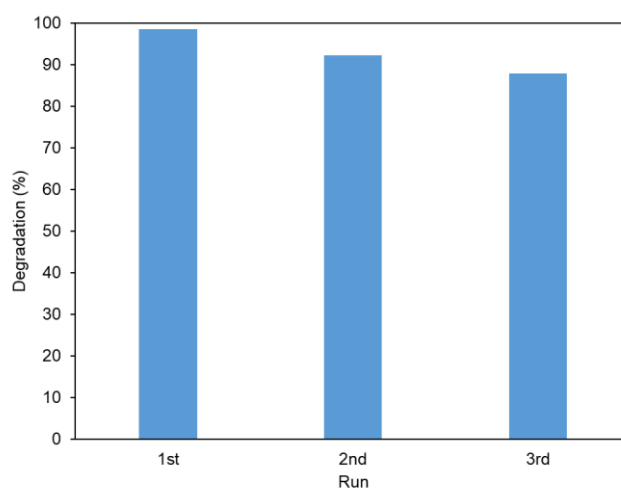


Figure 2.18 Reusability of ZnO/g-C₃N₄ composite on photocatalytic degradation of BPE.

2.3.18 Mechanism

In the ZnO/g-C₃N₄ composite, the electrons in the g-C₃N₄ spontaneously transferred to the ZnO through the interface until their fermi level energy exist at equilibrium [58,59]. It is assumed that an intermediate band in the mid band gap exists in the composite due to fermi level energy equilibrium and the position of intermediate energy band is equal to the conductance band edge potential (E_{CB}) of ZnO. Furthermore, the VBXPS analysis

indicated that the VB position of the composite was 1.88 eV (Figure 2.19). The valence band edge potential (E_{VB}) of the composite was estimated according to the eq. 2.4 [60].

$$E_{NHE}/V = \Phi_{WF} + \Phi_{sample} - 4.44 \quad (2.4)$$

where E_{NHE} , Φ_{WF} , and Φ_{sample} are the VB potential of the photocatalyst, electron work function of the analyzer (4.33 eV), and VB position of the photocatalyst (eV) determined using VB-XPS, respectively. The E_{VB} of composite was estimated at 1.77 eV. The E_{CB} of g-C₃N₄ and intermediate energy band position of the composite were estimated according to the eq. 2.5 and the DRS result of band gap of the g-C₃N₄ and composite [60].

$$E_{CB} = E_{VB} - E_g \quad (2.5)$$

where E_g is the band gap of the semiconductor. The E_{CB} of g-C₃N₄ and intermediate band energy position of the composite were determined at -1.12 eV and -0.45 eV, respectively. Since the intermediate energy band position and E_{CB} of ZnO was equal, E_{CB} and E_{VB} of ZnO were estimated at -0.45 eV and 2.75 eV, respectively.

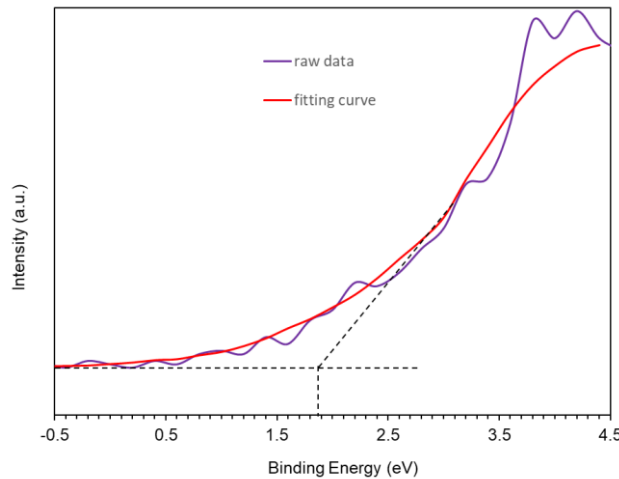
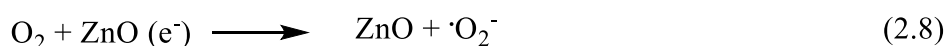
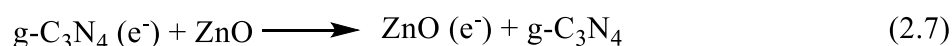
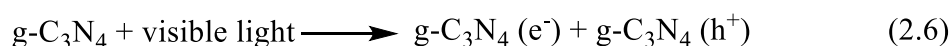


Figure 2.19 VB XPS of ZnO/g-C₃N₄ composite.

Two possible mechanisms of the photocatalytic degradation of BPE with ZnO/g-C₃N₄ composite can be proposed. Firstly, conventional charge transfer mechanism is proposed

as shown in Figure 2.20a. Electrons in g-C₃N₄ were excited to the CB, while the holes are created in the VB upon the visible light irradiation. The value of E_{CB} of g-C₃N₄ is more negative than that of ZnO. Hence, the photogenerated electrons are shifted to the CB of ZnO, which further promoted to the surface. Thus, the recombination of e⁻/h⁺ pairs can be reduced. Secondly, interfacial charge transfer mechanism (IFCT) is proposed as shown in Figure 2.20b. Photogenerated electrons are transferred from VB of g-C₃N₄ to intermediate energy band of the composite through IFCT mechanism. Then, the electrons are shifted to the CB of ZnO. Thus, the photogenerated charge separation may improve.

Due to the CB position of ZnO is more negative to the standard reduction potential of O₂/[•]O₂⁻ (-0.28 eV), O₂ in the environment are reacted with the photogenerated electrons to produce [•]O₂⁻ radicals. Therefore [•]O₂⁻ radicals plays as the major efficient active species for degradation of BPE. In contrary, the generated holes in g-C₃N₄ are not able to react with H₂O to produce [•]OH radicals due to the VB position of g-C₃N₄ is less positive compared to the standard redox potential of H₂O/[•]OH (2.27 eV) [22]. Therefore, BPE is directly oxidized by the holes. The relevant photocatalytic reactions of degradation of BPE with ZnO/g-C₃N₄ composite under visible light irradiation are expressed as following equations:



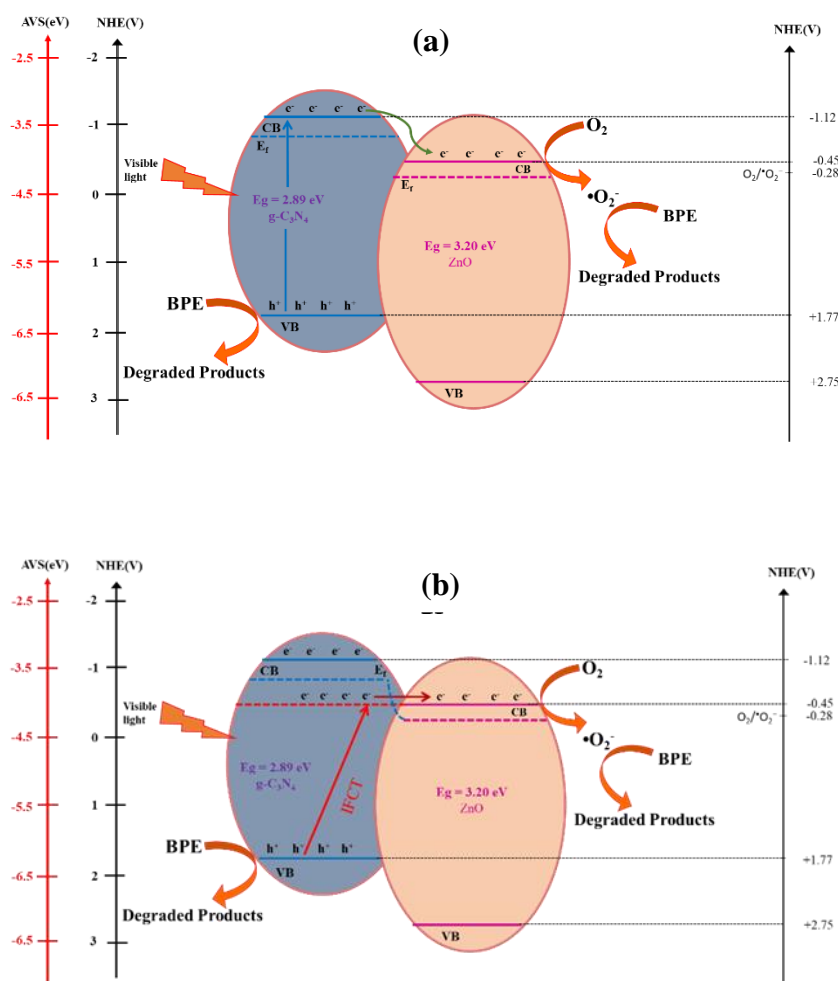


Figure 2.20 (a) Conventional charge transfer mechanism and (b) IFCT mechanism for photocatalytic degradation of BPE with ZnO/g-C₃N₄ composite.

2.4 Conclusions

Cheap and non toxic ZnO, g-C₃N₄ and ZnO/g-C₃N₄ composite were synthesized by facile calcination method. The formation of the composite was confirmed by FTIR, XPS, SEM and TEM analysis. The higher absorption ability of visible light of the composite was detected by UV-Vis DRS analysis. The decrement of photogenerated electron hole pairs recombination was evaluated by PL and EIS investigation. As a result, the composite showed admirable photocatalytic activity on degradation of BPE. Possible two mechanisms of the photocatalytic reaction have been proposed.

2.5 References

1. Tian, B.; Wu, N.; Pan, X.; Wang, Z.; Yan, C.; Sharma, V.K.; Qu, R. Ferrate(VI) Oxidation of Bisphenol E–Kinetics, Removal Performance, and Dihydroxylation Mechanism. *Water Res.* **2022**, *210*, 118025, doi:10.1016/j.watres.2021.118025.
2. Savage, P.E.; Hunter, S.E.; Hoffee, K.L.; Schuelke, T.J.; Smith, M.J. Bisphenol E Decomposition in High-Temperature Water. *Ind. Eng. Chem. Res.* **2006**, *45*, 7775–7780, doi:10.1021/ie060888l.
3. Garg, R.; Gupta, R.; Bansal, A. Synthesis of g-C₃N₄/ZnO Nanocomposite for Photocatalytic Degradation of a Refractory Organic Endocrine Disrupter. *Mater. Today Proc.* **2021**, *44*, 855–859, doi:10.1016/j.matpr.2020.10.787.
4. Uzzaman, M.; Hasan, M.K.; Mahmud, S.; Yousuf, A.; Islam, S.; Uddin, M.N.; Barua, A. Physicochemical, Spectral, Molecular Docking and ADMET Studies of Bisphenol Analogues; A Computational Approach. *Informatics Med. Unlocked* **2021**, *25*, 100706, doi:10.1016/j.imu.2021.100706.
5. Reddy, P.V.L.; Kim, K.-H.; Kavitha, B.; Kumar, V.; Raza, N.; Kalagara, S. Photocatalytic Degradation of Bisphenol A in Aqueous Media: A Review. *J. Environ. Manage.* **2018**, *213*, 189–205, doi:10.1016/j.jenvman.2018.02.059.
6. Pozdnyakov, I.P.; Guo, L.; Glebov, E.M.; Wu, F.; Plyusnin, V.F.; Grivin, V.P.; Deng, N. Aqueous Photochemistry of Bisphenol E in the Presence of β -Cyclodextrin. *High Energy Chem.* **2011**, *45*, 214–221, doi:10.1134/S001814391103012X.
7. Amaterz, E.; Bouddouch, A.; Tara, A.; Taoufyq, A.; Bakiz, B.; Benlhachemi, A.; Jbara, O. Electrochemical Degradation of Bisphenol A Using Electrodeposited SrHPO₄ Thin Films. *Nanotechnol. Environ. Eng.* **2021**, *6*, 18, doi:10.1007/s41204-

- 021-00112-5.
8. Lei, Y.-Q.; He, Z.-X.; Luo, Y.; Lu, S.-N.; Li, C.-J. Chemical Degradation of Bisphenol A Diglycidyl Ether/methyl Tetrahydrophthalic Anhydride Networks by P-Toluenesulfonic-Acetic Anhydride. *Polym. Degrad. Stab.* **2016**, *123*, 115–120, doi:10.1016/j.polymdegradstab.2015.11.010.
 9. Zhou, N.; Liu, Y.; Cao, S.; Guo, R.; Ma, Y.; Chen, J. Biodegradation of Bisphenol Compounds in the Surface Water of Taihu Lake and the Effect of Humic Acids. *Sci. Total Environ.* **2020**, *723*, 138146, doi:10.1016/j.scitotenv.2020.138164.
 10. Kaneco, S.; Rahman, M.A.; Suzuki, T.; Katsumata, H.; Ohta, K. Optimization of Solar Photocatalytic Degradation Conditions of Bisphenol A in Water Using Titanium Dioxide. *J. Photochem. Photobiol. A Chem.* **2004**, *163*, 419–424, doi:10.1016/j.jphotochem.2004.01.012.
 11. Wang, Y.; Hu, K.; Yang, Z.; Ye, C.; Li, X.; Yan, K. Facile Synthesis of Porous ZnO Nanoparticles Efficient for Photocatalytic Degradation of Biomass-Derived Bisphenol A Under Simulated Sunlight Irradiation. *Front. Bioeng. Biotechnol.* **2021**, *8*, 616780, doi:10.3389/fbioe.2020.616780.
 12. Paul, D.R.; Gautam, S.; Panchal, P.; Nehra, S.P.; Choudhary, P.; Sharma, A. ZnO-Modified g-C₃N₄: A Potential Photocatalyst for Environmental Application. *ACS Omega* **2020**, *5*, 3828–3838, doi:10.1021/acsomega.9b02688.
 13. Ngullie, R.C.; Alaswad, S.O.; Bhuvaneswari, K.; Shanmugam, P.; Pazhanivel, T.; Arunachalam, P. Synthesis and Characterization of Efficient ZnO/g-C₃N₄ Nanocomposites Photocatalyst for Photocatalytic Degradation of Methylene Blue. *Coatings* **2020**, *10*, 500, doi:10.3390/COATINGS10050500.
 14. Ismael, M. The Photocatalytic Performance of the ZnO/g-C₃N₄ Composite

- Photocatalyst toward Degradation of Organic Pollutants and Its Inactivity toward Hydrogen Evolution: The Influence of Light Irradiation and Charge Transfer. *Chem. Phys. Lett.* **2020**, 739, 136992, doi:10.1016/j.cplett.2019.136992.
15. Pérez-Molina, Á.; Pastrana-Martínez, L.M.; Pérez-Poyatos, L.T.; Morales-Torres, S.; Maldonado-Hódar, F.J. One-Pot Thermal Synthesis of g-C₃N₄/ZnO Composites for the Degradation of 5-Fluoruracil Cytostatic Drug under UV-LED Irradiation. *Nanomaterials* **2022**, 12, 340, doi:10.3390/nano12030340.
 16. Zhang, S.; Su, C.; Ren, H.; Li, M.; Zhu, L.; Ge, S.; Wang, M.; Zhang, Z.; Li, L.; Cao, X. In-Situ Fabrication of g-C₃N₄/ZnO Nanocomposites for Photocatalytic Degradation of Methylene Blue: Synthesis Procedure Does Matter. *Nanomaterials* **2019**, 9, 215, doi:10.3390/nano9020215.
 17. Zhou, J.; Zhang, M.; Zhu, Y. Preparation of Visible Light-Driven g-C₃N₄@ZnO Hybrid Photocatalyst via Mechanochemistry. *Phys. Chem. Chem. Phys.* **2014**, 16, 17627–17633, doi:10.1039/c4cp02061h.
 18. Ravichandran, K.; Kalpana, K.; Ibrahim, M.M.; Seelan, K.S. Effect of Source Material of g-C₃N₄ on the Photocatalytic Activity of ZnO/g-C₃N₄ thin Film Coated on Stainless Steel Mesh Substrate. In *Proceedings of the Materials Today: Proceedings*; Elsevier Ltd, 2019; Vol. 48, pp. 207–215.
 19. Li, L.; Sun, S.-Q.; Wang, Y.-X.; Wang, C.-Y. Facile Synthesis of ZnO/g-C₃N₄ Composites with Honeycomb-like Structure by H₂ Bubble Templates and Their Enhanced Visible Light Photocatalytic Performance. *J. Photochem. Photobiol. A Chem.* **2018**, 355, 16–24, doi:10.1016/j.jphotochem.2017.12.016.
 20. Sun, Q.; Sun, Y.; Zhou, M.; Cheng, H.; Chen, H.; Dorus, B.; Lu, M.; Le, T. A 2D/3D g-C₃N₄/ZnO Heterojunction Enhanced Visible-Light Driven Photocatalytic

- Activity for Sulfonamides Degradation. *Ceram. Int.* **2022**, *48*, 7283–7290, doi:10.1016/j.ceramint.2021.11.289.
21. Uma, R.; Ravichandran, K.; Sriram, S.; Sakthivel, B. Cost-Effective Fabrication of ZnO/g-C₃N₄ Composite Thin Films for Enhanced Photocatalytic Activity against Three Different Dyes (MB, MG and RhB). *Mater. Chem. Phys.* **2017**, *201*, 147–155, doi:10.1016/j.matchemphys.2017.08.015.
 22. Zhang, Z.; Sun, Y.; Wang, Y.; Yang, Y.; Wang, P.; Shi, L.; Feng, L.; Fang, S.; Liu, Q.; Ma, L.; et al. Synthesis and Photocatalytic Activity of g-C₃N₄/ZnO Composite Microspheres under Visible Light Exposure. *Ceram. Int.* **2022**, *48*, 3293–3302, doi:10.1016/j.ceramint.2021.10.104.
 23. Zhong, Q.; Lan, H.; Zhang, M.; Zhu, H.; Bu, M. Preparation of Heterostructure g-C₃N₄/ZnO Nanorods for High Photocatalytic Activity on Different Pollutants (MB, RhB, Cr(VI) and Eosin). *Ceram. Int.* **2020**, *46*, 12192–12199, doi:10.1016/j.ceramint.2020.01.265.
 24. Kumaresan, N.; Sinthiya, M.M.A.; Sarathbavan, M.; Ramamurthi, K.; Sethuraman, K.; Babu, R.R. Synergetic Effect of g-C₃N₄/ZnO Binary Nanocomposites Heterojunction on Improving Charge Carrier Separation through 2D/1D Nanostructures for Effective Photocatalytic Activity under the Sunlight Irradiation. *Sep. Purif. Technol.* **2020**, *244*, 116356, doi:10.1016/j.seppur.2019.116356.
 25. Zhang, Y.; Liu, H.; Gao, F.; Tan, X.; Cai, Y.; Hu, B.; Huang, Q.; Fang, M.; Wang, X. Application of MOFs and COFs for Photocatalysis in CO₂ Reduction, H₂ Generation, and Environmental Treatment. *EnergyChem* **2022**, *4*, 100078, doi:10.1016/j.enchem.2022.100078.
 26. Liu, X.; Verma, G.; Chen, Z.; Hu, B.; Huang, Q.; Yang, H.; Ma, S.; Wang, X.

- Metal-Organic Framework Nanocrystal-Derived Hollow Porous Materials: Synthetic Strategies and Emerging Applications. *Innov.* **2022**, 3, 100281, doi:10.1016/j.xinn.2022.100281.
27. Kumar Kuila, S.; Kumbhakar, P.; Sekhar Tiwary, C.; Kumar Kundu, T. Photon and Vibration Synergism on Planar Defects Induced 2D-Graphitic Carbon Nitride for Ultrafast Remediation of Dyes and Antibiotic Ampicillin. *J. Mater. Sci.* **2022**, 57, 8658–8675, doi:10.1007/s10853-022-07196-7.
28. Kuila, S.K.; Sarkar, R.; Kumbhakar, P.; Kumbhakar, P.; Tiwary, C.S.; Kundu, T.K. Photocatalytic Dye Degradation under Sunlight Irradiation Using Cerium Ion Adsorbed Two-Dimensional Graphitic Carbon Nitride. *J. Environ. Chem. Eng.* **2020**, 8, 103942, doi:10.1016/j.jece.2020.103942.
29. de Sousa, J.G.M.; da Silva, T.V.C.; de Moraes, N.P.; da Silva, M.L.C.P.; Rocha, R. da S.; Landers, R.; Rodrigues, L.A. Visible Light-Driven ZnO/g-C₃N₄/carbon Xerogel Ternary Photocatalyst with Enhanced Activity for 4-Chlorophenol Degradation. *Mater. Chem. Phys.* **2020**, 256, 123651, doi:10.1016/j.matchemphys.2020.123651.
30. Zhang, S.; Liu, Y.; Ma, R.; Jia, D.; Wen, T.; Ai, Y.; Zhao, G.; Fang, F.; Hu, B.; Wang, X. Molybdenum (VI)-Oxo Clusters Incorporation Activates g-C₃N₄ with Simultaneously Regulating Charge Transfer and Reaction Centers for Boosting Photocatalytic Performance. *Adv. Funct. Mater.* **2022**, 32, 2204175, doi:10.1002/adfm.202204175.
31. Liu, W.; Wang, M.; Xu, C.; Chen, S. Facile Synthesis of g-C₃N₄/ZnO Composite with Enhanced Visible Light Photooxidation and Photoreduction Properties. *Chem. Eng. J.* **2012**, 209, 386–393, doi:10.1016/j.cej.2012.08.033.

32. Guan, R.; Li, J.; Zhang, J.; Zhao, Z.; Wang, D.; Zhai, H.; Sun, D. Photocatalytic Performance and Mechanistic Research of ZnO/g-C₃N₄ on Degradation of Methyl Orange. *ACS Omega* **2019**, *4*, 20742–20747, doi:10.1021/acsomega.9b03129.
33. Kumbhakar, P.; Pramanik, A.; Biswas, S.; Kole, A.K.; Sarkar, R.; Kumbhakar, P. In-Situ Synthesis of rGO-ZnO Nanocomposite for Demonstration of Sunlight Driven Enhanced Photocatalytic and Self-Cleaning of Organic Dyes and Tea Stains of Cotton Fabrics. *J. Hazard. Mater.* **2018**, *360*, 193–203, doi:10.1016/j.jhazmat.2018.07.103.
34. Adhikari, S.P.; Pant, H.R.; Kim, H.J.; Park, C.H.; Kim, C.S. Deposition of ZnO Flowers on the Surface of g-C₃N₄ Sheets via Hydrothermal Process. *Ceram. Int.* **2015**, *41*, 12923–12929, doi:10.1016/j.ceramint.2015.06.134.
35. Kumar, K.V.A.; Vinodkumar, T.; Selvaraj, M.; Suryakala, D.; Subrahmanyam, C. Visible Light-Induced Catalytic Abatement of 4-Nitrophenol and Rhodamine B Using ZnO/g-C₃N₄ Catalyst. *J. Chem. Sci.* **2021**, *133*, 41, doi:10.1007/s12039-021-01903-8.
36. Wang, Y.; Shi, R.; Lin, J.; Zhu, Y. Enhancement of Photocurrent and Photocatalytic Activity of ZnO Hybridized with Graphite-like C₃N₄. *Energy Environ. Sci.* **2011**, *4*, 2922–2929, doi:10.1039/c0ee00825g.
37. Liu, W.; Wang, M.; Xu, C.; Chen, S.; Fu, X. Significantly Enhanced Visible-Light Photocatalytic Activity of g-C₃N₄ via ZnO Modification and the Mechanism Study. *J. Mol. Catal. A Chem.* **2013**, *368-369*, 9–15, doi:10.1016/j.molcata.2012.11.007.
38. Qin, J.; Yang, C.; Cao, M.; Zhang, X.; Saravanan, R.; Limpanart, S.; Ma, M.; Liu, R. Two-Dimensional Porous Sheet-like Carbon-Doped ZnO/g-C₃N₄ nanocomposite with High Visible-Light Photocatalytic Performance. *Mater. Lett.*

- 2017**, 189, 156–159, doi:10.1016/j.matlet.2016.12.007.
39. Wang, J.; Yang, Z.; Gao, X.; Yao, W.; Wei, W.; Chen, X.; Zong, R.; Zhu, Y. Core-Shell g-C₃N₄@ZnO Composites as Photoanodes with Double Synergistic Effects for Enhanced Visible-Light Photoelectrocatalytic Activities. *Appl. Catal. B Environ.* **2017**, 217, 169–180, doi:10.1016/j.apcatb.2017.05.034.
 40. Naseri, A.; Samadi, M.; Pourjavadi, A.; Ramakrishna, S.; Moshfegh, A.Z. Enhanced Photocatalytic Activity of ZnO/g-C₃N₄ Nanofibers Constituting Carbonaceous Species under Simulated Sunlight for Organic Dye Removal. *Ceram. Int.* **2021**, 47, 26185–26196, doi:10.1016/j.ceramint.2021.06.026.
 41. Park, T.J.; Pawar, R.C.; Kang, S.; Lee, C.S. Ultra-Thin Coating of g-C₃N₄ on an Aligned ZnO Nanorod Film for Rapid Charge Separation and Improved Photodegradation Performance. *RSC Adv.* **2016**, 6, 89944–89952, doi:10.1039/C6RA16300A.
 42. Li, X.; Li, M.; Yang, J.; Li, X.; Hu, T.; Wang, J.; Sui, Y.; Wu, X.; Kong, L. Synergistic Effect of Efficient Adsorption g-C₃N₄/ZnO Composite for Photocatalytic Property. *J. Phys. Chem. Solids* **2014**, 75, 441–446, doi:10.1016/j.jpcs.2013.12.001.
 43. Fu, J.; Yu, J.; Jiang, C.; Cheng, B. g-C₃N₄ -Based Heterostructured Photocatalysts. *Adv. Energy Mater.* 2018, 8, 1701503.
 44. Gayathri, M.; Sakar, M.; Satheeshkumar, E.; Sundaravadivel, E. Insights into the Mechanism of ZnO/g-C₃N₄ Nanocomposites toward Photocatalytic Degradation of Multiple Organic Dyes. *J. Mater. Sci. Mater. Electron.* **2022**, 33, 9347–9357, doi:10.1007/s10854-021-07302-6.
 45. Zong, H.; Zhao, T.; Zhou, G.; Qian, R.; Feng, T.; Pan, J.H. Revisiting Structural

- and Photocatalytic Properties of g-C₃N₄/TiO₂: Is Surface Modification of TiO₂ by Calcination with Urea an Effective Route to “solar” Photocatalyst? *Catal. Today* **2019**, *335*, 252–261, doi:10.1016/j.cattod.2018.12.015.
46. Dong, J.; Zhang, Y.; Hussain, M.I.; Zhou, W.; Chen, Y.; Wang, L.N. g-C₃N₄: Properties, Pore Modifications, and Photocatalytic Applications. *Nanomaterials* **2022**, *12*, 121, doi:10.3390/nano12010121.
 47. Lee, S.; Jeong, S.; Kim, D.; Hwang, S.; Jeon, M.; Moon, J. ZnO Nanoparticles with Controlled Shapes and Sizes Prepared Using a Simple Polyol Synthesis. *Superlattices Microstruct.* **2008**, *43*, 330–339, doi:10.1016/j.spmi.2008.01.004.
 48. Molla, M.A.I.; Furukawa, M.; Tateishi, I.; Katsumata, H.; Suzuki, T.; Kaneco, S. Photocatalytic Decolorization of Dye with Self-Dye-Sensitization under Fluorescent Light Irradiation. *ChemEngineering* **2017**, *1*, 8, doi:10.3390/chemengineering1020008.
 49. Moussa, H.; Chouchene, B.; Gries, T.; Balan, L.; Mozet, K.; Medjahdi, G.; Schneider, R. Growth of ZnO Nanorods on Graphitic Carbon Nitride gCN Sheets for the Preparation of Photocatalysts with High Visible-Light Activity. *ChemCatChem* **2018**, *10*, 4973–4983, doi:10.1002/cctc.201801206.
 50. Zhu, Y.-P.; Li, M.; Liu, Y.-L.; Ren, T.-Z.; Yuan, Z.-Y. Carbon-Doped ZnO Hybridized Homogeneously with Graphitic Carbon Nitride Nanocomposites for Photocatalysis. *J. Phys. Chem. C* **2014**, *118*, 10963–10971, doi:10.1021/jp502677h.
 51. Jingyu, H.; Ran, Y.; Zhaohui, L.; Yuanqiang, S.; Lingbo, Q.; Nti Kani, A.; Kani, A.N. In-Situ Growth of ZnO Globular on g-C₃N₄ to Fabrication Binary Heterojunctions and Their Photocatalytic Degradation Activity on Tetracyclines.

- Solid State Sci.* **2019**, 92, 60–67, doi:10.1016/j.solidstatesciences.2019.02.009.
52. Liu, J.; Zhang, T.; Wang, Z.; Dawson, G.; Chen, W. Simple Pyrolysis of Urea into Graphitic Carbon Nitride with Recyclable Adsorption and Photocatalytic Activity. *J. Mater. Chem.* **2011**, 21, 14398–14401, doi:10.1039/c1jm12620b.
53. Yue, B.; Li, Q.; Iwai, H.; Kako, T.; Ye, J. Hydrogen Production Using Zinc-Doped Carbon Nitride Catalyst Irradiated with Visible Light. *Sci. Technol. Adv. Mater.* **2011**, 12, 034401, doi:10.1088/1468-6996/12/3/034401.
54. Islam, J.B.; Islam, M.R.; Furukawa, M.; Tateishi, I.; Katsumata, H.; Kaneco, S. Ag-Modified g-C₃N₄ with Enhanced Activity for the Photocatalytic Reduction of Hexavalent Chromium in the Presence of EDTA under Ultraviolet Irradiation. *Environ. Technol.* **2022**, doi:10.1080/09593330.2022.2068379.
55. Xing, H.; Ma, H.; Fu, Y.; Xue, M.; Zhang, X.; Dong, X.; Zhang, X. Preparation of g-C₃N₄/ZnO Composites and Their Enhanced Photocatalytic Activity. *Mater. Technol.* **2015**, 30, 122–127, doi:10.1179/1753555714Y.00000000216.
56. Yang, P.; Wang, J.; Yue, G.; Yang, R.; Zhao, P.; Yang, L.; Zhao, X.; Astruc, D. Constructing Mesoporous g-C₃N₄/ZnO Nanosheets Catalyst for Enhanced Visible-Light Driven Photocatalytic Activity. *J. Photochem. Photobiol. A Chem.* **2020**, 388, 112169, doi:10.1016/j.jphotochem.2019.112169.
57. Yu, W.; Xu, D.; Peng, T. Enhanced Photocatalytic Activity of g-C₃N₄ for Selective CO₂ Reduction to CH₃OH via Facile Coupling of ZnO: A Direct Z-Scheme Mechanism. *J. Mater. Chem. A* **2015**, 3, 19936–19947, doi:10.1039/C5TA05503B.
58. Liao, G.; Li, C.; Li, X.; Fang, B. Emerging Polymeric Carbon Nitride Z-Scheme Systems for Photocatalysis. *Cell Reports Phys. Sci.* 2021, 2, 100355.
59. Lu, X.; Quan, L.; Hou, H.; Qian, J.; Liu, Z.; Zhang, Q. Fabrication of 1D/2D Y-

- Doped $\text{CeO}_2/\text{ZnIn}_2\text{S}_4$ S-Scheme Photocatalyst for Enhanced Photocatalytic H_2 Evolution. *J. Alloys Compd.* **2022**, 925, 166552, doi:10.1016/j.jallcom.2022.166552.
60. Katsumata, H.; Islam Molla, M.A.; Islam, J.B.; Tateishi, I.; Furukawa, M.; Kaneco, S. Dual Z-Scheme Heterojunction $\text{g-C}_3\text{N}_4/\text{Ag}_3\text{PO}_4/\text{AgBr}$ Photocatalyst with Enhanced Visible-Light Photocatalytic Activity. *Ceram. Int.* **2022**, 48, 21898–21905, doi:10.1016/j.ceramint.2022.04.176.

CHAPTER THREE

*Visible Light Induced Photocatalytic Degradation
of Diclofenac in Aqueous Solution Using Fabricated
ZnO/g-C₃N₄ by Facile Calcination Technique*

3.1 Introduction

Pharmaceutical products and personal care items have been found in aquatic environments more frequently as a consequence of an enormous increase in utilization [1]. The synthetic non-steroidal anti-inflammatory drug diclofenac (DCF), as its sodium salt, is most frequently applied in the treatment of inflammatory illnesses, dysmenorrhea for both humans and animals, and in personal care items [2–4]. The widely used DCF releases continuously into the aquatic environment through a variety of sources, including the metabolism of human and animal urine and feces after medical treatment, production site disposal, and domestic waste discharge [1,5]. Due to the low biodegradability and longtime environmental persistence of DCF, it is very frequently found in wastewater treatment plants, surface water, drinking water, groundwater, seawater, suspended soil, sediments, landfills, and sludge [6,7]. Furthermore, despite the fact that DCF concentrations in the environment have been reported to be numerous mg/L or ng/L, they may have negative impacts on ecosystems or human health [8,9]. For example, DFC impacts aquatic life, including rainbow and brown trout, by drastically mutating their gill cells, kidneys, and liver. Moreover, DFC is lethal to vultures while they consume the dead bodies of birds and animals treated with it [4,10]. Therefore, it is urgently needed to develop efficient techniques for removing DCF from wastewater and effluents. However, the DCF is not fully removed by conventional techniques such as adsorption, oxidation, coagulation, membrane, and electrochemical methods [11–15]. Advanced oxidation processes (AOPs), including ozonation, UV/H₂O₂, sonolysis, and Fenton and photo-Fenton, have been used as promising methods to accomplish efficient removal of DCF as it is entirely mineralized [2,16–22]. Among these technologies, visible light-responsive semiconductor base photocatalytic degradation of DCF is regarded as an effective technique due to the high efficacy, cost-effectiveness, and potential utilization of solar energy [7,23]. This technique is based on the generation of electron-hole pairs, hydroxyl radicals, and superoxide radicals upon the irradiation of light on

the photocatalysts. All of the abovementioned reactive species have the ability to attack organic contaminants, break them up into smaller pieces, and then mineralize carbon dioxide, water, and other inorganic species [6]. Numerous semiconductor- based photocatalysts have been utilized for the removal of DFC from water [24].

The graphitic carbon nitride ($g\text{-C}_3\text{N}_4$) is widely used as a visible light-responsive photocatalyst owing to its appealing characteristics such as a narrow band gap (~ 2.70 eV), good chemical stability, π -conjugated electronic structure, and suitable redox potential for the degradation of organic pollutants [2,25]. In addition, it is facile to fabricate $g\text{-C}_3\text{N}_4$ from several nitrogen-rich chemical substances, including dicyandiamide, urea, melamine, and thiourea, by thermally treating [26]. Nevertheless, the short lifetime of photogenerated charges due to the fast recombination of electron (e^-) and hole (h^+) pairs on pure $g\text{-C}_3\text{N}_4$ results in low photocatalytic activity of pure $g\text{-C}_3\text{N}_4$ [3]. Moreover, a single-component photocatalyst with a broad range of light-absorption ability and good charge-separation efficacy is very challenging [10]. Hence, a large number of modified $g\text{-C}_3\text{N}_4$ by heterostructure formation with other semiconductors and doping with metals and nonmetals elements have been reported for the removal of DCF. For instance, $\text{Ag}/g\text{-C}_3\text{N}_4$, $\text{AgI}/g\text{-C}_3\text{N}_4$, $\text{V}_2\text{O}_5/\text{boron doped } g\text{-C}_3\text{N}_4$, $\text{Ti}_3\text{C}_2/g\text{-C}_3\text{N}_4$, $\text{TiO}_2/g\text{-C}_3\text{N}_4$, $\text{Co}_3\text{O}_4/g\text{-C}_3\text{N}_4$, and $\text{Ag}_3\text{PO}_4/g\text{-C}_3\text{N}_4$ composites have been utilized to degrade DCF as visible light-driven photocatalysts [1–3,10,27–29].

ZnO is considered a well-known, cost-effective, and non-toxic photocatalytic semiconductor [26]. But it is inactive in the visible region and shows photocatalytic activity only in the ultraviolet region due to its higher band gap energy of about 3.2 eV [30]. However, band level positions for ZnO and $g\text{-C}_3\text{N}_4$ match suitably. Hence, composites of $g\text{-C}_3\text{N}_4$ (medium band gap) and ZnO (wider band gap) may enhance the efficacy of photogenerated electron hole pair separation and transfer for the appropriate band position, resulting in enhanced photocatalytic activity [31,32]. Hence, the $\text{ZnO}/g\text{-C}_3\text{N}_4$ composite has attracted a lot

of interest because of its excellent structure, dimensional anisotropy, optical, and electronic characteristics [33]. The ZnO/g-C₃N₄ composites have been fabricated in several research works using numerous techniques like calcination, ball milling, vapor condensation, reflux, ultrasonic dispersion, etc [34–37].

In recent years, numerous research articles have been reported on the enhanced visible light-driven photocatalytic efficacy of ZnO/g-C₃N₄ composites for various applications such as generation of H₂, reduction of CO₂, inactivation of bacteria, degradation of dyes, removal of pharmaceutical products, and reduction of Cr(VI) [33,38–46]. For instances, Meena et al. reported the synthesis of g-C₃N₄/ZnO nanostructures through mechano-thermal procedures for enhanced visible light-illuminated photocatalytic degradation of methylene blue dye [47]. Girish et al. prepared Z-scheme ZnO/g-C₃N₄ heterostructure using simply microwave irradiation as efficient visible light-driven photocatalysts for dye degradation and hydrogen evolution reactions [48]. Pham et al. reported the synthesis of ZnO/g-C₃N₄ composite by calcination technique and applied it to the solar light-assisted photodegradation of tetracycline in wastewater and the conversion of CO₂ as efficient photocatalyst [49]. Hosseini-Hosseiniabad et al. reported the development of g-C₃N₄/ZnO nanocomposite as a highly effective photocatalytic and antibacterial novel cotton fabric coating [50].

In the removal of pharmaceutical waste from aqueous effluent, the ZnO/g-C₃N₄ composites have been utilized to the degradation of sulfamethoxazole, nitenpyram, tetracycline, sulfonamides, endocrine disruptors, and more [51–55]. However, photocatalytic degradation of DCF using ZnO/g-C₃N₄ composites has been rarely reported

In this study, ZnO/g-C₃N₄ composites have been fabricated by facile deposition and calcination of ZnO and g-C₃N₄. The visible light induced photocatalytic degradation of DCF using fabricated ZnO/g-C₃N₄ composites has been studied. Furthermore, the effects of the types of g-C₃N₄ and ZnO and the calcination temperature during the composite formation have been

inspected. The various parameters, including ZnO content in the composite, catalyst dosage, and initial concentration of DCF, have been optimized for visible light-driven photocatalytic DCF removal in aqueous solution. In addition, radical scavenger tests were also conducted to predict the degradation mechanism. The photocatalysts were also characterized utilizing different characterization methods.

3.2 Materials AND Methods

3.2.1 Materials

Diclofenac sodium (DCF, 98.0%), urea (99.0%), melamine (99.0%), zinc nitrate hexahydrate (99.9%), zinc acetate dihydrate (99.0%), ethanol (99.5%), isopropanol (IPA, 99.7%), benzoquinone (BQ, 98.0%), ethylenediaminetetraacetic acid (EDTA, 98.0%), nitric acid (61.0%), and sodium hydroxide (97.0%) were obtained from FUJIFILM Wako Pure Chemical Corporation, Japan. Two types of ZnO nanoparticles were purchased from Sigma Aldrich (50-90 nm, $1\text{-}25\text{ m}^2\text{g}^{-1}$) and FUJIFILM WAKO Pure Chemical Corporation ($\sim 5\text{ }\mu\text{m}$). Formic acid (98.0%) and acetonitrile (99.5%) were obtained from Nacalai Tesque Inc., and Japan Kanto Chemical Co., Inc., Japan, respectively. All of the chemicals were analytical grade and utilized without more purification. An ultrapure water system (Advantec MFS Inc., Tokyo, Japan) was used for pure water supply.

3.2.2 Synthesis of g-C₃N₄

Pure g-C₃N₄ was synthesized by the calcination of urea. Typically, 12 g of urea was ground manually, placed in a crucible, and covered by a cap and aluminum foil. Then it was calcined at 550 °C for 2 hours with a heating increasing rate of 2 °C min⁻¹ using an electric muffle furnace. Finally, the obtained light-yellow sample was grounded manually.

3.2.3 Preparation of ZnO/g-C₃N₄ Composite

A mixture of 150 mg of g-C₃N₄ and 50 mg of ZnO in 10 mL of ethanol was dispersed ultrasonically for 30 minutes, followed by stirring at a constant speed for 2 hours. After that,

the mixture was dried by centrifugation and vacuum oven. Finally, the dried mixture was calcined at 400 °C for 1 hour with a heating increasing rate of 2 °C min⁻¹ and ground in a mortar manually into a light-yellow powder. The schematic diagram of the fabrication of the ZnO/g-C₃N₄ composite is presented in Figure 3.1.

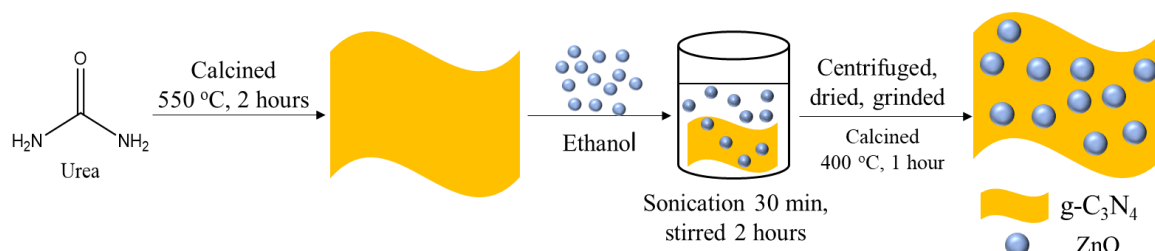


Figure 3.1 Schematic diagram for the synthesis of ZnO/g-C₃N₄ composite.

3.2.4 Characterization

The samples were characterized by X-ray diffraction (XRD), Fourier transform infrared (FTIR) spectroscopy, X-ray photoelectron spectroscopy (XPS), scanning electron microscope (SEM), energy-dispersive X-ray spectroscopy (EDS), transmitted electron microscope (TEM), UV–vis diffuse reflectance spectroscopy (DRS), PL spectroscopy, nitrogen adsorption and desorption isotherms, and electrochemical impedance spectroscopy (EIS) analysis. XRD patterns of the samples were attained utilizing a Rigaku RINT Ultima-IV diffractometer by Cu K α radiation in a scan range of 10–80° at a scan rate of 0.04 °/s. The FTIR spectra of the photocatalysts were obtained by means of a Perkin Elmer spectrometer (SPECTRUM 100 FTIR) with an attenuated total reflection assemblage. XPS of ZnO/g-C₃N₄ and g-C₃N₄ were characterized by using a PHI Quantera SXM photoelectron spectrometer with Al K α radiation. SEM and EDS of the samples were investigated by using a JEOL JEM-1400 Flash SEM. The TEM of the samples was analyzed by means of a JEOL JEM-1011 TEM. The UV-vis DRS of the samples were inspected by a JASCO V-750 UV–vis instrument equipped by an integrating sphere adaptor. Photoluminescence (PL) spectra of the samples were attained with an excitation wavelength of 340 nm utilizing a Shimadzu fluorescence spectrophotometer (RF-5300PC).

The specific surface area, total pore volume, and average pore size of the photocatalysts were assessed from the N_2 adsorption-desorption isotherm utilizing a BELSORPminiII (MicrotracBE) instrument. The EIS and Mott-Schottky measurement of the photocatalysts was achieved on an electrochemical Versa STAT 3 workstation (Princeton Applied Research) equipped by a conventional three-electrode system. Here, uniform slurry of the sample by nafion solution was coated on a fluorine-doped tin oxide glass plate to make the working electrode, and an aqueous solution of Na_2SO_4 (0.5 mol L^{-1}) was utilized as the electrolyte. Pt wire and KCl-saturated AgCl/Ag were used as counter electrode and reference electrode, respectively.

3.2.5 Photocatalytic Degradation Experiment

The photocatalytic degradation of DCF by fabricated $ZnO/g-C_3N_4$ was investigated for 3 hours with the irradiation of visible light at room temperature. A 50 mL pyrex glass cell was utilized for the photocatalytic degradation experiment. At optimal condition, 30 mg of $ZnO/g-C_3N_4$ and 30 mL of aqueous solution of DCF (10 mg L^{-1}) were added to the glass cell and allowed for 30 minutes by magnetically stirring in the dark condition to establish adsorption-desorption equilibrium. Then, an LED lamp (OptoCode LDA14L-G/100W) with a UV (400 nm) cut-off filter (Y-44, HOYA) was placed on one side of the glass cell and used to expose the aqueous solution containing DCF and photocatalyst. Through the experiment, 1.5 mL of suspensions were collected at regular intervals of 30 minutes for analysis and centrifuged for 5 minutes at 10000 rpm to isolate the photocatalyst. Then, the supernate was analyzed for the determination of the DCF concentration. A high-performance liquid chromatograph assembled with a separation column ODS-2 (GL Science Inc.) and a SHIMADZU UV/Vis detector (UV 7750) was used to assess the quantity of DCF in the solution. The chromatogram was observed at wavelength of 274 nm. A mixture of acetonitrile and water (60:40, v/v) with 0.02 % (v/v) of formic acid was used as mobile phase at isocratic mode. The flow rate of the mobile phase was

1.0 mL min⁻¹. The degradation experiment of DCF by other photocatalyst was also investigated at analogous photocatalytic experimental conditions. Moreover, the photolysis of DCF was also inspected at similar conditions. For establishing the optimal photocatalytic degradation condition DCF by synthesized ZnO/g-C₃N₄, impact of variable operational conditions such as ZnO content in the composite (different ratio of used ZnO and g-C₃N₄), calcination condition of the fabrication of composite (different calcination temperature), types of ZnO and g-C₃N₄ in composite (sources of the precursors), dosage of catalyst (5 mg/30 mL to 50 mg/30 mL), and initial concentration of DCF (5 mg L⁻¹ to 50 mg L⁻¹) were also inspected. To study the role of reactive species of •OH, h⁺ and •O₂⁻ for photocatalytic degradation of DCF with ZnO/g-C₃N₄, scavenger tests were carried out in the same optimal condition utilizing IPA, EDTA and BQ as scavenger of the radical, respectively. The recyclability of the using of ZnO/g-C₃N₄ composite for photodegradation of DCF was inspected.

Moreover, the reaction rates as well as kinetics of the photocatalytic degradation procedure have been investigated accordingly the Langmuir–Hinshelwood (L–H) theory transformed by Turchi and Ollis. The theory was stated by eq. 3.1.

$$r_0 = -\frac{dC}{dt} = \frac{kKC}{1 + KC} \quad (3.1)$$

where r_0 , k , C , and K are the degradation rate, the rate constant, reactant concentration, and adsorption equilibrium constant of the reaction, respectively. The eq. 3.1 can be shortened to eq. 3.2 if the initial concentration C_0 is insignificant.

$$-\ln\left(\frac{C}{C_0}\right) = kKt = k_{obs}t \quad (3.2)$$

With regard to the $-\ln(C/C_0)$, the eq. 3.2 forms a linear expression on time t , where k_{obs} is the reaction rate constant. The k_{obs} in degradation reactions were determined by plotting $-\ln(C/C_0)$ versus time (t).

3.3 Results and Discussion

3.3.1 FTIR Analysis

The fabrication of the ZnO/g-C₃N₄ composite was investigated by FTIR spectroscopy. The FTIR spectra of g-C₃N₄ and ZnO/g-C₃N₄ are shown in Figure 3.2a. Pure g-C₃N₄ revealed peak at 1623 cm⁻¹ attributed to the C-N stretching vibration mode and a number of peaks from 1200 cm⁻¹ to 1600 cm⁻¹ assigned to aromatic C-N stretching. Furthermore, a peak was observed at 803 cm⁻¹ corresponding to the out-of-plane stretching vibrational mode of the C-N heterocycle of the triazine ring [56]. A wide band of a few peaks with small intensity in the FTIR spectrum of g-C₃N₄ was observed between 2950 cm⁻¹ and 3300 cm⁻¹ due to the O-H bond stretching vibration from the moisture or adsorbed water and deformed N-H stretching modes [57]. The FTIR spectra of the ZnO/g-C₃N₄ showed similar peaks, like those of g-C₃N₄. Moreover, the positions of a few peaks corresponding to different C-N stretching and bending in the FTIR spectra of the ZnO/g-C₃N₄ were slightly shifted to the higher wavenumber compared to relevant peaks in the FTIR spectra of the pure g-C₃N₄, which indicated the interaction between ZnO and g-C₃N₄ in the ZnO/g-C₃N₄ [58].

3.3.2 XRD Analysis

Figure 3.2b shows the XRD patterns of ZnO, g-C₃N₄, and ZnO/g-C₃N₄ composite. The diffraction peaks at 2θ values of 31.92, 34.64, 36.42, 47.68, 56.76, 63.14, 66.44, 67.98, 69.80, 72.92, and 77.28 were observed conforming to the plane of (100), (002), (101), (102), (110), (103), (200), (112), (201), (004), and (202), respectively, attributed to the structure of hexagonal wurtzite ZnO (JCPDS card no. 36-1451) [59,60]. In addition, it can be seen from the XRD pattern of g-C₃N₄ that two distinct peaks were observed at 2θ values of 12.98 and 27.88, assigning them to the planes of (100) and (002) corresponding to the repeating arrangement of the s-triazine unit and the conjugated aromatic system containing interplanar C-N stacking, respectively. The obtained XRD pattern shows that g-C₃N₄ is in its crystalline

phase and that no secondary phases or contaminants are present (JCPDS card no. 87-1526) [52,61]. As shown in the XRD pattern of the ZnO/g-C₃N₄, both the representative diffraction peaks of ZnO and g-C₃N₄ were detected, and no new extra peaks were noticed. Moreover, the position of the corresponding characteristic peaks of ZnO and g-C₃N₄ remains unchanged. This demonstrates that two-phase compositions of g-C₃N₄ and ZnO were present in the prepared ZnO/g-C₃N₄, and there were no effects on the lattice structure of g-C₃N₄ and ZnO [62].

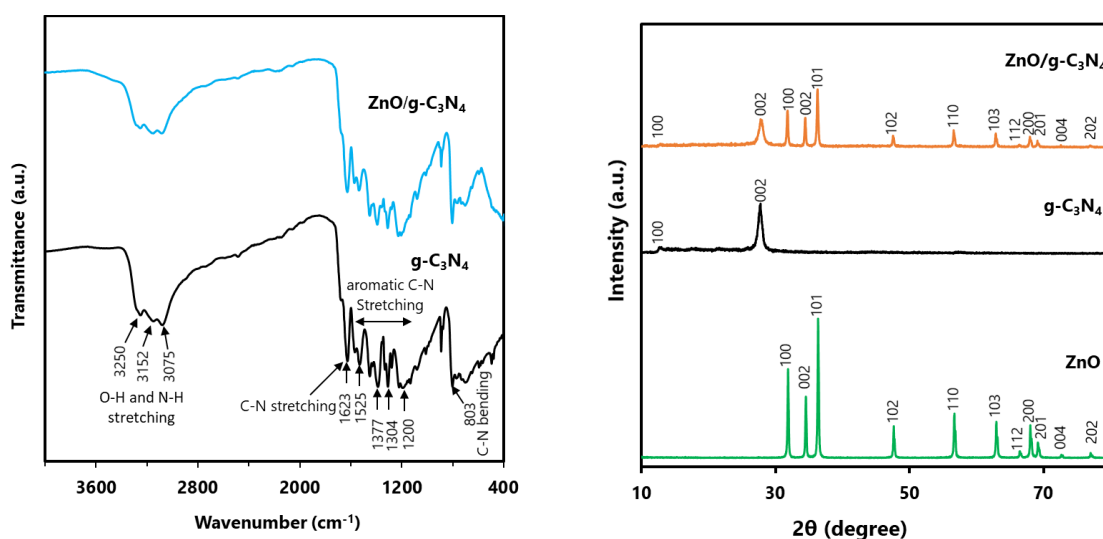


Figure 3.2 (a) FTIR spectra of g-C₃N₄ and ZnO/g-C₃N₄, and (b) XRD patterns of ZnO, g-C₃N₄ and ZnO/g-C₃N₄.

3.3.3 XPS Analysis

Using the X-ray photoelectron spectroscopy (XPS) survey spectrum, the surface elemental composition and their oxidation states of the g-C₃N₄ and ZnO/g-C₃N₄ composite were studied. As shown in Figure 3.3a, the fundamental-level binding energy peaks of C and N were clearly visible in both spectra. Moreover, for the spectra of ZnO/g-C₃N₄, characteristic peaks that corresponded to the binding energy values of Zn and O were appeared. The results suggested the formation and purity of the ZnO/g-C₃N₄ composite [32]. As shown in Figure 3.3b, the high-resolution C 1s XPS spectra of ZnO/g-C₃N₄ can be deconvoluted into four peaks at 284.8, 286.0, 288.4, and 289.5 eV, which are ascribed to the C=C or C-C bond, sp³ C-N bond, s-triazine ring

containing N=C-N groups, and C-O groups carried by the inevitable oxidation of the sample, respectively [63]. As shown in Figure 3.3c, the high-resolution N 1s XPS spectra of ZnO/g-C₃N₄ was fitted by three peaks at 399.0, 400.8, and 404.9 eV. The major peak at 399.0 eV was ascribed to the sp² hybridized N atoms (C-N=C) contained in the s-triazine ring. The peak at 400.8 eV is attributed to the [N-(C)₃] containing bridging N atoms and (C-NH₂) containing terminal amino groups, and the peak at 404.9 eV belonged to the charging effect in triazine [52,64]. The relative peak intensity of the C 1s and N 1s XPS spectra corresponding to the N=C-N group decreased in ZnO/g-C₃N₄ compared to g-C₃N₄. These findings indicated that the ZnO doping partially broke the g-C₃N₄ containing aromatic ring structure [63]. In addition, the pathway of charge carrier movement in the composite photocatalyst may be predicted using the measurement of binding energy shift [65,66]. Hence, it could be inspected that the major peaks of high-resolution C 1s and N 1s of ZnO/g-C₃N₄ were shifted toward higher binding energies compared to g-C₃N₄. The result indicated that the electrons are transferred from g-C₃N₄ to ZnO, which reveals significant support for the electron transfer mechanism of the ZnO/g-C₃N₄ heterojunction [67,68]. As shown in Figure 3.3d, the high-resolution O 1s XPS spectra of ZnO/g-C₃N₄ was deconvoluted into three peaks. The main peak at 531.8 eV is associated with the O₂²⁻ in the wurtzite structure of ZnO [69]. The other two small peaks at 529.6 and 533.6 eV may be ascribed to the -OH groups in the adsorbed H₂O or -OH groups on the ZnO/g-C₃N₄ surface. On the contrary, the high-resolution O 1s XPS spectra of g-C₃N₄ exhibited only one peak with small intensity, which is attributed to the -OH groups in the adsorbed H₂O or -OH groups on the g-C₃N₄ surface [70]. In Figure 3.3e, the high-resolution Zn 2p XPS spectra of ZnO/g-C₃N₄ revealed two peaks at 1022.4 and 1045.5 eV corresponding to the binding energies of Zn 2p_{3/2} and Zn 2p_{1/2}, and the peaks are separated by 23.1 eV. The observations are in good agreement with the reported binding energy of the high-resolution Zn 2p XPS spectra of the ZnO/g-C₃N₄ composite [71,72]. Moreover, as shown in the survey

spectrum of the ZnO/g- C_3N_4 , the Auger peaks of Zn LMM were detected, which indicate the existence of Zn-N bonds [52].

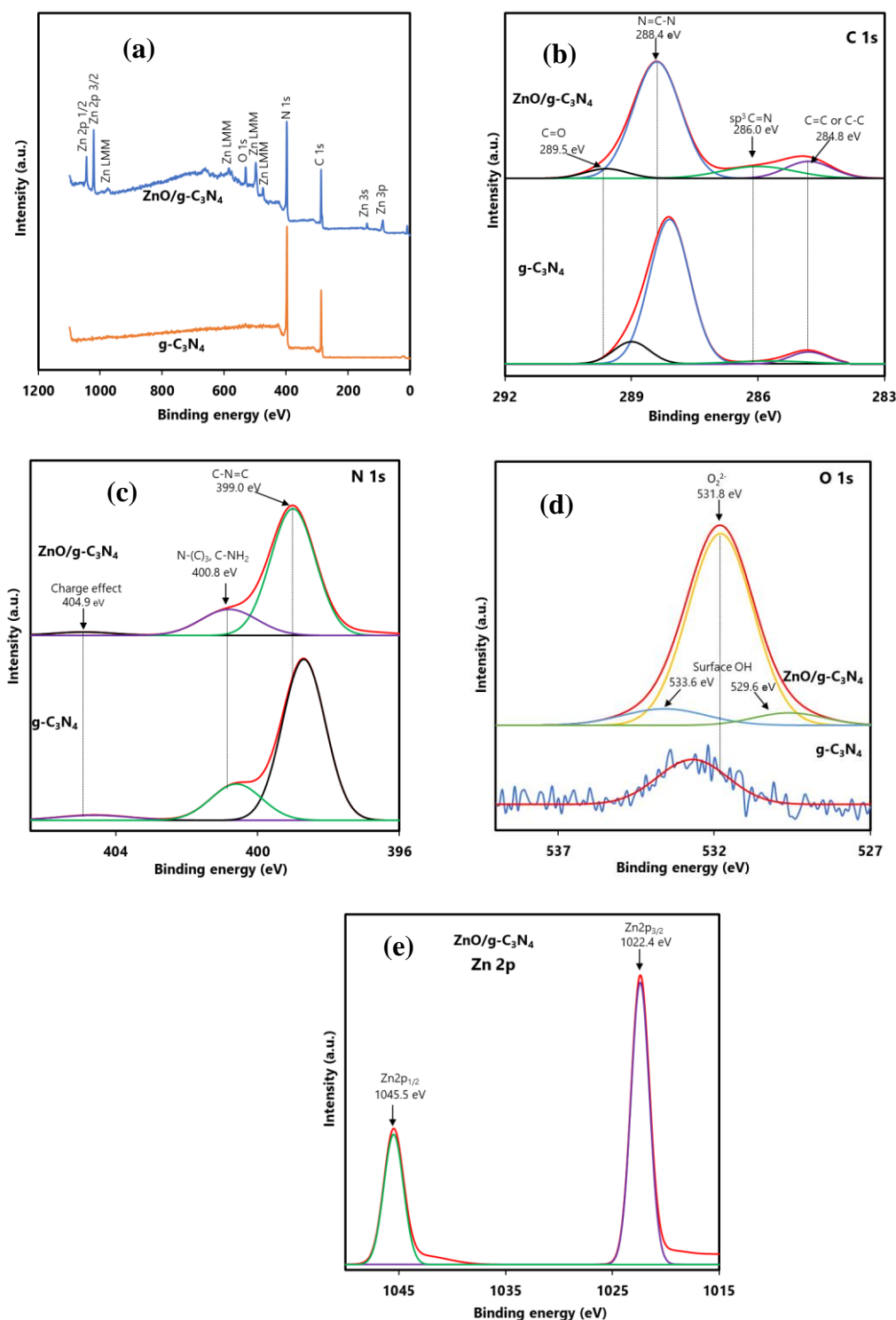


Figure 3.3 (a) Survey XPS spectra of g- C_3N_4 and ZnO/g- C_3N_4 ; overlap high resolution XPS (b) C 1s, (c) N 1s and (d) O 1s spectra of g- C_3N_4 and ZnO/g- C_3N_4 and (e) High resolution XPS Zn 2p spectra of ZnO/g- C_3N_4 .

3.3.4 DRS Analysis

The optical characteristics of photocatalysts have an influence on their photocatalytic ability. Thus, UV-Vis DRS of the g-C₃N₄, ZnO, and ZnO/g-C₃N₄ composite were analyzed at room temperature in order to inspect their light absorption abilities. The UV-Vis DRS data as expressed by the Kubelka-Munk function of the samples are shown in Figure 3.4a. The ZnO nanoparticles can only absorb UV light, with an absorption edge at around 390 nm [46]. The prepared g-C₃N₄ has an absorption edge at about 430 nm, including the visible region [73]. A slightly red-shifted absorption edge of the ZnO/g-C₃N₄ was observed compared to both g-C₃N₄ and ZnO. The small amount of N atoms in the s-triazine rings may be replaced by the O in the ZnO, which slightly influenced the electron distribution and increased the visible light absorption ability to a small extent [46,53,70]. The optical band gap of g-C₃N₄ and ZnO/g-C₃N₄ was determined by using the Tauc equation of indirect transition [74].

$$\alpha h\nu = A(h\nu - E_g)^2 \quad (3.3)$$

Furthermore, the optical band gap of ZnO was determined by using the Tauc equation of direct transition [74].

$$\alpha h\nu = A(h\nu - E_g)^{1/2} \quad (3.4)$$

where α is the absorption coefficient, $h\nu$ is the photoenergy, A is a constant, and E_g is the optical band gap. Hence, by plotting the value of $(\alpha h\nu)^{1/2}$ versus $h\nu$, the optical band gap of g-C₃N₄ and ZnO/g-C₃N₄ was determined, and by plotting the value of $(\alpha h\nu)^2$ versus $h\nu$, the optical band gap of ZnO was determined (Figure 3.4b). The optical band gaps of g-C₃N₄, ZnO, and ZnO/g-C₃N₄ are estimated to be 2.93, 3.20, and 2.81 eV, respectively.

3.3.5 PL Analysis

The decrease in electron hole-pair recombination rate of photocatalysts has an influence on their photocatalytic activity. In order to investigate the relative electron hole-pair

recombination rate of g-C₃N₄, ZnO, and ZnO/g-C₃N₄, PL analysis was carried out at an excitation wavelength of 340 nm. It was observed that the PL intensity of the composite decreased by a substantial amount compared to that of both g-C₃N₄ and ZnO (Figure 3.4c). The PL quenching specifies that the electron-hole pair recombination rate was suppressed and photogenerated charge separation was facilitated due to the synergic effect of ZnO and g-C₃N₄ in the composite [53]. Hence, the decrease in electron hole-pair recombination rate indicated the enhanced photocatalytic activity of the prepared ZnO/g-C₃N₄ composite.

3.3.6 EIS Analysis

A lower charge transfer resistance of a photocatalyst denotes its better photocatalytic efficiency. In order to analyze the relative charge transfer resistance of g-C₃N₄ and ZnO/g-C₃N₄, EIS analysis was carried out. The charge transfer resistance is denoted by the curvature radius of the EIS graph. The reduction of resistance as well as the increment of charge transfer were indicated by the smaller curvature radius. As shown in Figure 3.4d, the EIS resultant Nyquist plot of ZnO/g-C₃N₄ showed a smaller curvature radius compared to the curvature radius of g-C₃N₄, which indicated the greater charge transfer separation of the ZnO/g-C₃N₄ compared to that of bare g-C₃N₄.

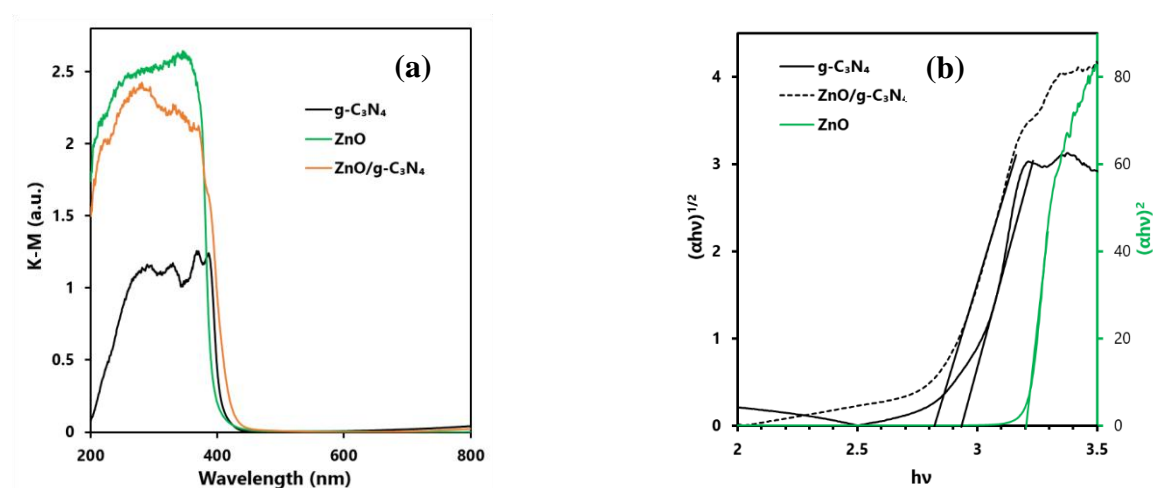


Figure 3.4 (a) Kubelka-Munk function of UV-Vis DRS, (b) Tauc plot of ZnO, g-C₃N₄, ZnO/g-C₃N₄.

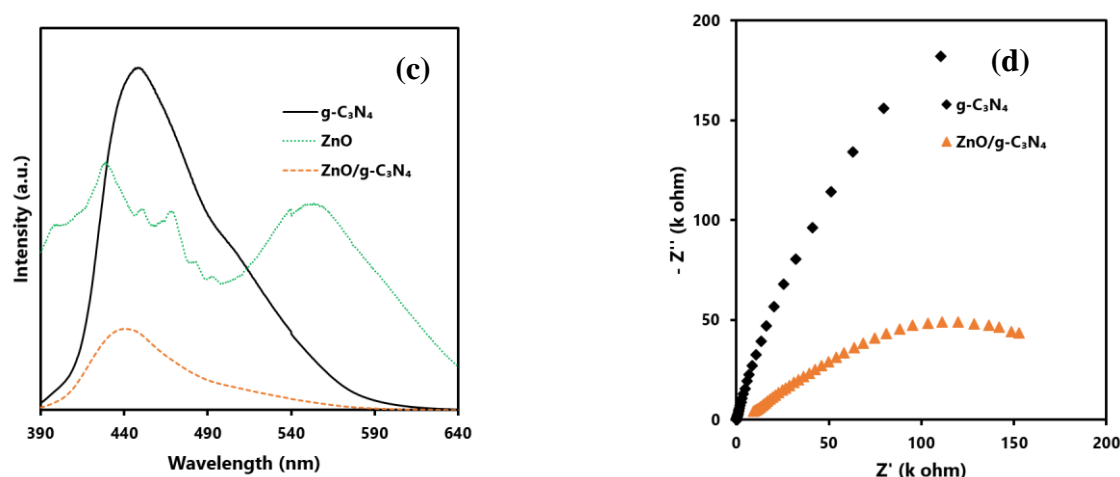


Figure 3.4 (c) PL spectra (upon the excitation at 340 nm wavelength) of ZnO, g-C₃N₄, ZnO/g-C₃N₄, and (d) EIS resultant Nyquist plot of g-C₃N₄ and ZnO/g-C₃N₄.

3.3.7 Morphological Study

The morphologies of g-C₃N₄, ZnO, and ZnO/g-C₃N₄ were explored using SEM and TEM analysis (Figure 3.5). The SEM and TEM images of g-C₃N₄ show a sheet-like layered morphology of the particles (Figure 3.5a,d). As shown in Figure 3.5b,e the semispherical particles of different sizes are observed in the SEM and TEM images of ZnO. The SEM and TEM images of the ZnO/g-C₃N₄ composites show that particles with different sizes and shapes corresponding to ZnO are well attached to the surface of sheet like layered g-C₃N₄ (Figure 3.5c,f). Hence, ZnO could be inserted and distributed to the surface of g-C₃N₄ after the thermal treatment [30,32]. Thus, the fabricated binary nanocomposite materials are expected to play a vital role in visible light-driven photocatalytic applications.

The elemental mapping of the ZnO/g-C₃N₄ was investigated by EDS analysis. From Figure 3.6, it can be clearly seen that C, N, O, and Zn are dispersed on the surface of the composite. Furthermore, the ratio of relative color intensities for all elements is similar over all surfaces in Figure 3.6b-e, which indicates that the elements are homogeneously distributed. Hence, the morphological analysis confirms the formation and purity of the composite.

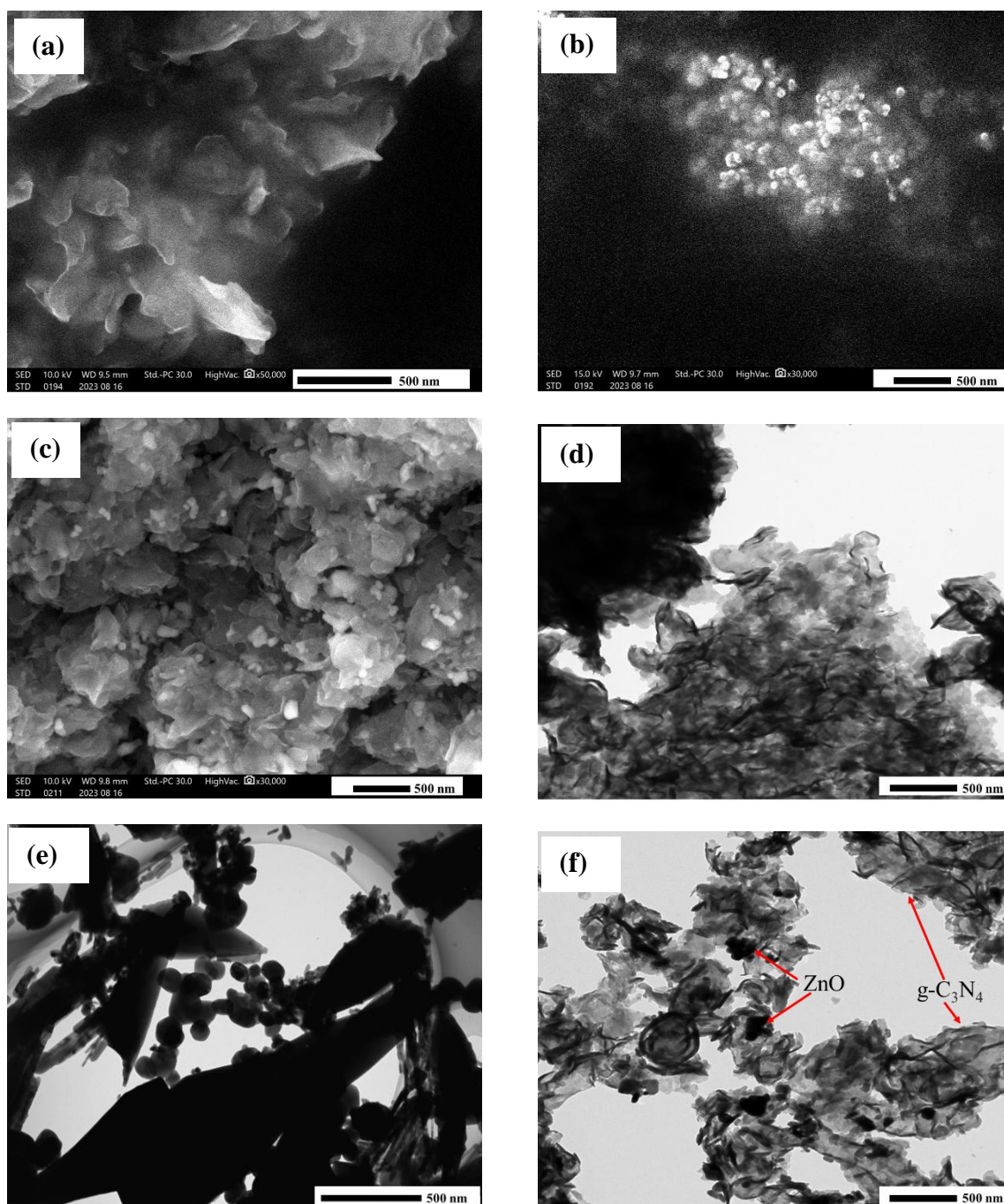


Figure 3.5 SEM images of (a) g-C₃N₄, (b) ZnO, and (c) ZnO/g-C₃N₄ and TEM images of (d) g-C₃N₄, (e) ZnO, and (f) ZnO/g-C₃N₄.

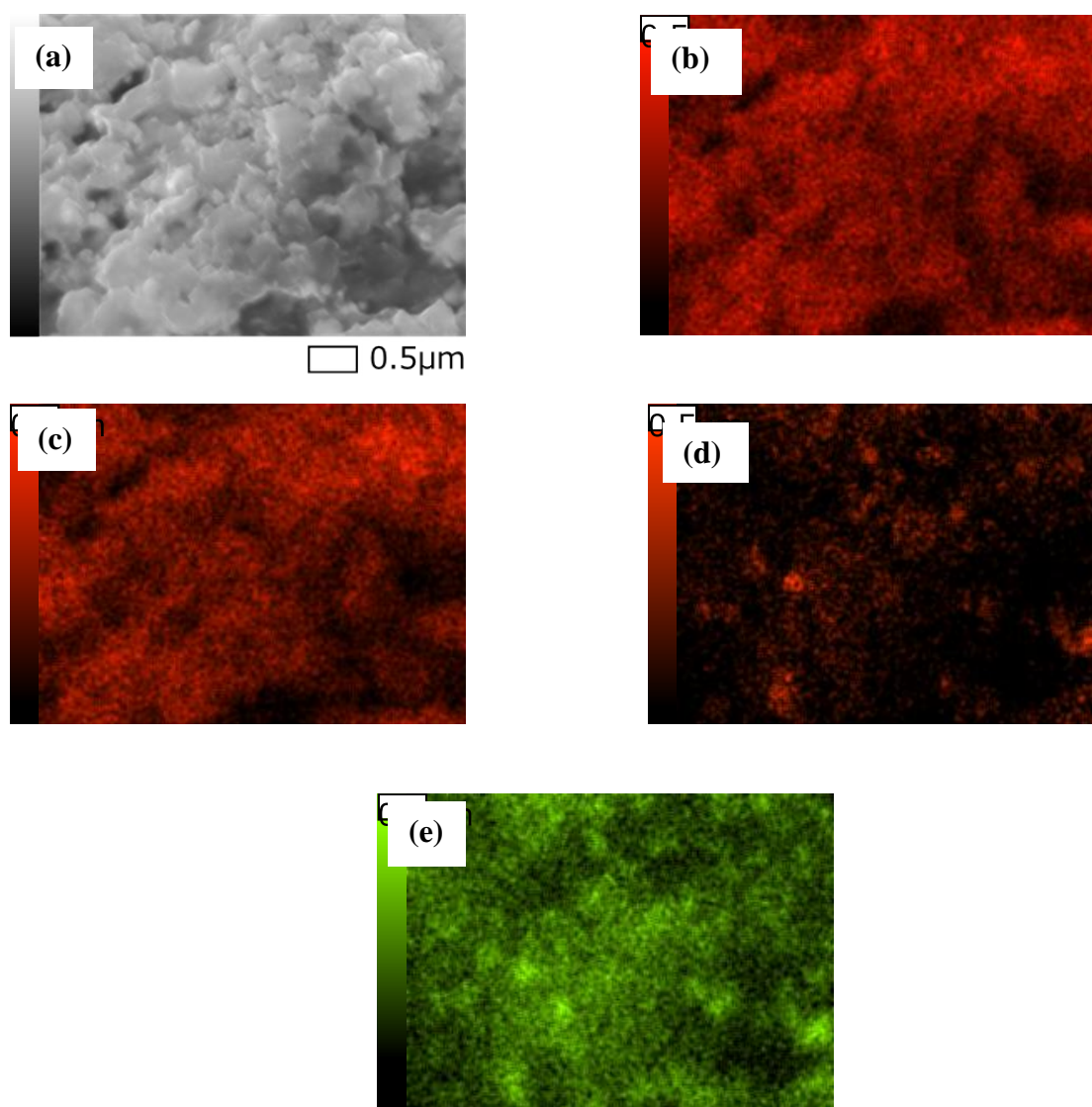


Figure 3.6 (a) SEM and EDS elemental mapping of (b) C, (c) N, (d) O and (e) Zn of ZnO/g-C₃N₄.

3.3.8 BET Surface Area and Pore Size Distribution Analysis

In order to determine the surface area and porous structure characteristics of the composite, measurements of N₂ adsorption-desorption isotherms and pore-size distributions of bare g-C₃N₄ and ZnO/g-C₃N₄ composite were carried out. As shown in Figure 3.7, both g-C₃N₄ and ZnO/g-C₃N₄ displayed typical type IV adsorption-desorption isotherm with H3 hysteresis loops. These indicated the existence of mesoporous material in the structure of g-C₃N₄ and ZnO/g-C₃N₄ [75]. The specific surface areas, total pore volumes, and average pore sizes of the g-C₃N₄

and ZnO/g-C₃N₄ are given in Table 3.1. It was observed that these values did not change significantly after the formation of the composite. The specific surface areas, total pore volumes, and average pore size values of the ZnO/g-C₃N₄ are slightly smaller than those of the g-C₃N₄. Hence, the changes may not contribute to the enhanced photocatalytic efficiency of the composite.

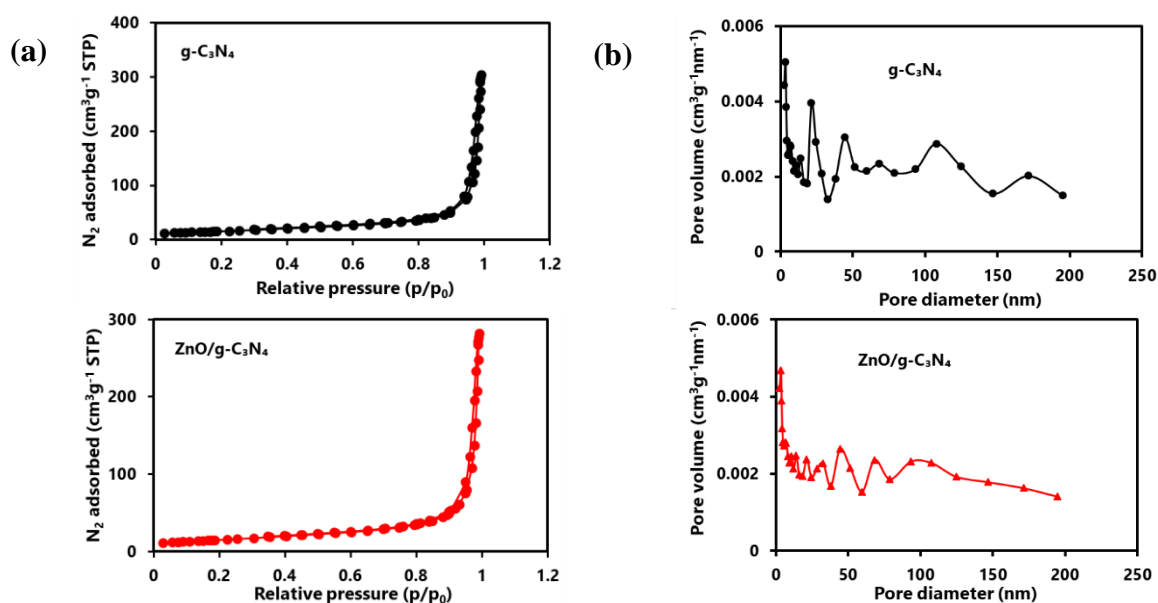


Figure 3.7 (a) N₂ adsorption-desorption isotherms, (b) pore size distribution curves of g-C₃N₄ and ZnO/g-C₃N₄.

Table 3.1 Surface area, pore volume, and pore diameter of the g-C₃N₄ and ZnO/g-C₃N₄

Photocatalyst	BET surface area (m ² /g)	Total pore volume (cm ³ /g)	Average pore diameter (nm)
C ₃ N ₄	55.67	0.44	31.88
ZnO/g-C ₃ N ₄	53.67	0.40	30.32

3.3.9 Mott–Schottky Plot and Valence Band (VB)-XPS Analysis

In order to determine the flat-band potential (E_{FB}) as well as the conduction band potential (E_{CB}) of the ZnO/g-C₃N₄ composite, a Mott-Schottky plot has been constructed. As shown in Figure 3.8a, the positive slope of the plot indicates the composite is an n-type semiconductor, and the major charge carriers in the composite are electrons. The E_{FB} value of ZnO/g-C₃N₄ was determined with respect to the abscissa axis and intercept among the tangent lines of the plot. The E_{FB} value was estimated at -1.09 V (vs. Ag/AgCl at pH 0), which can be converted to -0.48 V (vs. normal hydrogen scale electrode (NHE) at pH 0) using the eq. 3.5 [67].

$$E (NHE \text{ at } pH \ 0) = E (Ag/AgCl \text{ at } pH \ 7) + 0.196 + 0.059 \times 7 \quad (3.5)$$

According to the previous literature report, the position of the E_{CB} exist by is 0.1 eV upper than that of the E_{FB} [76]. Hence, the E_{CB} of the composite was estimated at -0.58 V (vs. NHE at pH 0). The E_{VB} of the composite can be determined using the eq. 3.6.

$$E_g = E_{VB} - E_{CB} \quad (3.6)$$

where the band gap of the composite (E_g) is 2.81 eV, which was determined by the Tauc plot as shown in Figure 3.4b. Thus, the calculated E_{VB} of the composite was 2.23 V (vs. NHE at pH 0).

Moreover, the E_{VB} of the composite was calculated using the VB-XPS analysis. As shown in Figure 3.8b, the VB edge of the ZnO/g-C₃N₄ was observed at about 1.93 eV. Hence, the VB position of the ZnO/g-C₃N₄ was corrected to the NHE scale using the following equation [77].

$$E_{NHE} / V = \Phi_{WF} + \Phi_{sample} - 4.44 \quad (3.7)$$

where E_{NHE} is the E_{VB} of the composite at the NHE scale at pH 7.0, Φ_{WF} is the electron work function of the analyzer (4.33 eV), and Φ_{sample} is the VB edge of the ZnO/g-C₃N₄ (eV) in VB-XPS analysis. Hence, the corrected E_{VB} of ZnO/g-C₃N₄ is 1.82 V (vs. NHE scale at pH 7.0). By addition of 0.413 V, the obtained E_{VB} of ZnO/g-C₃N₄ is corrected to be 2.23 V (vs. NHE

scale at pH 0). Hence, the result of VB-XPS is consistent with the result attained from the Mott-Schottky plot.

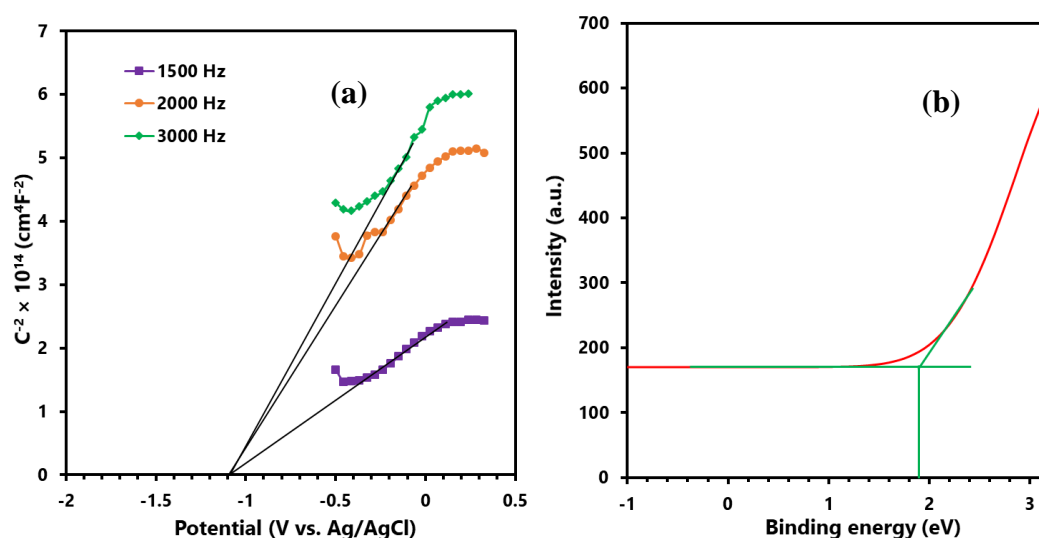


Figure 3.8 (a) Mott-Schottky and (b) VB-XPS plot of ZnO/g-C₃N₄ composite.

3.3.10 Photocatalytic Degradation of DCF

Figure 3.9 shows the photocatalytic degradation of DCF using ZnO/g-C₃N₄ composite and other corresponding catalysts at optimal condition. The photolysis reaction of DCF was also investigated. It was observed that the DCF was not degraded in the photolysis reaction, and g-C₃N₄ and ZnO showed negligible photocatalytic activity to degrade the DCF with visible light irradiation, while the physical mixture of the ZnO and g-C₃N₄ at 1:3 ratio showed moderate photocatalytic activity. Moreover, the ZnO/g-C₃N₄ exhibited excellent photocatalytic degradation ability for DCF. From Figure 3.9b, it was observed that the degradation processes followed the pseudo first order reaction kinetics equation (eq. 3.2). It was observed that the rate constant of visible light-driven DCF degradation using the ZnO/g-C₃N₄ was 0.0541 min⁻¹, which was about 34 and 27 times higher than that attained with bare commercial ZnO and prepared g-C₃N₄, respectively, and 11 times higher than that attained with the physical mixture of ZnO and g-C₃N₄ (Table 3.2). The decrease in electron hole-pair recombination rate and the increment in charge transfer separation were responsible for the enhancement of the

photocatalytic ability of the ZnO/g-C₃N₄ composite. The enhanced visible light response capacity with small amounts of the ZnO/g-C₃N₄ composite also affected its efficient photocatalytic capacity. However, textural properties such as specific surface areas, total pore volumes, and average pore size of the photocatalysts in this study did not control their photocatalytic efficacy.

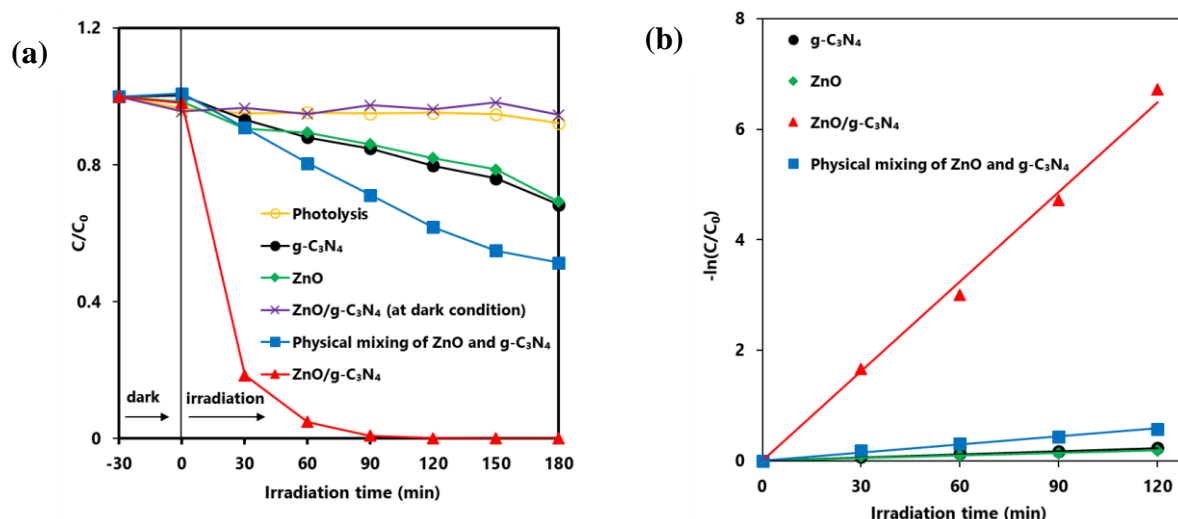


Figure 3.9 (a) Photocatalytic degradation of DCF using different catalyst with the irradiation of visible light and (b) the plot of $-\ln(C/C_0)$ versus irradiation time; DCF: 10 mg L⁻¹ (30 mL), photocatalyst: 30 mg.

Table 3.2 Kinetic parameters for photocatalytic degradation of DCF

Photocatalyst	Rate constant (min ⁻¹)	T _{1/2} (min)	R ²
ZnO	0.0016	433.1	0.92
g-C ₃ N ₄	0.0020	346.5	0.98
Physical mixing of ZnO and g-C ₃ N ₄	0.0049	141.4	0.99
ZnO/g-C ₃ N ₄	0.0541	12.8	0.99

3.3.11 Effect of ZnO Content

In order to determine the optimal mixing ratio of g-C₃N₄ and ZnO for fabricating the ZnO/g-C₃N₄ composite at photocatalytic degradation of DCF, the mixing ratio of g-C₃N₄ and

ZnO was changed such that the total quantity was 200 mg. From Figure 3.10 and Table 3.3, it was found that the maximum degradation of DCF was observed using the composite fabricated from 1:3 ratio of ZnO and g-C₃N₄. The photocatalytic degradation of DCF was improved with increasing amounts of g-C₃N₄ until the mentioned ratio, then decreased with further increasing g-C₃N₄ amounts. The synergistic effect of ZnO and g-C₃N₄ at this ratio could be responsible for improved photocatalytic degradation ability [71].

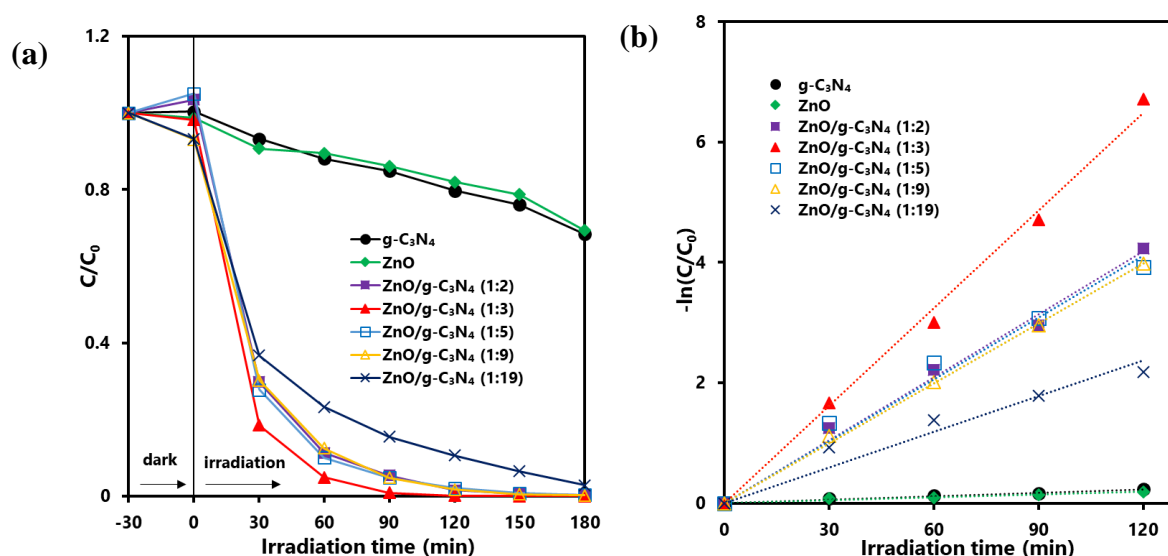


Figure 3.10 (a) Effect of ZnO content in the composite on the photocatalytic degradation of DCF using ZnO/g-C₃N₄, and (b) the plot of $-\ln(C/C_0)$ versus irradiation time; DCF: 10 mg L⁻¹ (30 mL), photocatalyst: 30 mg.

Table 3.3 Effect of ZnO content in the ZnO/g-C₃N₄ composite on kinetic parameters for photocatalytic degradation of DCF using ZnO/g-C₃N₄

Mixing ratio		Rate constant (min ⁻¹)	T _{1/2} (min)	R ²
ZnO	g-C ₃ N ₄			
1	2	0.0349	19.9	0.99
1	3	0.0541	12.8	0.99
1	5	0.0344	20.2	0.98
1	9	0.0320	21.7	1
1	19	0.0198	35.0	0.93

3.3.12 Effect of Calcination Temperature

To understand the role of calcination temperature during the fabrication of the ZnO/g-C₃N₄ composite on the photocatalytic degradation of DCF, composites were prepared at different calcination temperatures, such as 350 °C, 400 °C, and 450 °C. The composite was also prepared without calcination. In every case, the other conditions for fabricating composites were the same. As shown in Figure 3.11 and Table 3.4, it can be observed that the composite formed at 400 °C showed maximum photocatalytic activity compared to others. The composite formed without calcination could not show significant photocatalytic activity. The ZnO nanoparticles may be covered perfectly by g-C₃N₄, due to the lower degree of thermal polymerization of g-C₃N₄ framework at 400 °C. The synergistic effect of ZnO and g-C₃N₄ at 400 °C as calcination temperature are attributed to the electron transfer from g-C₃N₄ to ZnO could be responsible for enhanced photocatalytic degradation efficiency. Thus, temperature plays an effective role in the formation of optimal composite. It means that the mixture of ZnO and g-C₃N₄ in a 1:3 ratio was calcined at 400 °C, which was the optimal condition for the composite fabrication.

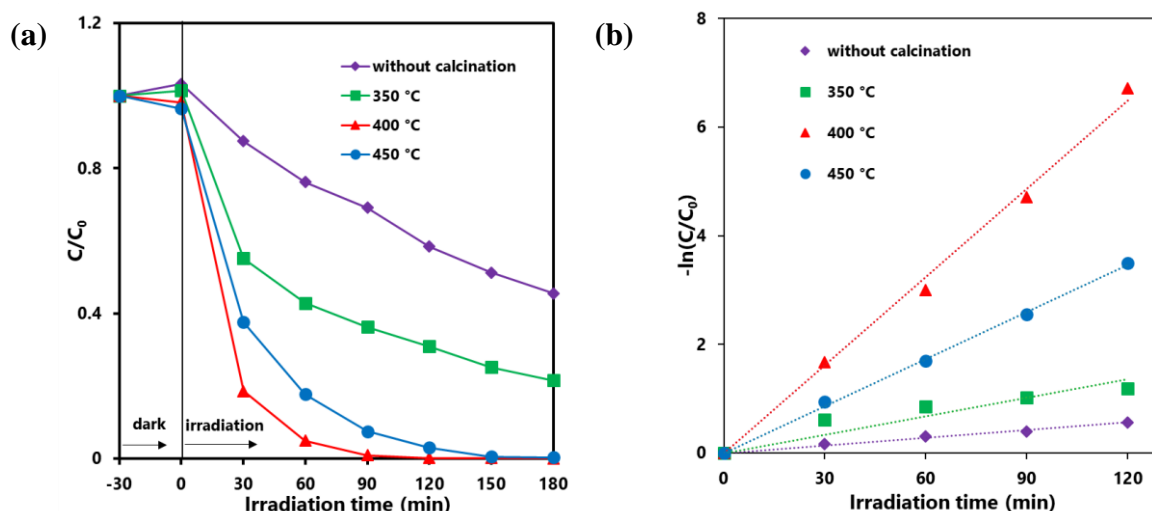


Figure 3.11 (a) Effect of calcination temperature of the composite fabrication on the photocatalytic degradation of DCF using ZnO/g-C₃N₄, and (b) the plot of $-\ln(C/C_0)$ versus irradiation time; DCF: 10 mg L⁻¹ (30 mL), photocatalyst: 30 mg.

Table 3.4 Effect of calcination temperature in the preparation of ZnO/g-C₃N₄ composite on kinetic parameters for photocatalytic degradation of DCF using ZnO/g-C₃N₄

Calcination Temperature	Rate constant (min ⁻¹)	T _{1/2} (min)	R ²
Without calcination	0.0047	147	0.99
350 °C	0.0113	61.3	0.85
400 °C	0.0541	12.8	0.99
450 °C	0.0289	24.0	1

3.3.13 Effect of Types of ZnO and g-C₃N₄

In order to investigate the effect of types of ZnO and g-C₃N₄ in the preparation of the composite on the photocatalytic degradation of DCF, commercially available ZnO was obtained from Sigma-Aldrich and Wako Chemicals, and two sets of ZnO were also prepared by calcination of zinc acetate and zinc nitrate at 550 °C for 2 hours. Moreover, two sets of g-

C_3N_4 were prepared by calcination of urea and melamine at 550 °C for 2 hours. After that, eight sets of composites were prepared according to the procedure mentioned in the experimental section. It was observed that the composite of commercially obtained ZnO from Sigma-Aldrich and prepared $g-C_3N_4$ from calcination of urea showed superior photocatalytic DCF degradation ability compared to other composites (Figure 3.12 and Table 3.5).

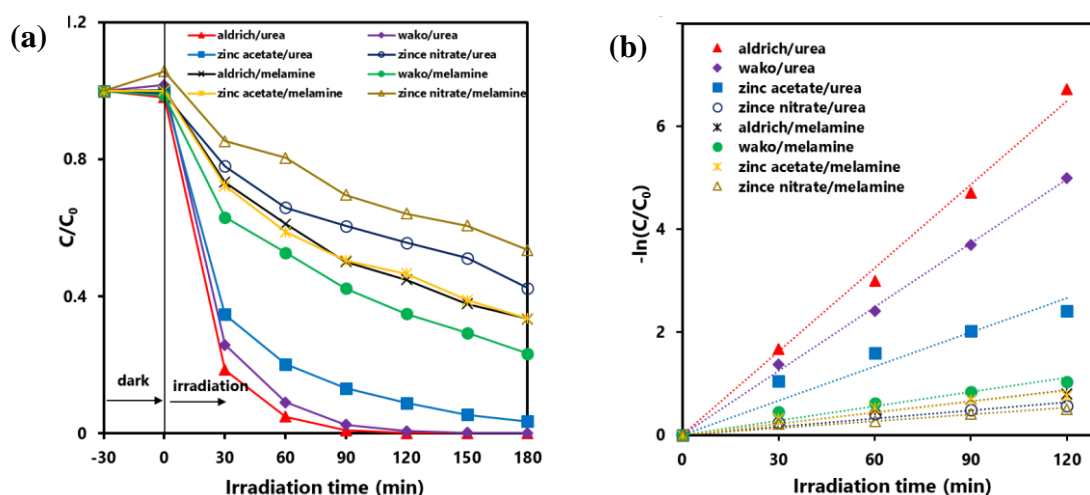


Figure 3.12 (a) Effect of types of ZnO and $g-C_3N_4$ in the ZnO/ $g-C_3N_4$ composite on the photocatalytic degradation of DCF using ZnO/ $g-C_3N_4$, and (b) the plot of $-\ln(C/C_0)$ versus irradiation time; DCF: 10 mg L⁻¹ (30 mL), photocatalyst: 30 mg.

Table 3.5 Effect of types of ZnO and g-C₃N₄ in the ZnO/g-C₃N₄ composite on kinetic parameters for photocatalytic degradation of DCF using ZnO/g-C₃N₄

Source		Rate constant (min ⁻¹)	T _{1/2} (min)	R ²
ZnO (manufacturer/precursor)	g-C ₃ N ₄ (precursor)			
aldrich	urea	0.0541	12.8	0.99
wako	urea	0.0414	16.7	1
zinc acetate	urea	0.0222	31.2	0.92
zince nitrate	urea	0.0054	128	0.91
aldrich	melamine	0.0073	94.9	0.95
wako	melamine	0.0093	74.5	0.94
zinc acetate	melamine	0.0072	96.3	0.91
zince nitrate	melamine	0.0045	154	0.95

3.3.14 Effect of Catalyst Dosage

In order to optimize the photocatalyst dosage for the degradation of DCF, the amount of ZnO/g-C₃N₄ composite was varied from 5 mg/30 mL to 50 mg/30 mL. It was observed that the degradation of DCF improved with rising the quantity of ZnO/g-C₃N₄ composite (Figure 3.13 and Table 3.6). The number of active sites could increase with an increasing amount of photocatalyst. But the increasing rate of degradation was slower, if the photocatalyst amount exceeded 30 mg/30 mL. An excess amount of ZnO/g-C₃N₄ may turbidize the reaction solution, hinder light penetration, saturate the number of active sites, and impact the increasing rate of degradation [54,78]. Hence, considering the degradation rate relative to the catalyst dosage and

to minimize the use of excess amounts of photocatalyst, 30 mg/30 mL of ZnO/g-C₃N₄ has been selected as the optimal amount of photocatalyst for further study.

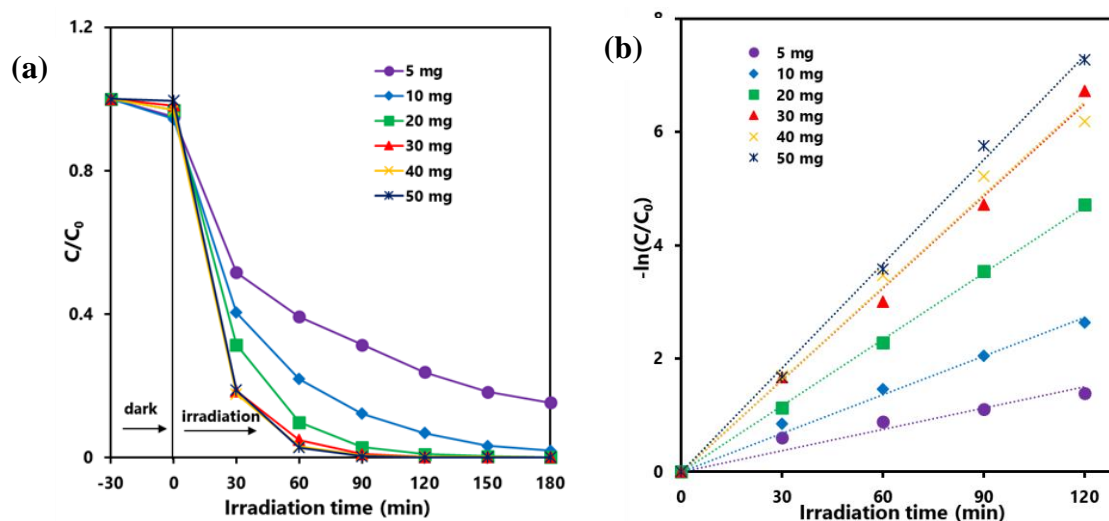


Figure 3.13 (a) Effect of catalyst dosage on the photocatalytic degradation of DCF using ZnO/g-C₃N₄, and (b) the plot of $-\ln(C/C_0)$ versus irradiation time; DCF: 10 mg L⁻¹ (30 mL).

Table 3.6 Effect of catalyst dosage on kinetic parameters for photocatalytic degradation of DCF using ZnO/g-C₃N₄

Amount of ZnO/g-C ₃ N ₄ composite (mg) in 30 mL solution	Rate constant (min ⁻¹)	T _{1/2} (min)	R ²
5	0.0125	55.4	0.92
10	0.0227	30.5	0.99
20	0.0391	17.7	1
30	0.0541	12.8	0.99
40	0.0545	12.7	0.99
50	0.0613	11.3	0.99

3.3.15 Effect of Initial Concentration of DCF

In order to inspect the effect of the initial concentration of DCF, the photocatalytic degradation of DCF using 30 mg/30 mL ZnO/g-C₃N₄ composite has been studied, with the initial concentration of DCF varying from 5 mg L⁻¹ to 50 mg L⁻¹. It was observed that the degradation rate of DCF decreased with increasing concentrations. Increasing the quantity of molecules attached to a fixed amount of the catalyst surface may prevent light absorption, and the probability of the creation of reactive species such as •OH and •O₂⁻ would decrease on the surface of the catalyst. Thus, the photocatalytic degradation rate was decreased [58]. Furthermore, as shown in Figure 3.14 and Table 3.7, the degraded amount of DCF increased with increasing initial concentrations of DCF. Eventually, the degradation rate decreased and the degraded amount increased with increasing initial concentrations of DCF. Since very low concentrations and very high concentrations of DCF were insignificant for the practical application, 10 mg L⁻¹ of DCF was selected as the initial concentration for the further experiment in this work.

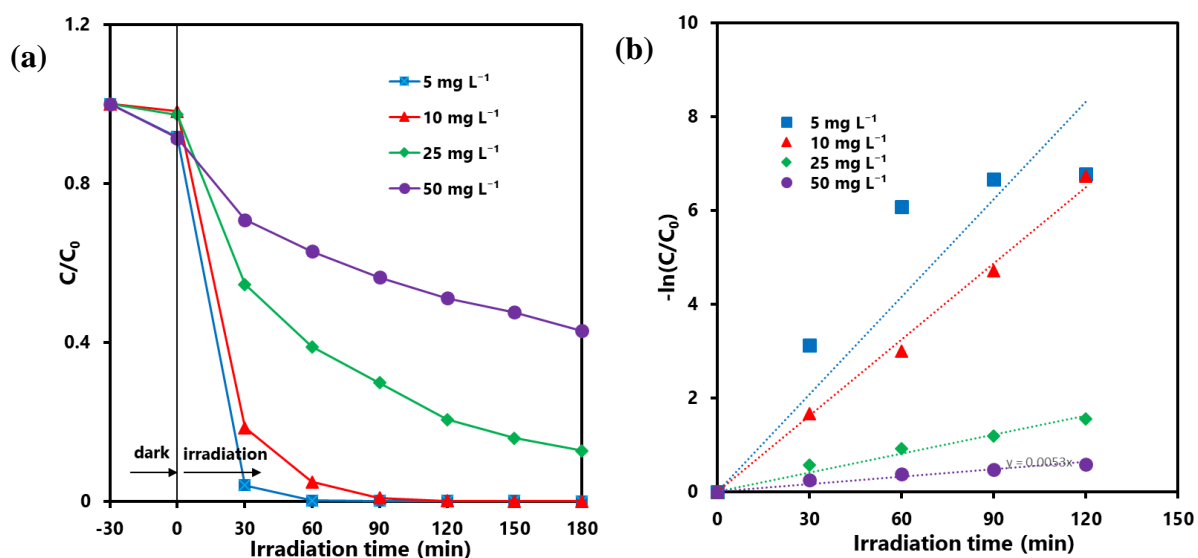


Figure 3.14 (a) Effect of initial concentration of DCF on the photocatalytic degradation of DCF using ZnO/g-C₃N₄, (b) the corresponding plot of $-\ln(C/C_0)$ versus irradiation time

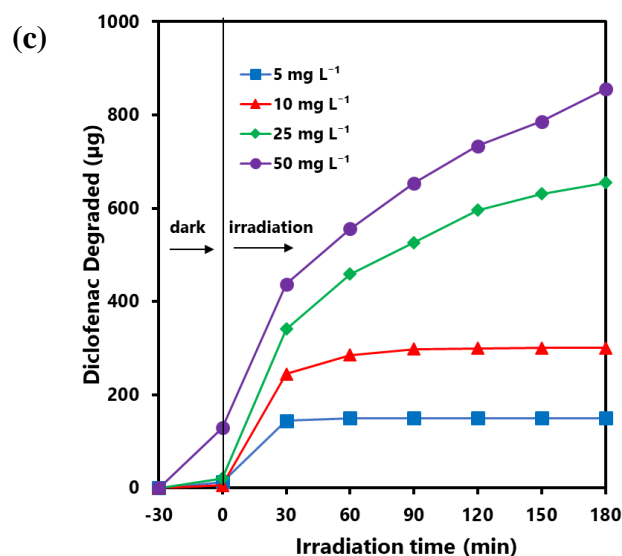


Figure 3.14 (c) Effect of initial concentration of DCF on degraded amount of DCF using ZnO/g-C₃N₄ composite; DCF: 30 mL, ZnO/g-C₃N₄: 30 mg.

Table 3.7 Effect of initial concentration of DCF on kinetic parameters for photocatalytic degradation of DCF using ZnO/g-C₃N₄

Initial concentration of DCF (mgL ⁻¹)	Rate constant (min ⁻¹)	T _{1/2} (min)	R ²
5	0.0693	10.0	0.79
10	0.0541	12.8	0.99
25	0.0135	51.3	0.97
50	0.0053	131	0.93

3.3.16 Scavenger Role

It has been demonstrated that the photodegradation of organic pollutants involves several promising reactive species, including $\bullet\text{O}_2^-$, $\bullet\text{OH}$, and h^+ . It was reported that BQ, IPA, and EDTA can function as efficient scavengers for $\bullet\text{O}_2^-$, $\bullet\text{OH}$, and h^+ , respectively [32]. Hence, in order to fully comprehend the visible light-induced photocatalytic degradation mechanism of

DCF by ZnO/g-C₃N₄ composite, a series of radical scavenger experiments were carried out by using BQ, IPA, and EDTA as the scavengers of $\bullet\text{O}_2^-$, $\bullet\text{OH}$, and h^+ , respectively. The obtained results are displayed in Figure 3.15 and Table 3.8. It can be seen that the photocatalytic degradation of DCF was almost inert in the presence of BQ, and the rate of degradation reaction was more than one thousand times slower than the rate without using any scavenger. On the other hand, IPA impacted the decrement of photocatalytic degradation of DCF significantly, and the degradation rate was about five times slower than the rate without using any scavenger. The results indicated that the $\bullet\text{O}_2^-$ plays a major reactive species in the photocatalytic degradation of DCF using fabricated ZnO/g-C₃N₄, while the $\bullet\text{OH}$ radical plays an important role. The EDTA also impacted the photocatalytic degradation of DCF slightly. Hence, the photogenerated h^+ may take part as a minor active radical on the degradation of DCF. The findings were in strong accordance with the scavenger function of the used ZnO/g-C₃N₄ on the photocatalytic degradation of methylene blue [32].

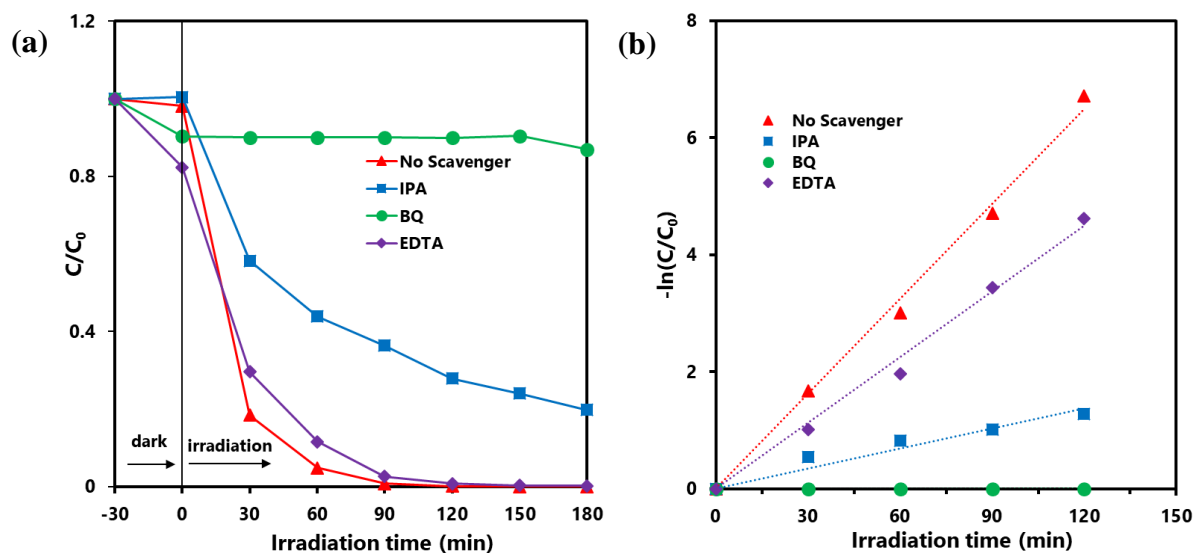


Figure 3.15 (a) Effect of scavenger on the photocatalytic degradation of DCF using ZnO/g-C₃N₄, and (b) the plot of $-\ln(C/C_0)$ versus irradiation time; DCF: 10 mg L⁻¹ (30 mL), ZnO/g-C₃N₄: 30 mg.

Table 3.8 Impact of scavenger on kinetic parameters for photocatalytic degradation of DCF using ZnO/g-C₃N₄

Scavenger	Rate constant (min ⁻¹)	T _{1/2} (min)	R ²
without	0.0541	12.8	0.99
IPA	0.0115	60.3	0.93
BQ	0.00005	13860	0.55
EDTA	0.0375	18.5	0.99

3.3.17 Stability

Another crucial factor in determining if a photocatalyst has a practical use in DCF degradation is its chemical durability upon application. Using five sequential reusability cycles of DCF degradation with visible light irradiation, the photostability of the ZnO/g-C₃N₄ composite was evaluated. It is evident, as shown in Figure 3.16, that the DCF degradation capacity of the composite considerably declined after the five cycles of reuse. The chemisorption of DCF molecules or intermediate products of reaction on the more potent active sites of the photocatalyst, which persist after the saturation of the accessible sites for subsequent reactions, may be the cause of a little decrement in photocatalytic activity [45]. Hence, the result was attributed to the stability of the composite.

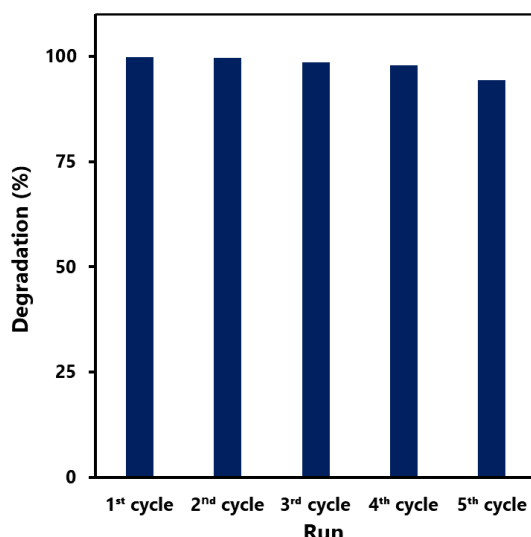


Figure 3.16 Photocatalytic stability test of ZnO/g-C₃N₄ on photocatalytic degradation of DCF.

3.3.18 Mechanism

On the basis of the XPS result, it can be concluded that the electrons in the ZnO/g-C₃N₄ composite are spontaneously transferred from g-C₃N₄ to ZnO, and it is continued until their flat band potentials reach in equilibrium. After that, an internal electric field have been formed at the interface of ZnO/g-C₃N₄ heterojunction (Figure 3.17). It can be assumed that a mid-level band have been appeared nearest to the CB of the ZnO in the composite which is the CB of the composite -0.58 V (vs. NHE at pH 0) (Figure 3.18). Considering the E_{CB} of ZnO and composite are equal, it can be said that The E_{CB} of ZnO was -0.58 V (vs. NHE at pH 0). The E_{VB} of ZnO can be calculated to be 2.62 V (vs. NHE at pH 0) using eq. 3.6 and the value of the band gap of ZnO. As during the irradiation of visible light, electrons are transferred from the VB of g-C₃N₄ to CB of g-C₃N₄ and CB to ZnO, the E_{VB} of the composite can be assumed to be the E_{VB} of g-C₃N₄ 2.23 V (vs. NHE at pH 0). The E_{CB} of g-C₃N₄ can be calculated to -0.7 V (vs. NHE at pH 0) using eq. 3.6 and the value of the band gap of g-C₃N₄.

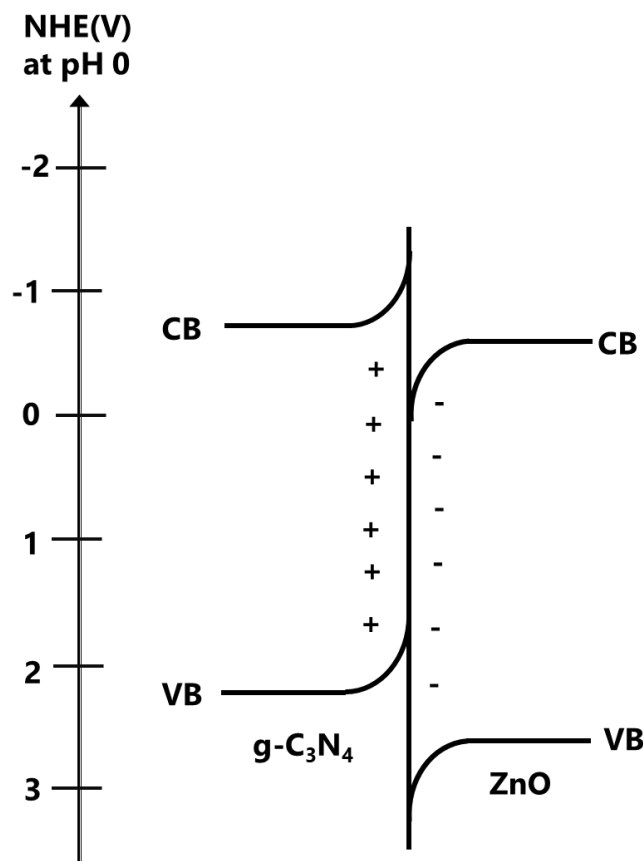
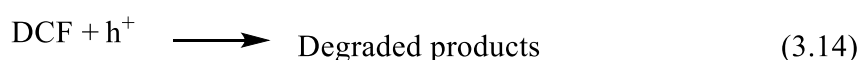
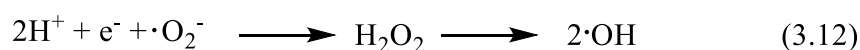
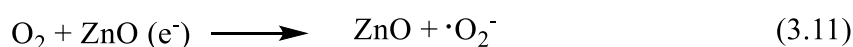
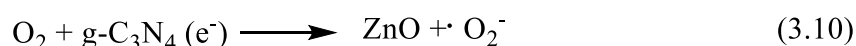
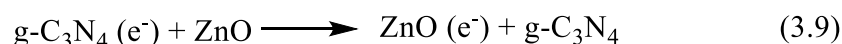
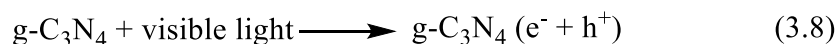


Figure 3.17 Formation of internal electric field in the ZnO/g-C₃N₄ composite.

The photocatalytic degradation mechanism of DCF using the ZnO/g-C₃N₄ composite can be proposed by the typical charge transfer and the interfacial charge transfer (IFCT) pathway. As shown in Figure 3.18, when g-C₃N₄ is subjected to visible light irradiation, photoelectrons and holes are generated on the CB and VB of the g-C₃N₄, respectively. Compared to ZnO, the E_{CB} in g-C₃N₄ has a greater negative value. In turn, this leads to the few photoelectrons in the CB of g-C₃N₄ being transferred to the CB of ZnO. Most of the photoelectrons are remained in the CB of g-C₃N₄ due to the formation of internal electric field as mentioned before. Furthermore, photoelectrons can be transferred from the VB of g-C₃N₄ to the mid-level, as well as to the CB of the composite or the CB of ZnO, through the IFCT pathway. As a result, e^-/h^+ pair recombination rate was suppressed. Hence, the separation efficiency of photogenerated charges was enhanced. The photoelectrons in both CB of ZnO and CB of g-C₃N₄ were captured

by the environmental oxygen and produced reactive radicals of $\bullet\text{O}_2^-$, as the CB potentials of both g-C₃N₄ and ZnO are significantly more negative compared to the standard O₂/ $\bullet\text{O}_2^-$ reduction potential (-0.28 V vs. NHE at pH 0) [79]. But the VB potential of g-C₃N₄ is less positive than the standard H₂O/ $\bullet\text{OH}$ redox potential (2.80 V vs. NHE at pH 0) [65]. Hence, holes in g-C₃N₄ did not react with H₂O and could not create the reactive radical $\bullet\text{OH}$. Noteworthy is the fact that the scavenger rule test indicates that not only the $\bullet\text{O}_2^-$ radical but also the $\bullet\text{OH}$ radical play important roles in the degradation of DCF in the present study. However, the $\bullet\text{OH}$ radical may be formed by the photochemical reaction of $\bullet\text{O}_2^-$, as shown in the eq. 3.12 [74].

Moreover, the scavenger test also indicates that photogenerated h^+ takes part as a minor reactive species in the photodegradation of DCF using fabricated ZnO/g-C₃N₄ composite. Hence, a small amount of DCF may be degraded by the direct reaction of photogenerated holes in the VB of g-C₃N₄. The following equations represent the corresponding photocatalytic reactions of DCF degradation with ZnO/g-C₃N₄ composite with visible light treatment.



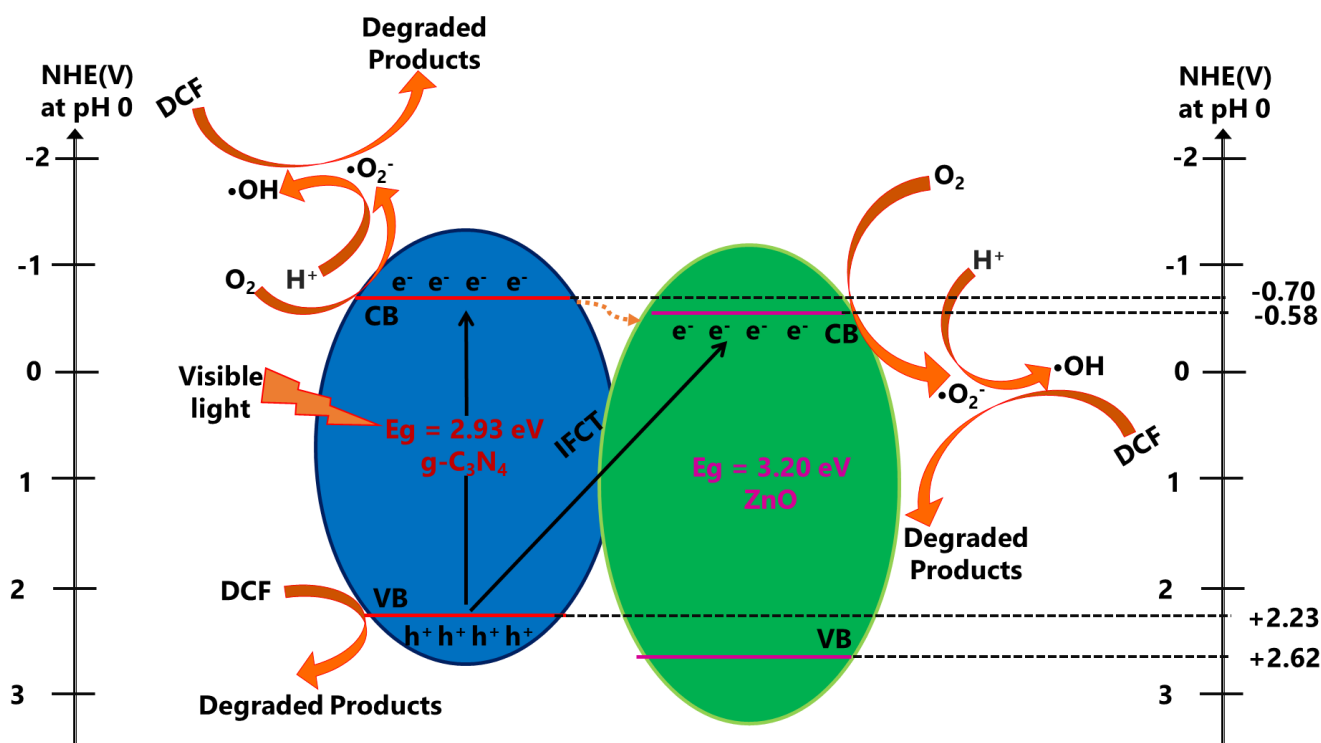


Figure 3.18 Mechanism of the photocatalytic degradation of DCF using ZnO/g-C₃N₄ composite.

3.4 Conclusions

In this study, the composite of commercially obtained ZnO (Sigma-Aldrich) and prepared g-C₃N₄ from calcination of urea resulted in enhanced photocatalytic activity. Structural and morphological analysis revealed the successful formation of the composite, while PL and EIS analysis revealed the reduced recombination of photocharges in the fabricated composite. The photocatalytic degradation rate of DCF using ZnO/g-C₃N₄ composite was 27 times higher than that attained with pure g-C₃N₄ and 11 times higher than that attained with physical mixture of ZnO and g-C₃N₄. Possible photocatalytic degradation mechanism and corresponding reactions have been proposed.

3.5 References

1. Zhang, W.; Zhou, L.; Shi, J.; Deng, H. Fabrication of Novel Visible-Light-Driven AgI/g-C₃N₄ Composites with Enhanced Visible-Light Photocatalytic Activity for Diclofenac Degradation. *J. Colloid Interface Sci.* **2017**, *496*, 167–176, doi:10.1016/j.jcis.2017.02.022.
2. Zhang, W.; Zhou, L.; Deng, H. Ag Modified g-C₃N₄ Composites with Enhanced Visible-Light Photocatalytic Activity for Diclofenac Degradation. *J. Mol. Catal. A Chem.* **2016**, *423*, 270–276, doi:10.1016/j.molcata.2016.07.021.
3. He, J.; Yang, J.; Jiang, F.; Liu, P.; Zhu, M. Photo-Assisted Peroxymonosulfate Activation via 2D/2D Heterostructure of Ti₃C₂/ g-C₃N₄ for Degradation of Diclofenac. *Chemosphere* **2020**, *258*, 127339, doi:10.1016/j.chemosphere.2020.127339.
4. Lara-Pérez, C.; Leyva, E.; Zermeño, B.; Osorio, I.; Montalvo, C.; Moctezuma, E. Photocatalytic Degradation of Diclofenac Sodium Salt: Adsorption and Reaction Kinetic Studies. *Environ. Earth Sci.* **2020**, *79*, 277, doi:10.1007/s12665-020-09017-z.
5. Tanveer, M.; Tezcanli, G.; Sadiq, M.T.; Kazmi, S.M.; Noshad, N.; Abbas, G.; Ali, A. Degradation of Diclofenac under Irradiation of UV Lamp and Solar Light Using ZnO Photo Catalyst. *Eng. Proc.* **2022**, *12*, 1–13, doi:10.3390/engproc2021012076.
6. Gerbaldo, M.V.; Marchetti, S.G.; Mendoza, S.M.; Elias, V.R.; Mendieta, S.N.; Crivello, M.E. Photocatalytic Degradation of Sodium Diclofenac Using Spinel Ferrites: Kinetic Aspects. *Top. Catal.* **2022**, *65*, 1419–1426, doi:10.1007/s11244-022-01627-0.
7. Liu, W.; Li, Y.; Liu, F.; Jiang, W.; Zhang, D.; Liang, J. Visible-Light-Driven Photocatalytic Degradation of Diclofenac by Carbon Quantum Dots Modified Porous g-C₃N₄: Mechanisms, Degradation Pathway and DFT Calculation. *Water Res.* **2019**, *151*, 8–19, doi:10.1016/j.watres.2018.11.084.

8. Lonappan, L.; Brar, S.K.; Das, R.K.; Verma, M.; Surampalli, R.Y. Diclofenac and Its Transformation Products: Environmental Occurrence and Toxicity - A Review. *Environ. Int.* **2016**, *96*, 127–138, doi:10.1016/j.envint.2016.09.014.
9. Oaks, J.L.; Gilbert, M.; Virani, M.Z.; Watson, R.T.; Meteyer, C.U.; Rideout, B.A.; Shivaprasad, H.L.; Ahmed, S.; Chaudhry, M.J.I.; Arshad, M.; et al. Diclofenac Residues as the Cause of Vulture Population Decline in Pakistan. *Nature* **2004**, *427*, 630–633, doi:10.1038/nature02317.
10. Zhang, W.; Zhou, L.; Shi, J.; Deng, H. Synthesis of Ag₃PO₄/g-C₃N₄ Composite with Enhanced Photocatalytic Performance for the Photodegradation of Diclofenac under Visible Light Irradiation. *Catalysts* **2018**, *8*, 45, doi:10.3390/catal8020045.
11. Malhotra, M.; Suresh, S.; Garg, A. Tea Waste Derived Activated Carbon for the Adsorption of Sodium Diclofenac from Wastewater: Adsorbent Characteristics, Adsorption Isotherms, Kinetics, and Thermodynamics. *Environ. Sci. Pollut. Res.* **2018**, *25*, 32210–32220, doi:10.1007/s11356-018-3148-y.
12. Chen, J.; Qian, Y.; Liu, H.; Huang, T. Oxidative Degradation of Diclofenac by Thermally Activated Persulfate: Implication for ISCO. *Environ. Sci. Pollut. Res.* **2016**, *23*, 3824–3833, doi:10.1007/s11356-015-5630-0.
13. Yang, W.; Wu, Y.; Zhang, L.; Jiang, J.; Feng, L. Removal of Five Selected Pharmaceuticals by Coagulation in the Presence of Dissolved Humic Acids and Kaolin. *Desalin. Water Treat.* **2015**, *54*, 1134–1140, doi:10.1080/19443994.2014.906325.
14. Park, J.; Yamashita, N.; Tanaka, H. Membrane Fouling Control and Enhanced Removal of Pharmaceuticals and Personal Care Products by Coagulation-MBR. *Chemosphere* **2018**, *197*, 467–476, doi:10.1016/j.chemosphere.2018.01.063.
15. Ji, Z.; Liu, T.; Tian, H. Electrochemical Degradation of Diclofenac for Pharmaceutical

- Wastewater Treatment. *Int. J. Electrochem. Sci.* **2017**, *12*, 7807–7816, doi:10.20964/2017.08.72.
16. Chen, P.; Zhang, Q.; Su, Y.; Shen, L.; Wang, F.; Liu, H.; Liu, Y.; Cai, Z.; Lv, W.; Liu, G. Accelerated Photocatalytic Degradation of Diclofenac by a Novel CQDs/BiO₂COOH Hybrid Material under Visible-Light Irradiation: Dechlorination, Detoxicity, and a New Superoxide Radical Model Study. *Chem. Eng. J.* **2018**, *332*, 737–748, doi:10.1016/j.cej.2017.09.118.
 17. Czech, B.; Buda, W. Multicomponent Nanocomposites for Elimination of Diclofenac in Water Based on an Amorphous TiO₂ Active in Various Light Sources. *J. Photochem. Photobiol. A Chem.* **2016**, *330*, 64–70, doi:10.1016/j.jphotochem.2016.07.024.
 18. Shi, J.W.; Wang, Z.; He, C.; Wang, H.; Chen, J.W.; Fu, M.L.; Li, G.; Niu, C. CdS Quantum Dots Modified N-Doped Titania Plates for the Photocatalytic Mineralization of Diclofenac in Water under Visible Light Irradiation. *J. Mol. Catal. A Chem.* **2015**, *399*, 79–85, doi:10.1016/j.molcata.2015.01.030.
 19. Kanakaraju, D.; Motti, C.A.; Glass, B.D.; Oelgemöller, M. Solar Photolysis versus TiO₂-Mediated Solar Photocatalysis: A Kinetic Study of the Degradation of Naproxen and Diclofenac in Various Water Matrices. *Environ. Sci. Pollut. Res.* **2016**, *23*, 17437–17448, doi:10.1007/s11356-016-6906-8.
 20. Hama Aziz, K.H.; Miessner, H.; Mueller, S.; Kalass, D.; Moeller, D.; Khorshid, I.; Rashid, M.A.M. Degradation of Pharmaceutical Diclofenac and Ibuprofen in Aqueous Solution, a Direct Comparison of Ozonation, Photocatalysis, and Non-Thermal Plasma. *Chem. Eng. J.* **2017**, *313*, 1033–1041, doi:10.1016/j.cej.2016.10.137.
 21. Das, L.; Barodia, S.K.; Sengupta, S.; Basu, J.K. Aqueous Degradation Kinetics of Pharmaceutical Drug Diclofenac by Photocatalysis Using Nanostructured Titania–

- zirconia Composite Catalyst. *Int. J. Environ. Sci. Technol.* **2015**, *12*, 317–326, doi:10.1007/s13762-013-0466-y.
22. Moreira, N.F.F.; Orge, C.A.; Ribeiro, A.R.; Faria, J.L.; Nunes, O.C.; Pereira, M.F.R.; Silva, A.M.T. Fast Mineralization and Detoxification of Amoxicillin and Diclofenac by Photocatalytic Ozonation and Application to an Urban Wastewater. *Water Res.* **2015**, *87*, 87–96, doi:10.1016/j.watres.2015.08.059.
 23. Moctezuma, E.; Leyva, E.; Lara-Pérez, C.; Noriega, S.; Martínez-Richa, A. TiO₂ Photocatalytic Degradation of Diclofenac: Intermediates and Total Reaction Mechanism. *Top. Catal.* **2020**, *63*, 601–615, doi:10.1007/s11244-020-01262-7.
 24. Jiménez-Salcedo, M.; Monge, M.; Tena, M.T. The Photocatalytic Degradation of Sodium Diclofenac in Different Water Matrices Using g-C₃N₄ Nanosheets: A Study of the Intermediate by-Products and Mechanism. *J. Environ. Chem. Eng.* **2021**, *9*, 105827, doi:10.1016/j.jece.2021.105827.
 25. Du, X.; Yi, X.; Wang, P.; Deng, J.; Wang, C.C. Enhanced Photocatalytic Cr(VI) Reduction and Diclofenac Sodium Degradation under Simulated Sunlight Irradiation over MIL-100(Fe)/g-C₃N₄ Heterojunctions. *Cuihua Xuebao/Chinese J. Catal.* **2019**, *40*, 70–79, doi:10.1016/S1872-2067(18)63160-2.
 26. Ravichandran, K.; Kalpana, K.; Ibrahim, M.M.; Seelan, K.S. Effect of Source Material of g-C₃N₄ on the Photocatalytic Activity of ZnO/ g-C₃N₄ thin Film Coated on Stainless Steel Mesh Substrate. In *Proceedings of the Materials Today: Proceedings*; Elsevier Ltd, 2019; Vol. 48, pp. 207–215.
 27. Oliveros, A.N.; Pimentel, J.A.I.; de Luna, M.D.G.; Garcia-Segura, S.; Abarca, R.R.M.; Doong, R.A. Visible-Light Photocatalytic Diclofenac Removal by Tunable Vanadium Pentoxide/boron-Doped Graphitic Carbon Nitride Composite. *Chem. Eng. J.* **2021**, *403*, 126213, doi:10.1016/j.cej.2020.126213.

28. Hu, Z.; Cai, X.; Wang, Z.; Li, S.; Wang, Z.; Xie, X. Construction of Carbon-Doped Supramolecule-Based g-C₃N₄/TiO₂ Composites for Removal of Diclofenac and Carbamazepine: A Comparative Study of Operating Parameters, Mechanisms, Degradation Pathways. *J. Hazard. Mater.* **2019**, *380*, 120812, doi:10.1016/j.jhazmat.2019.120812.
29. Shao, H.; Zhao, X.; Wang, Y.; Mao, R.; Wang, Y.; Qiao, M.; Zhao, S.; Zhu, Y. Synergetic Activation of Peroxymonosulfate by Co₃O₄ Modified g-C₃N₄ for Enhanced Degradation of Diclofenac Sodium under Visible Light Irradiation. *Appl. Catal. B Environ.* **2017**, *218*, 810–818, doi:10.1016/j.apcatb.2017.07.016.
30. Alharthi, F.A.; Ali Alghamdi, A.; Alanazi, H.S.; Alsyahi, A.A.; Ahmad, N. Photocatalytic Degradation of the Light Sensitive Organic Dyes: Methylene Blue and Rose Bengal by Using Urea Derived g-C₃N₄/ZnO Nanocomposites. *Catalysts* **2020**, *10*, 1457, doi:10.3390/catal10121457.
31. Prasad Adhikari, S.; Raj Pant, H.; Joo Kim, H.; Hee Park, C.; Sang Kim, C. Deposition of ZnO Flowers on the Surface of g-C₃N₄ Sheets via Hydrothermal Process. *Ceram. Int.* **2015**, *41*, 12923–12929, doi:10.1016/j.ceramint.2015.06.134.
32. Gayathri, M.; Sakar, M.; Satheeshkumar, E.; Sundaravadivel, E. Insights into the Mechanism of ZnO/g-C₃N₄ Nanocomposites toward Photocatalytic Degradation of Multiple Organic Dyes. *J. Mater. Sci. Mater. Electron.* **2022**, *33*, 9347–9357, doi:10.1007/s10854-021-07302-6.
33. Kumar, S.G.; Kavitha, R.; Manjunatha, C. Review and Perspective on Rational Design and Interface Engineering of g-C₃N₄/ZnO: From Type-II to Step-Scheme Heterojunctions for Photocatalytic Applications. *Energy & Fuels* **2023**, *37*, 14421–14472, doi:10.1021/acs.energyfuels.3c01032.
34. Qin, J.; Yang, C.; Cao, M.; Zhang, X.; Saravanan, R.; Limpanart, S.; Ma, M.; Liu, R.

- Two-Dimensional Porous Sheet-like Carbon-Doped ZnO/g-C₃N₄ nanocomposite with High Visible-Light Photocatalytic Performance. *Mater. Lett.* **2017**, *189*, 156–159, doi:10.1016/j.matlet.2016.12.007.
35. Liu, W.; Wang, M.; Xu, C.; Chen, S.; Fu, X. Significantly Enhanced Visible-Light Photocatalytic Activity of g-C₃N₄ via ZnO Modification and the Mechanism Study. *J. Mol. Catal. A Chem.* **2013**, *368-369*, 9–15, doi:10.1016/j.molcata.2012.11.007.
36. Park, T.J.; Pawar, R.C.; Kang, S.; Lee, C.S. Ultra-Thin Coating of g-C₃N₄ on an Aligned ZnO Nanorod Film for Rapid Charge Separation and Improved Photodegradation Performance. *RSC Adv.* **2016**, *6*, 89944–89952, doi:10.1039/C6RA16300A.
37. Wang, J.; Yang, Z.; Gao, X.; Yao, W.; Wei, W.; Chen, X.; Zong, R.; Zhu, Y. Core-Shell g-C₃N₄@ZnO Composites as Photoanodes with Double Synergistic Effects for Enhanced Visible-Light Photoelectrocatalytic Activities. *Appl. Catal. B Environ.* **2017**, *217*, 169–180, doi:10.1016/j.apcatb.2017.05.034.
38. Liu, B.; Bie, C.; Zhang, Y.; Wang, L.; Li, Y.; Yu, J. Hierarchically Porous ZnO/ g-C₃N₄ S-Scheme Heterojunction Photocatalyst for Efficient H₂O₂ production. *Langmuir* **2021**, *37*, 14114–14124, doi:10.1021/acs.langmuir.1c02360.
39. He, Y.; Wang, Y.; Zhang, L.; Teng, B.; Fan, M. High-Efficiency Conversion of CO₂ to Fuel over ZnO/g-C₃N₄ Photocatalyst. *Appl. Catal. B Environ.* **2015**, *168-169*, 1–8, doi:10.1016/j.apcatb.2014.12.017.
40. de Jesus Martins, N.; Gomes, I.C.H.; da Silva, G.T.S.T.; Torres, J.A.; Avansi, W.; Ribeiro, C.; Malagutti, A.R.; Mourão, H.A.J.L. Facile Preparation of ZnO:g-C₃N₄ Heterostructures and Their Application in Amiloride Photodegradation and CO₂ Photoreduction. *J. Alloys Compd.* **2021**, *856*, 156798, doi:10.1016/j.jallcom.2020.156798.

41. Liu, J.; Yan, X.T.; Qin, X. Sen; Wu, S.J.; Zhao, H.; Yu, W.B.; Chen, L.H.; Li, Y.; Su, B.L. Light-Assisted Preparation of Heterostructured g-C₃N₄/ZnO Nanorods Arrays for Enhanced Photocatalytic Hydrogen Performance. *Catal. Today* **2020**, *355*, 932–936, doi:10.1016/j.cattod.2019.02.028.
42. Khatun, A.; Suhag, M.H.; Tateishi, I.; Furukawa, M.; Katsumata, H.; Kaneco, S. Facile Synthesis of ZnO/g-C₃N₄ with Enhanced Photocatalytic Performance for the Reduction of Cr(VI) in Presence of EDTA Under Visible Light Irradiation. *Int. J. Environ. Res.* **2023**, *17*, 1–17, doi:10.1007/s41742-023-00522-0.
43. Paul, D.R.; Gautam, S.; Panchal, P.; Nehra, S.P.; Choudhary, P.; Sharma, A. ZnO-Modified g-C₃N₄: A Potential Photocatalyst for Environmental Application. *ACS Omega* **2020**, *5*, 3828–3838, doi:10.1021/acsomega.9b02688.
44. Nemiwal, M.; Zhang, T.C.; Kumar, D. Recent Progress in g-C₃N₄, TiO₂ and ZnO Based Photocatalysts for Dye Degradation: Strategies to Improve Photocatalytic Activity. *Sci. Total Environ.* **2021**, *767*, 144896.
45. Pérez-Molina, Á.; Pastrana-Martínez, L.M.; Pérez-Poyatos, L.T.; Morales-Torres, S.; Maldonado-Hódar, F.J. One-Pot Thermal Synthesis of g-C₃N₄/ZnO Composites for the Degradation of 5-Fluoruracil Cytostatic Drug under UV-LED Irradiation. *Nanomaterials* **2022**, *12*, 340, doi:10.3390/nano12030340.
46. Ismael, M. The Photocatalytic Performance of the ZnO/g-C₃N₄ Composite Photocatalyst toward Degradation of Organic Pollutants and Its Inactivity toward Hydrogen Evolution: The Influence of Light Irradiation and Charge Transfer. *Chem. Phys. Lett.* **2020**, *739*, 136992, doi:10.1016/j.cplett.2019.136992.
47. Meena, P.L.; Poswal, K.; Surela, A.K.; Saini, J.K. Synthesis of g-C₃N₄/ZnO Nanostructures via Mechano-Thermal Method for Photocatalytic Degradation of Methylene Blue Dye. *Int. J. Environ. Sci. Technol.* **2024**, *21*, doi:10.1007/s13762-024-

- 05704-7.
48. Girish, Y.R.; Udayabhanu; Byrappa, N.M.; Alnaggar, G.; Hezam, A.; Nagaraju, G.; Pramoda, K.; Byrappa, K. Rapid and Facile Synthesis of Z-Scheme ZnO/g-C₃N₄ Heterostructure as Efficient Visible Light-Driven Photocatalysts for Dye Degradation and Hydrogen Evolution Reaction. *J. Hazard. Mater. Adv.* **2023**, *9*, 100230, doi:10.1016/j.hazadv.2023.100230.
 49. Pham, T.H.; Tran, M.H.; Chu, T.T.H.; Myung, Y.; Jung, S.H.; Mapari, M.G.; Taeyoung, K. Enhanced Photodegradation of Tetracycline in Wastewater and Conversion of CO₂ by Solar Light Assisted ZnO/g-C₃N₄. *Environ. Res.* **2023**, *217*, 114825, doi:10.1016/j.envres.2022.114825.
 50. Hosseini-Hosseiniabad, S.M.; Minaeian, S.; Tavakoli, A.; Sabaei, M.; Yousefi Zoshk, M.; Laripour, R.; Ramezani, S.; Hoseini, M.; Chamanara, M. Development of g-C₃N₄/ZnO Nanocomposite as a Novel, Highly Effective and Durable Photocatalytic Antibacterial Coating for Cotton Fabric. *Ceram. Int.* **2023**, *49*, 12274–12284, doi:10.1016/j.ceramint.2022.12.080.
 51. Teye, G.K.; Huang, J.; Li, Y.; Li, K.; Chen, L.; Darkwah, W.K. Photocatalytic Degradation of Sulfamethoxazole, Nitenpyram and Tetracycline by Composites of Core Shell g-C₃N₄@ZnO, and ZnO Defects in Aqueous Phase. *Nanomaterials* **2021**, *11*, 2609, doi:10.3390/nano11102609.
 52. Jingyu, H.; Ran, Y.; Zhaohui, L.; Yuanqiang, S.; Lingbo, Q.; Nti Kani, A.; Kani, A.N. In-Situ Growth of ZnO Globular on g-C₃N₄ to Fabrication Binary Heterojunctions and Their Photocatalytic Degradation Activity on Tetracyclines. *Solid State Sci.* **2019**, *92*, 60–67, doi:10.1016/j.solidstatesciences.2019.02.009.
 53. Sun, Q.; Sun, Y.; Zhou, M.; Cheng, H.; Chen, H.; Dorus, B.; Lu, M.; Le, T. A 2D/3D g-C₃N₄/ZnO Heterojunction Enhanced Visible-Light Driven Photocatalytic Activity

- for Sulfonamides Degradation. *Ceram. Int.* **2022**, *48*, 7283–7290, doi:10.1016/j.ceramint.2021.11.289.
54. Garg, R.; Gupta, R.; Bansal, A. Synthesis of g-C₃N₄/ZnO Nanocomposite for Photocatalytic Degradation of a Refractory Organic Endocrine Disrupter. *Mater. Today Proc.* **2021**, *44*, 855–859, doi:10.1016/j.matpr.2020.10.787.
 55. Suhag, M.H.; Khatun, A.; Tateishi, I.; Furukawa, M.; Katsumata, H.; Kaneco, S. One-Step Fabrication of the ZnO/g-C₃N₄ Composite for Visible Light-Responsive Photocatalytic Degradation of Bisphenol E in Aqueous Solution. *ACS Omega* **2023**, *8*, 11824–11836, doi:10.1021/acsomega.2c06678.
 56. Sun, J.-X.; Yuan, Y.-P.; Qiu, L.-G.; Jiang, X.; Xie, A.-J.; Shen, Y.-H.; Zhu, J.-F. Fabrication of Composite Photocatalyst g-C₃N₄-ZnO and Enhancement of Photocatalytic Activity under Visible Light. *Dalt. Trans.* **2012**, *41*, 6756–6763, doi:10.1039/c2dt12474b.
 57. Zhu, Y.-P.; Li, M.; Liu, Y.-L.; Ren, T.-Z.; Yuan, Z.-Y. Carbon-Doped ZnO Hybridized Homogeneously with Graphitic Carbon Nitride Nanocomposites for Photocatalysis. *J. Phys. Chem. C* **2014**, *118*, 10963–10971, doi:10.1021/jp502677h.
 58. Kumar, K.V.A.; Vinodkumar, T.; Selvaraj, M.; Suryakala, D.; Subrahmanyam, C. Visible Light-Induced Catalytic Abatement of 4-Nitrophenol and Rhodamine B Using ZnO/g-C₃N₄ Catalyst. *J. Chem. Sci.* **2021**, *133*, 41, doi:10.1007/s12039-021-01903-8.
 59. Sharifalhoseini, Z.; Entezari, M.H.; Shahidi, M. Sonication Affects the Quantity and the Morphology of ZnO Nanostructures Synthesized on the Mild Steel and Changes the Corrosion Protection of the Surface. *Ultrason. Sonochem.* **2018**, *41*, 492–502, doi:10.1016/j.ultsonch.2017.10.012.
 60. Kumaresan, N.; Sinthiya, M.M.A.; Sarathbavan, M.; Ramamurthi, K.; Sethuraman, K.; Babu, R.R. Synergetic Effect of g-C₃N₄/ZnO Binary Nanocomposites Heterojunction

- on Improving Charge Carrier Separation through 2D/1D Nanostructures for Effective Photocatalytic Activity under the Sunlight Irradiation. *Sep. Purif. Technol.* **2020**, *244*, 116356, doi:10.1016/j.seppur.2019.116356.
61. Vu, M.-H.; Sakar, M.; Nguyen, C.-C.; Do, T.-O. Chemically Bonded Ni Cocatalyst onto the S Doped g-C₃N₄ Nanosheets and Their Synergistic Enhancement in H₂ Production under Sunlight Irradiation. *ACS Sustain. Chem. Eng.* **2018**, *6*, 4194–4203, doi:10.1021/acssuschemeng.7b04598.
62. Li, L.; Sun, S.-Q.; Wang, Y.-X.; Wang, C.-Y. Facile Synthesis of ZnO/ g-C₃N₄ Composites with Honeycomb-like Structure by H₂ Bubble Templates and Their Enhanced Visible Light Photocatalytic Performance. *J. Photochem. Photobiol. A Chem.* **2018**, *355*, 16–24, doi:10.1016/j.jphotochem.2017.12.016.
63. Yue, B.; Li, Q.; Iwai, H.; Kako, T.; Ye, J. Hydrogen Production Using Zinc-Doped Carbon Nitride Catalyst Irradiated with Visible Light. *Sci. Technol. Adv. Mater.* **2011**, *12*, 034401, doi:10.1088/1468-6996/12/3/034401.
64. Suhag, M.H.; Katsumata, H.; Tateishi, I.; Furukawa, M.; Kaneco, S. Black Phosphorus-Doped Graphitic Carbon Nitride with Aromatic Benzene Rings for Efficient Photocatalytic Hydrogen Production. *Langmuir* **2023**, *39*, 13121–13131, doi:10.1021/acs.langmuir.3c01518.
65. Xu, Q.; Zhang, L.; Cheng, B.; Fan, J.; Yu, J. S-Scheme Heterojunction Photocatalyst. *Chem* **2020**, *6*, 1543–1559, doi:10.1016/j.chempr.2020.06.010.
66. Wang, L.; Tan, H.; Zhang, L.; Cheng, B.; Yu, J. In-Situ Growth of Few-Layer Graphene on ZnO with Intimate Interfacial Contact for Enhanced Photocatalytic CO₂ Reduction Activity. *Chem. Eng. J.* **2021**, *411*, 128501, doi:10.1016/j.cej.2021.128501.
67. Huang, W.; Li, Z.; Wu, C.; Zhang, H.; Sun, J.; Li, Q. Delaminating Ti₃C₂ MXene by Blossom of ZnIn₂S₄ Microflowers for Noble-Metal-Free Photocatalytic Hydrogen

- Production. *J. Mater. Sci. Technol.* **2022**, *120*, 89–98, doi:10.1016/j.jmst.2021.12.028.
68. Bai, P.; Wang, P.; Wu, Y.; Pang, X.; Song, M.; Du, C.; Su, Y. Junction of $\text{Zn}_m\text{In}_2\text{S}_{3+m}$ and Bismuth Vanadate as Z-Scheme Photocatalyst for Enhanced Hydrogen Evolution Activity: The Role of Interfacial Interactions. *J. Colloid Interface Sci.* **2022**, *628*, 488–499, doi:10.1016/j.jcis.2022.08.078.
 69. Kotsis, K.; Staemmler, V. Ab Initio Calculations of the O1s XPS Spectra of ZnO and Zn Oxo Compounds. *Phys. Chem. Chem. Phys.* **2006**, *8*, 1490, doi:10.1039/b515699h.
 70. Zhong, Q.; Lan, H.; Zhang, M.; Zhu, H.; Bu, M. Preparation of Heterostructure g- $\text{C}_3\text{N}_4/\text{ZnO}$ Nanorods for High Photocatalytic Activity on Different Pollutants (MB, RhB, Cr(VI) and Eosin). *Ceram. Int.* **2020**, *46*, 12192–12199, doi:10.1016/j.ceramint.2020.01.265.
 71. Xing, H.; Ma, H.; Fu, Y.; Xue, M.; Zhang, X.; Dong, X.; Zhang, X. Preparation of g- $\text{C}_3\text{N}_4/\text{ZnO}$ Composites and Their Enhanced Photocatalytic Activity. *Mater. Technol.* **2015**, *30*, 122–127, doi:10.1179/1753555714Y.00000000216.
 72. Das, J.; Pradhan, S.K.; Sahu, D.R.; Mishra, D.K.; Sarangi, S.N.; Nayak, B.B.; Verma, S.; Roul, B.K. Micro-Raman and XPS Studies of Pure ZnO Ceramics. *Phys. B Condens. Matter* **2010**, *405*, 2492–2497, doi:10.1016/j.physb.2010.03.020.
 73. Islam, J.B.; Islam, M.R.; Furukawa, M.; Tateishi, I.; Katsumata, H.; Kaneco, S. Ag-Modified g- C_3N_4 with Enhanced Activity for the Photocatalytic Reduction of Hexavalent Chromium in the Presence of EDTA under Ultraviolet Irradiation. *Environ. Technol.* **2023**, *44*, 3627–3640, doi:10.1080/09593330.2022.2068379.
 74. Zhang, Z.; Sun, Y.; Wang, Y.; Yang, Y.; Wang, P.; Shi, L.; Feng, L.; Fang, S.; Liu, Q.; Ma, L.; et al. Synthesis and Photocatalytic Activity of g- $\text{C}_3\text{N}_4/\text{ZnO}$ Composite Microspheres under Visible Light Exposure. *Ceram. Int.* **2022**, *48*, 3293–3302, doi:10.1016/j.ceramint.2021.10.104.

75. Yang, P.; Wang, J.; Yue, G.; Yang, R.; Zhao, P.; Yang, L.; Zhao, X.; Astruc, D. Constructing Mesoporous g-C₃N₄/ZnO Nanosheets Catalyst for Enhanced Visible-Light Driven Photocatalytic Activity. *J. Photochem. Photobiol. A Chem.* **2020**, *388*, 112169, doi:10.1016/j.jphotochem.2019.112169.
76. Jiang, R.; Lu, G.; Liu, J.; Wu, D.; Yan, Z.; Wang, Y. Incorporation of π -Conjugated Molecules as Electron Donors in g-C₃N₄ Enhances Photocatalytic H₂-Production. *Renew. Energy* **2021**, *164*, 531–540, doi:10.1016/j.renene.2020.09.040.
77. Katsumata, H.; Islam Molla, M.A.; Islam, J.B.; Tateishi, I.; Furukawa, M.; Kaneco, S. Dual Z-Scheme Heterojunction g-C₃N₄/Ag₃PO₄/AgBr Photocatalyst with Enhanced Visible-Light Photocatalytic Activity. *Ceram. Int.* **2022**, *48*, 21898–21905, doi:10.1016/j.ceramint.2022.04.176.
78. Paul, D.R.; Sharma, R.; Nehra, S.P.; Sharma, A. Effect of Calcination Temperature, pH and Catalyst Loading on Photodegradation Efficiency of Urea Derived Graphitic Carbon Nitride towards Methylene Blue Dye Solution. *RSC Adv.* **2019**, *9*, 15381–15391, doi:10.1039/C9RA02201E.
79. Okunaka, S.; Kameshige, H.; Oozu, S.; Yang, Y.; Miyauchi, M.; Tokudome, H. Synthetic Strategies of BiVO₄ for Efficient Visible-Light-Induced Photocatalytic Oxidation Reactions: Activation via Nanoparticulation and Surface Modification. *J. Ceram. Soc. Japan* **2023**, *131*, 22153, doi:10.2109/jcersj2.22153.

CHAPTER FOUR

Purification of aqueous orange II solution through adsorption and visible-light-induced photodegradation using ZnO-modified g-C₃N₄ composites

4.1 Introduction

Dyes are basically organic substances that are usually embedded in fabrics or surfaces for coloring or pigmentation, and most of the dyes are typically large molecules [1]. Several industries, including textile, paper, rubber, leather tanning, plastic, food processing, cosmetics, printing, and dye manufacturing industries, extensively use synthetic dyes [1–6]. In order to measure the surface area of activated sludge, dirt and effluent purification, and the tracing of groundwater, synthetic dyes are also used [1]. The aquatic ecosystem is adversely affected by the improper release of highly colored effluent containing dyes from these industries, which also intensifies ecotoxicological effects, reduces light penetration and photosynthesis, and increases the risk of cancer and mutagenicity in humans. Consequently, effluent from industrial dye discharge has become a major threat to the environment [5–7]. Therefore, industrial effluents that contain dyes should be properly treated before discharge into the environment. Multiple techniques have been employed to remove dyes from effluent, including adsorption [8,9], membrane separation [10], electrocoagulation [11], electrochemical [12,13], biological [14,15], and advanced oxidation processes [16–18]. Among these techniques, adsorption is regarded as one of the most convenient and efficient methods of removing dyes due to its high efficiency, ease of use, and availability of adsorbent materials [1,19]. In view of their large surface area and adsorption efficacy, activated charcoal, fly ash, silica gel, molecular organic framework, and other conventional adsorbent materials have been used in the dye contaminated wastewater adsorption studies. However, the use of these adsorbents is costly and hostile to the environment [20].

In addition, oxidative degradation known as photocatalytic degradation of dye-containing effluents under solar irradiation has drawn a lot of interest because of its cost-effectiveness, cleanliness, high efficacy, and long-term sustainability. For instance, it is essential to pick, plan, and develop materials that have both adsorption and photocatalytic

activity for the purpose of removing dye from effluent. The bifunctional adsorptive photocatalysts are required to have high capacity, outstanding compatibility, and prolonged recyclability [21–23].

The textile dye orange II (4-(2-hydroxy-1-naphthyl)azobenzene) is a monoazo, anionic, and acidic dye. It is extensively utilized in the industrial sector because of its durability. Due to its multi-step elimination process and ability to infect people through the food chain, it poses a threat to the environment. Due to its lower biodegradability, wastewater treatment plants can't degrade it perfectly. The excessive use of orange II dye will significantly pollute water bodies, and prolonged exposure to this dye can result in a number of health problems for humans [24–26]. Many research works have been reported on the adsorption [27–33] and photocatalytic degradation [24–26] of orange II dye using different types of adsorbents and photocatalysts, respectively.

Graphitic carbon nitride (g-C₃N₄, abbreviated as g-CN), a carbon-based material, has attracted a lot of interest and is used in a variety of applications, including photocatalysis [34,35], electrogenerated chemiluminescence [36], lithium-ion batteries [37], hydrogen generation [38], fluorescent sensors [39], and adsorption [22]. The hexagonal ring-based C-N network of g-CN is composed of tri-s-triazine units. Due to the presence of delocalized π -electrons in tri-s-triazine units, aromatic compounds are attracted to g-CN via π - π interaction and hydrophobic effect. Thus, g-CN emerges as a potential efficient adsorbent for the adsorption of dyes with aromatic structures. However, the efficacy of g-CN as an adsorbent for dye adsorption is inadequate [40]. Therefore, it should be necessary to enhance the adsorption capacity of g-CN by increasing the surface area and pore size, changing the π - π stacking, forming an induced electric field, and increasing the H-bond ability [19,21,22,40]. Several modifications of the g-CN structure have been reported to enhance its adsorption ability. For instance, Yousefi *et al.* prepared oxidized g-CN as an effective adsorbent for organic dyes and

tetracycline for water remediation [19]. Ren *et al.* reported the preparation of carbon-doped g-CN for the adsorption of methylene blue from an aqueous solution. The adsorption kinetics, isotherm, and thermodynamics were also studied [40]. Yan *et al.* synthesized sodium-doped g-CN for the removal of aqueous contaminants via adsorption and photocatalysis. It was reported that the sodium-doped g-CN is a potential adsorbent for the adsorption of methylene blue, acriflavine, azure blue, rhodamine B, safranin O, and methyl orange dyes [22]. Panneri *et al.* reported carbon-doped g-CN as an effective adsorptive photocatalyst for the removal of tetracycline antibiotics from waste water [21]. Khosrowshahi *et al.* studied the application of sunflower stalk g-CN nanosheets as a green adsorbent in the extraction of polycyclic aromatic hydrocarbons from the liquid g-CN nanosheets phase [41]. Wang *et al.* reported the application of α -Fe₂O₃/g-CN composites for the synergistic adsorption and photodegradation of methyl orange and methylene blue dyes [42].

Some inherent characteristics of g-CN, especially low charge separation, poor quantum efficiency, and quick recombination rate of the photogenerated e^- - h^+ pairs, decrease its visible-light-responsive photocatalytic efficiency [43,44]. To boost the photocatalytic activity of g-CN, some attempts have been focused such as by elemental doping [45–47], molecular doping [48], and coupling with other semiconductors, including metal oxides [49–51], metal sulfides [52,53], and others [54,55]. It was reported that ZCN composites showed excellent photocatalytic activity due to the appropriate band gap alignment of g-C₃N₄ and ZnO. For example, Paul *et al.* fabricated the ZnO/g-C₃N₄ composites for enhanced photocatalytic degradation of methylene blue solution with visible light irradiation [56]. Zhang *et al.* synthesized the ZnO/g-C₃N₄ composites, which were applied to the efficient photocatalytic degradation of methyl orange and tetracycline under the irradiation of visible light [57]. Ismael *et al.* prepared the ZnO/g-C₃N₄ composites, and the effective photocatalytic activity of the prepared composite was evaluated under visible light irradiation [43]. Gayathri *et al.* reported

the improved photocatalytic degradation of methylene blue and acid blue 113 dyes with the irradiation of sunlight [50]. In our previous studies, we reported the different ZnO/g-C₃N₄ composites for the enhanced photocatalytic degradation of endocrine-disrupting chemical bisphenol E and reduction of hexavalent chromium solution under visible light irradiation [34,58].

In this paper, the adsorption and photocatalytic activity for orange II dye removal from aqueous solution using ZCN composites were reported as bifunctional adsorptive photocatalysts. The adsorption isotherms and thermodynamics properties were also studied. The photocatalytic degradation kinetics of the composites were also testified. The photocatalytic degradation efficiency of the composites was compared with their adsorption efficacy.

4.2 Materials and Methods

4.2.1 Fabrication of the ZCN Composites

The ZCN composites were fabricated according to our published paper [40,41]. In brief, ZCN composites were synthesized by the single-step thermal calcination of homogeneous mixtures of zinc acetate dihydrate and urea with different ratios. Typically, different amounts of zinc acetate dihydrate and 20 g of urea were homogeneously mixed with a dispersion of 5 mL of water in an alumina crucible. Then it was covered by a lid and aluminum foil and calcined at 550 °C for 2 hours with a heating increasing rate of 2 °C/min using an electric muffle furnace. Lastly, the calcined samples were ground manually into different colored powders. The obtained composites were labeled as ZCN-1, ZCN-2.5, ZCN-5, ZCN-10, and ZCN-15, in accordance with the various amounts of zinc acetate dihydrate that were used 0.2, 0.5, 1.0, 2.0, and 3.0 g, respectively. The content of the ZnO in the composites has been determined by thermal gravimetric analysis using a muffle furnace. The estimated ZnO contents are 7.2, 20.4, 30.0, 39.1, and 45.3% in the ZCN-1, ZCN-2.5, ZCN-5, ZCN-10, and

ZCN-15 composites, respectively. Urea and zinc acetate dehydrate were calcinated at similar temperatures separately to prepare bare g-CN and ZnO, respectively.

4.2.2 Characterization

The FTIR spectra of the ZCN composites and bare g-CN were recorded on a Perkin Elmer spectrometer (SPECTRUM 100 FTIR) at 5 number of scans with an attenuated total reflection assemblage and a resolution of 0.5 cm^{-1} . XRD patterns of the prepared ZCN composites, ZnO, and g-CN were analyzed by utilizing a Rigaku RINT Ultima-IV diffractometer with $\text{Cu K}\alpha$ radiation in a scan range of $10\text{--}80^\circ$ at a scan rate of $0.04^\circ/\text{s}$. The XPS of ZCN-2.5 composite and g-CN were characterized by using a PHI Quantera SXM photoelectron spectrometer with $\text{Al K}\alpha$ radiation. The C1s peak at 284.8 eV was used as a reference to adjust the binding energies. In order to observe the surface morphology, SEM images of the all prepared ZCN composites, ZnO, and g-CN and EDS elemental mapping of the ZCN-2.5 composite were recorded using a JEOL JEM-1400 Flash SEM. The TEM image of the ZCN-2.5 composite (slurry on methanol) was analyzed on a JEOL JEM-1011 TEM at 100 kV . In order to attain BET surface area, average pore size and total pore volume of all ZCN composites and g-CN, N_2 adsorption-desorption isotherms were recorded on the BELSORP-miniII (MicrotracBEL) apparatus. The UV-vis DRS of all composites, ZnO and g-CN were inspected by a JASCO V-750 UV-vis instrument equipped with an integrating sphere adaptor. Photoluminescence (PL) spectra of all composites, ZnO and g-CN were attained by a Shimadzu fluorescence spectrophotometer (RF-5300PC) with an excitation wavelength of 340 nm . The EIS measurement of all composites and g-CN were analyzed on an electrochemical Versa STAT 3 workstation (Princeton Applied Research) equipped with a conventional three-electrode system. In here, uniform slurry of the sample by nafion solution was coated on a fluorine-doped tin oxide glass plate to make the working electrode, and an aqueous solution of Na_2SO_4 (0.5 mol L^{-1}) was utilized as the electrolyte.

4.2.3 Adsorption Study

The orange II aqueous solution (100 mg L^{-1}) was prepared as the stock solution in a volumetric flask. Also, different concentrated diluted solutions were prepared by proper dilution. To study the adsorption of orange II solution by g-CN and different ZCN composites, a series of batch adsorption analyses were conducted. The relative standard deviation (RSD) of each experiment was calculated with triplicate measurements, and the observed RSD values were less than 10%. A pyrex glass cell (50 mL) was used for the adsorption experiment. Herein, 30 mg of adsorbents and 30 mL of orange II solution were poured into the glass cell, covered by aluminum foil, and magnetically stirred for the adsorption test. Throughout the experiment, 1.5 mL of sample solution was withdrawn at different time intervals. Then the collected sample solution centrifuged for 5 min at 12000 rpm to isolate the adsorbents. The absorbance of the supernatant was measured using a UV-Vis spectrophotometer at 485 nm wavelength to assess the concentration of orange II solution.

4.2.4 Photocatalytic Degradation Study

Thirty milliliters of orange II solution (10 mg L^{-1}) and 30 mg of photocatalyst were put into 50 mL of a pyrex glass cell. The adsorption process was then let run in the dark for 30 minutes to obtain adsorption-desorption equilibrium. Later, the solution was illuminated by using a light-emitting diode (LED) lamp (OptoCode LDA14L-G/100W) with a UV (400 nm) cutoff filter (Y-44, HOYA). The light source was set up on one side of the reaction cell. Through the degradation, 1.5 mL of the solution was collected every 30 minutes and centrifuged at 12000 rpm for 5 minutes to separate the photocatalyst from the liquid phase. Then the concentration of the orange II dye liquid phase was evaluated by measuring the absorbance with a UV-Vis spectrophotometer at 485 nm wavelength. The reproducibility of the photocatalytic degradations have also been investigated, and relative standard deviations were observed within 10% for more than three runs.

4.3 Results and Discussion

4.3.1 XRD Analysis

In order to assess the crystalline nature of the prepared photocatalysts, XRD analysis was performed. Figure 4.1a shows the powder XRD patterns of prepared g-CN, ZnO, and a series of fabricated ZCN composites. Two distinct peaks were observed in the XRD pattern of g-CN at 12.82° and 27.66° 2θ values, which can be indexed as (100) and (002) planes, respectively. The observed small peak at 12.82° was related to the periodic reflection of the s-triazine units. Moreover, the observed intense peak at 27.66° was associated with the long-range interlayer conjugated aromatic C-N stacking [44,59]. Several distinct diffraction peaks were found in the XRD pattern of prepared ZnO at 31.94° , 34.64° , 36.32° , 47.68° , 56.72° , 63.01° , 66.68° , 68.06° , 69.12° , 73.12° , and 77.52° 2θ values, which could resemble the plane of (100), (002), (101), (102), (110), (103), (200), (112), (201), (004), and (202), respectively, of the wurtzite structure of hexagonal ZnO[60]. A peak detected at about 27° 2θ value in the XRD pattern of ZCN-1 and ZCN-2.5 represents the diffraction phase of the g-C₃N₄. The peak in the XRD pattern of ZCN-2.5 was weaker and broader than that of ZCN-1, which corresponded to the decrease of the g-CN crystal phase. Moreover, the peak was boarded and disappeared in the XRD patterns of ZCN-5, ZCN-10, and ZCN-15, indicating the loss of g-CN crystallinity in the composites (Figure 4.1 a,b). Interestingly, no ZnO-related diffraction peak was observed in the XRD patterns of all ZCN composites, which denotes that the crystallinity of the ZnO was lost during the formation of all composites [56]. Hence, the fabricated ZCN composites containing higher content of ZnO exist in amorphous state.

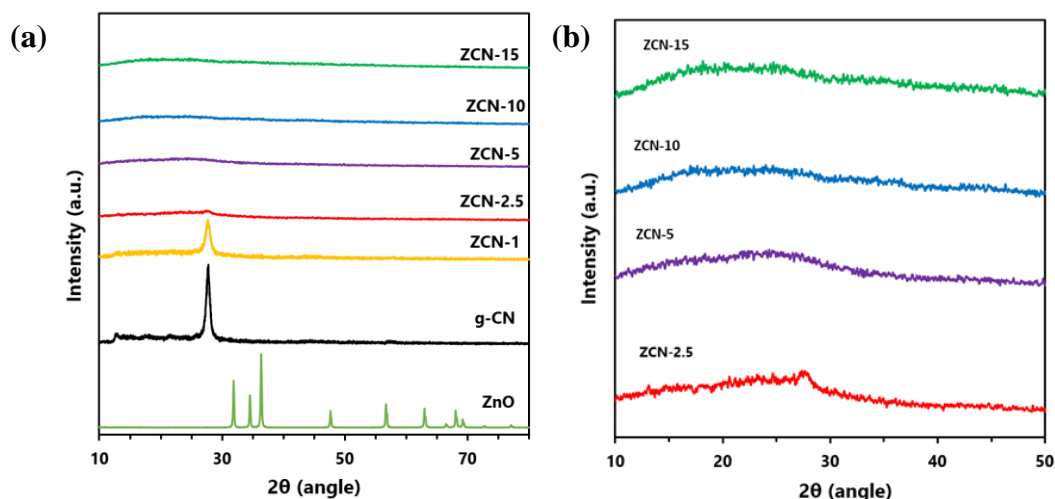


Figure 4.1 (a) XRD patterns of ZnO, g-CN and different ZCN composites and (b) Enlarged (2θ range 10-50°) XRD patterns of ZCN-2.5, 5, 10 and 15 composites.

4.3.2 FTIR Analysis

To study the bonding of ZnO with g-CN in the fabricated ZCN composites, the g-CN and all ZCN composites were characterized by FTIR spectroscopy (Figure 4.2). In the FTIR spectra of pure g-CN, an intense peak was observed at 807 cm^{-1} , which is attributed to the bending mode of the heterocyclic C-N bond in the s-triazine ring [61]. The peak was shifting to lower wave number and decreasing intensity with increasing the ZnO content in the ZCN composites, which suggested the bond strength of heterocyclic C-N was decreased by the interaction of ZnO and g-CN. Several peaks were observed at 1200 to 1650 cm^{-1} in the FTIR spectra of g-CN, corresponding to the stretching modes of C-N and C=N bonds in the aromatic heterocycles of the g-CN framework [62]. The intensity of the peaks decreased with increasing ZnO content in the ZCN composites and merged for higher ZnO-containing composites. A broad peak with small intensity was observed at 3000 to 3450 cm^{-1} associated with the stretching modes of O-H bonds in adsorbed moisture and water and uncondensed N-H bonds [61,62]. However, the peak was weaker or disappeared for the ZnO-incorporated composites. In addition, a new peak with lower intensity appeared at about 2160 to 2180 cm^{-1} in the FTIR spectra of all ZCN composites, which is absent in the FTIR spectra of g-CN. The new peak

indicated the formation of new C-N bond along with sp^2 C-N bonds in the g-CN network [56]. The results supported the chemical interaction between ZnO and g-CN during the formation of ZCN composites.

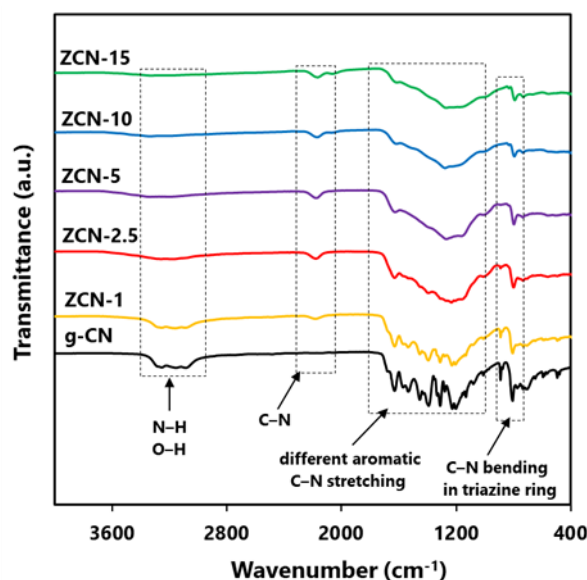


Figure 4.2 FTIR spectra of g-CN and all fabricated ZCN Composites.

4.3.3 XPS Analysis

To specify the sample element state, XPS analysis was employed (Figure 4.3). The full scan survey XPS spectra of ZCN-2.5 composite and g-CN demonstrated that g-CN is composed of C and N elements, whereas the ZCN-2.5 composite is composed of Zn, O, C, and N components (Figure 4.3a and Table 4.1). The findings indicated that the ZCN-2.5 composite was pure and well-formed [50,63]. The high-resolution spectra of C1s, N1s, O1s, and Zn2p are depicted in Figure 4.3b-e. As illustrated in Figure 4.3b, four peaks are fitted in the high resolution XPS spectra of C1s for ZCN-2.5 composite and g-CN. For bare g-CN, the binding energies of these four peaks were about 284.8, 285.7, 288.1, and 289.0 eV, which are attributed to the C=C or C-C bond, sp^3 C-N bond, N=C-N groups in the s-triazine ring, and the unavoidable oxidized carbon C=O bond, respectively [64]. The high resolution XPS spectra of N1s for both g-CN and ZCN-2.5 are associated with three distinct peaks (Figure 4.3c). In the

case of bare g-CN, the peak located at 398.7 eV is related to sp^2 nitrogen in the triazine ring ($N=C-N$). The peaks positioned at 400.6 eV is regarded as the bridging nitrogen N atoms ($N-(C)_3$) and terminal amino groups ($C-NH_2$), and at 404.6 eV is regarded as the charging effect in heterocycles or triazine [40,59]. In comparison to g-CN, ZCN-2.5 showed a decrease in peak intensity of the C1s and N1s XPS spectra, attributed to the $N=C-N$ group. This result suggested that the ZnO coupling restacks the π - π conjugation in the aromatic ring structure of g-CN [64]. Furthermore, the major peak at higher resolution C1s of ZCN-2.5 is shifted to higher binding energies than that of g-CN, indicating that the electrons are moved from g-CN to ZnO. This provides strong evidence that electrons are transferred from g-CN to ZnO in the ZCN-2.5 heterojunction, resulting in the formation of an induced electric field [65,66]. As indicated in Figure 4.3d, the O1s high resolution XPS spectrum of g-CN showed only one peak at 532.6 eV that was caused by surface absorbed H_2O or $O-H$ groups [44]. In contrast, there were two peaks in the ZCN-2.5 composite O1s high resolution XPS spectrum, which were situated at 531.9 and 533.6 eV, respectively. The major peak (531.9 eV) is assigned to the contribution of O_2^{2-} ions in the wurtzite structure of ZnO, while the tiny peak (533.6 eV) is associated with $-OH$ groups or the $H-O-H$ bond of adsorbed H_2O on the composite surface [67]. In addition, the peak of Zn $2p_{3/2}$ is at 1022.1 eV, and Zn $2p_{1/2}$ is at 1045.2 eV indicated the existence of Zn^{2+} in the ZCN-2.5 composite (Figure 4.3e) [50]. The binding energy difference between two peaks was 23.1, which is consistent with the standard ZnO reference value [68,69]. Also, Zn-N bonding can be detected by the Zn LMM Auger peaks in the ZCN-2.5 composite survey spectrum [64].

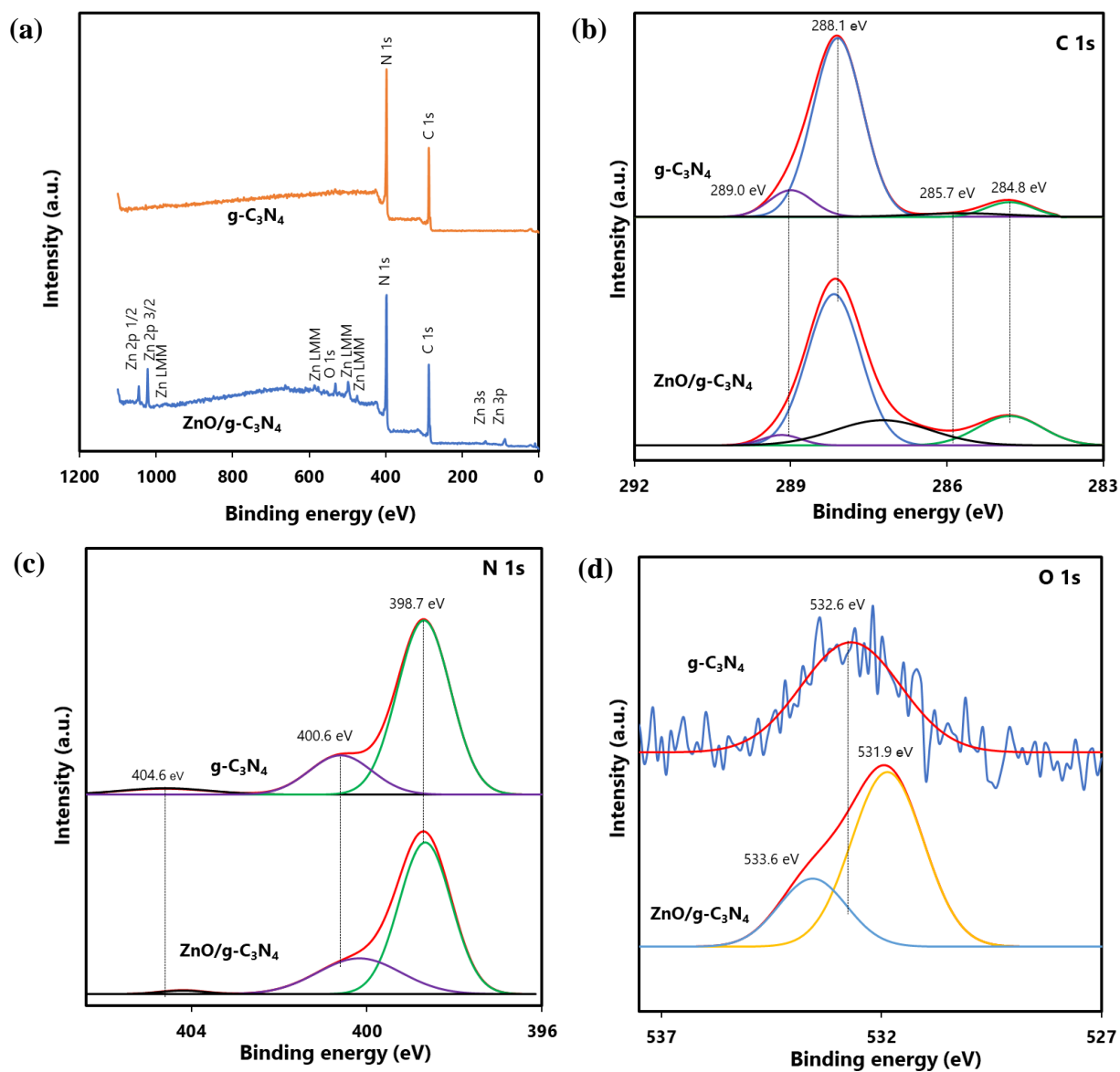


Figure 4.3 (a) Survey XPS spectra of g-CN and ZCN-2.5 and overlap high resolution XPS (b) C 1s (c) N 1s and (d) O1s spectra of g-CN and ZCN-2.5.

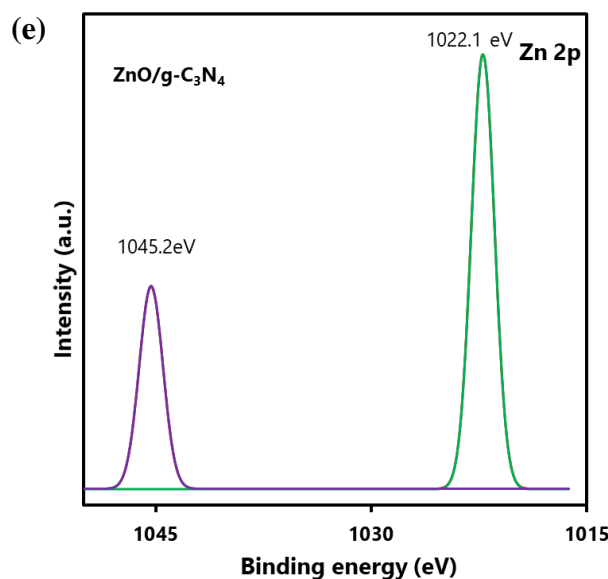


Figure 4.3 (e) High resolution XPS Zn 2p spectra of ZCN-2.5.

Table 4.1 Surface atomic ratios of g-CN and ZCN-2.5 composite

Sample	C (%)	N (%)	O (%)	Zn (%)	C/N molar ratio	C/O molar ratio
g-CN	43.8	56.0	0.1	-	0.78	438
ZCN-2.5	43.2	51.0	3.5	2.2	0.85	12.34

4.3.4 Morphological Analysis

The morphology of prepared pure ZnO, pure g-CN, and all ZCN composites was investigated by SEM analysis (Figure 4.4). The SEM image of ZnO shows spherical particles with different sizes [59]. The sheet-like layered structure was revealed in the SEM image of g-CN [70]. The SEM image of the ZCN-1 composite shows the existence of a sheet-like layered structure of g-CN with closely arranged ZnO particles. However, the surface morphology of other fabricated ZCN composites is blurred, which indicates the g-CN and ZnO are collapsed and aggregated during the composite formation.

The existence of spherical ZnO in the g-CN sheet is displayed in the TEM image of the ZCN-2.5 composite (Figure 4.5a). Further, in order to demonstrate the presence of C, N, O, and Zn in the ZCN-2.5 composite, EDS elemental mapping was analyzed. It is apparent in Figure 4.5b-f that C, N, O, and Zn are uniformly distributed on the composite's surface.

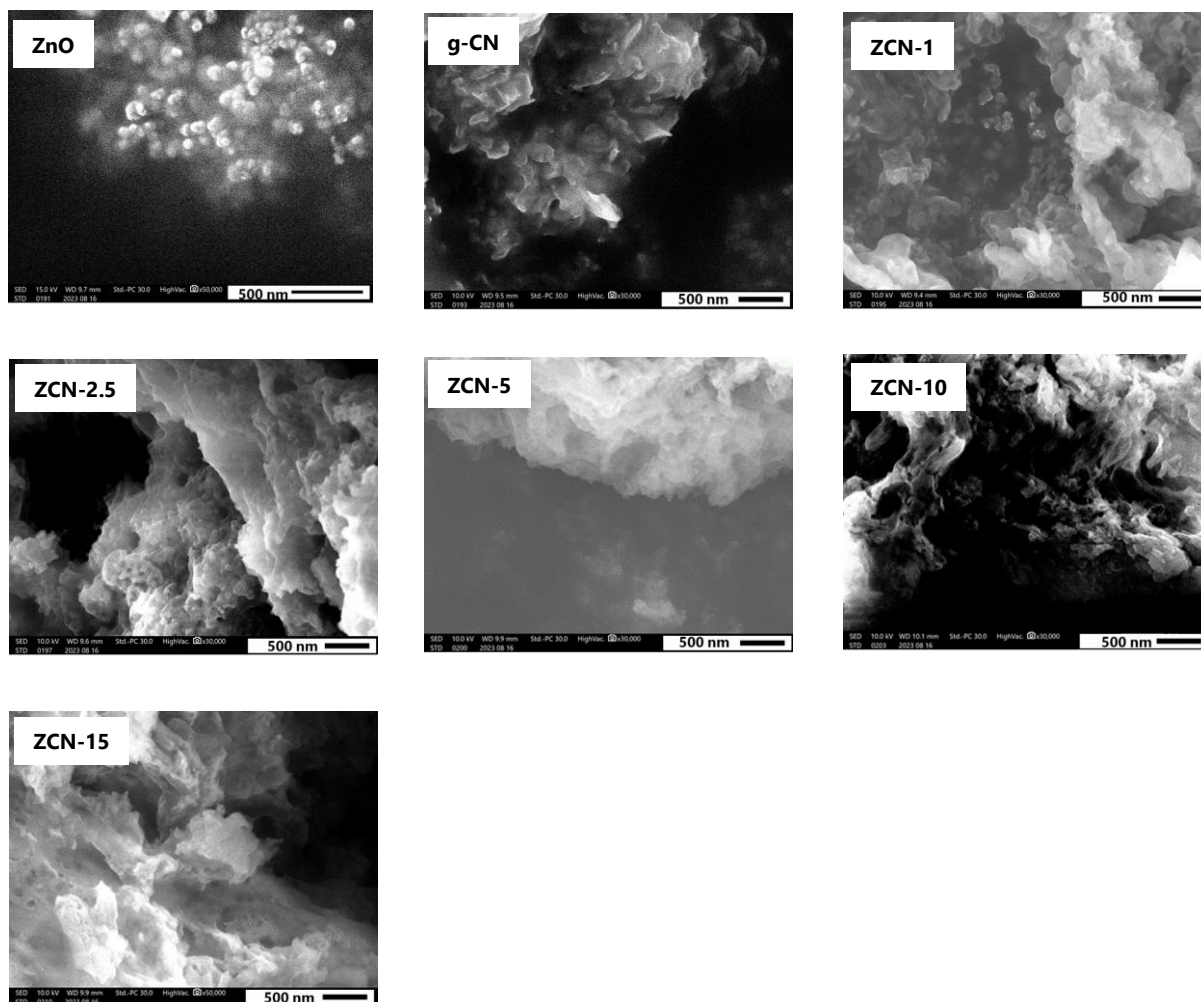


Figure 4.4 SEM images of ZCN composites, ZnO, and g-CN.

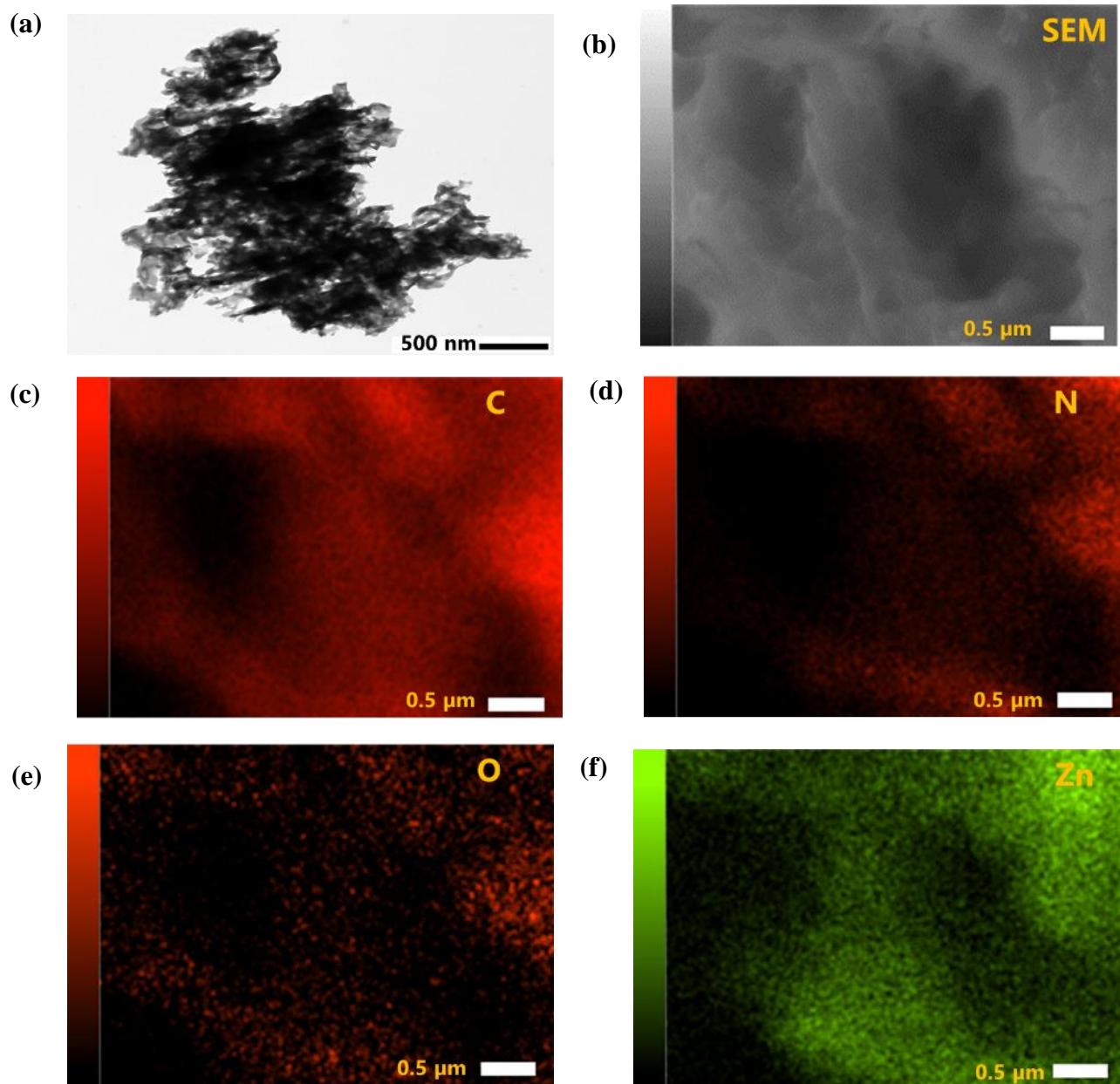


Figure 4.5 (a) TEM image and (b-f) EDS elemental mapping with corresponding SEM image of ZCN-2.5.

4.3.5 Textural Characterization

The textural properties such as surface area, average pore volume, and pore diameter of the pure g-CN and all fabricated ZCN composites were analyzed by measuring the physical adsorption ability of nitrogen. The N₂ adsorption desorption isotherms with pore size distribution curves of pure g-CN and ZCN composites are shown in Figure 4.6. It was confirmed that the isotherms are attributed to the classical IV type with the H3 hysteresis loop,

suggesting the existence of mesopores and slit-like pores within the structure [71,72]. From Table 4.2, it can be seen that the Brunauer-Emmett-Teller (BET) surface area of ZCN-1 was increased to a low extent, and ZCN-2.5 was slightly decreased compared to pure g-CN. By further increasing the ZnO content in the composite, the BET surface area was drastically decreased. The total pore volume and average pore diameter of ZCN-1 and ZCN-2.5 increased compared to pure g-CN. Furthermore, in the case of higher ZnO containing composites, these are decreased compared to pure g-CN. Excess ZnO in the composite may cause aggregation and block the original mesopores and slit-like pores in the g-CN segment [71,72].

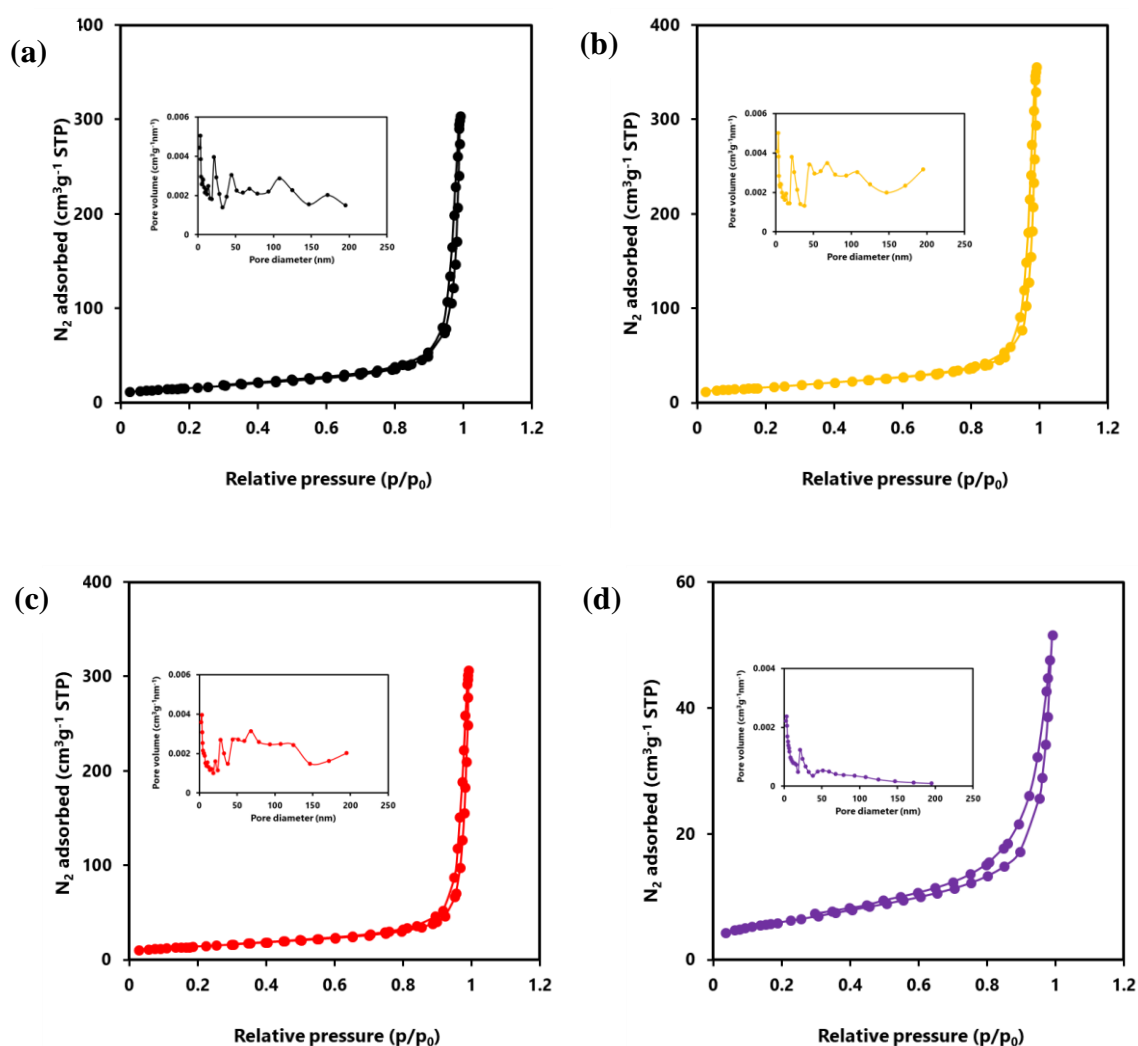


Figure 4.6 N_2 adsorption-desorption isotherms (inset: pore size distribution curves) of (a) g-CN and (b) ZCN-1, (c) ZCN-2.5 and (d) ZCN-5.

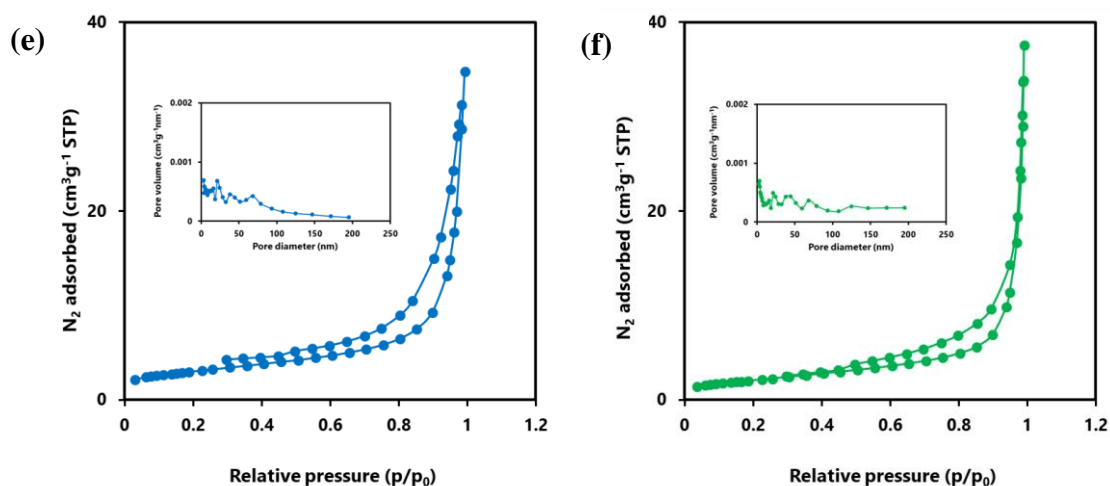


Figure 4.6 N₂ adsorption-desorption isotherms (inset: pore size distribution curves) of (e) ZCN-10 and (f) ZCN-15.

Table 4.2 Surface area, pore volume, and pore diameter of the pure g-CN and all fabricated ZCN composites

Photocatalyst	BET surface area (m ² /g)	Total pore volume (cm ³ /g)	Average pore diameter (nm)
g-CN	55.67	0.44	31.88
ZCN-1	56.00	0.53	37.64
ZCN-2.5	49.28	0.43	35.57
ZCN-5	21.4	0.08	14.9
ZCN-10	10.4	0.08	19.5
ZCN-15	7.49	0.06	30.56

4.3.6 UV-Vis DRS Analysis

In order to investigate the light absorption ability of prepared g-CN, ZnO, and all ZCN composites, the UV-Vis DRS was conducted at room temperature. Figure 4.7a shows the Kubelka-Munk-transformed UV-Vis DRS profile of prepared ZnO, g-CN, and all ZCN

composites. It is clearly seen that the absorption edge of ZnO is at about 390 nm, which indicates that it is non-responsive to visible light [73]. The absorption edge of g-CN was seen at about 430 nm, which is responsive to visible light [43]. Moreover, the absorption edges of the ZCN composites were red shifted to higher wavelength compared to pure ZnO and g-CN, with increasing the ZnO content in the composite. The enhancement of the visible light absorption ability of the composites indicates the interaction between ZnO and g-CN through chemical bonding [43]. Furthermore, the band gap of the samples was calculated using eq. 4.1.

$$\alpha h\nu = A(h\nu - E_g)^n \quad (4.1)$$

where α is the absorption coefficient, $h\nu$ is the photoenergy, A is a constant, and E_g is the optical band gap. The value of n is 2 or 1/2 for indirect transition (e.g., g-CN and ZCN composites) or direct (e.g., ZnO) transition, respectively [57]. As shown in Figure 4.7b and 4.7c, the estimated band gap values of ZnO, g-CN, ZCN-1, ZCN-2.5, ZCN-5, ZCN-10, and ZCN-15 are 3.20, 2.93, 2.74, 2.70, 2.62, 2.28, and 1.96, respectively. As shown in Figure 4.7d, the absorption edge and band gap change of the composites represent their color change.

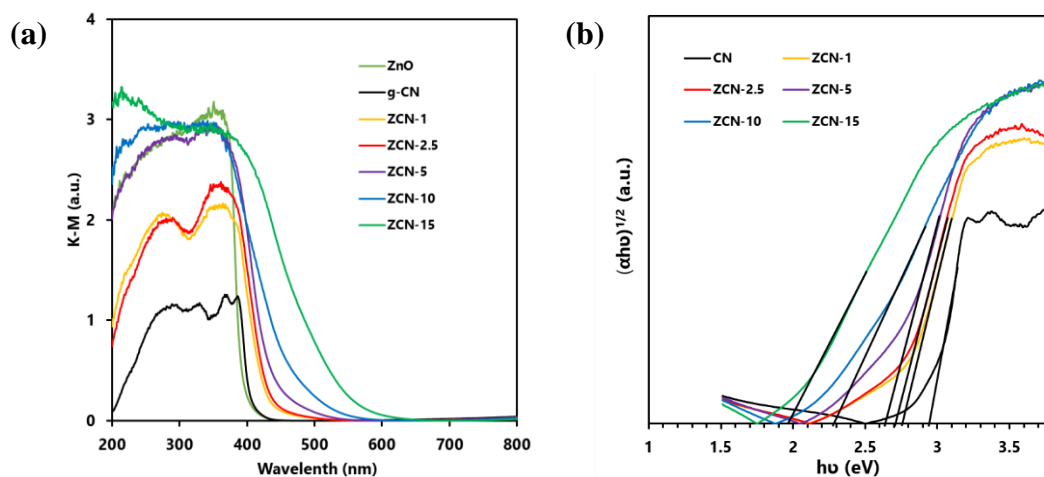


Figure 4.7 (a) Kubelka-Munk function of UV-Vis DRS and (b) Tauc plot of g-CN and different ZCN composites.

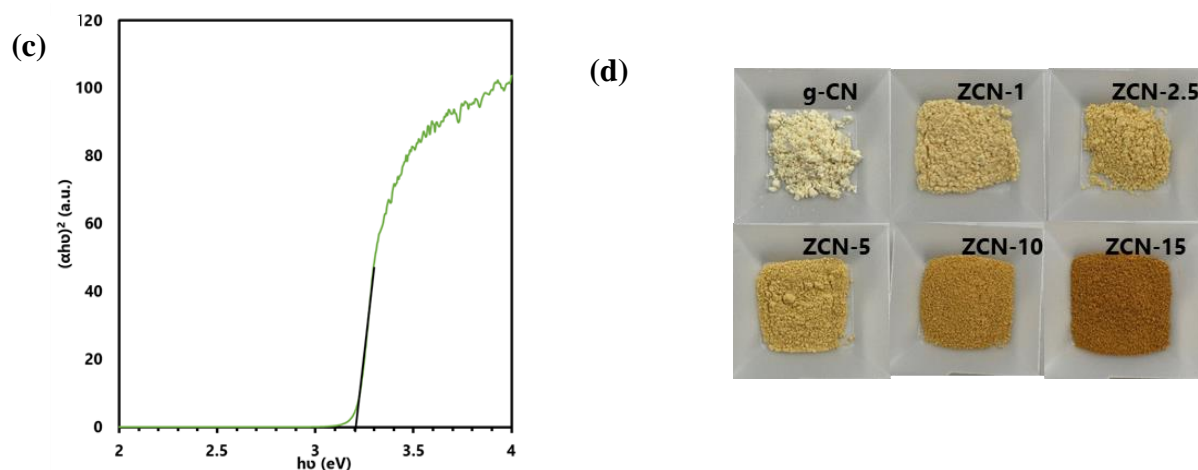


Figure 4.7 (c) Tauc plot of ZnO and (d) Photographs for appearance of all ZCN composites and bare g-CN.

4.3.7 PL Analysis

The recombination of charge carriers in the prepared pure g-CN, ZnO, and all fabricated ZCN composites was evaluated using PL analysis (Figure 4.8a). In general, the frequency of recombination of electron and hole pairs is closely proportional to the intensity of the PL spectra [57]. Upon excitation at 340 nm, the g-CN showed a very intense peak at wavelength of 440 nm. Furthermore, the ZnO showed several intense peaks. The findings suggested the higher electron hole pairs recombination in g-CN and ZnO separately. On the other hand, the PL intensity of the ZCN composites was drastically decreased and slightly shifted compared to the peak of g-CN with the increasing ZnO content in the composite, suggesting the decrement of electron hole pairs recombination. It may be caused by increments in electron transfer from the g-CN to ZnO upon the increase in ZnO content in the composite [74].

4.3.8 EIS Analysis

To learn about the process of photoinduced charge migration and transfer, EIS measurements were carried out. In the EIS resultant Nyquist plot, a smaller arc radius generally denotes reduced charge transfer resistance and more charge separation [43]. As shown in Figure 4.8b, the composites had smaller curvature radius compared to pure g-CN, which

suggested the enhanced photoinduced charge separation efficiency of g-CN after the formation of composites.

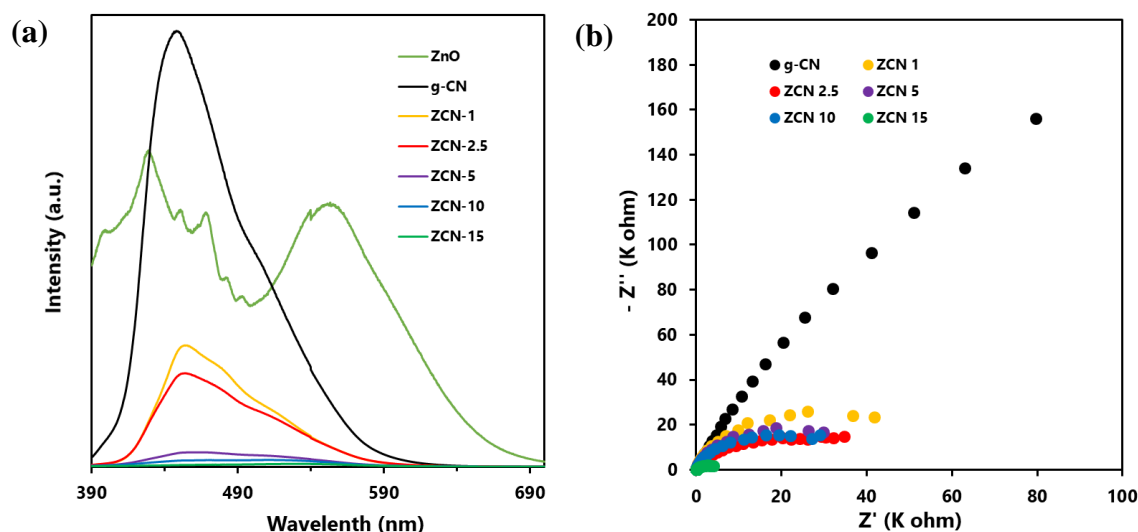


Figure 4.8 (a) PL spectra (upon the excitation at 340 nm wavelength) of ZnO, g-CN, and all fabricated ZCN composites and (b) EIS resultant Nyquist plot of g-CN and different ZCN composites.

4.3.9 Adsorption of Orange II Solution

To study adsorption of Orange II solution (10 p mg L^{-1}), 30 mg of adsorbents was used at different time intervals for adsorption capacity (q_t) of g-CN and ZCN composites. The experiments were carried out at room temperature and the pH was 3.0. Equation 4.2 was used for the quantity of q_t (mg/g) of various adsorbents at time t [40].

$$q_t = \frac{(C_0 - C_t)V}{m} \quad (4.2)$$

where m is the adsorbent mass and V , C_0 , and C_t are the volume, initial concentration, and concentrations at time t of the dye solution, respectively.

As depicted in Figure 4.9a, the equilibrium between adsorption and desorption was almost fully accomplished in about 30 minutes. It was also observed that the quantity of adsorption capability in ZCN composites enhanced with increasing amount of ZnO from bare g-CN to ZCN-2.5 composite and further decreased with increasing ZnO quantity.

For different dye adsorbents with various initial concentrations (3~100 mg L⁻¹), the quantity of adsorbed adsorbates q_e (mg/g) at equilibrium condition (30 minutes) was evaluated by eq. 4.3 [75].

$$q_e = \frac{(C_0 - C_e)V}{m} \quad (4.3)$$

where m is the adsorbent mass and V , C_0 , and C_e are the volume, initial concentration, and equilibrium concentrations at time t of the dye solution, respectively. As shown in Figure 4.9b, it was observed that the q_e values increased with the C_e value of adsorbed dye solution.

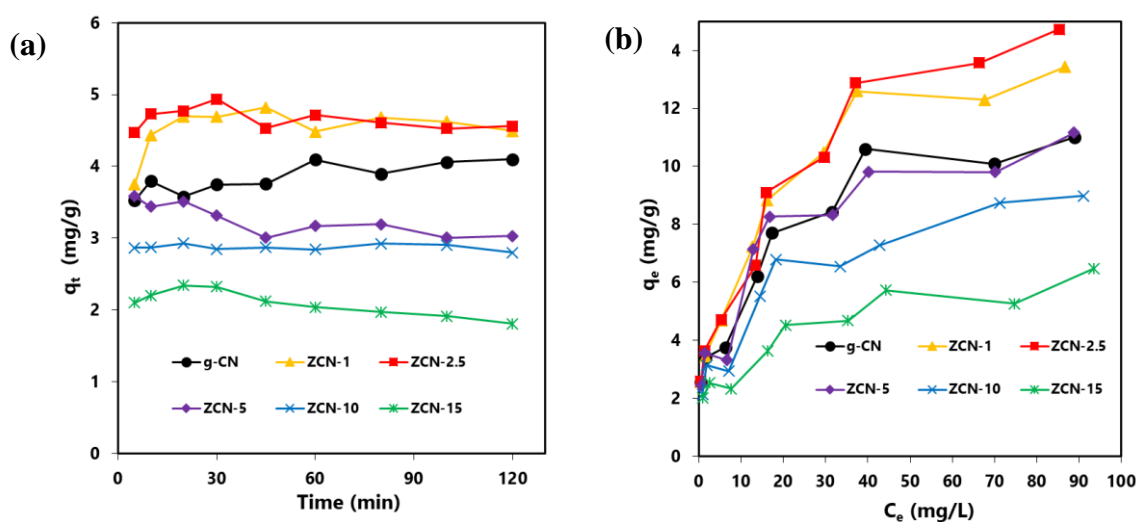


Figure 4.9 (a) Effect of contact time on the adsorption of orange II by prepared pure g-CN and different ZCN composites; Orange II solution, 10 mg L⁻¹ (30 mL); adsorbents, 30 mg. (b) Effect of equilibrium concentration on the adsorption of orange II prepared pure g-CN and different ZCN composites; Orange II solution, 30 mL (3~100 mg L⁻¹); adsorbents, 30 mg.

Generally, a number of equilibrium adsorption isotherm equations are used to describe experimental adsorption data. To understand the surface properties, the highest adsorption capacities and adsorbate affinity to adsorbents can be predicted using several adsorption isotherms. Hence, it is important to know the adsorption isotherm that fits the data acquired the best. Two widely utilized mathematical models are the Freundlich isotherm and the Langmuir

isotherm models. The Langmuir model assumes a monolayer coverage and uniformity of all adsorbent sorption sites. As seen in eq. 4.4, the Langmuir model is as follows [22]:

$$\frac{1}{q_e} = \frac{1}{q_{max}bC_e} + \frac{1}{q_{max}} \quad (4.4)$$

where q_{max} represents the maximum adsorption capacity and b is the Langmuir adsorption constant.

The curve fittings of the Langmuir isotherms for the adsorption of orange dye on the composites are shown in Figure 4.10a, and the maximum adsorption capacity (q_{max}) and Langmuir adsorption constant (b) are presented in Table 4.3.

In addition, the Freundlich isotherm model implies that all adsorption sites are heterogeneous and that the coverage is multilayer. As seen in eq. 4.5, the Freundlich model is as follows [22]:

$$\log q_e = \log K + \frac{1}{n} \log C_e \quad (4.5)$$

where K is the Freundlich adsorption constant and n represents the intensity of the adsorption. The curve fittings of the Freundlich isotherms for the adsorption of orange dye on the composites are shown in Figure 4.10b, and the Freundlich adsorption constant (K) and adsorption intensity (n) are presented in Table 4.4. Based on the R^2 values in Tables 4.3 and 4.4, the Langmuir model isotherm represents a better fit compared to the Freundlich model isotherm with the experimental data.

The results indicated that the adsorption was a monolayer process and that there were no interactions among the orange II dye molecules. The ZCN composites have a homogeneous character, and no more adsorption occurred at the site of the ZCN composites occupied by the orange II dye molecule [76]. The maximum adsorption capacity for ZCN-1 and ZCN-2.5 were 15.02 and 15.53 mg g^{-1} , respectively, which were slightly higher than that of bare g-CN (13.44 mg g^{-1}). The increment adsorption capacity of ZCN-1 and ZCN-2.5 and the decreases adsorption capacity of higher ZnO content composites compared to pure g-CN can be attributed

to various factors. The increase in π - π restacking, electron transfer from g-CN to ZnO, and the formation of an internal electric field in the composites enhance the π - π interaction and electrostatic attraction between the g-CN network and the aromatic ring of orange II dye [19,22]. The probability of hydrogen bond formation between the orange II dye and the g-CN network in the composite may increase due to the reduction of N-H bonds and adsorbed water or moisture content. Furthermore, increasing the total pore volume and average pore size of ZCN-1 and ZCN-2.5 composites can increase the adsorption capacity [77]. The surface area and crystallinity of these composites did not change significantly compared to pure g-CN. Hence, the adsorption ability of the ZCN-1 and ZCN-2.5 composites was increased compared to pure g-CN. On the contrary, for ZCN composites containing a further increasing amount of ZnO, the surface area and total pore volume are drastically decreased compared to pure g-CN. Average pore diameter values are also decreasing. Furthermore, the crystallinity of these composites was completely diminished. The decrement of factors such as surface area, pore volume, pore diameter, and crystallinity may influence the increment of factors such as the π - π interaction, electrostatic attraction, and hydrogen bond for these composites. Hence, the adsorption ability was decreased compared to pure g-CN.

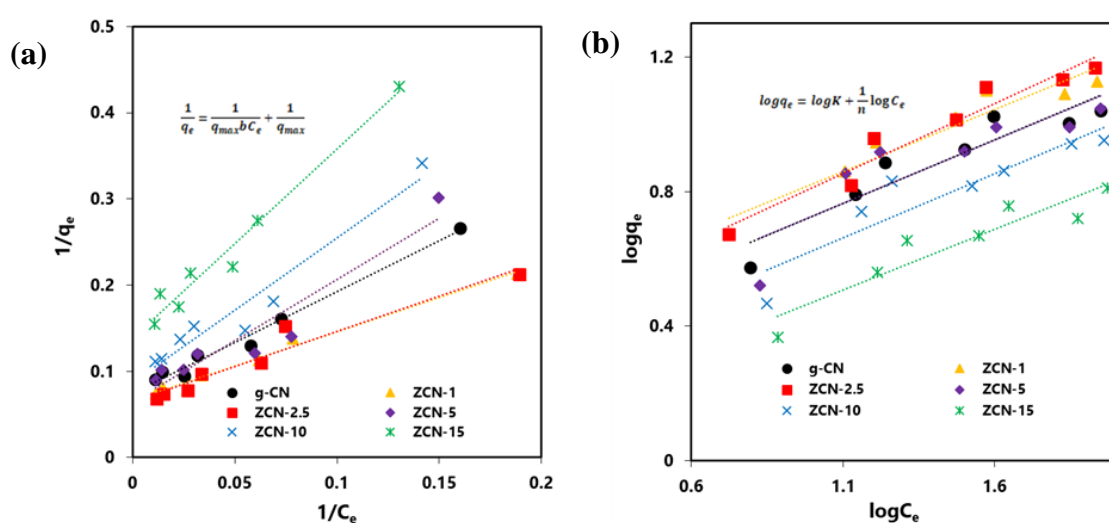


Figure 4.10 (a) Langmuir isotherm and (b) Freundlich isotherm for adsorption of Orange II dye by pure g-CN and different ZCN composites.

Table 4.3 Langmuir isotherm model fitting results

Photocatalysts	intercept	slope	q_{\max}	b	R^2
g-CN	0.074	1.778	13.441	0.042	0.983
ZCN-1	0.067	0.792	15.015	0.084	0.987
ZCN-2.5	0.064	0.821	15.528	0.078	0.987
ZCN-5	0.065	1.420	15.480	0.045	0.903
ZCN-10	0.087	1.679	11.507	0.052	0.942
ZCN-15	0.138	2.211	7.246	0.062	0.970

Table 4.4 Freundlich isotherm model fitting results

Photocatalysts	intercept	slope	K	n	R^2
g-CN	0.346	0.381	2.217	2.627	0.879
ZCN-1	0.454	0.369	2.846	2.711	0.920
ZCN-2.5	0.395	0.417	2.485	2.398	0.940
ZCN-5	0.349	0.378	2.235	2.648	0.762
ZCN-10	0.244	0.382	1.753	2.621	0.838
ZCN-15	0.109	0.361	1.286	2.768	0.874

The adsorption thermodynamics were investigated by keeping the mixture of orange II dye solution (10 mg L⁻¹) and ZCN-2.5 with constant stirring in a dark condition at 20, 30, 40, and 50 °C for 30 minutes. The adsorption of orange II solution onto ZCN-2.5 has been found to decrease with increasing temperature (Figure 4.11a.). A number of thermodynamic parameters, including Gibbs free-energy change (ΔG^0), enthalpy change (ΔH^0), and entropy

change (ΔS^0) were estimated to inspect the adsorption nature of the present work [75,78]. The Gibb's free energy change (ΔG^0) is computed by the following equation:

$$\Delta G^0 = -RT \ln k_d = -RT \ln \frac{q_e}{C_e} \quad (4.6)$$

where R is the universal gas constant ($8.3145 \text{ J mol}^{-1} \text{ K}^{-1}$), T is the temperature (K), Kd is the distribution coefficient (L g^{-1}), q_e is the equilibrium concentration of orange II on the adsorbent ZCN-2.5 (mg g^{-1}), and C_e is the equilibrium concentration of orange II in the aqueous phase (mg L^{-1}).

The Van't Hoff equation can be used to explain the relationship between enthalpy change and entropy change as follows:

$$\ln k_d = \frac{\Delta S_0}{R} - \frac{\Delta H^0}{RT} \quad (4.7)$$

As illustrated in Figure 4.11b, the values of enthalpy change (ΔH) and entropy change (ΔS) were determined from the slope and intercept of $\ln K_d$ vs. $1/T$ plots. The values of the estimated thermodynamic parameters are shown in Table 4.5.

The positive values of Gibb's free energy change (ΔG^0) suggested that the adsorption of orange II solution onto ZCN-2.5 was not a spontaneous process. Besides, as shown in Figure 4.11a and Table 4.5, Gibb's free energy change (ΔG^0) increased with increasing temperature, indicating the adsorption decreased with increasing temperature. The negative value of ΔS (-45.6 J/mol) exposed the decrease in randomness during the adsorption process. Furthermore, the negative value of ΔH (-13.1 KJ/mol) revealed the exothermic nature of the adsorption procedure.

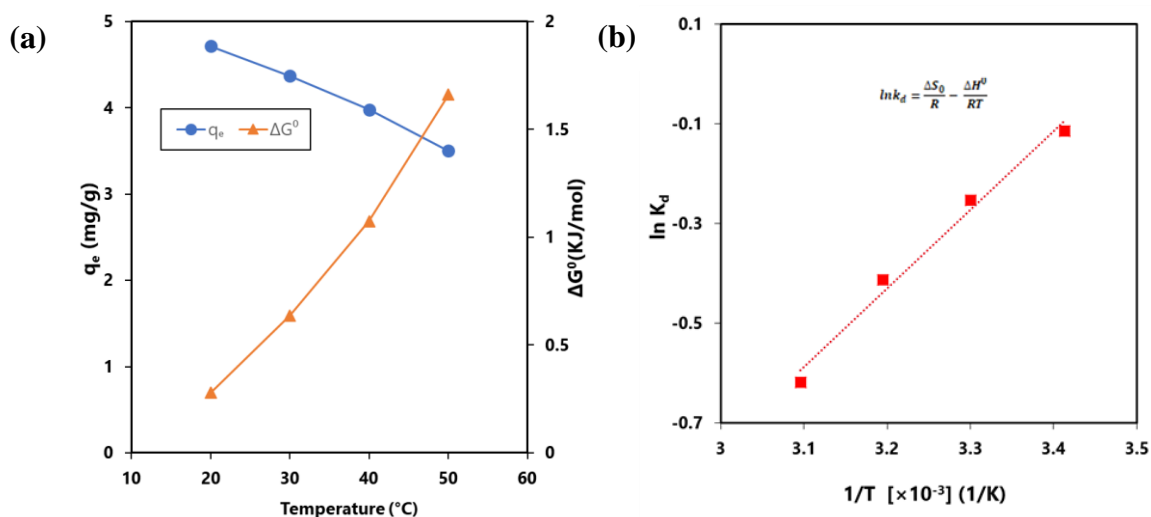


Figure 4.11 (a) The relationship between temperature and amount of orange II dye (10 ppm) adsorbed q_e on ZCN-2.5 composite as well as corresponding Gibbs free energy change (ΔG^0); (b) the plot of $\ln K_d$ versus $1/T$.

Table 4.5 Thermodynamics parameters for adsorption of orange II dye on ZCN-2.5 composite

Temperature (°C)	Gibbs free energy change (ΔG^0) (KJ mol ⁻¹)	enthalpy change (ΔH^0) (KJ mol ⁻¹)	entropy change (ΔS^0) (J mol ⁻¹)
20	0.279		
30	0.638		
40	1.075	-13.121	-45.568
50	1.662		

Furthermore, the pH value of the solution affects the surface charge of the adsorbent. Hereafter, the effect of the pH of the solution on the adsorption of the dye can be considered an important factor. The impact of pH on the adsorption of orange II dye solution (10 mg L⁻¹) at several pH such as 3, 5.5 (uncontrolled pH), 7, and 10 on ZCN-2.5 was investigated at room temperature (20 °C). As shown in Figure 4.12, the adsorption decreased with the increasing pH of the dye solution. At lower pH, the surface of the composite is positively charged and

negatively charged at higher pH. At lower pH, the positively charged surface of the composite may be electrostatically attracted to the anionic orange II dye, which could enhance the adsorption.

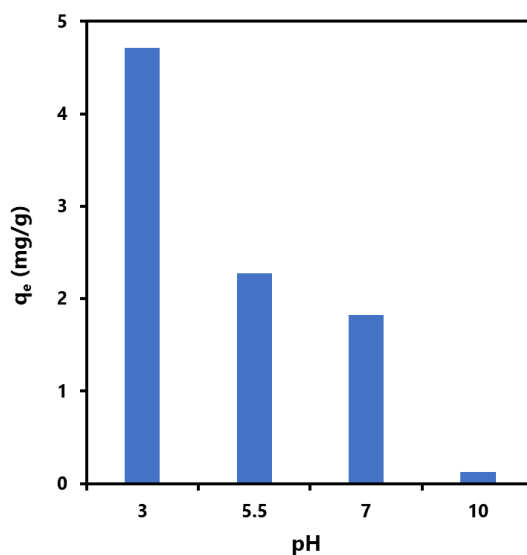


Figure 4.12. The effect of pH for adsorption of orange II dye (10 ppm) on ZCN-2.5 composite.

4.3.10 Photocatalytic Degradation of Orange II Solution

The photocatalytic degradation of aqueous orange II dye by using synthesized ZCN composites was investigated under visible light irradiation. As shown in Figure 4.13a, the degradation capacity of ZCN composites increased as the amount of ZnO in the composite increased. The ZCN-2.5 composite showed the highest photocatalytic degradation. The increase in visible light absorption ability as well as the decreased optical band gap and higher charge separation of the composites are responsible for enhanced photocatalytic degradation [79]. The composites containing higher amount of ZnO have very low surface area and crystallinity. Hence, the photocatalytic degradation ability of the composites decreased, further increasing the ZnO content after the ZCN-2.5 composite.

Furthermore, the Langmuir–Hinshelwood (L–H) model was utilized to investigate the reaction rate and kinetics of the photocatalytic degradation process. Equation 4.8 represents the L–H model that was developed by Turchi and Ollisand.

$$r_0 = -\frac{dC}{dt} = \frac{kKC}{1 + KC} \quad (4.8)$$

where, r_0 is the rate of the degradation reaction, k is the rate constant, and K and C are the adsorption equilibrium constant and reactant concentration, respectively. If the initial concentration C_0 is very small, it can be shortened to eq. 4.9 as follows:

$$-\ln\left(\frac{C}{C_0}\right) = kKt = k_{obs}t \quad (4.9)$$

In relation to $-\ln(C/C_0)$, the equation becomes a linear expression on time t , where k_{obs} is the reaction rate constant [80]. So as to check the assumption, $-\ln(C/C_0)$ was plotted as a function of irradiation time for the degradation of orange II by the photocatalysts. As shown in Figure 4.13b, the linear relations were attained as expected. Hence, the degradation process follows pseudo-first-order reaction kinetics. The kinetic parameters, such as rate constant, half-life, and correlation coefficient are presented in Table 4.6. It was found that the degradation rate of orange II with the ZCN-2.5 composite (0.02 min^{-1}) was 6.67 times higher than that obtained with bare g-CN (0.003 min^{-1}). Hence, the relative degradation ability of the ZCN-2.5 composite was significantly higher than its relative adsorption ability compared to bare g-CN (Table 4.3 and 4.6).

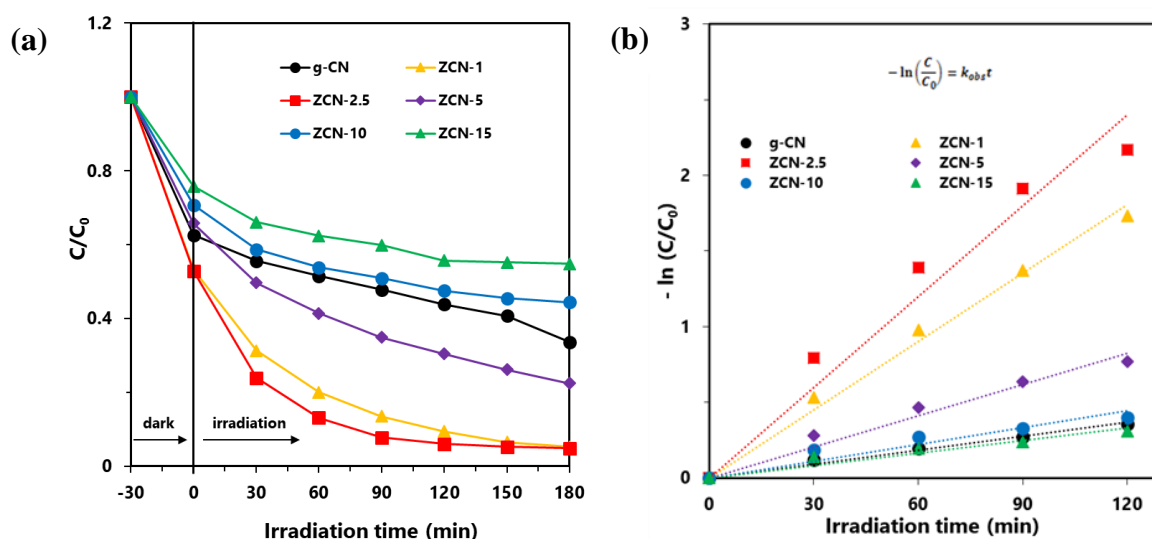


Figure 4.13 (a) Photocatalytic degradation of orange II dye solution using different catalyst with the irradiation of visible light and (b) the plot of $-\ln(C/C_0)$ versus irradiation time; orange II: 10 mg L^{-1} (30 mL), photocatalyst: 30 mg.

Table 4.6 Kinetic parameters on photocatalytic degradation of Orange (II) solution (10 mg L^{-1}) using pure g-CN and different ZCN composites

Photocatalysts	Rate constant (min^{-1})	Half-life (min)	R^2
g-CN	0.003	231	0.987
ZCN-1	0.015	46	0.991
ZCN-2.5	0.020	35	0.954
ZCN-5	0.007	100	0.968
ZCN-10	0.004	187	0.889
ZCN-15	0.003	257	0.916

Furthermore, the reusability of the ZCN-2.5 composite was evaluated by five sequential cycles of orange II dye degradation with visible light irradiation. As shown in Figure 4.14, it was observed that the degradation of orange II dye solution using ZCN-2.5 decreased by a

negligible amount after the five cycles. These findings suggest that the ZCN-2.5 composite is highly stable and has a repeatable ability to degrade orange II solution under visible light irradiation.

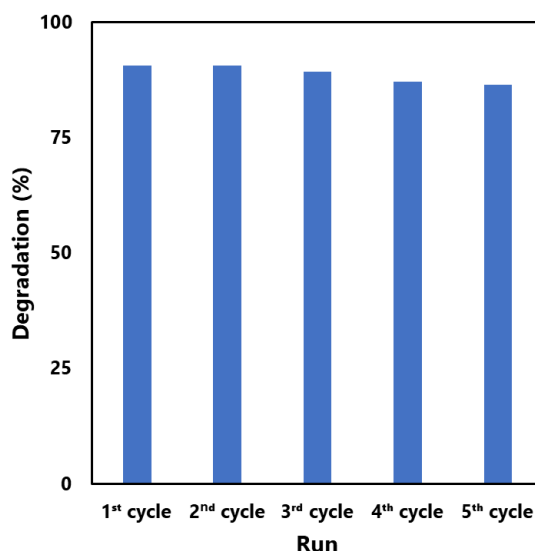


Figure 4.14 Photocatalytic reusability of ZCN-2.5 composite on photocatalytic degradation of orange II solution.

4.3.11 Mechanism

The removal of orange II dye from aqueous solution using ZCN composites involved adsorption and photodegradation processes. The adsorption is attributed to the π - π interactions, electrostatic interactions, H-bonding, acid-bas interactions between composite and dye, and pore filling of the composite by the dye molecule (Figure 4.15a). It can be seen that the π conjugations are restacking due to the reforming of the triazine ring of the g-CN network by ZnO [47]. Furthermore, electrons are transferred from the g-CN network to ZnO and form an internal electric field [48,49]. These may enhance the π - π interactions with the aromatic benzene ring of orange II dye. The induced positive charge of the g-CN network may attract the negative charge of the dye molecule through electrostatic interactions and enhance adsorption. The heterocyclic N-atoms of the s-triazine ring in the ZCN composites and g-CN

may interact with the dye molecule through hydrogen bonding, as shown in Figure 4.15a [19]. The g-CN network may have slightly basic properties due to the presence of N atoms [81]. Hence, acid-base interaction may involve g-CN and the acidic character of orange II during adsorption. Due to the presence of lower quantity of adsorbed water in the composites, the adsorption of orange II on the ZCN composites may increase through available pore filling. On the contrary, due to the excess amount of ZnO in the ZCN composites with higher content of ZnO, the pores of the g-CN framework are blocked, and the surface area is drastically decreased. Hence, adsorption ability decreased.

The photocatalytic degradation reaction involves the interaction of visible light with the ZCN composite and the formation of photocharges (Figure 4.15b). Electrons in the valence band of the g-CN were transferred to the conduction band of ZnO through the interfacial charge transfer pathway. As a result, e^-/h^+ pair recombination was decreased, and the separation of photocharges was enhanced. Based on the previously reported literature, the reactive species of $\bullet O_2^-$, $\bullet OH$, and h^+ are involved during the photocatalytic degradation reactions [57,79]. Environmental oxygen was reacted with the photoelectrons of g-CN to create the reactive radical of $\bullet O_2^-$. Then the $\bullet O_2^-$ reacted with H^+ to form the $\bullet OH$ radical. After that, the $\bullet O_2^-$ and $\bullet OH$ radicals reacted with the orange II dye solution and produced degraded products. The orange II dye was also degraded by the direct reaction of h^+ in the valence band of g-CN. Due to the extensively lowered surface area and crystallinity, the ZCN composites containing higher ZnO content showed lowered photocatalytic degradation activity.

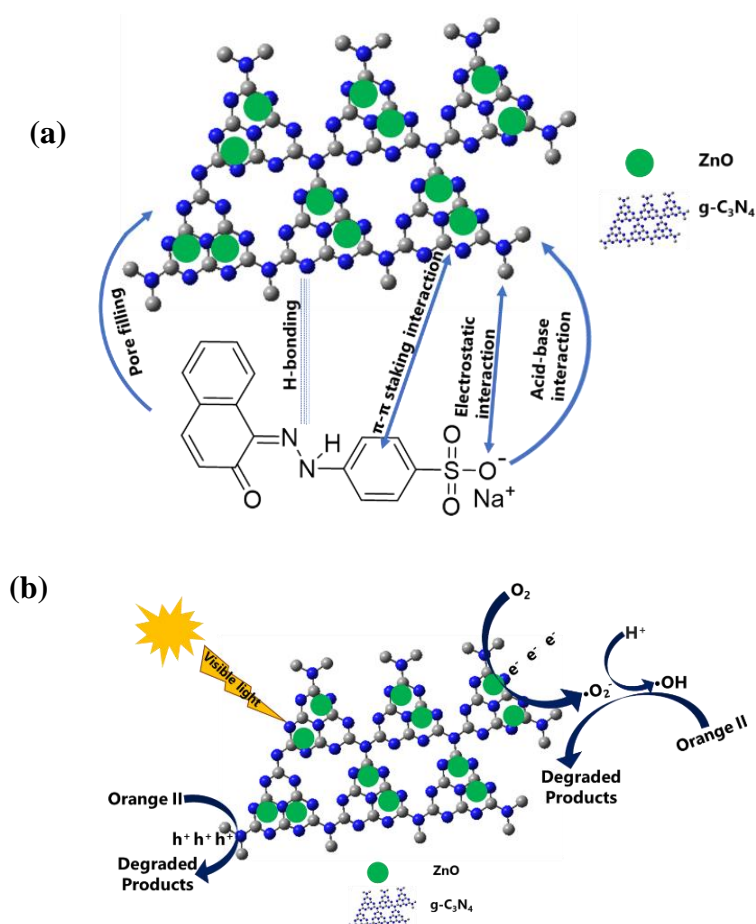


Figure 4.15 Proposed mechanism of (a) adsorption and (b) photocatalytic degradation of orange II dye solution using ZCN composites.

4.4 Conclusions

In summary, ZCN composites were fabricated by a simple calcination of mixtures of urea and zinc acetate. The adsorption of orange II dye on the ZCN composites is attributed to the π - π interactions, electrostatic interactions, H-bonding, acid-bas interactions between the composite and dye, and pore filling of the composites. The adsorption isotherms were fitted with the Langmuir isotherm, and the maximum adsorption ability of ZCN-2.5 was slightly higher than that of bare g-CN. The photocatalytic degradation of orange II dye solution using ZCN composites with visible light irradiation is attributed to the enhanced visible light absorption efficacy and decrement of photogenerated e^-/h^+ pair recombination. The photocatalytic degradation followed pseudo-first-order reaction kinetics. The ZCN-2.5 composite showed

significantly enhanced photodegradability compared to bare g-CN. Drastically decreased surface area and crystallinity of composites containing higher amount of ZnO are responsible for their lower adsorption and degradation abilities.

4.5 References

1. Yagub, M.T.; Sen, T.K.; Afroze, S.; Ang, H.M. Dye and Its Removal from Aqueous Solution by Adsorption: A Review. *Adv. Colloid Interface Sci.* **2014**, *209*, 172–184, doi:10.1016/j.cis.2014.04.002.
2. Dawood, S.; Sen, T.K.; Phan, C. Synthesis and Characterisation of Novel-Activated Carbon from Waste Biomass Pine Cone and Its Application in the Removal of Congo Red Dye from Aqueous Solution by Adsorption. *Water, Air, Soil Pollut.* **2014**, *225*, 1818, doi:10.1007/s11270-013-1818-4.
3. Sokolowska-Gajda, J.; Freeman, H.S.; Reife, A. Synthetic Dyes Based on Environmental Considerations. Part 2: Iron Complexes Formazan Dyes. *Dye. Pigment.* **1996**, *30*, 1–20, doi:10.1016/0143-7208(95)00048-8.
4. Wróbel, D.; Boguta, A.; Ion, R.M. Mixtures of Synthetic Organic Dyes in a Photoelectrochemical Cell. *J. Photochem. Photobiol. A Chem.* **2001**, *138*, 7–22, doi:10.1016/S1010-6030(00)00377-4.
5. Sen, T.K.; Afroze, S.; Ang, H.M. Equilibrium, Kinetics and Mechanism of Removal of Methylene Blue from Aqueous Solution by Adsorption onto Pine Cone Biomass of Pinus Radiata. *Water, Air, Soil Pollut.* **2011**, *218*, 499–515, doi:10.1007/s11270-010-0663-y.
6. Verma, A.K.; Dash, R.R.; Bhunia, P. A Review on Chemical Coagulation/flocculation Technologies for Removal of Colour from Textile Wastewaters. *J. Environ. Manage.* **2012**, *93*, 154–168, doi:10.1016/j.jenvman.2011.09.012.
7. Duman, O.; Tunç, S.; Polat, T.G.; Bozoğlan, B.K. Synthesis of Magnetic Oxidized

- Multiwalled Carbon Nanotube- κ -Carrageenan-Fe₃O₄ Nanocomposite Adsorbent and Its Application in Cationic Methylene Blue Dye Adsorption. *Carbohydr. Polym.* **2016**, *147*, 79–88, doi:10.1016/j.carbpol.2016.03.099.
8. Wang, Y.; Xie, Y.; Zhang, Y.; Tang, S.; Guo, C.; Wu, J.; Lau, R. Anionic and Cationic Dyes Adsorption on Porous Poly-Melamine-Formaldehyde Polymer. *Chem. Eng. Res. Des.* **2016**, *114*, 258–267, doi:10.1016/j.cherd.2016.08.027.
 9. Bedin, K.C.; Martins, A.C.; Cazetta, A.L.; Pezoti, O.; Almeida, V.C. KOH-Activated Carbon Prepared from Sucrose Spherical Carbon: Adsorption Equilibrium, Kinetic and Thermodynamic Studies for Methylene Blue Removal. *Chem. Eng. J.* **2016**, *286*, 476–484, doi:10.1016/j.cej.2015.10.099.
 10. Jirankova, H.; Mrazek, J.; Dolecek, P.; Cakl, J. Organic Dye Removal by Combined Adsorption—membrane Separation Process. *Desalin. Water Treat.* **2010**, *20*, 96–101, doi:10.5004/dwt.2010.1170.
 11. Kobya, M.; Bayramoglu, M.; Eyvaz, M. Techno-Economical Evaluation of Electrocoagulation for the Textile Wastewater Using Different Electrode Connections. *J. Hazard. Mater.* **2007**, *148*, 311–318, doi:10.1016/j.jhazmat.2007.02.036.
 12. Palanisamy, S.; Nachimuthu, P.; Awasthi, M.K.; Ravindran, B.; Chang, S.W.; Palanichamy, M.; Nguyen, D.D. Application of Electrochemical Treatment for the Removal of Triazine Dye Using Aluminium Electrodes. *J. Water Supply Res. Technol.* **2020**, *69*, 345–354, doi:10.2166/aqua.2020.109.
 13. Lin, S.H.; Peng, C.F. Treatment of Textile Wastewater by Electrochemical Method. *Water Res.* **1994**, *28*, 277–282, doi:10.1016/0043-1354(94)90264-X.
 14. Varjani, S.; Rakholiya, P.; Ng, H.Y.; You, S.; Teixeira, J.A. Microbial Degradation of Dyes: An Overview. *Bioresour. Technol.* **2020**, *314*, 123728, doi:10.1016/j.biortech.2020.123728.

15. Suhag, M.H.; Haque, K.A.U.; Hossen, M.Z.; Azad, A.K.; Younus, M. Biodegradation of Azo Dyes and Dyes Present in Textile Wastewaters Using *Bacillus* Sp. az28, Obtained from Industrial Effluents. *J. Bangladesh Acad. Sci.* **2021**, *45*, 117–122, doi:10.3329/jbas.v45i1.54263.
16. Gözmen, B.; Kayan, B.; Gizir, A.M.; Hesenov, A. Oxidative Degradations of Reactive Blue 4 Dye by Different Advanced Oxidation Methods. *J. Hazard. Mater.* **2009**, *168*, 129–136, doi:10.1016/j.jhazmat.2009.02.011.
17. Zhang, Y.; Shaad, K.; Vollmer, D.; Ma, C. Treatment of Textile Wastewater Using Advanced Oxidation Processes—A Critical Review. *Water* **2021**, *13*, 3515, doi:10.3390/w13243515.
18. Elias, M.; Akter, S.; Hossain, M.A.; Suhag, M.H. Fabrication of Zn₃(PO₄)₂/carbon Nanotubes Nanocomposite Thin Film via Sol-Gel Drop Coating Method with Enhanced Photocatalytic Activity. *Thin Solid Films* **2021**, *717*, 138472, doi:10.1016/j.tsf.2020.138472.
19. Yousefi, M.; Villar-Rodil, S.; Paredes, J.I.; Moshfegh, A.Z. Oxidized Graphitic Carbon Nitride Nanosheets as an Effective Adsorbent for Organic Dyes and Tetracycline for Water Remediation. *J. Alloys Compd.* **2019**, *809*, 151783, doi:10.1016/j.jallcom.2019.151783.
20. Ali, I. New Generation Adsorbents for Water Treatment. *Chem. Rev.* **2012**, *112*, 5073–5091, doi:10.1021/cr300133d.
21. Panneri, S.; Ganguly, P.; Mohan, M.; Nair, B.N.; Mohamed, A.A.P.; Warriar, K.G.; Hareesh, U.S. Photoregenerable, Bifunctional Granules of Carbon-Doped G-C 3 N 4 as Adsorptive Photocatalyst for the Efficient Removal of Tetracycline Antibiotic. *ACS Sustain. Chem. Eng.* **2017**, *5*, 1610–1618, doi:10.1021/acssuschemeng.6b02383.
22. Yan, L.; Gao, H.; Chen, Y. Na-Doped Graphitic Carbon Nitride for Removal of Aqueous

- Contaminants via Adsorption and Photodegradation. *ACS Appl. Nano Mater.* **2021**, *4*, 7746–7757, doi:10.1021/acsanm.1c01035.
23. Xing, R.; Wang, W.; Jiao, T.; Ma, K.; Zhang, Q.; Hong, W.; Qiu, H.; Zhou, J.; Zhang, L.; Peng, Q. Bioinspired Polydopamine Sheathed Nanofibers Containing Carboxylate Graphene Oxide Nanosheet for High-Efficient Dyes Scavenger. *ACS Sustain. Chem. Eng.* **2017**, *5*, 4948–4956, doi:10.1021/acssuschemeng.7b00343.
24. Gul, T.; Ahmad, S.; Khan, I.; Khan, I.; Almeahmadi, M.; Amer Alsaiani, A.; Allahyani, M.; Saeed, K. Photodegradation of Orange II Dye Using P-N Junction NiO/TiO₂ Composite, and Assessment of Its Biological Activities. *J. Saudi Chem. Soc.* **2023**, *27*, 101654, doi:10.1016/j.jscs.2023.101654.
25. Riaz, N.; Chong, F.K.; Dutta, B.K.; Man, Z.B.; Khan, M.S.; Nurlaela, E. Photodegradation of Orange II under Visible Light Using Cu–Ni/TiO₂: Effect of Calcination Temperature. *Chem. Eng. J.* **2012**, *185–186*, 108–119, doi:10.1016/j.cej.2012.01.052.
26. Khan, N.A.; Saeed, K.; Khan, I.; Gul, T.; Sadiq, M.; Uddin, A.; Zekker, I. Efficient Photodegradation of Orange II Dye by Nickel Oxide Nanoparticles and Nanoclay Supported Nickel Oxide Nanocomposite. *Appl. Water Sci.* **2022**, *12*, 131, doi:10.1007/s13201-022-01647-x.
27. Hung-Lung, C.; Kuo-Hsiung, L.; Shih-Yu, C.; Ching-Guan, C.; San-De, P. Dye Adsorption on Biosolid Adsorbents and Commercially Activated Carbon. *Dye. Pigment.* **2007**, *75*, 52–59, doi:10.1016/j.dyepig.2006.05.017.
28. Pedro Silva, J.; Sousa, S.; Rodrigues, J.; Antunes, H.; Porter, J.J.; Gonçalves, I.; Ferreira-Dias, S. Adsorption of Acid Orange 7 Dye in Aqueous Solutions by Spent Brewery Grains. *Sep. Purif. Technol.* **2004**, *40*, 309–315, doi:10.1016/j.seppur.2004.03.010.
29. Métivier-Pignon, H.; Faur-Brasquet, C.; Le Cloirec, P. Adsorption of Dyes onto

- Activated Carbon Cloths: Approach of Adsorption Mechanisms and Coupling of ACC with Ultrafiltration to Treat Coloured Wastewaters. *Sep. Purif. Technol.* **2003**, *31*, 3–11, doi:10.1016/S1383-5866(02)00147-8.
30. Chen, X.G.; Lv, S.S.; Ye, Y.; Cheng, J.P.; Yin, S.H. Preparation and Characterization of Rice Husk/ferrite Composites. *Chinese Chem. Lett.* **2010**, *21*, 122–126, doi:10.1016/j.cclet.2009.08.003.
31. Gupta, V.K.; Mittal, A.; Gajbe, V.; Mittal, J. Removal and Recovery of the Hazardous Azo Dye Acid Orange 7 through Adsorption over Waste Materials: Bottom Ash and De-Oiled Soya. *Ind. Eng. Chem. Res.* **2006**, *45*, 1446–1453, doi:10.1021/ie051111f.
32. Uzun, İ.; Güzel, F. Rate Studies on the Adsorption of Some Dyestuffs and P-Nitrophenol by Chitosan and Monocarboxymethylated(mcm)-Chitosan from Aqueous Solution. *J. Hazard. Mater.* **2005**, *118*, 141–154, doi:10.1016/j.jhazmat.2004.10.006.
33. Jin, X.; Jiang, M.; Shan, X.; Pei, Z.; Chen, Z. Adsorption of Methylene Blue and Orange II onto Unmodified and Surfactant-Modified Zeolite. *J. Colloid Interface Sci.* **2008**, *328*, 243–247, doi:10.1016/j.jcis.2008.08.066.
34. Khatun, A.; Suhag, M.H.; Tateishi, I.; Furukawa, M.; Katsumata, H.; Kaneco, S. Facile Synthesis of ZnO/g-C₃N₄ with Enhanced Photocatalytic Performance for the Reduction of Cr(VI) in Presence of EDTA Under Visible Light Irradiation. *Int. J. Environ. Res.* **2023**, *17*, 1–17, doi:10.1007/s41742-023-00522-0.
35. Shalom, M.; Inal, S.; Fettkenhauer, C.; Neher, D.; Antonietti, M. Improving Carbon Nitride Photocatalysis by Supramolecular Preorganization of Monomers. *J. Am. Chem. Soc.* **2013**, *135*, 7118–7121, doi:10.1021/ja402521s.
36. Cheng, C.; Huang, Y.; Wang, J.; Zheng, B.; Yuan, H.; Xiao, D. Anodic Electrogenerated Chemiluminescence Behavior of Graphite-Like Carbon Nitride and Its Sensing for Rutin. *Anal. Chem.* **2013**, *85*, 2601–2605, doi:10.1021/ac303263n.

37. Wu, M.; Wang, Q.; Sun, Q.; Jena, P. Functionalized Graphitic Carbon Nitride for Efficient Energy Storage. *J. Phys. Chem. C* **2013**, *117*, 6055–6059, doi:10.1021/jp311972f.
38. Uzzaman, M.; Suhag, M.H.; Katsumata, H.; Tateishi, I.; Furukawa, M.; Kaneco, S. A Graphitic Carbon Nitride Photocatalyst with a Benzene-Ring-Modified Isotype Heterojunction for Visible-Light-Driven Hydrogen Production. *Catal. Sci. Technol.* **2024**, *14*, 267–278, doi:10.1039/D3CY01461D.
39. Tian, J.; Liu, Q.; Asiri, A.M.; Al-Youbi, A.O.; Sun, X. Ultrathin Graphitic Carbon Nitride Nanosheet: A Highly Efficient Fluorosensor for Rapid, Ultrasensitive Detection of Cu 2+. *Anal. Chem.* **2013**, *85*, 5595–5599, doi:10.1021/ac400924j.
40. Ren, B.; Xu, Y.; Zhang, L.; Liu, Z. Carbon-Doped Graphitic Carbon Nitride as Environment-Benign Adsorbent for Methylene Blue Adsorption: Kinetics, Isotherm and Thermodynamics Study. *J. Taiwan Inst. Chem. Eng.* **2018**, *88*, 114–120, doi:10.1016/j.jtice.2018.03.041.
41. Marzi Khosrowshahi, E.; Razmi, H. Application of Sunflower Stalk-Carbon Nitride Nanosheets as a Green Sorbent in the Solid-Phase Extraction of Polycyclic Aromatic Hydrocarbons Followed by High-Performance Liquid Chromatography. *J. Sep. Sci.* **2018**, *41*, 2020–2028, doi:10.1002/jssc.201701248.
42. Wang, T.; Huang, M.; Liu, X.; Zhang, Z.; Liu, Y.; Tang, W.; Bao, S.; Fang, T. Facile One-Step Hydrothermal Synthesis of α -Fe₂O₃/g-C₃N₄ Composites for the Synergistic Adsorption and Photodegradation of Dyes. *RSC Adv.* **2019**, *9*, 29109–29119, doi:10.1039/C9RA05100G.
43. Ismael, M. The Photocatalytic Performance of the ZnO/g-C₃N₄ Composite Photocatalyst toward Degradation of Organic Pollutants and Its Inactivity toward Hydrogen Evolution: The Influence of Light Irradiation and Charge Transfer. *Chem.*

- Phys. Lett.* **2020**, 739, 136992, doi:10.1016/j.cplett.2019.136992.
44. Zhong, Q.; Lan, H.; Zhang, M.; Zhu, H.; Bu, M. Preparation of Heterostructure G-C₃N₄/ZnO Nanorods for High Photocatalytic Activity on Different Pollutants (MB, RhB, Cr(VI) and Eosin). *Ceram. Int.* **2020**, 46, 12192–12199, doi:10.1016/j.ceramint.2020.01.265.
 45. Kim, J.S.; Oh, J.W.; Woo, S.I. Investigation for the Effects of Ball Milling Process on the Physical Characteristics, the Behaviors of Carriers and the Photocatalytic Activity of Sulfur Doped G-C₃N₄. *Int. J. Hydrogen Energy* **2017**, 42, 5485–5495, doi:10.1016/j.ijhydene.2016.08.077.
 46. He, Q.; Zhou, F.; Zhan, S.; Yang, Y.; Liu, Y.; Tian, Y.; Huang, N. Enhancement of Photocatalytic and Photoelectrocatalytic Activity of Ag Modified Mpg-C₃N₄ Composites. *Appl. Surf. Sci.* **2017**, 391, 423–431, doi:10.1016/j.apsusc.2016.07.005.
 47. Zhao, F.; Khaing, K.K.; Yin, D.; Liu, B.; Chen, T.; Wu, C.; Huang, K.; Deng, L.; Li, L. Large Enhanced Photocatalytic Activity of G-C₃N₄ by Fabrication of a Nanocomposite with Introducing Upconversion Nanocrystal and Ag Nanoparticles. *RSC Adv.* **2018**, 8, 42308–42321, doi:10.1039/C8RA07901C.
 48. Suhag, M.H.; Katsumata, H.; Tateishi, I.; Furukawa, M.; Kaneco, S. Black Phosphorus-Doped Graphitic Carbon Nitride with Aromatic Benzene Rings for Efficient Photocatalytic Hydrogen Production. *Langmuir* **2023**, 39, 13121–13131, doi:10.1021/acs.langmuir.3c01518.
 49. Ali, A.; Amin, M.; Tahir, M.; Ali, S.S.; Hussain, A.; Ahmad, I.; Mahmood, A.; Farooq, M.U.; Farid, M.A. G-C₃N₄/Fe₃O₄ Composites Synthesized via Solid-State Reaction and Photocatalytic Activity Evaluation of Methyl Blue Degradation under Visible Light Irradiation. *Front. Mater.* **2023**, 10, 1180646, doi:10.3389/fmats.2023.1180646.
 50. Gayathri, M.; Sakar, M.; Satheeshkumar, E.; Sundaravadivel, E. Insights into the

- Mechanism of ZnO/g-C₃N₄ Nanocomposites toward Photocatalytic Degradation of Multiple Organic Dyes. *J. Mater. Sci. Mater. Electron.* **2022**, *33*, 9347–9357, doi:10.1007/s10854-021-07302-6.
51. Yongheng, D.; Huayu, Y.; Jiang, L.; Qi, S.; Qianwen, Y.; Yuntao, Z. Direct Z-Scheme P-TiO₂/g-C₃N₄ Heterojunction for the Photocatalytic Degradation of Sulfa Antibiotics. *RSC Adv.* **2023**, *13*, 5957–5969, doi:10.1039/D2RA07289K.
 52. Shoaib, M.; Naz, M.Y.; Shukrullah, S.; Munir, M.A.; Irfan, M.; Rahman, S.; Ghanim, A.A.J. Dual S-Scheme Heterojunction CdS/TiO₂/g-C₃N₄ Photocatalyst for Hydrogen Production and Dye Degradation Applications. *ACS Omega* **2023**, *8*, 43139–43150, doi:10.1021/acsomega.3c06759.
 53. Vuggili, S.B.; Gaur, U.K.; Sharma, M. 2D/2D Facial Interaction of Nitrogen-Doped G-C₃N₄/In₂S₃ Nanosheets for High Performance by Visible-Light-Induced Photocatalysis. *J. Alloys Compd.* **2022**, *902*, 163757, doi:10.1016/j.jallcom.2022.163757.
 54. Bhuvaneswari, K.; Palanisamy, G.; Bharathi, G.; Pazhanivel, T.; Upadhyaya, I.R.; Kumari, M. A.; Rajesh, R.P.; Govindasamy, M.; Ghfar, A.; Al-Shaalan, N.H. Visible Light Driven Reduced Graphene Oxide Supported ZnMgAl LTH/ZnO/g-C₃N₄ Nanohybrid Photocatalyst with Notable Two-Dimension Formation for Enhanced Photocatalytic Activity towards Organic Dye Degradation. *Environ. Res.* **2021**, *197*, 111079, doi:10.1016/j.envres.2021.111079.
 55. Katsumata, H.; Islam Molla, M.A.; Islam, J.B.; Tateishi, I.; Furukawa, M.; Kaneco, S. Dual Z-Scheme Heterojunction G-C₃N₄/Ag₃PO₄/AgBr Photocatalyst with Enhanced Visible-Light Photocatalytic Activity. *Ceram. Int.* **2022**, *48*, 21898–21905, doi:10.1016/j.ceramint.2022.04.176.
 56. Paul, D.R.; Gautam, S.; Panchal, P.; Nehra, S.P.; Choudhary, P.; Sharma, A. ZnO-

- Modified G-C 3 N 4 : A Potential Photocatalyst for Environmental Application. *ACS Omega* **2020**, *5*, 3828–3838, doi:10.1021/acsomega.9b02688.
57. Zhang, Z.; Sun, Y.; Wang, Y.; Yang, Y.; Wang, P.; Shi, L.; Feng, L.; Fang, S.; Liu, Q.; Ma, L.; et al. Synthesis and Photocatalytic Activity of G-C3N4/ZnO Composite Microspheres under Visible Light Exposure. *Ceram. Int.* **2022**, *48*, 3293–3302, doi:10.1016/j.ceramint.2021.10.104.
58. Suhag, M.H.; Khatun, A.; Tateishi, I.; Furukawa, M.; Katsumata, H.; Kaneco, S. One-Step Fabrication of the ZnO/g-C3N4 Composite for Visible Light-Responsive Photocatalytic Degradation of Bisphenol E in Aqueous Solution. *ACS Omega* **2023**, *8*, 11824–11836, doi:10.1021/acsomega.2c06678.
59. Jingyu, H.; Ran, Y.; Zhaohui, L.; Yuanqiang, S.; Lingbo, Q.; Nti Kani, A.; Kani, A.N. In-Situ Growth of ZnO Globular on G-C3N4 to Fabrication Binary Heterojunctions and Their Photocatalytic Degradation Activity on Tetracyclines. *Solid State Sci.* **2019**, *92*, 60–67, doi:10.1016/j.solidstatesciences.2019.02.009.
60. Sharifalhoseini, Z.; Entezari, M.H.; Shahidi, M. Sonication Affects the Quantity and the Morphology of ZnO Nanostructures Synthesized on the Mild Steel and Changes the Corrosion Protection of the Surface. *Ultrason. Sonochem.* **2018**, *41*, 492–502, doi:10.1016/j.ultsonch.2017.10.012.
61. Mathialagan, A.; Manavalan, M.; Venkatachalam, K.; Mohammad, F.; Oh, W.C.; Sagadevan, S. Fabrication and Physicochemical Characterization of G-C3N4/ZnO Composite with Enhanced Photocatalytic Activity under Visible Light. *Opt. Mater. (Amst)*. **2020**, *100*, 109643, doi:10.1016/j.optmat.2019.109643.
62. Li, L.; Sun, S.-Q.; Wang, Y.-X.; Wang, C.-Y. Facile Synthesis of ZnO/g-C3N4 Composites with Honeycomb-like Structure by H₂ Bubble Templates and Their Enhanced Visible Light Photocatalytic Performance. *J. Photochem. Photobiol. A Chem.*

- 2018, 355, 16–24, doi:10.1016/j.jphotochem.2017.12.016.
63. Liu, J.; Zhang, T.; Wang, Z.; Dawson, G.; Chen, W. Simple Pyrolysis of Urea into Graphitic Carbon Nitride with Recyclable Adsorption and Photocatalytic Activity. *J. Mater. Chem.* **2011**, *21*, 14398, doi:10.1039/c1jm12620b.
64. Yue, B.; Li, Q.; Iwai, H.; Kako, T.; Ye, J. Hydrogen Production Using Zinc-Doped Carbon Nitride Catalyst Irradiated with Visible Light. *Sci. Technol. Adv. Mater.* **2011**, *12*, 034401, doi:10.1088/1468-6996/12/3/034401.
65. Bai, P.; Wang, P.; Wu, Y.; Pang, X.; Song, M.; Du, C.; Su, Y. Junction of ZnIn_2S_3 and Bismuth Vanadate as Z-Scheme Photocatalyst for Enhanced Hydrogen Evolution Activity: The Role of Interfacial Interactions. *J. Colloid Interface Sci.* **2022**, *628*, 488–499, doi:10.1016/j.jcis.2022.08.078.
66. Huang, W.; Li, Z.; Wu, C.; Zhang, H.; Sun, J.; Li, Q. Delaminating Ti_3C_2 MXene by Blossom of ZnIn_2S_4 Microflowers for Noble-Metal-Free Photocatalytic Hydrogen Production. *J. Mater. Sci. Technol.* **2022**, *120*, 89–98, doi:10.1016/j.jmst.2021.12.028.
67. Zhu, Y.-P.; Li, M.; Liu, Y.-L.; Ren, T.-Z.; Yuan, Z.-Y. Carbon-Doped ZnO Hybridized Homogeneously with Graphitic Carbon Nitride Nanocomposites for Photocatalysis. *J. Phys. Chem. C* **2014**, *118*, 10963–10971, doi:10.1021/jp502677h.
68. Xing, H.; Ma, H.; Fu, Y.; Xue, M.; Zhang, X.; Dong, X.; Zhang, X. Preparation of g- $\text{C}_3\text{N}_4/\text{ZnO}$ Composites and Their Enhanced Photocatalytic Activity. *Mater. Technol.* **2015**, *30*, 122–127, doi:10.1179/1753555714Y.0000000216.
69. Das, J.; Pradhan, S.K.; Sahu, D.R.; Mishra, D.K.; Sarangi, S.N.; Nayak, B.B.; Verma, S.; Roul, B.K. Micro-Raman and XPS Studies of Pure ZnO Ceramics. *Phys. B Condens. Matter* **2010**, *405*, 2492–2497, doi:10.1016/j.physb.2010.03.020.
70. Kumaresan, N.; Sinthiya, M.M.A.; Sarathbavan, M.; Ramamurthi, K.; Sethuraman, K.; Babu, R.R. Synergetic Effect of g- $\text{C}_3\text{N}_4/\text{ZnO}$ Binary Nanocomposites Heterojunction on

- Improving Charge Carrier Separation through 2D/1D Nanostructures for Effective Photocatalytic Activity under the Sunlight Irradiation. *Sep. Purif. Technol.* **2020**, 244, 116356, doi:10.1016/j.seppur.2019.116356.
71. Yang, P.; Wang, J.; Yue, G.; Yang, R.; Zhao, P.; Yang, L.; Zhao, X.; Astruc, D. Constructing Mesoporous g-C₃N₄/ZnO Nanosheets Catalyst for Enhanced Visible-Light Driven Photocatalytic Activity. *J. Photochem. Photobiol. A Chem.* **2020**, 388, 112169, doi:10.1016/j.jphotochem.2019.112169.
 72. Yu, W.; Xu, D.; Peng, T. Enhanced Photocatalytic Activity of g-C₃N₄ for Selective CO₂ Reduction to CH₃OH via Facile Coupling of ZnO: A Direct Z-Scheme Mechanism. *J. Mater. Chem. A* **2015**, 3, 19936–19947, doi:10.1039/C5TA05503B.
 73. Pérez-Molina, Á.; Pastrana-Martínez, L.M.; Pérez-Poyatos, L.T.; Morales-Torres, S.; Maldonado-Hódar, F.J. One-Pot Thermal Synthesis of g-C₃N₄/ZnO Composites for the Degradation of 5-Fluoruracil Cytostatic Drug under UV-LED Irradiation. *Nanomaterials* **2022**, 12, 340, doi:10.3390/nano12030340.
 74. Moussa, H.; Chouchene, B.; Gries, T.; Balan, L.; Mozet, K.; Medjahdi, G.; Schneider, R. Growth of ZnO Nanorods on Graphitic Carbon Nitride gCN Sheets for the Preparation of Photocatalysts with High Visible-Light Activity. *ChemCatChem* **2018**, 10, 4973–4983, doi:10.1002/cctc.201801206.
 75. Liu, T.; Li, Y.; Du, Q.; Sun, J.; Jiao, Y.; Yang, G.; Wang, Z.; Xia, Y.; Zhang, W.; Wang, K.; et al. Adsorption of Methylene Blue from Aqueous Solution by Graphene. *Colloids Surfaces B Biointerfaces* **2012**, 90, 197–203, doi:10.1016/j.colsurfb.2011.10.019.
 76. Liang, X.; Fan, J.; Liang, D.; Xu, Y.; Zhi, Y.; Hu, H.; Qiu, X. Surface Hydroxyl Groups Functionalized Graphite Carbon Nitride for High Efficient Removal of Diquat Dibromide from Water. *J. Colloid Interface Sci.* **2021**, 582, 70–80, doi:10.1016/j.jcis.2020.08.011.

-
77. Guo, X.-Z.; Han, S.-S.; Yang, J.-M.; Wang, X.-M.; Chen, S.-S.; Quan, S. Effect of Synergistic Interplay between Surface Charge, Crystalline Defects, and Pore Volume of MIL-100(Fe) on Adsorption of Aqueous Organic Dyes. *Ind. Eng. Chem. Res.* **2020**, *59*, 2113–2122, doi:10.1021/acs.iecr.9b05715.
78. Yao, Y.; Xu, F.; Chen, M.; Xu, Z.; Zhu, Z. Adsorption Behavior of Methylene Blue on Carbon Nanotubes. *Bioresour. Technol.* **2010**, *101*, 3040–3046, doi:10.1016/j.biortech.2009.12.042.
79. Sun, Q.; Sun, Y.; Zhou, M.; Cheng, H.; Chen, H.; Dorus, B.; Lu, M.; Le, T. A 2D/3D g-C₃N₄/ZnO Heterojunction Enhanced Visible-Light Driven Photocatalytic Activity for Sulfonamides Degradation. *Ceram. Int.* **2022**, *48*, 7283–7290, doi:10.1016/j.ceramint.2021.11.289.
80. Khatun, A.; Furukawa, M.; Tateishi, I.; Katsumata, H.; Suhag, M.H.; Islam, J.B.; Kaneco, S. Photocatalytic Degradation of Endocrine Disrupting Chemical 17- α Ethinylestradiol by TiO₂ Nanoparticles Under Solar Light Irradiation. *Environ. Process.* **2024**, *11*, 1, doi:10.1007/s40710-023-00678-z.
81. Zhang, Y.; Thomas, A.; Antonietti, M.; Wang, X. Activation of Carbon Nitride Solids by Protonation: Morphology Changes, Enhanced Ionic Conductivity, and Photoconduction Experiments. *J. Am. Chem. Soc.* **2009**, *131*, 50–51, doi:10.1021/ja808329f.

CHAPTER FIVE

Summary and Thesis Conclusions

5.1 Summary and Thesis Conclusions

Due to the improper discharge of organic pollutants, water is polluted. These pollutants are harmful for both human health and the aquatic environment. Hence, it is very necessary to treat the effluent containing organic pollutants prior to discharge to the environment. Photocatalytic degradation of organic pollutants has been considered one of the most effective methods. Among numerous photocatalysts, g-C₃N₄ based heterojunction composites have been considered potential visible light-responsive photocatalysts. This work demonstrated the fabrication and characterization of several ZnO/g-C₃N₄ composites and was applied to the photocatalytic degradation of bisphenol E and diclofenac aqueous solutions. Furthermore, the ZnO/g-C₃N₄ composites have been applied to the removal of orange II dye from its aqueous solution via adsorption and photocatalysis approaches.

✧ In Chapter One

A literature review on the source and adverse effects of bisphenols, diclofenac, and synthetic dyes has been reported. The possible organic pollutant removal techniques have been mentioned briefly. The benefits and drawbacks of using g-C₃N₄ based materials have been mentioned. The advantages of composites containing g-C₃N₄ as a photocatalyst and adsorbent have been discussed.

✧ In Chapter two

A facile one-step calcination of urea and zinc acetate mixture produced the ZnO/g-C₃N₄ composite. The percentage of ZnO content in the composite was determined by TGA. By using FTIR, XPS, SEM, FE-EPMA, and TEM investigation, the formation of the composite was confirmed. UV-Vis DRS analysis revealed the higher visible light absorption ability of the composite. By using PL and EIS analysis of the composite, the reduction of photogenerated electron hole pair recombination was assessed. The photocatalytic efficiency of the synthesized

composite was assessed in the degradation of bisphenol E (BPE). Under optimal condition, the degradation rate of BPE with ZnO/g-C₃N₄ composite was 8 times higher than that attained with pure g-C₃N₄. The radical scavenger studies specified that the $\cdot\text{O}_2^-$ and h^+ species were mainly responsible for the degradation of BPE. The stability experiment indicated the chemical and photo stability of the synthesized composite. Possible two photocatalytical mechanisms have been proposed.

✧ In Chapter Three

ZnO was simply deposited on g-C₃N₄ and calcined to generate ZnO/g-C₃N₄ composites. According to structural (XRD, FTIR, and XPS) and morphological (SEM, TEM, and EDS elemental mapping) analysis, the composite was successfully formed. On the other hand, based on PL and EIS analysis, the recombination of photocharges was reduced in the fabricated composite. The photocatalytic activity of the synthesized composite was evaluated in the degradation of diclofenac (DCF). The photocatalytic degradation rate of DCF using ZnO/g-C₃N₄ composite was 27 times higher than that attained with pure g-C₃N₄ and 11 times higher than that attained with physical mixture of ZnO and g-C₃N₄. The radical scavenger studies indicated that the superoxide anion radical ($\cdot\text{O}_2^-$) and hydroxyl radical ($\cdot\text{OH}$) act as reactive species during the degradation reaction. Possible photocatalytic degradation mechanism and corresponding reactions have been proposed.

✧ In Chapter Four

ZnO modified g-C₃N₄ (ZCN) composites were fabricated by a simple calcination of mixtures of urea and zinc acetate. The ZCN composites were utilized as bifunctional adsorptive photocatalysts for orange II removal from aqueous solution through adsorption and photocatalysis processes. The adsorption isotherm data of the g-C₃N₄ (g-CN) and ZCN composites on orange II solution were better fitted with the Langmuir isotherm compared to

the Freundlich isotherm. The maximum adsorption capacity for ZCN-2.5 was slightly higher than that of bare g-CN. According to the adsorption thermodynamics investigation of ZCN-2.5 on orange II solution, the positive values of Gibb's free energy change (ΔG^0) suggested non-spontaneous adsorption process. Furthermore, the negative values of entropy change (ΔS) and enthalpy change (ΔH) indicated the decrement of randomness and exothermic nature during the adsorption process. The adsorption of orange II dye on the ZCN composites is attributed to the π - π interactions, electrostatic interactions, H-bonding, acid-bas interactions between the composite and dye, and pore filling of the composites. The photocatalytic degradation kinetics of g-CN and ZCN composites indicated that the degradation process follows the pseudo-first-order reaction kinetic. The degradation rate of orange II with the ZCN-2.5 composite was 6.67 times higher than that obtained with bare g-CN. The enhanced photocatalytic degradation of orange II dye solution using ZCN composites with visible light irradiation is attributed to the enhanced visible light absorption efficacy and decrement of photogenerated e^-/h^+ pair recombination. Possible adsorption and photocatalytic mechanisms have been proposed.

✧ In Chapter Five

The conclusion about the advancement of visible light-induced photocatalytic technology for degradation of BPE, DCF, and orange II using ZnO/g-C₃N₄ composites is described.

List of Published Articles

1. “One-Step Fabrication of ZnO/g-C₃N₄ Composite for Visible Light-Responsive Photocatalytic Degradation of Bisphenol E in Aqueous Solution.”

Mahmudul Hassan Suhag, Aklima Khatun, Ikki Tateishi, Mai Furukawa, Hideyuki

Katsumata, Satoshi Kaneco, ACS Omega, 2023, 8, 11824-11836.

<https://doi.org/10.1021/acsomega.2c06678>

2. “Visible Light Induced Photocatalytic Degradation of Diclofenac in Aqueous Solution Using Fabricated ZnO/g-C₃N₄ by Facile Calcination Technique.”

Mahmudul Hassan Suhag, Aklima Khatun, Ikki Tateishi, Mai Furukawa, Hideyuki Katsumata,

Satoshi Kaneco, ACS Omega (in press)

<https://doi.org/10.1021/acsomega.4c05679>

3. “Purification of aqueous orange II solution through adsorption and visible-light-induced photodegradation using ZnO-modified g-C₃N₄ composites.”

Mahmudul Hassan Suhag, Aklima Khatun, Ikki Tateishi, Mai Furukawa, Hideyuki Katsumata,

Satoshi Kaneco, RSC Advances, 2024, 14, 17888-17900.

<https://doi.org/10.1039/D4RA01481B>

List of Attending Conference

1. “Photocatalytic Degradation of Bisphenol E by ZnO/g-C₃N₄ Composite Photocatalyst Under Visible Light Irradiation”

Mahmudul Hassan Suhag, Mai Furukawa, Ikki Tateishi, Hideyuki Katsumata, Satoshi Kaneco

12th International Symposium for Sustainability by Engineering.

Mie University, Japan. 27-28th September 2022.

2. “Visible Light Responsive Photocatalytic Degradation of Diclofenac in water using ZnO/g-C₃N₄ Composite Photocatalyst”

Mahmudul Hassan Suhag, Mai Furukawa, Ikki Tateishi, Hideyuki Katsumata, Satoshi Kaneco

13th International Symposium for Sustainability by Engineering.

Mie University, Japan. 27-28th September 2023.

3. “ZnO/g-C₃N₄ Composites for Removal of Aqueous Orange II Solution via Adsorption and Photodegradation”

Mahmudul Hassan Suhag, Aklima Khatun, Ikki Tateishi, Mai Furukawa, Hideyuki Katsumata,

Satoshi Kaneco 13th Int. Conf. on Geotechnique, Construction Materials & Environment.

Tsu, Mie, Japan, 14-16th November 2023.